

Design and Development of ZnO Nanosheet based Nanogenerators to Drive Self-Powered Systems

*Thesis submitted in partial fulfillment of the requirements
for the award of the degree of*

DOCTOR OF PHILOSOPHY

by

SUPRAJA POTU

(Roll No:701965)

Supervisor:

Dr. R. RAKESH KUMAR



**DEPARTMENT OF PHYSICS
NATIONAL INSTITUTE OF TECHNOLOGY
WARANGAL-506 004, (T.S.), INDIA**

JAN 2024

Dedicated to.....

My Parents

*Balreddy &
Vinodha*

My Brother

Arun Kumar

My Family Members and Friends

*“There are no secrets to success.
It is the result of preparation,
hard work, and learning
from failures”*

- Colin Powell



DEPARTMENT OF PHYSICS
NATIONAL INSTITUTE OF TECHNOLOGY
WARANGAL – 506 004

CERTIFICATE

This is to certify that the work presented in the thesis entitled "***Design and Development of ZnO Nanosheet based Nanogenerators to Drive Self-Powered Systems***" is being submitted by **Ms. Supraja Potu** (Roll No. 701965) to the Department of Physics, National Institute of Technology (NIT) Warangal, for the award of degree ***Doctor of Philosophy***, is a record of bonafide research work carried out by her under our supervision/guidance. We further state that this work has not been submitted to any other University or Institution in part or full for the award of any degree.

R. Rakesh Kumar
(Dr. R. RAKESH KUMAR) 11124
Supervisor

T. Venkappa Rao
(Prof. T. VENKATAPPA RAO)
Prof. & Head, Physics Dept
01/01/2024

Date: 01st January 2024
Place: NIT Warangal

Declaration

This is to certify that the work presented in the Ph.D. thesis entitled ***Design and Development of ZnO Nanosheet based Nanogenerators to Drive Self-Powered Systems*** is a bonafide work done by me under the supervision of **Dr. R. Rakesh Kumar** in the Department of Physics, National Institute of Technology (NIT) Warangal and was not submitted elsewhere for the award of any degree.

I declare that this written submission represents my ideas in my own words and where others' ideas or words have been included, I have adequately cited and referenced the original sources. I also declare that I have adhered to all principles of academic honesty and integrity and have not misrepresented or fabricated or falsified any idea/data/fact/source in my submission. I understand that any violation of the above will be a cause for disciplinary action by the Institute and can also invoke penal action from the sources which have thus not been properly cited or from whom proper permission has not been taken when needed.

P. supraba.
(SUPRAJA POTU)
Ph.D. Scholar
Roll No.: 701965

Place: NIT Warangal
Date: 01st January 2024

Table of Contents

Acknowledgements.....	(i)
Preface	(vi)
List of Figures	(xi)
List of Tables	(xx)
List of Abbreviations	(xxi)
List of Symbols	(xxii)

Chapter-1 Introduction

1.1 Research motivation	2
1.2 Non-renewable and Renewable energy sources	3
1.3 Nanogenerators	4
1.4 Origin of nanogenerators	5
1.4.1 Maxwell's displacement current in nanogenerators	6
1.4.2 Capacitive model	9
1.5 Types of nanogenerator technologies	10
1.5.1 Pyroelectric nanogenerators	10
1.5.2 Thermoelectric nanogenerators	11
1.5.3 Piezoelectric nanogenerators	12
1.5.4 Triboelectric nanogenerators	13
(a) Electronic band structure model	
(b) Interatomic interaction model	
1.6 Bio-Mechanical energy harvesting	17
1.7 PENG: materials, and applications	18
1.7.1 Piezoelectric materials	18
1.7.2 Applications	19
1.8 TENG: working modes, materials, and applications	20
1.8.1 TENG modes	20
1.8.1.1 Contact separation mode	21
1.8.1.2 Lateral sliding mode	22
1.8.1.3 Single electrode mode	22
1.8.1.4 Free-standing mode	23
1.8.2 Triboelectric series	23
1.8.3 Surface modification	24
1.8.4 Applications	26
1.9 Selection of source material and its properties	28
1.9.1 Basic properties of ZnO	30
1.9.2 Piezoelectricity in ZnO	31
1.10 Objectives of thesis	32
1.11 Conclusions	33
1.12 References	33

Chapter-2 Experimental Methods and Characterization

2.1	Synthesis of ZnO nanosheets using hydrothermal method	43
2.2	Characterization techniques	45
2.2.1	X-ray diffraction (XRD)	45
2.2.2	Scanning electron microscopy (SEM)	46
2.2.3	Transmission electron microscopy (TEM)	47
2.2.4	Energy dispersive spectroscopy (EDS)	48
2.2.5	Fourier transform infrared spectroscopy (FTIR)	49
2.2.6	Raman spectroscopy	50
2.2.7	Photoluminescence spectroscopy (PL)	51
2.2.8	Atomic force microscopy (AFM)	52
2.2.9	Polarizing optical microscope (POM)	53
2.2.10	Scanning kelvin probe microscopy (SKP)	54
2.3	Nanogenerator Device Design	55
2.3.1	Piezoelectric nanogenerator device fabrication	55
2.3.2	Triboelectric nanogenerator device fabrication	56
2.4	Instruments used to test nanogenerator device electrical properties	57
2.4.1	Digital storage oscilloscope	58
2.4.2	Current pre-amplifier	58
2.4.3	Tapping machine	59
2.4.4	Other components	59
2.4.4.1	Resistance box	59
2.4.4.2	Bridge rectifier and different Capacitors	61
2.4.5	COMSOL multi-physics software	62
2.4.6	Some of important calculated parameters	63
2.4.6.1	Force calculation	63
2.4.6.2	Efficiency calculation	64
2.5	The circuits used in applications of TENG	65
2.6	Conclusions	65
2.7	References	66

Chapter-3 Synthesis and Fabrication of Zinc Oxide Nanosheet based Piezo and Triboelectric Nanogenerator for Energy Harvesting

3.1	Introduction	70
3.2	Experimental section	71
3.2.1	Materials	71
3.2.2	ZnO nanosheets synthesis	71
3.2.3	Nanogenerator device fabrication	71

3.2.3.1	Piezoelectric nanogenerator device fabrication	71
3.2.3.2	Triboelectric nanogenerator device fabrication	71
3.3	Results and Discussion	72
3.3.1	SEM and EDS analysis	72
3.3.2	XRD analysis	74
3.3.3	TEM analysis	75
3.3.4	Piezoelectric nanogenerator device studies	75
3.3.5	Triboelectric nanogenerator device studies	79
3.4	Applications of TENG device	82
3.5	Conclusions	83
3.6	References	83

Chapter-4 A Simple and Low-cost Triboelectric Nanogenerator Based on Two Dimensional ZnO Nanosheets and Its Application in Portable Electronics

4.1	Introduction	89
4.2	Experimental section	92
4.2.1	Materials	92
4.2.2	ZnO nanosheets synthesis	92
4.2.3	Triboelectric nanogenerator device fabrication	92
4.3	Results and Discussion	92
4.3.1	SEM and XRD analysis	93
4.3.2	Triboelectric nanogenerator device studies	94
4.4	Applications	100
4.5	Conclusions	101
4.6	References	101
4.7	Supplementary Information	107

Chapter-5 High-Performance and Low-Cost Overhead Projector Sheet-Based Triboelectric Nanogenerator for Self Powered Cholesteric Liquid Crystal, Electroluminescence, and Portable Electronic Devices

5.1	Introduction	110
5.2	Experimental section	113
5.2.1	Materials	113
5.2.2	ZnO nanosheets synthesis	113
5.2.3	Triboelectric nanogenerator device fabrication	113
5.2.4	Preparation of different color CLC devices and testing with TENG	113
5.3	Results and Discussion	115
5.3.1	SEM, EDAX, and AFM analysis	115
5.3.2	XRD, FTIR, PL, and TEM analysis	116
5.3.3	Triboelectric nanogenerator device studies	117

5.4	Applications	124
5.4.1	Self-powered electroluminescence and portable electronic devices application	124
5.4.2	Self-powered CLC device applications	126
5.5	Conclusions	130
5.6	References	130
5.7	Supporting information	138

Chapter-6 Enhancing Triboelectric Nanogenerator Performance with Metal-Organic Framework Modified ZnO Nanosheets for Self-Powered Electronic Devices and Energy Harvesting

6.1	Introduction	141
6.2	Experimental section	144
6.2.1	Materials	144
6.2.2	ZnO nanosheets synthesis	144
6.2.3	Synthesis of ZIF-8@ZnO	144
6.2.4	Triboelectric nanogenerator device fabrication	146
6.3	Results and Discussions	146
6.3.1	SEM studies	146
6.3.2	XRD and Raman analysis	147
6.3.3	TENG output performance	148
6.4	Applications	154
6.4.1	Self-powered and portable electronic devices application	154
6.5	Conclusions	155
6.6	References	156
6.7	Supporting information	166

Chapter-7 Surface-Engineered High-Performance Triboelectric Nanogenerator for Self-Powered Health Monitoring and Electronics

7.1	Introduction	169
7.2	Experimental section	172
7.2.1	Materials	172
7.2.2	Surface modification of aluminum substrates using sandpapers	172
7.2.3	ZnO nanosheets synthesis	173
7.2.4	Synthesis of the PDMS film	173
7.2.5	Triboelectric nanogenerator device fabrication	174
7.3	Results and discussion	174
7.3.1	SEM and optical microscopic studies	174
7.3.2	AFM and XRD studies	175

7.3.3	FTIR and Raman analysis	177
7.3.4	SKP characterization of frictional layers	178
7.3.5	TENG output performance	180
7.4	Applications	188
7.4.1	Self-powered and portable electronic devices application	188
7.4.2	Applications of TENG in Bio-mechanical energy harvesting	190
7.4.3	Applications of TENG in health monitoring	191
7.5	Conclusions	192
7.6	References	192
7.7	Supporting information	201

Chapter-8 Summary, Conclusions and Scope for Future work

8.1	Summary and Conclusions	208
8.2	Scope for Future work	209
List of Publications		210
(A)	Publications related to thesis	210
(B)	Journal publications other than thesis	211
Curriculum Vitae		215

ACKNOWLEDGEMENTS

I extend my sincere gratitude to all individuals who made meaningful contributions to the research presented in this thesis. The completion of this work would not have been feasible without the invaluable support and close association with many individuals who consistently assisted me when needed. I take this opportunity to formally acknowledge and express my profound thanks for their significant role in making the realization of this thesis possible.

Foremost, I wish to convey my heartfelt appreciation to my advisor, **Dr. R. Rakesh Kumar**, for unwavering support throughout my Ph.D. study and research. His patience, motivation, enthusiasm, and profound knowledge have been instrumental in guiding me through the entire research process and thesis writing. I am immensely grateful for the privilege of having such a dedicated and knowledgeable advisor and mentor for my Ph.D. His scholarly insights, unwavering interest, consistent assistance, and affable demeanor have served as a constant source of inspiration. I anticipate that his invaluable suggestions will endure as an everlasting fount of scientific learning throughout my academic and professional journey. His support during personal struggles has left an indelible mark on my journey. Thank you for guiding me through both scholarly challenges and providing valuable insights that have contributed to my personal growth and well-being.

I convey my sincere thanks to present and former Directors **Prof. Bidyadhar Subudhi** and **Dr. N.V. Ramana Rao** of the National Institute of Technology, Warangal, for providing the opportunity to conduct this research and permitting the submission of this work in the form of a thesis. Additionally, my heartfelt thanks go to the Ministry of Human Resource Development (MHRD), New Delhi, for the financial support in the form of a fellowship.

I extend my sincere gratitude to **Prof. T. Venkata Appa Rao**, Head of the Department of Physics at NITW, for his invaluable suggestions and support. Furthermore, I express my sincere thanks to **Prof. D. Dinakar** and **Prof. K. Venugopal Reddy**, former Heads of the Department of Physics at NITW, for their valuable assistance and support.

Beyond acknowledging my appreciation for my advisor, I wish to extend my thanks to the remaining members of my thesis Doctoral Scrutiny Committee, **Prof. P. Abdul Azeem**, **Prof. D. Haranath**, Department of Physics, NITW, and **Prof. Vishnu Shankar**, Department of Chemistry NITW for their encouragement, insightful comments, and thought-provoking queries. Their commitment to dedicating time for valuable feedback during each progress meeting has played a significant role in enhancing the quality of my work.

I take this opportunity to convey my sincere thanks to **Prof. B. Sobha**, **Prof. P. Syam Prasad**, **Prof. Sourabh Roy**, **Prof. K. Thangaraju**, **Dr. Vijay Kumar**, **Dr. Surya K. Ghosh**, **Dr. Hitesh Borkar**, and **Dr. Aalu Boda** faculty from the Department of

Physics at NITW, for their invaluable advice, encouragement, and moral support throughout my career.

I express my utmost gratitude to my research collaborators, **Dr. Paul Joseph**, **Dr. V. Jayalakshmi**, Department of Physics, and **Dr. S Nagarajan**, Department of Chemistry, for generously sharing their expertise and insights to address my scientific and technical challenges.

I express my gratitude to **Prof. Murali Banavoth**, School of chemistry, University of Hyderabad, **Prof. C. Vanitha**, and **Dr. R. Arockia Kumar**, department of Department of Metallurgical and Materials Engineering, NITW, for providing instrumental facilities that significantly contributed to the progress of my research.

I extend my sincere gratitude to **Dr. K. Uday Kumar**, Department of Physics, and **Dr. K. Prakash**, Department of Electronics and Communication Engineering, for their various forms of support and collaboration in this research as well as in times when I needed it.

I extend my sincere appreciation to **Dr. Yuvaraj Sivalingam** of the Department of Nanotechnology at SRM Research Institute of Technology for the invaluable support and resources provided, which have significantly contributed to the success of my research endeavors.

I extend my special thanks to **Indian Science Technology and Engineering facilities Map (ISTEM)** for providing **COMSOL software** access for data simulation, your support is greatly appreciated.

I am indebted to my friends who shared challenging moments, provided encouragement, and celebrated every achievement. Special thanks go to my fellow lab mates in the **Energy Materials and Devices Group**, including **S. Chand Rakesh Roshan, Dr. Siju Mishra, P. Ravishankar, Anjaly Babu, Lakshmi Suneetha Vikram, M. Navaneeth, B. Laksha Koti, V. Mahesh, and K. Rajesh**. Our stimulating discussions and collaborative efforts that we developed while working before deadlines have been invaluable. The enjoyable moments we shared over the past four years are also fondly appreciated.

I express my gratitude to **all my research fellows** for dedicating their time and providing valuable suggestions. I have learnt many things from you, which have greatly contributed to both my research and personal growth.

I would like to express my special thanks to **R. Arun Kumar, R. Muniramaiah, Ravi Ketavath, and Arbacheena Bora** for their collaboration on our work. Their contributions have significantly contributed to the progress of my research profile. I extend my sincere thanks to **Mrs. Shirisha w/o Dr. Rakesh Kumar** for her support and encouragement.

I extend my heartfelt thanks to **Dr. K. Anu**, who played a pivotal role in assisting me at the end of my thesis. She is truly a god-gifted sister, and her support has been invaluable to me.

My special thanks to **Dr. Buchaiah Gollapelli** for his encouragement, support, and motivation during my tough times. I'm grateful for his mentorship and positive impact on my personal and professional journey.

I extend my gratitude to all those individuals, not explicitly mentioned here, who provided assistance, both direct and indirect, throughout this work. I am appreciative of the **non-teaching staff** in the Department of Physics and all other members of the **Central Research Instrument Facility** at NITW for their unwavering support.

Expressing my special thanks to **my best friend Sarika** for being part of the joyful moments since childhood and standing by me through the ups and downs. Grateful for the enduring friendship and shared memories.

Finally, I wish to express my gratitude to **friends and family members** who provided unwavering support during my tenure here. Foremost, I extend my thanks to my family—**my parents, Sri. Balreddy and Smt. Vinodha**, for bringing me into this world and supporting me spiritually throughout my life. Additionally, I appreciate the affection and constant support of **my brother Arun Kumar**, in every moment of my life.

(Supraja Potu)

Abstract

The never-ending quest for sustainable energy sources has led to the development of novel technology capable of harvesting ambient mechanical energy. Among these, piezoelectric and triboelectric nanogenerators have emerged as attractive opportunities for energy harvesting that are both efficient and environmentally beneficial. The investigation opens with a detailed examination of piezoelectric nanogenerators, clarifying the piezoelectric phenomenon and its application in transforming mechanical vibrations into electrical energy. Various materials are investigated for their applicability in improving the performance of piezoelectric nanogenerators. Following that, the thesis delves into triboelectric nanogenerators, which use the triboelectric effect to generate electricity through material friction. The detailed mechanism of the TENG that drives triboelectric charge generation is investigated, with a focus on the wide range of materials used, such as polymers, metals, and nanostructures. Innovative fabrication processes and surface engineering methodologies are being investigated to improve the output performance, scalability, and adaptability of the triboelectric nanogenerator.

The synthesis process involves the direct growth of ZnO nanosheets on an aluminum substrate, and their structural, morphological, compositional, and surface potential analyses are conducted to gain insights into the material's properties. Further, discusses a detailed analysis of the open circuit voltage, short circuit current, and durability of the ZnO nanosheet-based nanogenerators (PENG/TENG). The devices exhibit promising results, showcasing their potential for efficient energy harvesting. Notably, the study explores various applications, demonstrating the device's ability to charge capacitors and power small electronic devices such as light-emitting diodes (LEDs), digital thermometers, digital watches, etc, owing to the adaptability of PENGs and TENGs used in real-world applications, proving their adaptability in multiple domains.

Chapter 1 provides an introduction to the field of energy harvesting and its diverse energy sources. It briefly outlines the various types of nanogenerators and delves into strategies and methods to improve the output performance of TENGs. Additionally, this chapter explores the selection of materials and potential applications for the PENG and TENG devices.

Chapter 2 the process of synthesizing zinc oxide nanosheets (ZnO) using the hot plate-assisted hydrothermal method is detailed. This chapter discusses material characterization and justifies the usage of specialized approaches of the synthesized material, utilizing advanced tools for understanding its structural, morphological, compositional, and surface detail. The chapter also

provides insights into the steps involved in creating piezoelectric and triboelectric nanogenerator devices for mechanical energy harvesting. Furthermore, it elucidates the techniques employed for characterizing the devices characterizing devices and using instrumentation to assess their properties.

Chapter 3 deals with the synthesis of ZnO nanosheets, covering their characterization, results, and a detailed discussion. The chapter's focus includes optimizing the growth temperature and time for the synthesis of ZnO nanosheets. The study encompassed a range of temperatures from 50°C to 90°C, with a consistent growth duration of 4 hrs. Additionally, at a fixed growth temperature of 85°C, the growth time was varied from 1 hour to 6 hours. Surface morphology, crystalline properties, and microstructure analysis of the ZnO nanosheets were conducted using SEM, XRD, and TEM techniques. TEM revealed the 2D structure of the ZnO nanosheets, while EDAX confirmed their purity. Furthermore, PENG device was fabricated using the ZnO nanosheet film as the active piezoelectric layer, and ITO and aluminum served as electrodes. The chapter includes a comprehensive exploration of the device characterizations. Multiple PENG devices were tested, each employing ZnO nanosheets synthesized at varying growth temperatures and times. The growth conditions of 85°C for 4 hrs were optimized for the PENG device. The chapter also explores the switching polarity test and load characteristics of the PENG device. Notably, the maximum output voltage and power density for the PENG were recorded at 225 mV and 77 μ W/m², respectively. The response of the PENG to different finger-tapping forces was studied, demonstrating that increased pressure and deformation of the nanosheets resulted in higher output. This finding suggests potential applications in pressure and force sensing.

Additionally, the chapter discusses the fabrication of a Triboelectric Nanogenerator (TENG) device utilizing ZnO nanosheets as the tribo-layer, ITO, and aluminum as electrodes. Under hand tapping force, the TENG yielded an output voltage of 2 V, a current of 7 μ A, and a power density of 0.1 mW/m². The TENG was also used to charge various capacitors, achieving a maximum stored energy of 2.8 μ J. Notably, the TENG was capable of directly powering one LED under each hand-tapping force.

Chapter 4 delves into the synthesis and the characteristic properties of ZnO nanosheets and PET (Polyethylene Terephthalate). X-ray Diffraction (XRD) analysis confirmed the polycrystalline nature of ZnO nanosheets, and their distinctive nanosheet structure was verified through SEM analysis. A notable achievement discussed in this chapter is the fabrication of a simple and cost-effective TENG using ZnO nanosheet film and PET as triboelectric layers for

the first time. This TENG device demonstrated an impressive output, with an output voltage of 4.9 V, a current of 10 μ A, and a power density of 1 mW/m². The chapter also explored the TENG's output response at different frequencies of hand tapping, ranging from 1 to 7 Hz, and varied the active areas of the devices for comprehensive study.

The TENG's stability was rigorously tested, more than 1000 cycles, demonstrating its durability and reliability over numerous cycles. Furthermore, the chapter delved into the charging characteristics of various capacitors and examined stored voltage, charge, and energy concerning the load capacitor. The TENG achieved a maximum stored charge of 40 μ C and stored energy of 16.9 μ J. Further, The TENG successfully powered three LEDs directly, and the stored energy in the capacitor enabled the activation of a digital watch and 24 LEDs. This underscores its potential as a promising solution for self-powered sensors and devices.

Chapter 5 focuses shifts to the utilization of ZnO nanosheets in conjunction with Overhead Projector (OHP) sheets for TENG devices in various applications. An innovative addition to this chapter is the introduction of OHP sheets as a novel triboelectric layer. OHP sheets, composed of transparent PET material, possess pre-charged properties on one side, making them efficient at receiving ink particles. The existence of charge on the OHP sheets reduces the surface ion injection step. Comprehensive morphological, elemental, and structural analyses were conducted using SEM, EDX, and XRD techniques. Additionally, Atomic Force Microscopy (AFM) confirmed that the ZnO nanosheet film exhibited greater roughness compared to the OHP sheet. This rougher surface configuration forms a more effective contact area, contributing to the generation of high output power in the TENG. A high-performance TENG device was fabricated, leveraging ZnO nanosheets and OHP sheets as frictional layers. The TENG device exhibited notable characteristics, with an output voltage of 150 V, a current of 34.5 μ A, and an impressive power density of 424 mW/m².

The stability of the TENG was rigorously tested, demonstrating its robust performance with over 4,300 cycles under hand tapping and 10,000 cycles under machine tapping. Moreover, the effects of different active areas of TENG devices, varying frequencies of applied forces, and different magnitudes of applied force were thoroughly investigated. Notably, the TENG device achieved remarkable results, with a maximum stored voltage of up to 9 V, a stored charge of 150 μ C, and a stored energy of 160 μ J, observed under the optimal load capacitance of 47 μ F. In a practical demonstration of its capabilities, the TENG directly powered 135 LEDs and a digital watch when subjected to hand-tapping forces. Additionally, the TENG was employed to power an electroluminescence device, which finds potential applications in e-paper and

digital billboard technologies. Leveraging the TENG's high-output performance, it was integrated with Cholesteric liquid crystal (CLC) devices, opening the door to a range of real-time applications. These applications include secure authentication devices, such as facial unlocking in mobile phones and QR code scanning. Furthermore, the TENG was used to drive smart windows and CLC displays, which capitalize on the CLC's ability to control transparency in the planar state and opacity in the focal conic state. This integration allowed for the display of letters and various information on CLC devices, expanding their utility.

Chapter 6 A key innovation in this chapter was the surface modification of ZnO nanosheets was introduced to enhance the output of the TENG. We have synthesized ZnO nanosheets on aluminum substrate with any seed layer using hotplate assisted hydrothermal method. The surface of ZnO nanosheets was modified by the direct growth of Zeolitic imidazolate framework-8 (ZIF-8) crystals using the hydrothermal method. ZIF-8, belonging to the Metal-Organic Framework (MOF) family, consists of metal ions (Zn^{2+}) and organic linkers (imidazolate). Structural and morphological analyses of both ZnO and ZnO modified with ZIF-8 ($ZnO@ZIF-8$) were conducted. XRD and Raman spectra confirmed the successful formation of ZIF-8 on ZnO nanosheets. The TENG device employing $ZnO@ZIF-8$ and PMMA as triboelectric layers exhibited significant improvements, achieving an output voltage of 200 V, a current of 41.5 μ A, and a substantial power density of 800 mW/m². This performance represented nearly a twofold increase compared to ZnO-based TENGs. To validate this enhancement, the work function of ZnO and $ZnO@ZIF-8$ films was studied. The work function difference was notably greater for $ZnO@ZIF-8$ and PMMA compared to ZnO and PMMA. A larger work function difference enhances electron transfer, contributing to the enhanced output performance of the TENG. Additionally, the chapter explored the characteristics of charging capacitors under hand-tapping forces, examined the TENG's stability over an extended duration, and tested it under machine tapping for approximately 20 minutes, equivalent 4800 cycles. Notably, the $ZnO@ZIF-8$ TENG demonstrated its ability to directly power various electronic devices, including an electronic watch, calculator, and thermometer. Impressively, it directly powered 180 LEDs without any storage element, highlighting its potential for real-time self-powered devices and biomechanical energy harvesting applications.

Chapter 7 discusses a high-performance TENG is achieved through a surface engineering method involving emery papers to modify the surface of one of the triboelectric layers. This innovative approach offers several advantages, notably its cost-effectiveness and simplicity. The methodology involves scratching the aluminum substrate surface with different grit sizes

of emery papers, ranging from 80 to 400, in one direction multiple times, followed by the incorporation of ZnO nanosheets using a hydrothermal method. This process not only increases the surface area but also enhances contact points, resulting in improved output.

Under an optical microscope, all the samples were examined, and it was observed that the use of P220 grit-size emery paper created optimum roughness and provided more contact points. SEM analysis of the ZnO nanosheets confirmed that the density of the nanosheets increased after the modification of the aluminum substrate, while PDMS exhibited a smoother surface. The work function of various samples was measured, and it was found that ZnO nanosheets incorporated on scratched aluminum with P220 grit size (ZnO-Al₂₂₀) had a lower work function. Additionally, the work function difference was higher between PDMS and ZnO-Al₂₂₀(T12). This TENG exhibited the potential for the highest output due to its enhanced electron transfer between the tribo-layers.

Multiple TENG devices were fabricated and tested for their output responses, with the T12 TENG producing the highest output voltage, aligning with the work function measurements. The T12 TENG generated the highest output voltage, current, and power density, reaching 1442 V, 155 μ A, and 10.8 W/m², respectively. To gain insights into the electrical potential distribution and charge transfer process of the TENG device, finite element simulations were conducted using COMSOL 6.0 software. The stability of the TENG was thoroughly tested through repeated applied forces over 13,000 cycles at a frequency of 3-4 Hz.

The chapter also explored various experimental parameters affecting the TENG device (T12), including the active area, frequency of hand-tapping forces, spacing between triboelectric layers, and application of different hand-tapping forces. Impressively, the TENG powered 820 LEDs and activated various electronic gadgets. The TENG device's high sensitivity was further harnessed by attaching it to the human body's chest to monitor output voltage and current signals generated by different breathing patterns. This allowed for the detection of various respiration rates, including normal, deep, and rapid breathing. The TENG device holds significant promise for convenient and accurate breath monitoring, potentially impacting health management and optimizing athletic performance.

Chapter 8 describes the general summary, conclusions, and scope for future work

List of Figures

Figure. No	Figure Caption	Page. No
Figure. 1.1	Energy sources are available in nature: renewable and non-renewable energy sources.	2
Figure. 1.2	The energy sources usage in OCED countries	3
Figure. 1.3	Benefits and limitations of the mechanical energy harvesters.	6
Figure. 1.4	A comparison of theoretical foundation between the EMG and the nanogenerator	7
Figure. 1.5	A visual representation of the revised Maxwell's displacement current	9
Figure. 1.6	Mechanism of pyroelectric effect. (a) before and (b) after applied the temperature	11
Figure. 1.7	(a) Operating principle, (b) Schematic diagram of thermoelectric nanogenerator	12
Figure. 1.8	Principle of piezoelectric effect.	12
Figure. 1.9	Triboelectric nanogenerator working principle (a) contact electrification, (b) electrostatic induction.	13
Figure. 1.10	Schematic representation of the energy band diagram for the contact between two dielectric materials, (i) contacting, (ii) separating, (iii) separated, and (iv) approaching to contact.	15
Figure. 1.11	Schematic representation of the interatomic interaction model for the contact between two dielectric materials, (i) contacting, (ii) separating, (iii) separated, and (iv) approaching to contact.	16
Figure. 1.12	The list of piezoelectric materials.	18
Figure. 1.13	PENG applications	19
Figure. 1.14	Fundamental working modes of TENG.	21
Figure. 1.15	List of tribo-materials based on its triboelectric charge density.	24
Figure. 1.16	Surface modification methods	25
Figure. 1.17	Applications of TENG	27
Figure 1.18	(a) load vs Displacement curves of ZnO nanorods and nanosheets by using Nanoindentation testing, Schematic representation of the (b-d) ZnO nanorods and (e-g) nanosheets, respectively, depending on the applied load of below and above critical load (Pcrit)	30

Figure. 1.19	Crystal structures of ZnO: (a) Zinc blende, (b) rock salt, (c) wurtzite.	31
Figure. 1.20	Piezoelectricity in ZnO.	31
Figure. 2.1	(a). Schematic of the preparation steps of ZnO nanosheets and experimental setup of hot plate synthesis of ZnO nanosheets. Real-time images of the preparation steps of ZnO nanosheets (b) bare aluminum substrate, (c) aluminum substrate sealed with Kapton tape (d) substrate suspended in the growth solution in a sealed glass beaker, (e)-(f) growth solution beaker placed over the hot plate and solution temperature observed by using digital thermometer and thermocouple (g)-(h) aluminum substrate after the growth of ZnO nanosheets with the removal of Kapton tape.	43
Figure. 2.2	(a) Schematic representation of the X-ray diffraction principle, (b) Photograph of PANanalytical powder diffractometer instrument	45
Figure. 2.3	(a) Schematic representation of the SEM principle, (b) Photograph of SEM instrument.	46
Figure. 2.4	(a) Schematic representation of interaction between specimen and electron beam, (b) Photograph of TEM instrument.	47
Figure. 2.5	Schematic representation of the EDX principle.	48
Figure. 2.6	(a) Schematic representation of working of FTIR (b) Photograph of FTIR instrument	49
Figure. 2.7	Raman spectroscopy instrumentation	50
Figure. 2.8	Basic instrumentation of Photoluminescence spectrometer	51
Figure. 2.9	(a) the schematic view of the AFM instrumentation (b) AFM instrument	52
Figure. 2.10	(a) Schematic representation of the optical polarizing microscopy instrumentation, (b) Visual depiction of the optical polarizing microscope setup.	53
Figure. 2.11	(a) schematic of Scanning Kelvin Probe Microscopy instrumentation, (b) Scanning Kelvin Probe Microscopy setup.	54
Figure. 2.12	Schematic and real time images of (a & e) ZnO coated aluminum (b & f) ITO coated PET (c& g) fabricated PENG device (d & h) the PENG interfaced with connecting wires.	56
Figure. 2.13	(a) Schematic of the TENG fabrication steps, real-time images of TENG device fabrication steps (b) acrylic base sheets, ZnO film, another tribo-layer, (c) ZnO nanosheet film on aluminum attached to one of the acrylic bases, (d) another tribo-layer	57

attached to another acrylic base with tribo-layer facing up, (e) final TENG device with electrode connection for response measurement.

Figure. 2.14	Photographs of digital storage oscilloscopes (a) Tektronix TBS1102 (b) GW Instek GDS-1102B.	58
Figure. 2.15	(a) Schematic of circuit connections of current to voltage converter circuit, (b) Photograph of the developed circuit on PCB.	58
Figure. 2.16	Photograph of SR 570 Current pre amplifier.	59
Figure. 2.17	(a-b) photograph of developed tapping test set up, (c) Sewing machine tapping. we have developed a proto-type homemade setup for tapping the TENG using a simple DC motor and sewing machine Figure 2.17 (a-c). Furthermore, we have linear motor and sewing machine set up to test the stability of TENG.	60
Figure 2.18	Decade resistance box	61
Figure. 2.19	(a) Bridge rectifier, (b) capacitor box	61
Figure. 2.20	Window of the COMSOL software.	62
Figure. 2.21	Current peak at load resistance of $4M\Omega$ in (a) forward (b) reverse.	64
Figure. 2.22	Schematic of powering electronic devices through the (a) rectifier directly, (b) capacitor integrated to rectifier.	65
Figure. 3.1	(a)-(j) Morphology and EDS spectra of the ZnO films obtained at different temperatures from 50 to 95°C.	72
Figure. 3.2	(a)-(j) Morphology and EDS spectra of the ZnO films obtained at different growth duration times from 1 hr to 6 hrs.	73
Figure. 3.3	(a)-(b) XRD of the ZnO films obtained at different growth temperatures and duration time.	74
Figure. 3.4	(a) TEM image of the ZnO nanosheet, (b) SAED pattern recorded on the ZnO nanosheets, (c) EDX spectrum recorded on the ZnO nanosheet.	75
Figure. 3.5	Output response of ZnO nanosheets based PENG (a,c) Output voltage, and (b,d) Average output voltage at different growth temperatures and durations, respectively.	76
Figure. 3.6	Nanogenerator output characteristics against finger tapping (a) Forward and reverse connection response, (b) Output voltage of the series connected seven nanogenerators, (c) Average output voltage of the nanogenerator across different load resistances, (d) Output power variation with variable load resistance, (e) Response of the nanogenerator against different finger tapping	78

pressures, (f) Average output voltage of the nanogenerator as a function of different finger tapping pressures.	
Figure. 3.7 (a) Nanogenerator response over 1100 cycles of finger tapping, (b)-(c) Magnified view of the selected region of the cycle test, (d) Nanogenerator output at different cycle numbers.	79
Figure. 3.8 (a) SEM image of ITO thin film, (b) schematic view of TENG device, (c) V_{oc} in forward and reverse connection of TENG device, (d) I_{sc} in forward and reverse connection of TENG device. TENG reponse at different R_L values (e) Average values of V_{oc} , I_{sc} as a function of different R_L (f) Instantaneous power the TENG device at across different R_L .	80
Figure. 3.9 (a) Stability of TEN response over 593 cycles, (b) Enlarged view of selected portion of the stability graph. SEM images of (c) ZnO nanosheets (d) ITO thin film after the stability test.	81
Figure. 3.10 Different capacitors (a) Charging curves, b) Stored charge curves as function of time, (c) Charged voltage, and stored charge, (d) Stored energy as a function of load capacitance.	82
Figure. 4.1 SEM images of (a) ZnO nanosheets, (b) PET surface, XRD pattern of (c) ZnO nanosheet film, (d) PET surface.	93
Figure. 4.2 (a) V_{oc} of TENG device with different electrodes. V_{oc} of TENG device under switching polarity test of (b) acrylic support, (c) cardboard support, (d) I_{sc} of TENG device under switching polarity test, (e) V_{oc} and I_{sc} measured as a function of different load resistances, (f) instantaneous output power of the TENG device as a function of different load resistances.	94
Figure. 4.3 TENG output voltage as a function of (a) different frequency, (b) different area, (c) different spacing and, (d) different force, variation of average output voltage with (e) different frequency, (f) different area, (g) different spacing and, (h) different force, respectively.	96
Figure. 4.4 (a) TENG stability under 1395 cycles, (b) TENG response of some random cycles selected from the stability graph (c) every 50th cycle number output voltage values from the Figure (a). (d) stability of the TENG at different time points.	98
Figure. 4.5 (a) response of the TENG against hand tapping with (black) and without (red) antistatic gloves, (b) TENG open-circuit voltage after rectification, (c) Different load capacitors charging curves as a function of time, (d) stored charge curves of different load capacitors as a function of time, (e) the charged voltage and stored charges as a function of load capacitance (C_L), (f) the stored energy as a function of C_L .	99
Figure. 4.6 (a) Schematic connections for charging of capacitor using TENG and powering electronic devices, capacitor charging and	100

discharging curves before and after power up the electronic devices (b) 24 red LEDs, (c) digital watch, (d) snapshot of the continuous switching on 3 LEDs under cyclic application of force.

Figure S4.1	Cross-sectional view of the aluminum substrate in the Optical microscope for the thickness measurement.	107
Figure S4.2	(a) Schematic of general piezoelectric nanogenerator device, (b) present TENG design, (c) TENG converted to piezo-geometry with PET surface above the ZnO nanosheets, (d) TENG converted to piezo-geometry with ITO surface above the ZnO nanosheets, (e) open circuit piezo voltage of the fabricated PENG (Figure 3(c)) against hand tapping, (f) open circuit piezo voltage of the fabricated PENG (Figure 3(d)) against hand tapping.	108
Figure. S4.3	(a) Stability response of TENG with Sewing machine tapping and magnified view of few cycles from the stability graph, (b) photograph of TENG response during the stability testing, (c) Developed tapping test set up and photograph of the TENG response during the measurement, (d) response of TENG for 2055 cycles and magnified view of few cycles from the stability graph.	108
Figure. 5.1	(a) Schematic of TENG device, (b) schematic view of the fabrication of the different colored CLC devices, (c) photographs of the original CLC devices on a black background, (d) schematic view of the TENG integrated CLC device, (e) Photograph of actual CLC device integrated in TENG.	114
Figure. 5.2	Topographical images of the (a) ZnO nanosheet film, (b) OHP sheet, and morphological images of the (c) ZnO nanosheet film, (d) OHP sheet, and EDX spectrum of the (e) ZnO nanosheet film and, (f) OHP sheet.	115
Figure. 5.3	ZnO nanosheet film (a) XRD pattern, (b) FT-IR spectrum, (c) PL spectrum of ZnO nanosheet powder, (d) TEM image of the ZnO nanosheet (inset SAED pattern), OHP sheet (e) XRD pattern, (f) FT-IR spectrum.	116
Figure. 5.4	Electrical characteristics of TENG ($5 \times 5 \text{ cm}^2$) (a) open-circuit voltage, and (b) short circuit current in forward and reverse connections, (c) magnified view of short circuit current of TENG response in one cycle, (d) TENG response with another side of OHP sheet surface, (e) schematic of TENGs with different tribo-pairs, (f-g) TENG responses with different tribo-pairs of Al-ITO, ZnO-ITO, OHP-Al, ZnO-OHP (h) plot of output voltage and current with different load resistances, (i) Instantaneous power density with the load resistance.	118
Figure. 5.5	Comparative study of TENG V_{oc} and I_{sc} with (a)-(b) different	120

	frequencies of the applied force, (c)-(d) different active areas of the devices, and (e)-(f) different magnitudes of applied forces.	
Figure. 5.6	Stability of TENG (a) 4300 cycles with hand tapping (inset few cycles from stability graph), (b) 12,220 cycles with linear motor, (c) TENG output voltage vs number of cycles, and (d) Stability test of TENG over a period of 6 months. (e-g) SEM images of ZnO nanosheets after stability test of 10,000 cycles.	122
Figure. 5.7	Response 10 x 10 cm ² TENG (a) open circuit voltage, (b) short circuit current. (c) TENG output voltage before and after rectification. (d) Charging curves different load capacitors, (e) stored charge at different load capacitances, (f) output voltage and stored charges behaviour as a function of the load capacitance, (g) the maximum stored energy as a function of the load capacitance.	123
Figure. 5.8	(a) Schematic of the electroluminescence device and its components, on and off state photographs of (b) electroluminescence, (c) digital watch, (d) LEDs.	124
Figure. 5.9	Capacitor charging and discharging curves before and after power up the electronic devices (a) calculator, (b) digital thermometer.	126
Figure. 5.10	(a) Working principle of self-powered CLC device driven with TENG device before and after applying force on TENG, (b) Polarizing optical microscopy images of different CLC's in red, blue, green cells driven from planar to focal conic by TENG device, (c) Real-time images of different CLC's in red, blue, green cells driven from planar to focal conic by TENG device, (d) transmission spectra of CLC devices in planar and focal conic state.	127
Figure. 5.11	(a) switching action of CLC, (b) photograph of the CLC device integrated with mobile phone camera, practical applications of CLC devices integrated with TENG are (c) switchable smart windows, (d) optical switches, (e) secured/ authenticated or unauthenticated QR codes, (f) mobile phone face lock security, and (g) display of patterned of "LC" letters of CLC connected to TENG device.	128
Figure. S5.1	(a)-(b) Photographs of PET and OHP sheets. Photographs of the different sides of the OHP sheet during the test, (c) non-charged side of OHP, (d) charged side of OHP.	138
Figure S5.2	(a) cross-sectional view of OHP sheet in the optical microscope to measure the thickness.	139
Figure. 6.1	(a) Schematic synthesis procedure of the ZnO and ZIF-8@ZnO, (b) Mechanism of ZIF-8 particles growth on ZnO nanosheets, (c) Schematic diagram of the ZnO, ZIF-8@ ZnO based TENG devices and its components.	145

Figure. 6.2	SEM images of (a) ZnO nanosheets (b)-(d) ZIF-8@ ZnO.	146
Figure. 6.3	(a) XRD pattern of ZnO nanosheets and ZIF-8@ZnO, (b-c) Raman spectra of the ZnO nanosheets and ZIF-8@ZnO.	147
Figure. 6.4	The electrical response bar diagrams of the ZnO and ZIF-8@ ZnO based TENG devices with different opposite triboelectric layers (a) open circuit voltage (b) short circuit current. The ZIF-8@ ZnO based TENG output response with PMMA (c) open circuit voltage (d) short circuit current, (e) The behavior of the ZIF-8@ZnO TENG under the external load resistance, (f) instantaneous power density of the ZnO and ZIF-8@ZnO TENG.	148
Figure. 6.5	2D work function mapping of (a) ZnO, (b) ZIF-8@ ZnO; (c)-(d) Electron transfer mechanism between ZIF-8@ZnO and PMMA during the contact electrification.	150
Figure. 6.6	Z8-TENG responses as a function of (a-b) different frequencies of applied force(c-d) different spacing (e-f) different impact of the forces.	152
Figure. 6.7	(a) Stability of the ZIF-8@ZnO based TENG; (b) Schematic of circuit diagram used for rectification of TENG output and charging capacitors, (c) charged voltage vs time for various capacitors; (d) Saturated stored voltage and charge as function capacitive load; (e) calculated stored energy as function of capacitive load.	153
Figure. 6.8	Real time photographs of powering LEDs and electronic devices by TENG (a) real time image of the 180 LEDs lighting up by TENG; powering electronic devices momentarily using charged capacitor of 4.7 μ F (b) wrist watch, (c) calculator and (d) thermometer.	155
Figure. S6.1	Waveform representation of different dielectrics with fixed tribo layer of (a-b) ZnO (c-d) ZnO@ZIF-8.	166
Figure S6.2	The output (a) voltage and (b) current of the ZnO-based TENG with PMMA as an opposite triboelectric layer	167
Figure 7.1	Real-time images of sand papers with different grit sizes of P80,120,180, 220, 320, and 400, respectively.	172
Figure 7.2	(a) Schematic view of the fabrication of PDMS film and photographs of prepared PDMS. Real time images of PDMS film, (b) elongated, (c) folded, and (d) twisted.	173
Figure 7.3.	(a) Surface morphology of PDMS; (b) optical images of sandpaper with a grit size of 220; SEM images of (c) Plane Al, (d) scratched Al; optical images of ZnO nanosheets film on (e) plane, (f) scratched aluminum; SEM images of ZnO nanosheets on (g) Plane Al and (h) scratched Al, respectively.	174

Figure 7.4	ZnO nanosheets on Al substrate and PDMS films (a-b) AFM images, (c-d) XRD pattern	176
Figure 7.5	ZnO nanosheets on Al substrate and PDMS films, (a-b) IR spectra range from 400-4000cm ⁻¹ , and (c-d) Raman spectra, respectively.	177
Figure 7.6	SKP raster scan images of samples (a) Scratched Al with 220 grit sandpaper; ZnO nanosheet film on (b) Plan aluminum, (c) Scratched Al with 80 grit size (d) Scratched Al with 220 grit size (e) Scratched Al with 400 grit size (f) comparison of work functions of all films.	179
Figure 7.7	The average output voltage and current of the TENGs using, (a) plane aluminum and scratched aluminum with different grit sizes of sandpapers, (b) plane aluminum, ZnO deposited plane aluminum and ZnO deposited scratched aluminum with different grit sizes of sandpapers, and, (c) ZnO deposited scratched aluminum at different scratching time with fixed grit size (P220).	180
Figure 7.8	(a-b) open circuit voltage and short circuit current of the TENG(T12), respectively; (c) Single output current response of the TENG; (d-e) output voltage, current response, and maximum power density of the TENG under the Load resistance; (f) Plane Al, ZnO coated Plane Al, ZnO coated scratched Al (grit size 220) Power density of bar diagram, respectively.	183
Figure 7.9	(a) Long-term stability of the T12 TENG device, (b) photographs of prepared PDMS films with different thicknesses, (c) the output voltage, and (d) current of the TENG with different thicknesses of PDMS film.	184
Figure 7.10	TENG device (T12) device output response as a function of (a)-(b) different active areas of the devices, (c)-(d) different spacing between the triboelectric layers, (e)-(f) different frequencies of applied force, (g)-(h) different applied force.	187
Figure 7.11	Capacitor charging curves with various capacitances charged by a TENG, (a) voltage (b) stored charge (c) the relationship between voltage and stored charge as a function of load capacitance (d) stored energy.	188
Figure 7.12	Photographs of (a) 824LEDs, (b) stopwatch, (c) calculator, (d) digital watch, directly driven by a Contact separation mode of the TENG; (e) circuit diagram of the self-powered system to power electronics with energy storage units; (f) Charging capacitor curves correspond to thermometer; Photographs of (g) thermometer, (h) hygrometer, and (i) digital vernier callipers, driven by charging capacitors of 4.7 μ F, 47 μ F and 100 μ F, respectively.	189

Figure 7.13	Output voltage generated by different body parts and motion states (a–b) Output voltage was driven by muscle movement and knee joint movement, (c-d) The output voltage was measured by wrist bending and finger tapping, respectively, (e–g) Output voltage was driven by walking, running, and jumping, respectively.	190
Figure 7.14	(a) Schematic of the proposed health (breath) monitoring patients in ICU using TENG, (b) real-time photograph of the person during the respiration rate testing, TENG output response for different breathing rates (c) current (d) voltage.	191
Figure S7.1	Optical images of the surface of plane aluminum and scratched aluminum with different grit sizes (a) Plane (b) P80, (c) P120, (d) P150, (e) P180, (f) P320, and (g) P400 respectively.	202
Figure S7.2	Optical images of aluminum scratched for various time durations of (a) 0 min, (b) 1 min, (c) 3 min, (d) 5 min, (e) 7 min, (f) 9 min with fixed grit size sandpaper of P220.	203
Figure S7.3	Output voltage and current response of the TENG, (a-b) plane and scratched aluminum with different grits (80, 120, 180, 220, 320, 400), (c-d) ZnO nanosheets deposited on scratched aluminum with different grits, and (e-f) ZnO sheets deposited on aluminum with 220 grits size at different scratching timings (0 min, 1 min, 3 min, 5 min, 7 min, 9 min), respectively.	205
Figure S7.4	Optical microscope images of sand papers with different grit sizes (80,150,180,220,320,400).	205
Figure S7.5	Finite element simulation of TENG: (a) schematic configuration TENG device model, (b) Time lapse images of the electric potential distribution from contact to separate state of triboelectric layers, (c) open-circuit voltage as a function of spacing distance (x), (d) transferred short-circuit charge as a function of spacing distance(x), and, (e) capacitance between the electrodes as a function of spacing distance (x).	206
Figure S7.6	(a) Schematic representation of TENG with rectifier circuit and rectified out directly connected to LEDs (b-c) Charging capacitor curves corresponds to hygrometer and digital vernier callipers.	206

List of Tables

Table No	Table Caption	Page. No
Table 4.1	Literature review of triboelectric nanogenerators based on ZnO nanostructures.	91
Table. 5.1	List of pairing materials that formed TENG with ZnO nanostructure films and their output voltage, and power/power density, and explored applications.	112
Table 5.2	Functional groups and their absorption bands observed for PET sheet.	117
Table 6.1	MOF based TENGs and its output performance	142
Table 7.1	Comparison of Electrical Output Performance of ZnO nanostructures-PDMS based TENG as reported in the literature with present reported work.	170
Table 7.2	vibrational modes of the Raman spectra of PDMS	178
Table 7.3	The TENG devices code and its output voltage and current are listed below	181
Table 7.4	Device parameters used in the COMSOL simulation	186
Table S7.1	Comparison table of various surface modification methods and their TENG output performance.	202
Table S7.2	Different TENGs with fixed PDMS as another tribo-layer: device codes, device structure and output responses listed below.	203
Table S7.3	Amount of enhancement in the output voltage and current of ZnO on Scratched Al with respect to the ZnO on plane Al TENG devices.	204
Table 8.1	Efficiency of the TENG devices	209

Abbreviations

AC	Alternating Current	V_{oc}	Open-circuit Voltage
DC	Direct Current	I_{sc}	Short-circuit Current
XRD	X-Ray Diffraction	R_L	Load Resistance
FE-SEM	Field Emission-Scanning Electron Microscopy	P	Power density
SAED	Selected Area Electron Diffraction	C_L	Load Capacitance
TEM	Transmission Electron Microscopy	IoT	Internet of Things
EDX	Energy Dispersive X-ray	VB	Valence Band
FTIR	Fourier Transform Infrared spectroscopy	CB	Conduction Band
PL	Photoluminescence	LS	Lateral Sliding
AFM	Atomic Force Microscopy	VCS	Vertical Contact-Separation
POM	Polarizing Optical Microscopy	SE	Single Electrode
SKP	Scanning kelvin Probe Microscopy	FS	Free-standing
PENG	Piezoelectric Nanogenerator	EFM	Electrostatic Force Microscopy
TENG	Triboelectric Nanogenerator	MEMs	Micro electro mechanical system
PyENG	Pyroelectric Nanogenerator	PTFE	Polytetrafluoroethylene
TEG	Thermoelectric Nanogenerator	LED	Light Emitting Diode
Al	Aluminum	LCD	Liquid Crystal Display
ZnO	Zinc Oxide	EMG	Electromagnetic generator
ITO	Indium Tin Oxide	PDMS	Polydimethylsiloxane
PET	Polyethylene terephthalate	PMMA	Poly (methyl poly) methyl methacrylate
OHP	Overhead Projector	CLC	Cholesteric Liquid Crystal
MOF	Metal organic Framework		
ZIF-8	Zeolitic Imidazole Framework		

List of Symbols

ρ	Electric charge density
\mathbf{J}_f	Electric current density
ϵ_0	Permittivity in vacuum
ϵ	Permittivity in dielectric
σ	Surface Charge density
Φ	Work function
η	Efficiency
d	Interplanar spacing
θ	Angle of incidence
λ	wavelength
Q_s	Charge

Chapter 1

Introduction

The chapter provides an overview of the motivation underlying energy harvesting, as well as available sources and their significance as well and the various types of nanogenerator technologies, their operating models, and their fundamental principles. Furthermore, it explores the selection of the material for the nanogenerator device, strategies to improve TENG output, and its application in different fields. This chapter outlines the justifications for selecting ZnO as a source material, as well as its major characteristics. This chapter will provide readers with the major objectives and a route map.

Publications:

1. “*Advances in Zinc Oxide (ZnO) Nanostructure-Based Nanogenerators: Challenges and Opportunities*”, **Supraja Potu**, Siju Mishra, R. Rakesh Kumar, D. Haranath, K. Uday Kumar, Hitesh Borkar, *Advances in Energy Research (Nova Science Publishers, Inc.)* 36, 43-71.

1.1 Research motivation

Recently, the rapid advancement of electronic devices has greatly impacted and transformed numerous aspects of human everyday lives. To operate these electronic devices, a capable power source for generating electricity is essential. Power consumption is currently a serious concern in the worldwide field of electronics, particularly in the Internet of Things [1,2]. Since being portable and easily accessible, rechargeable batteries are now the most popular method of powering such devices. This strategy, however, has drawbacks such as limited battery life, environmental effects, maintenance difficulties, and a reliance on incremental technological breakthroughs [3,4]. To resolve these difficulties, self-sustaining and long-term energy sources that are environmentally friendly need to be developed. Investigating energy from the environment and developing wireless power transmission technologies attract curiosity. These interdisciplinary efforts aim to create more sustainable and efficient solutions for the power consumption of electronic devices as technology continues to develop gradually. Among these, energy harvesting technologies have emerged as a promising solution [5]. These technologies can harvest various energy resources, including non-renewable and renewable energy sources (Figure 1.1).



Figure 1.1. Energy sources are available in nature: renewable and non-renewable energy sources.

1.2 Non-renewable and Renewable energy sources

Non-renewable energy sources such as petroleum, coal, natural gas, and nuclear power, are finite resources, and once these resources are exhausted, they cannot be easily replaced on human timescale. These energy sources contribute to environmental issues like carbon monoxide emissions and climate change. Many countries heavily depend on non-renewable resources, leading to geopolitical tensions and conflicts over access to these valuable energy sources. The International Energy Outlook (2021) predicts a 15% increase in overall energy consumption in Organization for Economic Co-operation and Development (OECD) countries by 2050. Figure 1.2 illustrates the energy mix, revealing that fossil fuels, including coal (38%), natural gas (28%), and oil (14%), continue to dominate their energy usage [6]. This highlights the ongoing reliance on non-renewable sources, emphasizing the need for sustainable alternatives in the future.

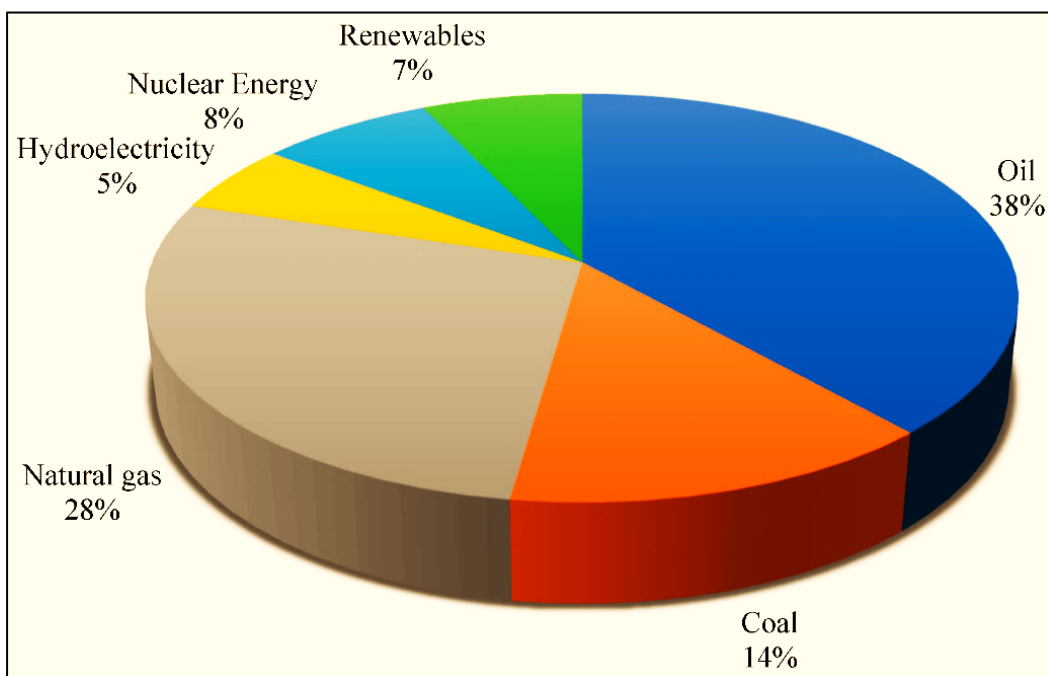


Figure 1.2. The energy sources usage in OCED countries (Reproduced from) [6].

Renewable energy sources such as solar power, wind energy, hydropower, geothermal energy, mechanical energy, and biofuels are more environmentally friendly and sustainable [7,8]. compared to non-renewable sources, these resources can be naturally replaced, providing a permanent solution to our energy demands. Moreover, these sources usually don't harm the environment and do not produce greenhouse gases. Using these sources is crucial for addressing concerns about climate change, and offering a sustainable and continuous energy supply.

There are two types of renewable energy sources: large-scale and small-scale. Large-scale renewable energy sources are ambient, transient sources include solar power, wind, hydropower, and geothermal energy, used for the large power generation. Due to their inexhaustible availability, these sources are becoming more and more crucial for a sustainable energy supply. These are well established energy sources that contribute to addressing the energy demand at mega- to gigawatt-scale. Energy harvesting also refers to small-scale generation of energy in which both the energy consumer and also the energy sources are localised. Small-scale renewable energy sources include mechanical energy, water flow, heat energy, and biomass, etc. The development of wearable and portable electronics, mobile phones, sensors, automated security systems, wearable technology, etc. in the last few decades. These devices run using batteries for a power source, but these batteries have limited life and environmental hazards. In this context, to power these devices nanogenerators emerging as a promising option, which can convert ambient small-scale energy into electricity.

1.3 Nanogenerators

Nanogenerators are the energy harvesting devices, designed to convert ambient energy available in the form of mechanical vibrations, human body movements (breathing, running, heart beat), waste heat, rain drops, water flow, into electrical power. These devices utilize the use of a variety of physical theories, including thermoelectricity, photovoltaics, pyroelectricity, piezoelectricity, and triboelectricity. By harnessing energy from mechanical vibrations, movements, temperature changes, or light, nanogenerators actively contribute to the development of self-powered electronic devices, sensors, wearables, and other applications [9,10]. Ongoing research focuses on improving materials and efficiency to enhance the practicality and versatility of nanogenerators in diverse applications.

In the literature, Z. Zhang et al. [11] proposed the integration of multiple features into socks, designed for traditional applications, including gait sensor technologies for walking, jumping, and running pattern detection and also full human activity monitoring. H. Xue et al. [12] introduced an innovative wearable nanogenerator integrated into a respirator. This device is driven by human breathing and serves as a self-powered breathing monitoring, offering a new and sustainable solution for respiratory monitoring. In another work, W. Qin et al. designed a flexible nanogenerator with high sensitivity and fast response to ultraviolet (UV) illumination. The designed composites showcased their potential application as self-powered UV photodetectors, highlighting their effectiveness in capturing and responding to UV light [13]. Nanogenerators also able to power pH sensors, LEDs ad low power electronic devices [14–

16]. Finally, owing to its high output power, potentially reaching up to 500W/m^2 , nanogenerators have the capability to charge energy storage systems. Super capacitors and lithium batteries. The reason for the ongoing efforts in the development of energy-efficient electronics includes the adaptability of nanogenerator technology. This technology plays a crucial role in aiding effective energy storage, particularly in devices like lithium batteries and supercapacitors [17,18]. The energy harvesting approach employs four basic mechanisms mainly such as piezoelectric, pyroelectric, thermoelectric, and triboelectric. In pyroelectric nanogenerators the electricity generated due to the temperature changes between the two materials. This technology proves valuable in thermal energy scavenging systems, particularly in applications such as temperature sensors and the harvesting of energy from temperature variations.

Triboelectric energy harvesting exploits the triboelectric effect, a phenomenon in which electric charge is generated through the contact and subsequent separation of materials that exhibit different electronegativities. TENG phenomena takes place when materials undergo applied mechanical forces, resulting in the contact and subsequent separation of the materials and facilitating the transfer of electrons between them. Practical applications of this phenomenon can be found in wearable devices, smart textiles, and self-powered sensors [19]. Similarly, piezoelectric energy harvesting makes use of materials that generate an electric charge in response to mechanical stress or vibrations. This technology serves diverse purposes, including powering wireless sensors and capturing energy from footsteps or machinery vibrations [20].

1.4 Origin of nanogenerators

The nanogenerator concept the first introduced by wang and his group in 2006,they proposed a (Piezoelectric nanogenerator) PENG fabricated using ZnO nanosheets as a piezoelectric materials [21]. The generation of electricity across the external circuit is caused by the deformation of ZnO nanowires under the application of a small mechanical strain. Thus, the first concept for a nanogenerator, this marks significant progress for applications involving the scavenging of nano energy. After that, in coming year of 2012 same group proposed a device called Triboelectric nanogenerator [22]. The (Triboelectric nanogenerator) TENG operates based on the induction of electrostatic charges on the surfaces of two distinct materials upon contact under mechanical pressure. The resulting triboelectric charges create a potential difference upon separation, enabling the flow of electrons from one electrode to another. Beyond piezo and triboelectric nanogenerators, various methods can convert mechanical energy into electricity, those are electromagnetic induction, electrostatic techniques. Each of

these approaches is characterized by its unique set of advantages and disadvantages, as detailed in Figure 1.3.

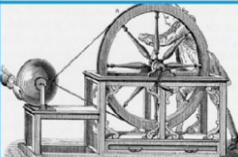
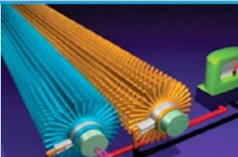
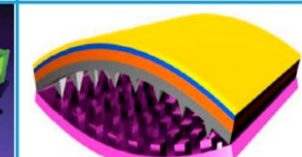
Mechanical energy harvesting	Electromagnetic	Electrostatic	Piezoelectric	Triboelectric
				
Harvesting principle	Electromagnetic induction	Electrostatic induction	Piezoelectric effect & Electrostatic induction	Contact electrification & Electrostatic induction
Impedance type	Resistive	Capacitive	Capacitive	Capacitive
Pros	High efficiency, easy to scale up	Light weight	Easy to scale down to nanoscale	Large output power, high efficiency, low weight, cost effective materials, simple fabrication
Cons	Heavy magnet required, low output for small-scale devices	Precharge required, low output, high matched impedance	Low output & low efficiency, pulsed output, high matched impedance	Pulsed output, high matched impedance

Figure 1.3. Benefits and limitations of the mechanical energy harvesters (Reproduced from) [23].

1.4.1 Maxwell's displacement current in nanogenerators

Maxwell's equations are the fundamental principles to understand the governing electric and magnetic fields. The specific form of Maxwell's equations can be expressed as:

$$\nabla \cdot \mathbf{D} = \rho_f \text{ (Gauss's law)} \quad \text{----- (1.1)}$$

$$\nabla \cdot \mathbf{B} = 0 \text{ (Gauss's law in magnetism)} \quad \text{----- (1.2)}$$

$$\nabla \times \mathbf{E} = -\frac{\partial \mathbf{B}}{\partial t} \text{ (Faraday's law)} \quad \text{----- (1.3)}$$

$$\nabla \times \mathbf{H} = \mathbf{J}_f + \frac{\partial \mathbf{D}}{\partial t} \text{ (Ampere's circuital law with Maxwell's addition)} \quad \text{----- (1.4)}$$

Here the physical quantities are, the electric field (\mathbf{E}); the magnetic field (\mathbf{B}); the magnetizing field (\mathbf{H}), the free electric charge density (ρ_f), the free electric current density (\mathbf{J}_f), and the displacement field (\mathbf{D}).

Maxwell's equations, including Gauss's law, Faraday's law, and Ampère's circuital law, are the origin of the theoretical frameworks of electromagnetic generators (EMG) and nanogenerators. Figure 4 is showing that the comparison of the EMG and nanogenerator theory.

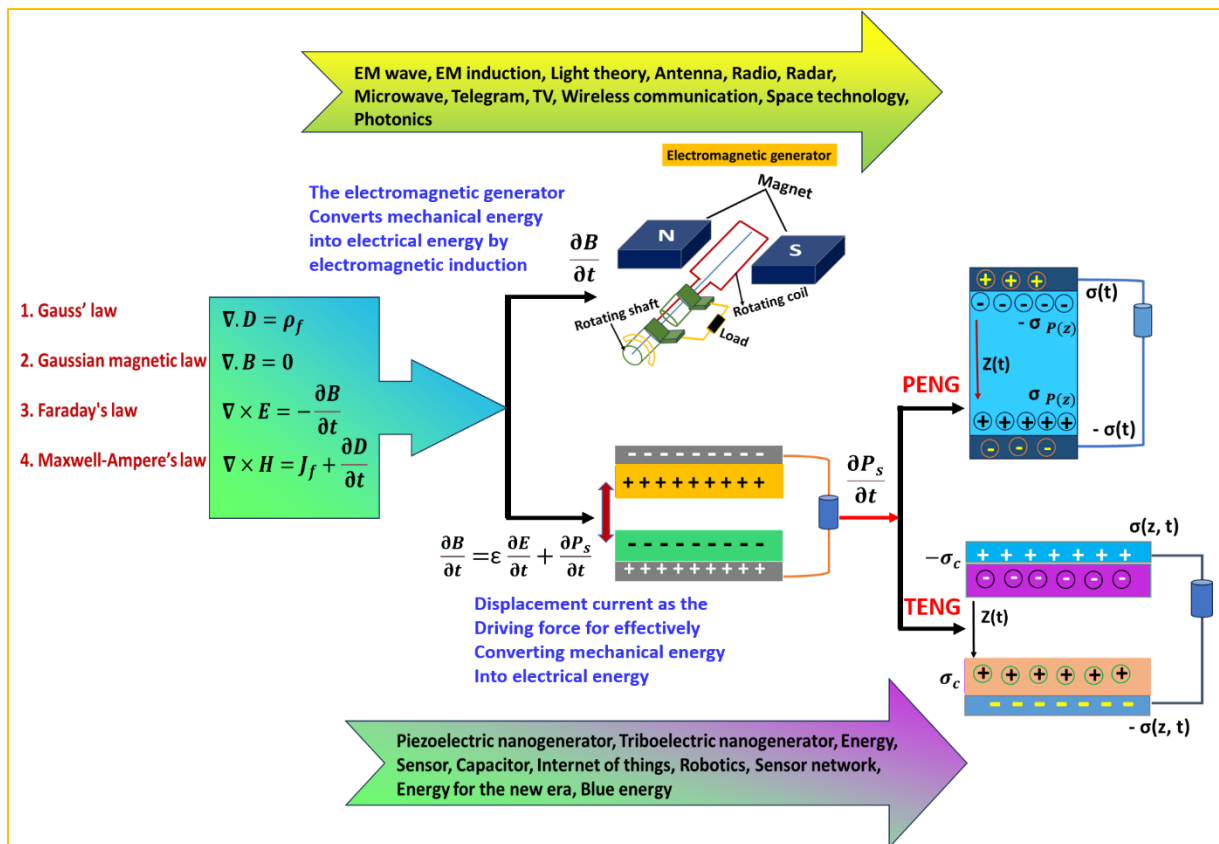


Figure 1.4. A comparison of theoretical foundation between the EMG and the nanogenerator (Adopted from) [24]

In the case of the EMG, invented by Faraday in 1831, it operates by applying a varying magnetic field to generate current. The power generation process involves the Lorentz force inducing electron flow in a conductor. The output current is directly related to the time-variation of the magnetic field ($\frac{\partial B}{\partial t}$). In other words, the EMG produces current as a result of the changing magnetic field over time. However, the nanogenerator concept, introduced by Z.L. Wang, operates on a different principle compared to traditional electromagnetic generators. In this concept, the current is generated by varying the polarization field induced by surface polarization charges. This process is a crucial component of Maxwell's displacement current. The concept of displacement current was first introduced by Maxwell in 1861. The introduction of the displacement current was specifically aimed at ensuring the continuity equation for electric charges [25].

The electric displacement vector, $D = \epsilon_0 E + P$, where the P is the medium polarization vector and ϵ_0 is permittivity in vacuum.

$$\text{Displacement current density} \quad J_D = \frac{\partial D}{\partial t} = \epsilon_0 \frac{\partial E}{\partial t} \quad \text{-----(1.5)}$$

The term in displacement current ($\frac{\partial E}{\partial t}$), it leads to the prediction of propagating electromagnetic waves. This laid the foundation for technologies like wireless communication.

In isotropic media $D = \epsilon E$, here ϵ is the permittivity of the dielectric. $(\partial D/\partial t)$ is related to the rate of change of electric field ($\partial E/\partial t$) in a region. Even if the electric field (E) is zero, there can still be a displacement current exist if the electric field is changing with time. The second term in eqn (1.5) leads to polarization (P) in a material arises when an external electric field (E) induces the alignment or movement of charges within the material. In the absence of an external electric field, polarization is typically absent, as there is no force acting on charges to prompt their shift or alignment.

However, in real-world situations, polarization in materials doesn't always need an external electric field. For instance, the piezoelectric effect shows that strain on certain materials creates polarization charges on surfaces. Another example is the triboelectric effect in devices like TENGs. Here, simply rubbing different materials together generates charges on surfaces, leading to polarization. To incorporate the influence of polarization of electrostatic charges induced on the surfaces in Maxwell's equations, Wang introduced an additional term, denoted a, in the displacement vector (D) in 2017 [23]. That is,

$$J_D = \frac{\partial D}{\partial t} = \epsilon_0 \frac{\partial E}{\partial t} + \frac{\partial P_s}{\partial t} \quad \text{-----(1.6)}$$

The first term represents the induced current resulting from a changing electric field, while the second term accounts for the current caused by the polarization field of surface electrostatic charges. This second term serves as the theoretical foundation for nanogenerators.

As, shown in the Figure 1.4, the piezoelectric material caused to the deformation under the applied force, which resulting in the polarization of charges. These charges create an electrostatic potential, balanced by electron flow through an external load. This process converts mechanical energy into electric power. The polarization charges density on the surface is $\sigma_p(z)$, charge density of the free electrons in the electrode is $\sigma(x)$, and the thickness of piezo-material is z . Where in TENG, when two dielectrics come into physical contact, electrostatic charges are transferred due to contact electrification (triboelectricity). This process creates static charges on the surfaces, forming a surface charge density (σ). The charges accumulate as contacts increase, reaching saturation, independent of the gap distance (z). The electrostatic field generated by these charges drives electrons to flow through an external load, leading to

the accumulation of free electrons in the electrode ($sI(z, t)$), a function of the varying gap distance ($z(t)$) between the dielectrics.

The interplay between Maxwell's theoretical foundations and the practical implementation of Piezo and triboelectric nanogenerators underscores their significance in pushing the boundaries of energy harvesting and sensor development as shown in Figure 1.5.

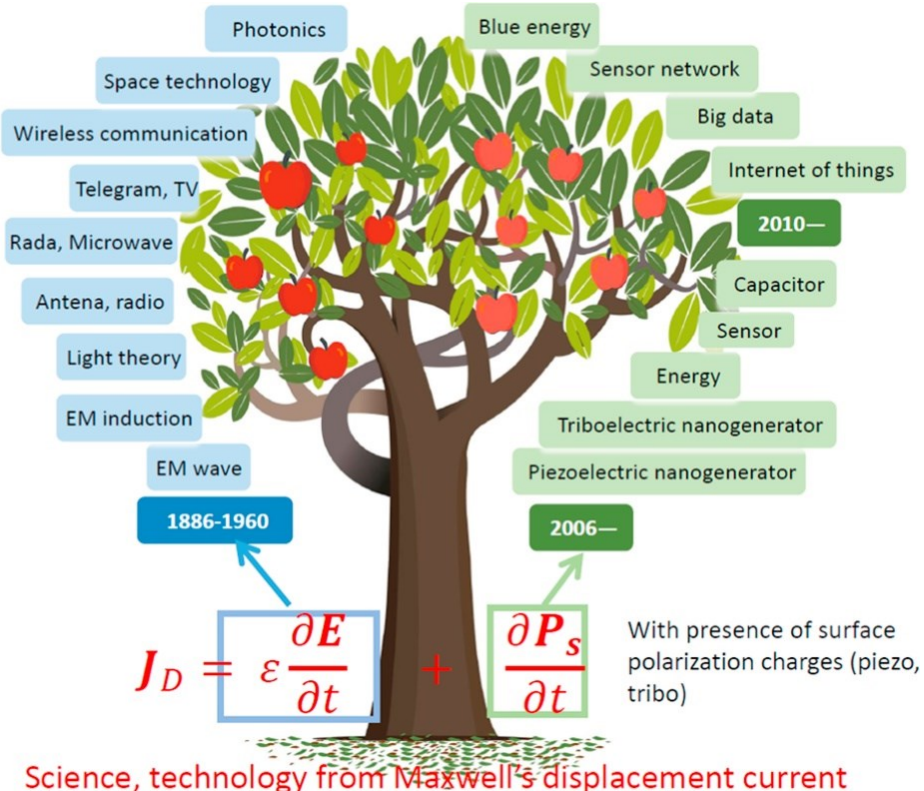


Figure 1.5. A visual representation of the revised Maxwell's displacement current
(Reproduced from) [26].

1.4.2 Capacitive model

The nanogenerators device design explained by charging and discharging of the capacitors. The term "capacitive conduction" refers to nanogenerators, where the displacement current serves as the sole conduction mechanism for the transfer of electricity. Instead of free charges moving across the capacitor's electrodes, the power is transferred by electromagnetic waves and induction. The output current of a nanogenerator can be expressed using a capacitor model as a basis,

$$I = \frac{dQ}{dt} = C \frac{dV}{dt} + V \frac{dC}{dt} \quad \text{-----(1.7)}$$

Where, Q- stored charge, the first term in the eqn (1.7) is the current introduced by the change in applied voltage. the second term in eqn (1.7) current introduced by the variation in capacitance.

In the case of a PENG, the strain-induced change in crystal size/thickness results in a very small variation in capacitance, which indicates that the current is primarily caused by the strain induced voltage

$$I = C \frac{dV}{dt} \approx A \frac{d\sigma}{dt}, \quad \text{-----(1.8)}$$

Here, A is area of the electrode, under the short circuit condition, the displace current derived from the eqn (1.8),

$$I = A \frac{d\sigma_p}{dz} \frac{dz}{dt} \quad \text{-----(1.9)}$$

For the TENG, Regarding TENG, given the significant variation in gap distance, both parts in Eq. (1.7) contribute to the observed output current,

$$I = \frac{dQ}{dt} = A \frac{d\sigma_I}{dz} \quad \text{-----(1.10)}$$

As a result, the capacitive model has been derived from Maxwell's displacement current.

1.5 Types of nanogenerator technologies

Nanogenerators can be classified based on the energy sources they utilize. Piezoelectric and Triboelectric nanogenerators convert mechanical energy, while Thermoelectric and Pyroelectric nanogenerators utilize temperature differences to generate electrical energy. Each of these nanogenerator types offers unique mechanisms for harvesting energy from different sources, contributing to the advancement of energy harvesting technologies.

1.5.1 Pyroelectric nanogenerators

Pyroelectric nanogenerators (PyENGs) are novel energy harvesting devices that can convert thermal energy into electric energy by utilising nano-sized pyroelectric materials. These devices use materials with asymmetric crystal structures to generate electric charge in reaction to temperature changes, based on the pyroelectric phenomenon [27].

PyENGs, operates on the pyroelectric effect, exhibited in specific materials. Under conditions of no temperature variation over time, the spontaneous polarization intensity of the pyroelectric material remains constant, resulting in no current in the external circuit. However, once there

is change in temperature, the material's spontaneous polarization intensity undergoes a corresponding change, leading to the generation of a pyroelectric current (Figure 1.6) [28]. This current persists until a new equilibrium is established. Significantly, the dual property of many piezoelectric materials, encompassing both piezoelectric and pyroelectric characteristics, facilitates the harvesting of mechanical and thermal energies from the same material. PyENGs are especially useful in applications with frequent temperature fluctuations, including wearable electronics, environmental sensors, and IoT devices.

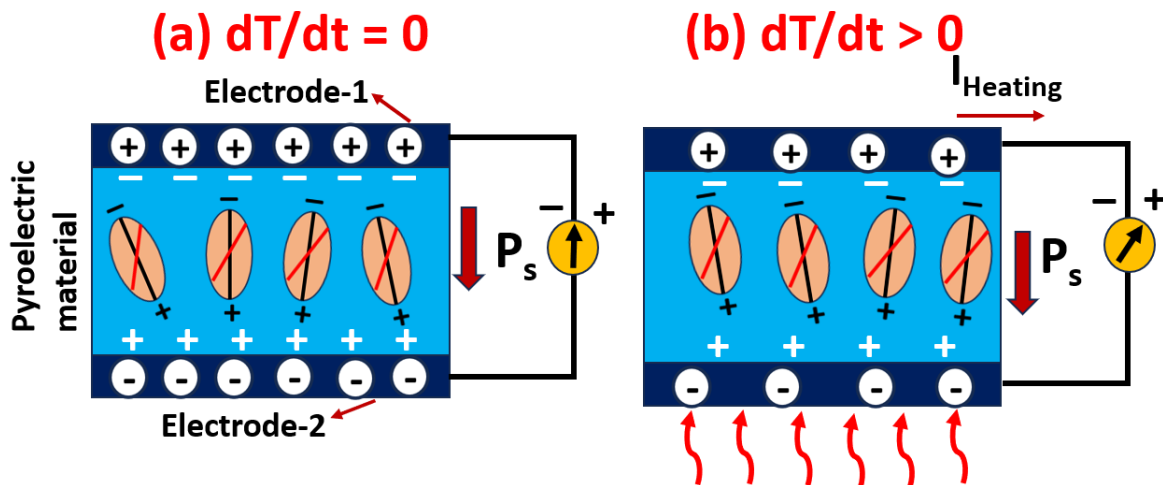


Figure 1.6. Mechanism of pyroelectric effect. (a) before and (b) after applied the temperature (adopted from) [28]

The Wang group developed the first pyroelectric nanogenerator in 2012, which was based on ZnO nanowire arrays. The output of the PyENG is dependent on the pyroelectric coefficient, temperature change and film thickness. The vast amount of heat energy generated by human bodies, vehicle exhausts, conventional processes, and solar radiation often goes to waste. By utilizing this it is possible to power liquid crystal displays (LCDs), light-emitting diodes (LEDs), wireless gadgets, and other electronic systems.

1.5.2 Thermoelectric nanogenerators

Thermoelectric nanogenerators are energy harvesting devices, which operate on the phenomena called seebeck effect [29]. The voltage is generated across the materials under the applied temperature gradient. The thermoelectric effect exhibited by the materials having high electrical conductivity, low thermal conductivity and having high seebeck coefficient. When a material is subjected to a temperature gradient, charge carriers like electrons or holes move from the hotter side to the colder side, creating an electric potential difference (Figure 1.7). The

careful selection of materials with ideal thermoelectric characteristics is essential to the efficiency of thermoelectric nanogenerators. These nanogenerators can be used for waste heat recovery, the engine of moving automobiles, solar panels, CPU of computers, the human body, and possibly even powering small electronic devices or sensors in temperature-sensitive situations[29–32].

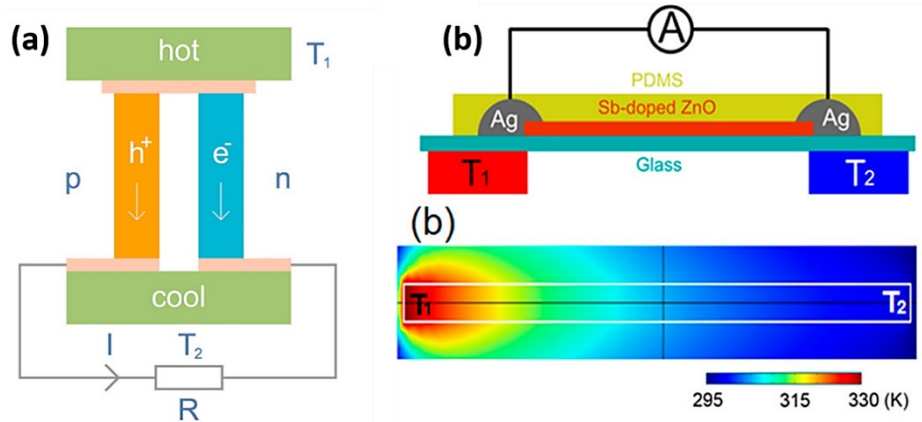


Figure 1.7. (a) Operating principle, (b) Schematic diagram of thermoelectric nanogenerator (Reproduced from)[27,33].

1.5.3 Piezoelectric nanogenerators

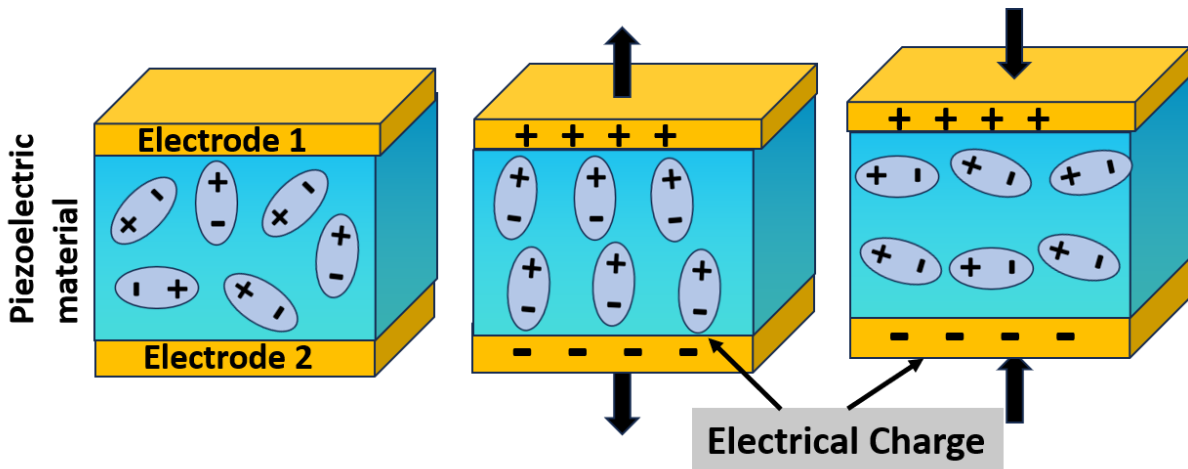


Figure 1.8. Principle of piezoelectric effect.

The piezoelectric phenomena discovered by Pierre and Jacques Curie in 1880. The word piezo means stress/pressure in Greek. This is a special property exhibited by only certain materials. In the direct piezoelectric effect, these materials generate an electric field or current when subjected to physical stress [34,35]. This phenomenon is connected to the materials

nanostructures. In its initial state, the charge centers of anions and cations align, coinciding with each other. Upon the application of an external force, such as stretching or compressing the material, the structure undergoes deformation. Consequently, the negative and positive charge centers become separated, forming an electric dipole and giving rise to a piezoelectric potential. When an external load is connected to the deformed material, free electrons are compelled to partially screen the piezoelectric potential, flowing through the external circuit. As a result, a continuous current pulse is generated in the external circuit, as the piezoelectric potential undergoes sequential alterations through the application of external physical forces (Figure 1.8). This phenomenon illustrates the conversion of mechanical energy into electrical energy, a fundamental principle behind the practical applications in various technologies, such as sensors, actuators, and transducers, showcasing the versatility and significance of piezoelectric materials in modern applications.

1.5.4 Triboelectric nanogenerators

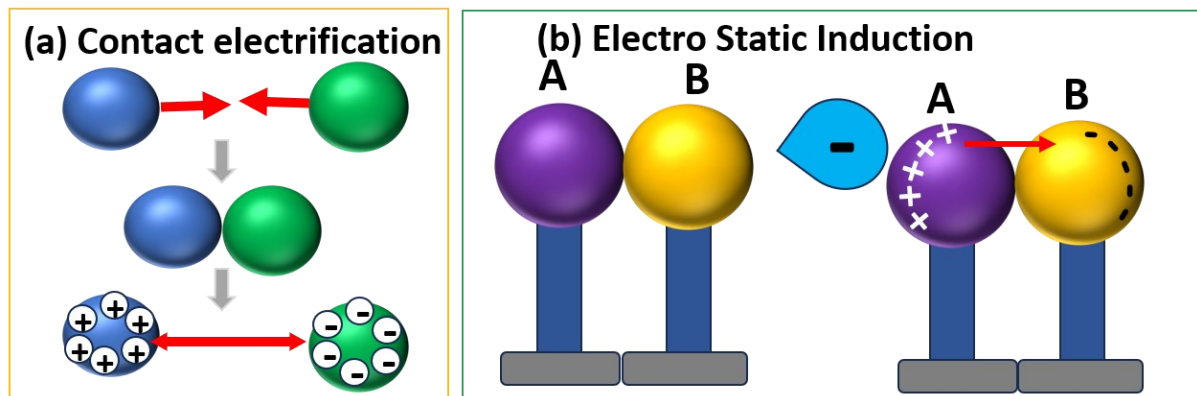


Figure 1.9. Triboelectric nanogenerator working principle (a) contact electrification, (b) electrostatic induction. (Adopted from) [36]

Greek terms "Tribo" (which means "rub" or "friction") and "electric" (which comes from "amber") are combined to get the word "triboelectric." The triboelectric nanogenerators works based on the triboelectric effect (contact electrification and electrostatic induction), which can convert mechanical energy into electricity. This phenomenon characterized by the generation and transfer of the charges between two materials, when it comes to physical contact. When two materials with different electron affinities come to contact, one material tends to get a negative charge, while another material get a positive charge [37].

Three distinct methods have been identified for the generation of triboelectric charge: electron transfer, ion transfer, and material transfer [38–41]. Triboelectrification is an inevitable process, occurring at the interfaces not only between solid-to-solid interface but also solid-liquid and

solid-gas interfaces. Among the numerous aspects of triboelectrification is the process by which neutral, insulating materials, when brought into contact and separate, also become oppositely charged. It also appears in natural occurrences, including lightning in thunderstorms. Here, air layer movement results in the formation of soft hail and ice crystals, which in turn cause the production of triboelectric charges. These stored charges then cause high-potential electrostatic discharges, which are a major factor in the breathtaking lightning show that occurs during thunderstorms [42]. It is particularly challenging to refer to the underlying theory of contact electrification, despite the fact that the concept is theoretically evident and supported by observations from ordinary life, industrial applications, natural occurrences, and studies of empirically consistent triboelectric series.

In Metals, when two metals brought into contact, there will be an electron flow from a lower work function to the metal with a higher work function, to equalize the metals fermi energy levels. In the case of metal-dielectric and dielectric-dielectric interfaces, the research group of Z. L. Wang has proposed an electron-dominated transition process. Their explanation for the origin of this effect relies on the electronic band structure model and the interatomic interaction model [43,44]. By employing these models, they offer insights into the mechanisms governing electron transfer dynamics at these interfaces.

(a) *Electronic Band Structure Model*

The process of charge transfer mechanism of the metal-dielectric contact, comprehensively studied through energy band diagrams. In metal, at absolute zero temperature, electrons entirely occupy the below fermi level of energy states. To remove these electrons to vacuum energy level the required minimum energy called work function. In dielectrics, the fermi energy level in between the valence band and conduction band. However, the presence of surface defects, impurities, or point defects causes quantized energy levels to be introduced within the band gap due to structural imperfections. Electrons from the metal occupy some of the energy levels of dielectric below the fermi level, when these two come into contact, as a result a dynamic exchange of electrons occurs, which is the process of triboelectric charge transfer. This transfer of the electrons results in the negative charges on the dielectric and, the positive charges on the metal surfaces. This exchange of excess charges is generated on each surface, resulting in a potential difference and the formation of an electric field between the metal and dielectric.

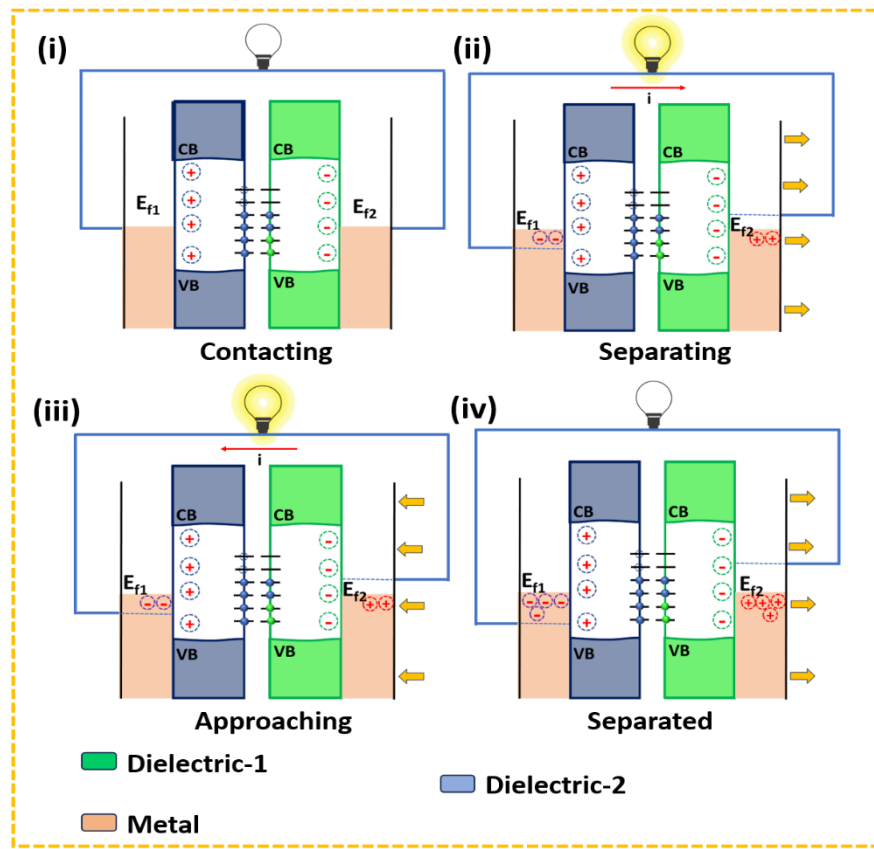


Figure 1.10. Schematic representation of the energy band diagram for the contact between two dielectric materials, (i) contacting, (ii) separating, (iii) separated, and (iv) approaching to contact. (Adopted from) [45]

The same process followed in the dielectric- dielectric energy band, as shown in Figure 1.10. Then two dielectrics come to contact, the dielectric having higher the electron occupied energy states dielectric states to transfer electrons and occupy the lower electron energy states of dielectric. As a result, the higher the electron energy states of dielectric will get the positive surface charge and another dielectric will get the negative surface charge. Once, they separated the electrons not free to move due to its low conductivity.

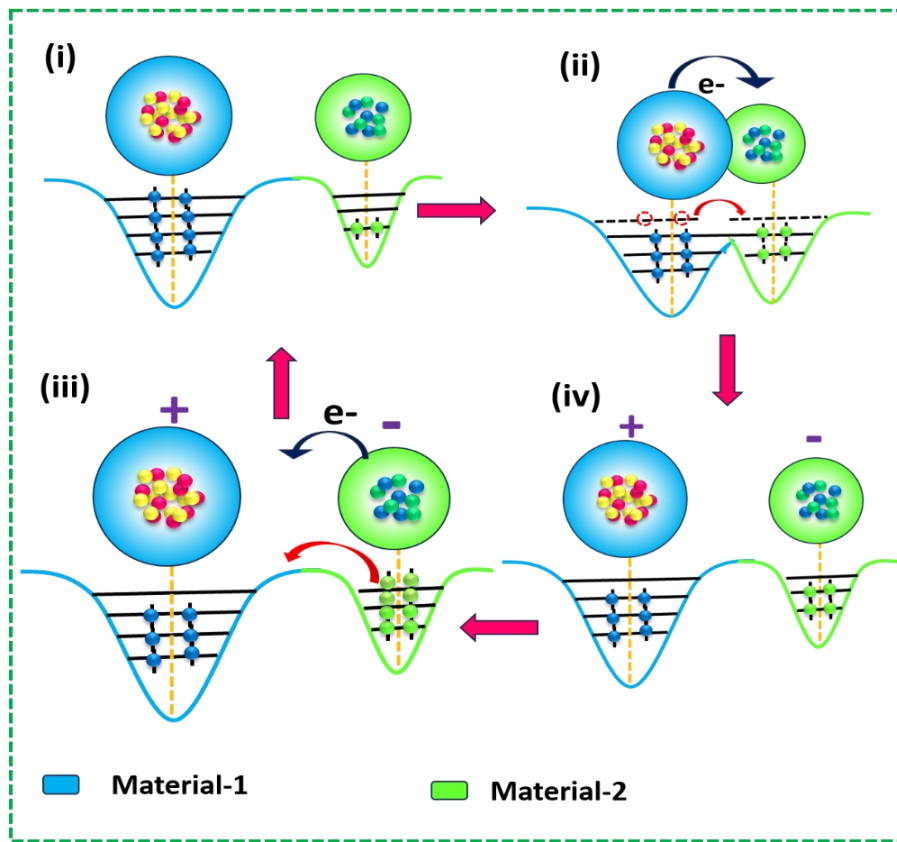
(b) *Interatomic Interaction Model*

Figure 1.11. Schematic representation of the interatomic interaction model for the contact between two dielectric materials, (i) contacting, (ii) separating, (iii) separated, and (iv) approaching to contact. (Adopted from)[45]

The electron band structure fails in the explaining some of the materials like polymers, rubbers, and natural triboelectric materials including fur, hair, wand wool. Another method called interatomic interaction model is explained the general materials based on the electron cloud interaction shown in the Figure 1.11. For example, the contact materials named as material 1 and material 2. Initially, when there is no contact between the materials, they are in attractive force region, the distance between the atoms of materials is larger than the bond length or the interatomic distance is in equilibrium, and electron clouds are separated. Once material A and material B come to contact, the electrons clouds will be overlap and the potential well merge together, the potential barrier between these two wells sinks. The higher occupied energy states of atom of the material 1 transfer the electrons to unoccupied energy states of atom of the material B. Results in, the energy releases in the form of photon emission, plasmon excitation and/or phonon excitation. When the compressive force applied by rubbing, sliding, or contacting causes the distance between the atoms of material 1 and material 2 to be lower than

the bond length or the interatomic distance at equilibrium, this effect takes place in a repulsive force region. After the materials separated from one to another, the electrons trapped in the potential well of material 2 due to its higher potential barrier and remain there. But when the temperature rises and the electrons' energy fluctuations surpass the potential barrier separating the atoms, for instance, these electrons may jump out of the potential well and return to higher energy levels.

1.6 Bio-Mechanical energy harvesting

Mechanical energy is abundant and readily available, exhibiting itself in a wide range of forms such as motion, vibrations, and deformation. This widespread availability suggests an inherent advantage in harvesting mechanical energy compared to other sources. Capturing this energy is simple and easy for example, capturing motion from wind or water may be relatively simple, but energy conversion efficiency is still an important factor to take into account. Although certain mechanical energy conversion devices, piezoelectric and triboelectric nanogenerators can be highly efficient in converting mechanical energy into electrical power at the nanoscale [46]. Generally, human body also produces the mechanical energy, per day the human body used the energy an average of 1.07×10^7 J per day [47], which is equal to 800 AA (2500 mAh) batteries.

Human body motion indeed contains a large and unexplored source of energy that can be in the form of heat or motion. This novel approach to energy harvesting opens up a new era, particularly in the context of powering of low-power electronic and wearable devices within the range of 10 μ W to 10 mW. The idea of capturing energy producing from the body in the form of various body movements includes ankle, knee, and hip motions, foot strike (jumping, walking, and running), hand force, eye blinking, finger tapping etc, can convert into electrical energy. In piezoelectric and triboelectric nanogenerator technology, the mechanical energy derived from the human body effectively employed to capture and convert into useful power [48]. This innovative strategy holds immense promise for diverse applications, including wearable devices, health monitoring systems, and other portable electronics. It offers a sustainable and convenient means of powering these devices by harnessing the natural movements of the human body. Through the utilization of this mechanical energy, PENG and TENG are able convert into electricity.

1.7 PENG: materials, and applications

1.7.1 Piezoelectric materials

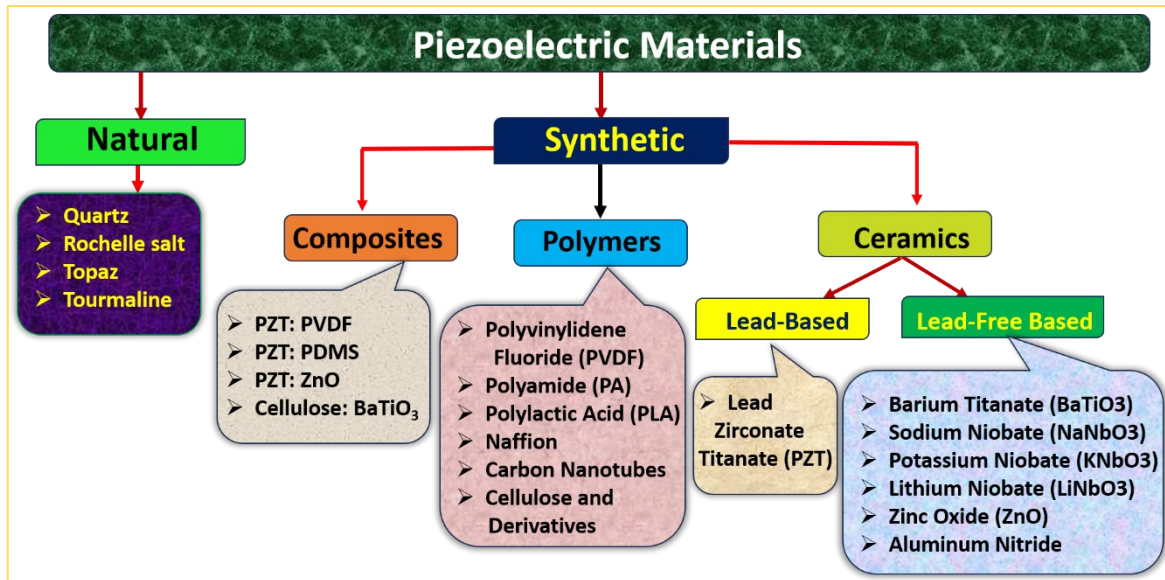


Figure 1.12. The list of piezoelectric materials.

The materials which can generate electricity under the small mechanical stress is called the piezoelectric materials, which works based on piezoelectricity principle. The operating principle of piezoelectric materials is that when a compressive or tensile force is applied, a potential difference develops, which is known as a positive piezoelectric effect. When an electric field is applied to a piezoelectric material, it produces mechanical stress, which is known as the inverse piezoelectric effect. The materials utilized for energy harvesting is crucial to the performance of the PENG device and functionality. These devices are capable of producing electrical energy from natural sources such as vibrations, heat, mechanical action, water flow, and airflow. Now a days, Piezoelectric materials are using in vast range of applications, due to their cost effectiveness, can be easily formed in different nanostructures such as thin films, 2D structures, fibers, and cylindrical shapes. Many piezo electric materials created from last few years, such as organic, inorganic, and composite materials, etc [49,50]. The list of some of piezo electric materials has provided in the **Figure 1.12**. Lead zirconate titanate (PZT) was the first widely investigated piezoelectric material, exhibiting desirable piezo, ferro, and dielectric properties, however, the lead content will affect humans and the environment [51]. Researchers more focused on lead free materials, includes ZnO, ZnS, BaTiO₃, and PVDF etc, when compared to PZT, these materials demonstrated equivalent or even greater piezoelectric characteristics. Furthermore, they are eco-friendly, easy synthesis,

simple structure, suitable mass production, and biocompatible, and they are predicted to replace their lead-based counterparts shortly after.

1.7.2 Applications of PENG

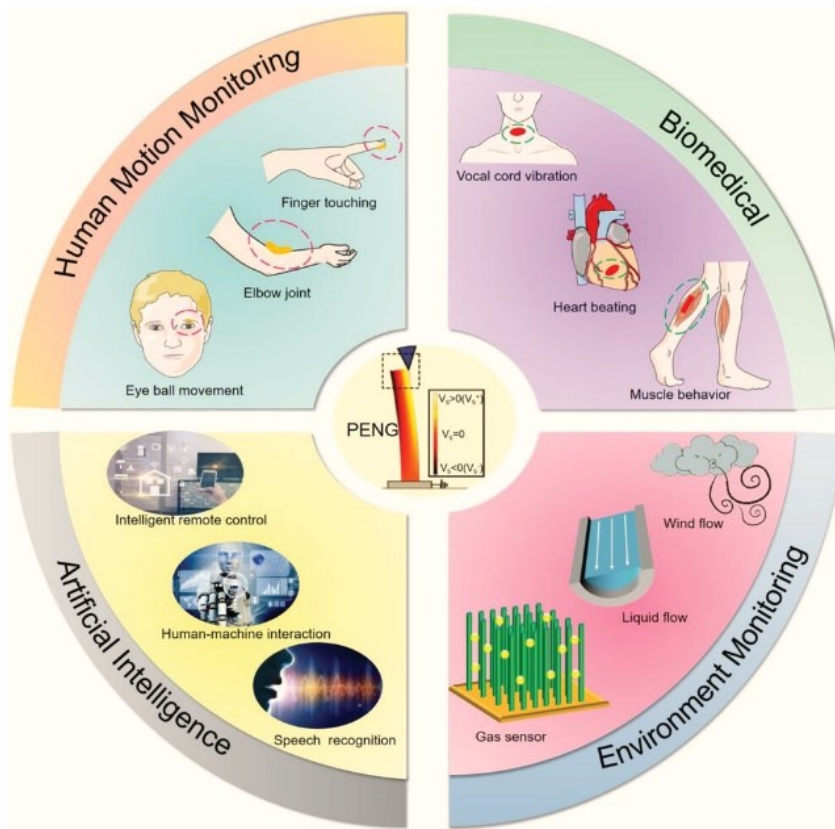


Figure 1.13. PENG applications (reproduced from) [52]

PENG devices convert mechanical energy into electricity based on the piezoelectricity phenomena, which is generation of charge under the applied mechanical pressure. Due to their small size, flexibility, and ability to capture low-frequency movements and vibrations, PENGs are used in diverse applications across various fields. Recently developed portable mobile communication gadgets are greatly improving human lives due to the quick advancement of science and technology. Because of their limited energy storage capacity and significant reliance on external power sources, mobile electronic devices have a shorter working lifespan. A desirable alternative to a continuous power source for portable communication devices is the best idea of self-powering. PENGs are the excellent choice for low-energy power sources in applications [52] like wearable electronics, medical implants, microelectronic systems, Artificial intelligence, environmental monitoring, etc. (Figure-1.13). Especially, these PENG devices are essential to the improvement of wearable technology because these are suitable

for smartwatches, fitness trackers, and clothes with ease. There, these devices effectively harvest movement energy from the wearer to increase battery life and enable wearables that run on their power [53]. Within the medical field, piezoelectric nanogenerators are used in biomedical apparatuses, providing energy from physical motions in the body to power implants and sensors. Their importance also extends to the use of wireless sensor networks, where they reduce dependence on traditional power sources by offering an independent and sustainable energy supply, especially in difficult or isolated situations. The Internet of Things (IoT) is a large-scale sensor system, which need the electricity to power the sensors, and actuators, increases the energy efficiency and reduce the battery replacements. The integration of piezoelectric nanogenerators into flooring materials represents a novel technique for energy harvesting, capturing energy from footsteps. This approach can be used in a variety of scenarios, including public spaces, commercial structures, and residential areas. Furthermore, piezoelectric nanogenerators aid in the creation of self-powered devices, ranging from remote controls to wireless keyboards, by providing enhanced functionality. In addition, their flexibility extends to environmental monitoring, where they can power self-powered sensors in difficult or remote environments. By emphasizing high output, conversion efficiency, and sensitivity through novel materials and structures, the flexible and wearable PENG is advancing the technology of nanogenerators. It can operate as a self-powered system, supplying sustainable energy for multifunctional sensors in various types of applications.

1.8 TENG: working modes, materials, and applications

1.8.1 TENG modes

Mainly, four fundamental working modes of the TENG have been postulated [54,55], depending on the direction of the polarization change and electrode arrangement, which are contact separation mode (CS), Free-standing mode (FS), Single electrode mode (SE), and lateral sliding mode (LS), respectively (Figure 1.14). Based on the applications, different kinds of arrangements are being developed to generate energy through the use of freely moving triboelectric sources in the environment and triboelectrification of structural dielectrics.

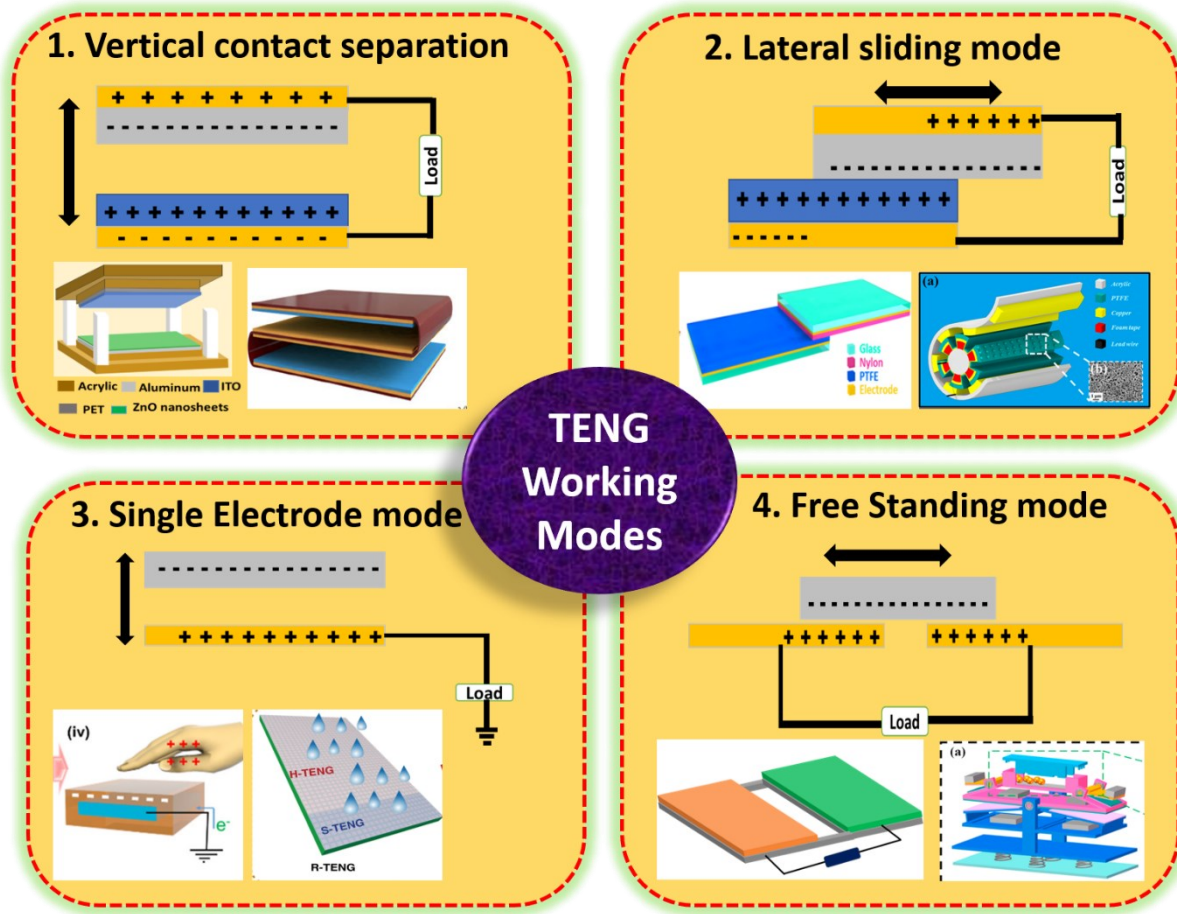


Figure 1.14. Fundamental working modes of TENG (Reproduced from)[56–61].

1.8.1.1 Contact Separation Mode

Contact separation mode is the basic working mode of TENG, which is having two configurations; one is dielectric to electrode and another one is dielectric to dielectric. In the thesis work we have used both the configurations [62]. In this mode, TENG designed as sandwich type structure, top and bottom electrodes connected to the two dielectric layers and finite separation distance. In TENG functionality, electrodes work as source of free electron and integrated to dielectric surfaces through different methods such as deposition, coating and adhesive electrode tapes. The separation distance also having the significant role in the contact separation mode, which typically maintained by springs or sponges, because of self-releasing ability. Initially dielectric layers separated by finite distance, once these dielectric layers brought to contact by the external applied force, depends on their electron affinity charges induced on their surfaces. Results in one triboelectric layer surface get positive and another triboelectric layer surface get negative charges. When released the applied force, triboelectric layers get separated, potential difference is established between two planar electrodes that are positioned on the outer sides of dielectrics and the charges start flow through the top electrode

to bottom electrode in order to balance electrostatic field. If the triboelectric layers pressed, due to an external force result in a reduction of electrostatic potential, causing the gradual disappearance of this potential upon full contact. Consequently, electrons flow back, and the repetitive sequence of contact and separation induces the generation of alternating current (AC) through an external electrical load.

1.8.1.2 *Lateral sliding mode*

Lateral sliding mode having the same structure as contact separation mode [63]. In this mode, sliding lead the generation of charges on the triboelectric layer surfaces. Initially, there is no potential difference between the electrodes due to the absence of applied force, the triboelectric layers are fully aligned (overlapped). Once top triboelectric layer sliding on the bottom triboelectric layer due to the applied force, potential difference occurs in the non-overlapping parts of the electrodes and resulting in the electrons start flow from top electrode to bottom electrode. Once the triboelectric layers come aligned to its original position, the electrons flow back through the external circuit to balance the potential difference. Periodic sliding of one triboelectric layer over another causes the AC as an output.

1.8.1.3 *Single electrode mode*

While the previously mentioned modes center around triboelectrification within a solid and compact device relying on dielectrics, this design restricts the harnessing of triboelectric charges from the surrounding environment. To overcome this limitation, the single electrode mode has been introduced. In this mode, energy can be harvested by capturing triboelectric charges freely generated by various sources in the environment, including human skin, tires, and raindrops. In CS and LS modes requires two triboelectric layers which need to be attached to two electrodes. Coming to Single electrode mode, which requires only one electrode and one triboelectric layer [64]. For example, Human skin used as arbitrary triboelectric layer to operate on vertical/ sliding contact to another triboelectric layer, the electrode attached to the triboelectric layer is the primary electrode, to serve as a source of electrons, which is connected to the ground. Once contact the two triboelectric layers (human skin one of the triboelectric layers), induce the tribo charges on the two triboelectric layers with opposite polarity. Upon the removal of human skin, the electrons flow from primary electrode to the ground to balance the developed potential difference. If again contact with the human skin with triboelectric layer leads to electrons flow back from ground to the primary electrode. Repeated contacts and departs of human skin on a triboelectric layer generate alternating electricity.

1.8.1.4 *Free-standing mode*

The freestanding method requires a freely moving part. This mode has a dielectric layer and two symmetric electrodes, and similar to SE-mode, triboelectric layer can move freely without the use of an electrode or an electrical connection [65]. In this mode, TENG can be designed fixed layers can be electrode attached triboelectric layers or only the electrodes, both generate the tribo electric charge generation. When a triboelectric layer (ex: positive) is contact with one electrode, electrons attracted to that electrode due to increase in electrical potential. Once the triboelectric layer contact with second electrode, the electrons start flow from first to second electrode. An AC output is produced through the external load by triboelectric layer moving relative to one another electrodes.

1.8.2 Triboelectric series

Triboelectric series, Wilcke initially proposed in 1757, is an early posteriori over triboelectrification in which various materials are arranged according to their respective triboelectric polarity [66]. In this series, materials are arranged in the order of their tendency to gain the electrons and loose the electrons. In the given arrangement, the material at the top of the series is more positively charged and the material at the bottom of the series is negatively charged. In the later part of the nineteenth century, Faraday, Jamin, and Bouthy delved into the examination of empirical triboelectric series lists. This was succeeded by Shaw in 1917, who conducted extensive experiments using a gold-leaf electroscope to establish triboelectric series for elementary metals, diverse furs and woods, and various insulators (Figure 1.15) [67]. The output of the TENG is mainly depends on the surface charge density(σ) of the materials. These are two methods to optimize σ , one is increasing the contact area by introducing the nanostructures to the tribo materials and another one is selection of materials from tribo series. Greater charge transfer between the materials at the top and bottom of the series is possible. In recent years, numerous quantitative methods for measuring generated triboelectric charge densities have been developed. 1) inductive probe technique, this method involves placing a inductive probe above the a source material surface, where current is induced on an inductive probe through electrostatic potential [68,69]. 2) Solid state electrometers are a commonly used tool, measured the amount of induced charge density on electrodes that are either connected to a triboelectric source or encircled by a Faraday cup [70]. In the past few years utilization of scanning probe techniques, including electrostatic force microscopy (EFM) and Kelvin probe

force microscopy (KPFM), to conduct more detailed examinations of the contact electrification process [71,72].

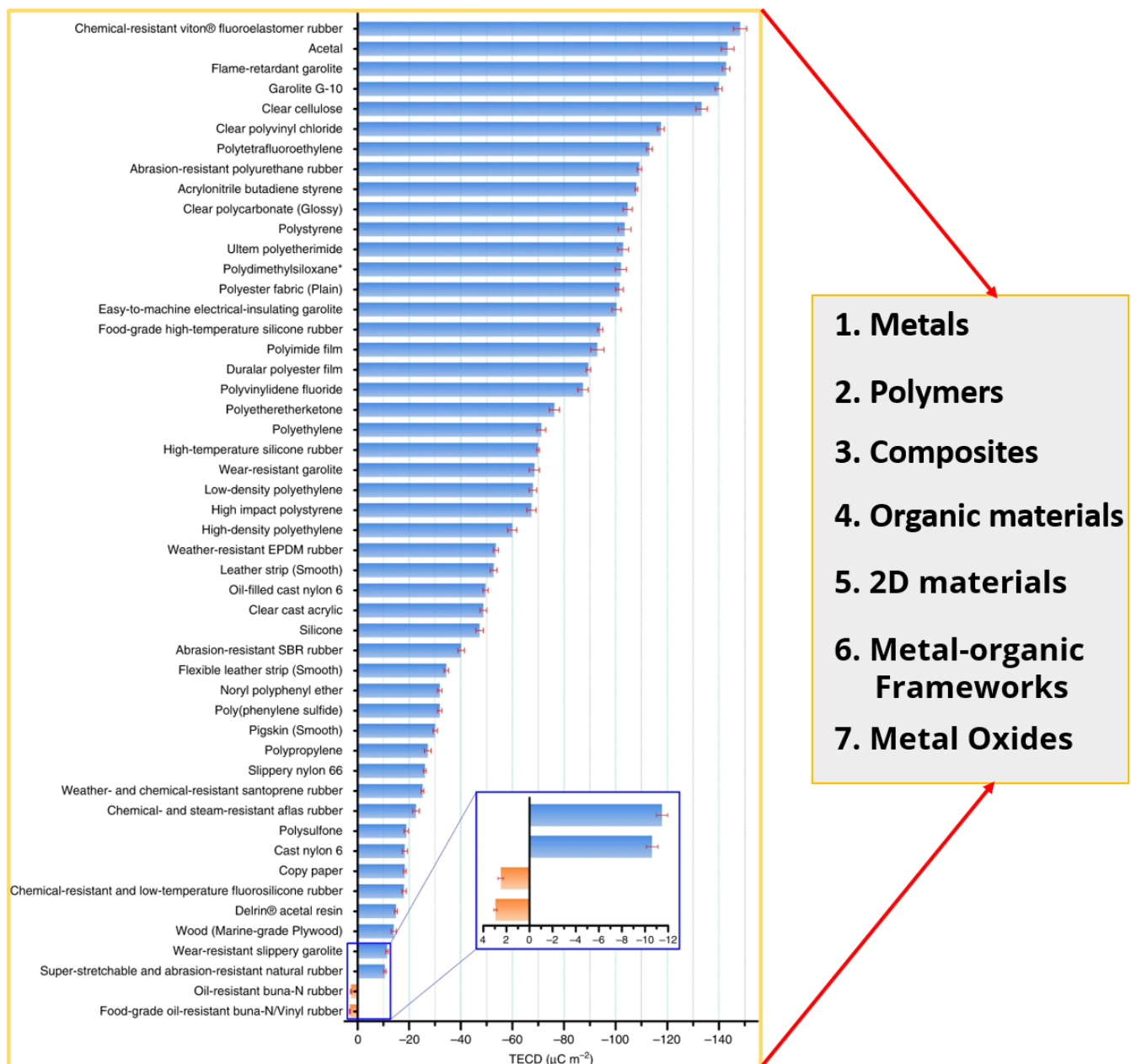


Figure 1.15. List of tribo-materials based on its triboelectric charge density (Reproduced from) [73].

1.8.3 Surface modification

Significant progress has been made in the development of TENGs, with particular attention focused on three important areas: the friction material, surface modification of the friction layer, and the structural design of the TENG device. Among these, surface modification emerged as a versatile and efficient strategy. The surface charge density of the two materials

involved is closely related to the performance of TENGs. Factors influencing surface charge density include the quantity of charges carried and the material's ability to gain or lose electrons. Surface modification is crucial method in improving the electrical output performance of TENGs [74]. This enhancement is attributed to the increase in the effective contact area, achieved through surface modification (Figure 1.16). This modification method not only multiplies the number of sites capable of generating charges but also enhances the site trapping ability. The morphological and chemical modifications applied to the friction material surface contribute to this improvement in charge generation capabilities.

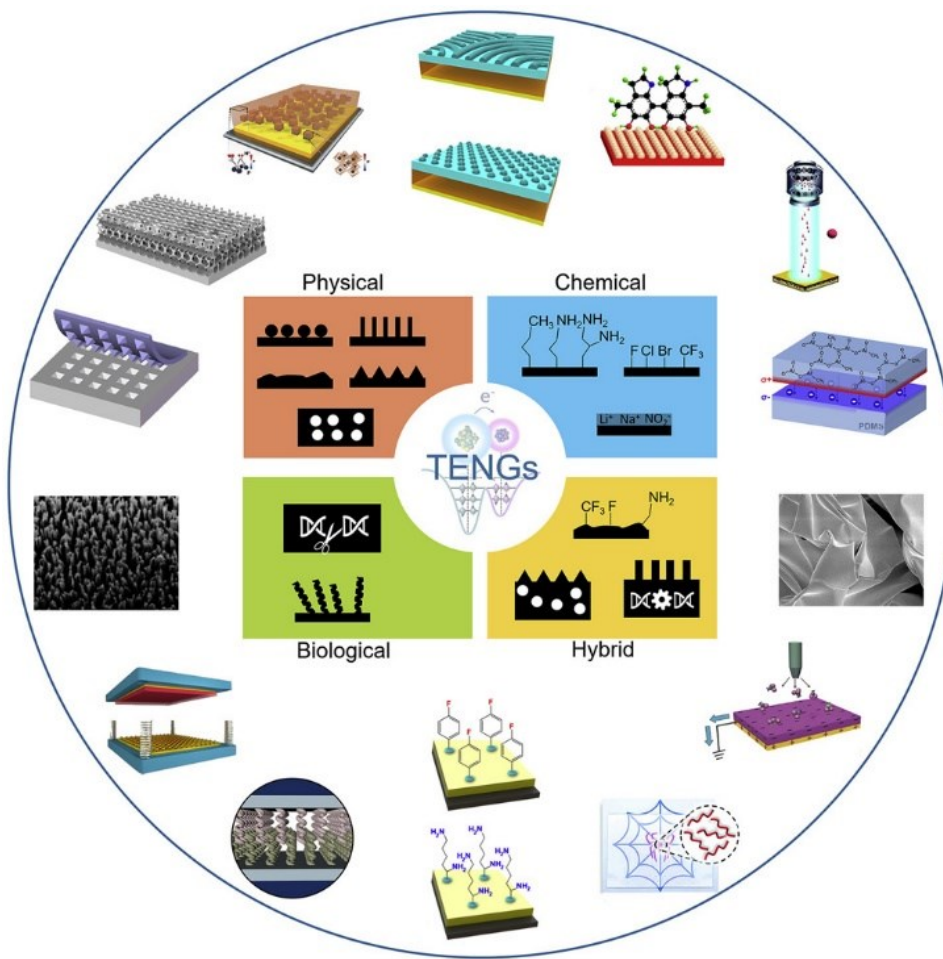


Figure 1.16. Surface modification methods (Reproduced from) [45].

Physical surface modification technique is a crucial in the modifying the properties of the materials surfaces for the particular purposes, and they have significant role in the TENG technology. One common method is lithography, which is used to create a precise micro/nanostructure on the surface of the material utilizing masking, removal or addition of specific materials. Electrospinning is another method that includes the production of different nanostructures by applying the electric field to the polymer solution or melt. Another technique

is called etching, which modifies the material's surface to the appropriate structure by physically or chemically removing certain elements. A process named 3D printing allows for the production of complex patterns and structures on a material's surface, enhancing the area of the contact surface and achieving improved outcomes.

The method of chemical modification involves enhancing the properties and structure of the materials to increase the TENG's output. In coating process, a thin chemical layer applies on the surface the materials, which influence the triboelectric properties of the material. Functioning of the materials surfaces significantly effect on the TENG performance, in this process specific functional groups introduced on the material surface, which increases the TENG characteristics. Plasma treatment is the surface functioning technique, which offers to modify the chemical composition under the plasma environment. These techniques are often used to modify TENG materials, helping to improve surface energy, triboelectric characteristics, and general efficiency. The chemical composition also effects on the TENG performance, polymer mixtures and composites and nanostructures implementation improve triboelectric performances.

These surface modifications are crucial in influencing surface of the material, as result increases the overall efficiency

1.8.4 Applications of TENG

TENG has the potential to be used in a wide range of energy-harvesting applications (Figure 1.17). TENG technology is a needful approach in the ocean energy harvesting. Through the incorporation of these apparatuses into buoyant structures, TENGs have the ability to transform the mechanical energy produced by wave motion into electrical energy. This application has the potential to significantly advance the field of blue energy by providing renewable and sustainable power sources. In direct high voltage power sources, the TENGs show that they can provide high voltage outputs from the mechanical motion. Because of this characteristics, TENGs especially well-suited for electrostatic precipitators, where the high voltage requires to remove the particles from the gas streams. The capacity of TENGs to produce the high voltages directly open up possibilities for improving the productivity of a range of industrial operations.

TENGs also capable to use in wearable electronics on a micro- and nano power levels. If we incorporate TENG as a wearable device, it may capture energy from human body movements and convert it into electricity. The resulting technology is environmentally friendly, beneficial, self-sustaining, and convenient for the wearer. It also reduces the need for regular recharging

batteries, enhancing the overall development of wearable electronic devices. Another technology is microelectromechanical systems (MEMs), which frequently demand minimal power requirements at the microscale. TENG can eliminate these problems and provide a consistent and continuous power supply in remote sensing applications where traditional power sources can't be used for a long period. TENG technology is also utilized in environmental monitoring since the energy captured from environmental vibrations provides the structural condition of the building, so that does not harm the environment. TENG also aids in medical applications by placing a device on the human body that can monitor the user's physiological movements, temperature, and other health issues. Because they are self-sustaining, there is no need for frequent battery changes.

Finally, TENGs are a reliable and self-sustaining power source in the development of a wide range of applications, capable of converting any mechanical energy into sustainable electricity. Because of these advantages, TENG continues to be utilized in a wide range of applications using energy from various sources in the future.

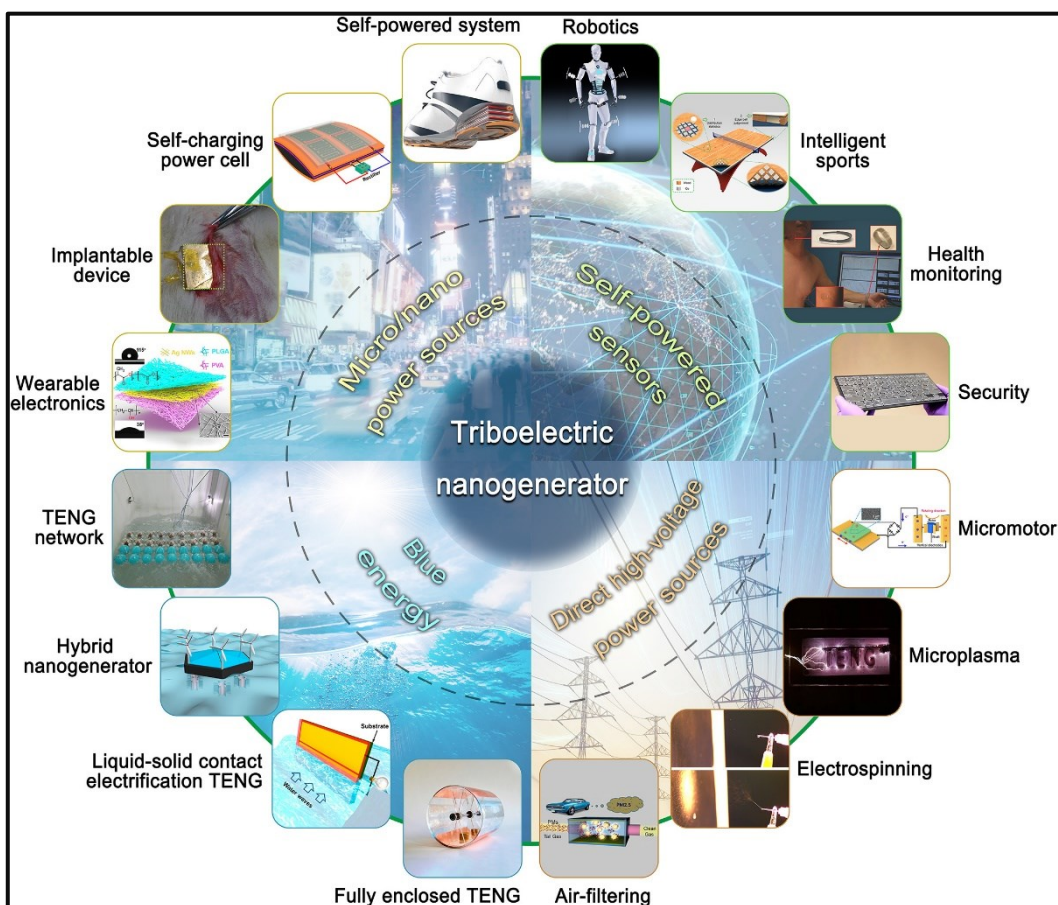


Figure 1.17. Applications of TENG (Reproduced from) [37].

1.9 Selection of material and its properties

Material selection is a crucial component of optimizing the performance of nanogenerators (PENGs and TENGs) in energy harvesting applications. PENGs are typically constructed from materials with high piezoelectric coefficients and having non-centrosymmetric wurtzite structure materials are considered excellent candidates, such as zinc oxide (ZnO), lead zirconate titanate (PZT), aluminium nitride (AlN), polyvinylidene fluoride (PVDF), or Barium Titanate (BaTiO₃), etc. Even though PZT material having high piezoelectric coefficient, lead-based materials will be limited in future uses due to the toxicity of lead and its negative impact on the environment. Recently, lead-free materials have gained attention for use in the fabrication of piezoelectric nanogenerators (PENGs), particularly barium titanate (BaTiO₃), zinc oxide (ZnO), Zinc sulfide (ZnS), and polyvinylidene fluoride (PVDF), having its own benefits and drawbacks. In response to environmental concerns, there has been a shift towards lead-free alternatives, which highlights the continuous endeavors to develop sustainable materials for piezoelectric energy harvesters. In which, BaTiO₃ offers a high dielectric constant and stability, but can be brittle. PVDF is a lightweight, flexible polymer but, environmental factors and mechanical stress contributing to degradation, which might affect the stability and lifespan of the device. ZnS possesses a good piezoelectric coefficient, but its synthesis is challenging, and stability issues are a concern. ZnO is having high stability and easy to handle, but faces challenges related to lower piezoelectric coefficient.

In PENGs, the generation of piezoelectric charges relies on material characteristics such as nanostructures, dielectric constant, and crystal structures. Coming to TENGs, in which materials produce charge through contact and separation of two triboelectric materials with dissimilar charge affinities. Practical material selection is difficult, even if a large difference in charge affinities theoretically results in the creation of more charges and higher TENG output. In addition to chemical compositions, physical characteristics like friction, elasticity, and surface morphology are taken into account when selecting material. Among these factors, the surface morphology of selected materials is a critical factor in material selection to fabricate the PENG and TENG devices. It significantly influences the effective contact area and, consequently, the overall performance of these energy-harvesting devices. In this contest, the desired material should have a large contact area and the capacity to produce diverse nanostructures. These characteristics are critical for optimising the piezoelectric and triboelectric effects in nanogenerators to improve energy conversion efficiency.

ZnO have several significant characteristics, so that it can be used in numerous applications. [75]. ZnO is an promising material, which can be form in different nanostructures including nanorods, wires, sheets, thin films etc in high quality and orientation in single direction [76–78]. Second, it enables cost-effective growth on a variety of substrates, including crystalline and amorphous substrates, as well as hard and flexible surfaces, making it compatible with critical materials such as silicon or polymers. Furthermore, ZnO is well-known for its biocompatibility and environmental friendliness. Finally, ZnO properties can be easily modified using different surface modification strategies, which helpful mainly in electronic and optoelectronic devices. Notably, because of their advantageous geometry and size, ZnO nanomaterials are considered excellent for PENGs and TENGs. Some of the reports has discussed here based on different ZnO nanostructures. Firstly, Wang et al. [21], PENG device fabricated with ZnO nanowires arrays as active layer. The oriented NWs are displaced using a conductive atomic force microscope tip in contact mode and generated the maximum output of 10 mV. Qiu et al.[79] piezoelectric ZnO nanorods are synthesized on a paper substrate to constrict the PENG device. This PENG device has high flexibility and sensitivity, and it generated an output voltage of 10 mV and current of 10 nA. Further, PENG can be used to capture low-frequency mechanical energy, such as body movements, for practical use. Wang et al.[80] developed a nanogenerator device using ZnO nanoparticles and PANI as triboelectric layers, and produced an output voltage of 4V. Further, TENG used to detect various respiratory characteristics, including trace-level NH₃ concentration, human respiratory flow, and respiratory frequency. In another study, Liu et al. [81] constructed a TENG using zinc oxide (ZnO) bilayer film/ chitosan (CTS) and PDMS, which is having good sensitivity in detecting acetone and superior humidity resistance performance at room temperature. Among these nanostructures of ZnO, ZnO nanosheets selected in this thesis, because of the following advantages: (i) Synthesis of ZnO nanosheets is a simple single-step process with no extra seed layer deposition, unlike seed layer-assisted ZnO nanorods or nanowires. (ii) Direct growth of ZnO nano sheets on aluminium substrate has two advantages: (a) no extra electrode deposition, (b) aluminum substrate itself acts as a bottom electrode for the PENG/TENG with good contact with ZnO nanosheets. (iii) During PENG/TENG operation, ZnO nanosheets provide more surface compared to nanorods films, nanoparticle films for contact electrification. (iv) ZnO nanosheets' mechanical strength is more than nanorods; as a result, the device can withstand high-value forces and produce electrical energy [82].

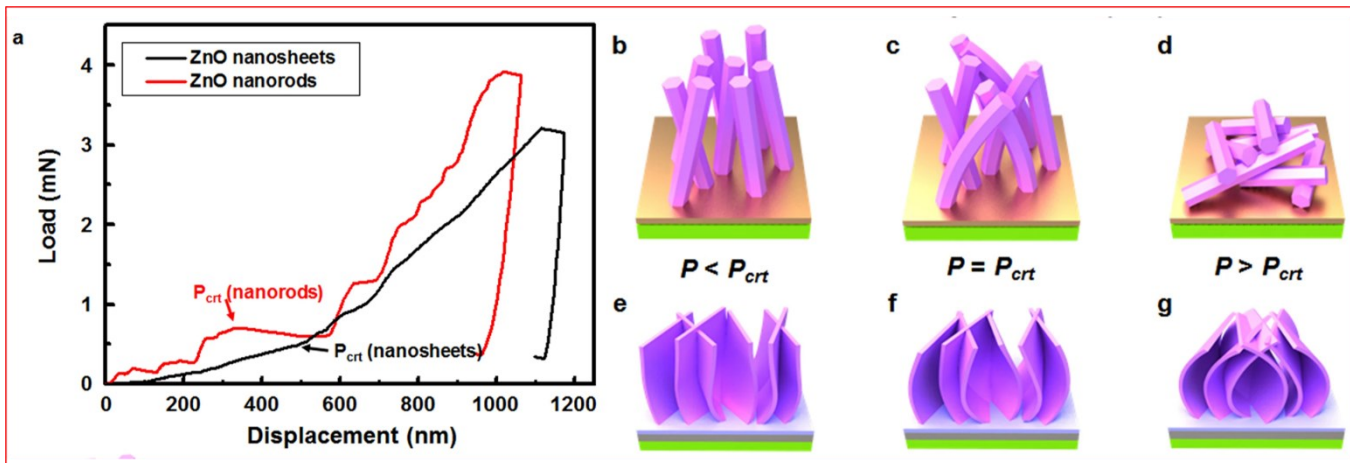


Figure 1.18. (a) load vs Displacement curves of ZnO nanorods and nanosheets by using Nanoindentation testing, Schematic representation of the (b-d) ZnO nanorods and (e-g) nanosheets, respectively, depending on the applied load of below and above critical load (P_{crt}) (Reproduced from) [82].

1.9.1 Basic properties of ZnO

ZnO is an II-VI group n-type semiconducting material due to the presence of Zn interstitial sites and oxygen vacancies. ZnO has three crystalline phases (a) wurtzite-type, (b)cubic zinc blende-type, and (c) rock salt structures, as shown in Figure 1.18 [78,83]. The wurtzite structure type is thermodynamically stable at ambient conditions. The zinc blende structure is not stable, which can be stable only by grown on cubic substrates, and the rock salt (Rochelle salt) structure like NaCl can be stable at high pressure (in GaN case). Cubic zinc blende or hexagonal wurtzite structure where each Zn^{+2} ion is surrounded by four O^{-2} ions tetrahedrally and vice versa. The tetrahedral structure of ZnO is the intrinsic cause of its non-centrosymmetric characteristic, which directly leads to its piezoelectric effect and thermoelectric effect.

The tetrahedrally coordinated wurtzite-type crystal structure is a characteristic for covalent chemical binding with sp^3 hybridization. The lattice parameters of semiconductor materials generally depend on the factors are: (i) free-electron concentration acting via deformation potential of a conduction band minimum occupied by these electrons, (ii) concentration of foreign atoms and defects, and their difference of ionic radii with respect to the substituted matrix ion, (iii) external strains (e.g., those induced by substrate), and (iv) temperature.

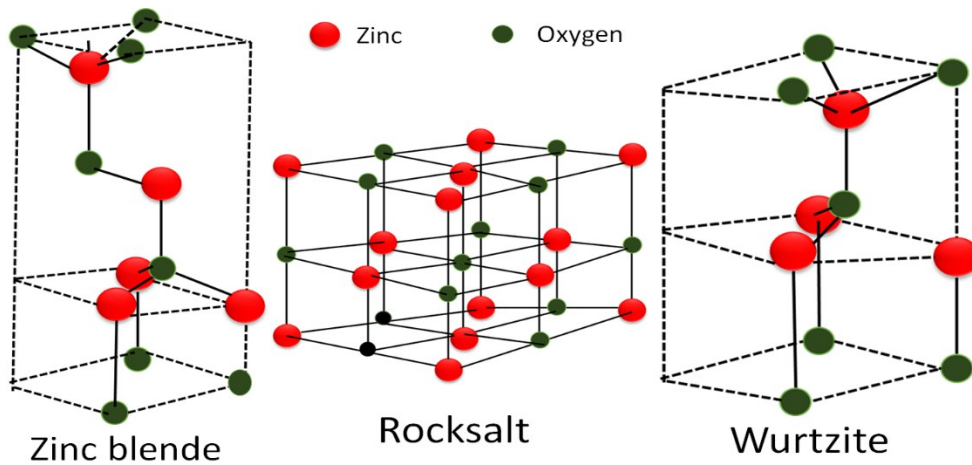


Figure 1.19. Crystal structures of ZnO: (a) Zinc blende, (b) rock salt, (c) wurtzite.

The lattice constants of wurtzite ZnO at room temperature were determined as $a=3.2475\text{ \AA}$, $c=5.2075\text{ \AA}$. The most common faces of wurtzite ZnO are the polar surfaces of Zn (0001) and O (000 $\bar{1}$) (c-axis oriented), and the non-polar (11 $\bar{2}$ 0) (a-axis) and (10 $\bar{1}$ 0). The point defects such as zinc antisites, oxygen vacancies, and extended defects such as threading dislocations also increase the lattice constants. The bonding nature between Zn and O ions is right between covalent and ionic binding. Due to ionic binding of ZnO, the bottom of the conduction band is formed by the 4s levels of Zn^{2+} . Further, the top of the valence band by the 2p levels of O^{2-} . The bandgap of ZnO between the conduction band and the highest valence band is about 3.437 eV.

1.9.2 Piezoelectricity in ZnO

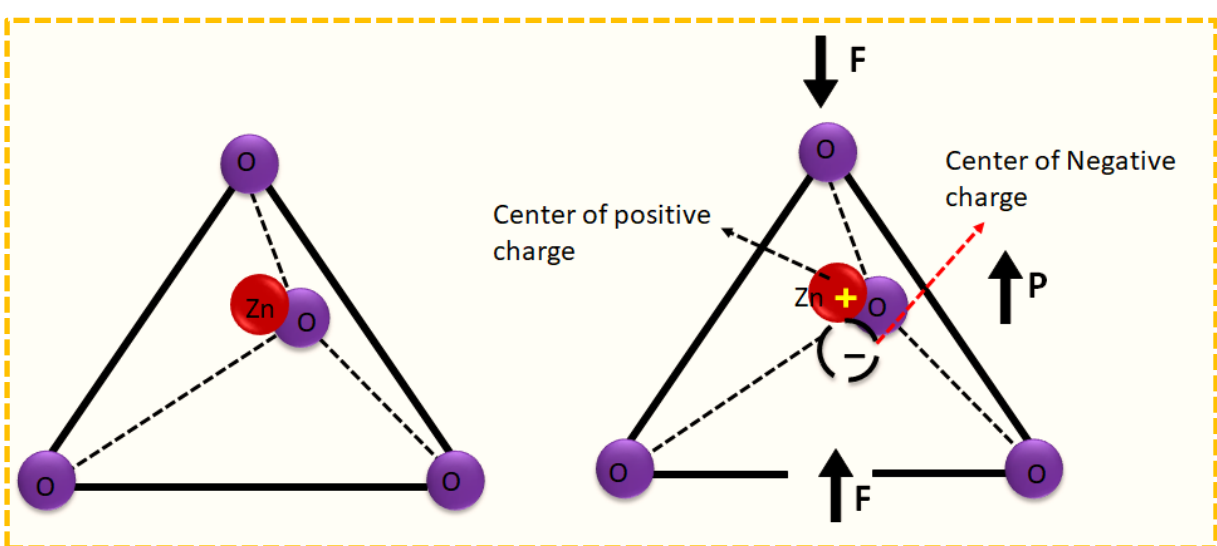


Figure 1.20. Piezoelectricity in ZnO.

The piezoelectric effect is the ability of certain materials to generate an electric charge in response to applied mechanical stress. The generation of electrical polarization when a piezoelectric material is strained is called the direct piezoelectric effect. The wurtzite structure of ZnO has a lack of center of symmetry, combined with a large electromechanical coupling, due to that, it has strong piezoelectric property. This piezoelectric property of ZnO is explored in many applications like actuators, piezoelectric sensors, and transducers.

Piezoelectricity is a phenomenon of coupling between the electrical and mechanical states of material by crystal structure deformation. In the absence of the applied force, positive- and negative-charge centers overlap, and the crystal is electrically neutral (no potential difference). When mechanical pressure is applied to the piezoelectric (ZnO) crystal structure, the charge centers of Zn^{2+} cations and O^{2-} anions will separate and produce piezoelectric potential across the material as shown in Figure 1.19 [84,85].

1.10 Objectives of thesis

The main aim of the thesis is to fabricate the innovative PENG and TENG devices using ZnO nanosheet film for energy harvesting from the human body motions. In the fabrication of the nanogenerator, ZnO nanosheets were used as an active layer, these ZnO nanosheets synthesized utilizing a low-cost hot plate hydrothermal approach. The PENG/TENG can be harnessed to drive small electronic devices, with potential applications encompassing the illumination and powering of LEDs, as well as the empowerment of various self-powered systems.

The objectives of this research are as follows:

- To synthesize ZnO nanosheets using a simple, single step, and cost effective hot-plate assisted hydrothermal method and to study the control synthesis parameters, including growth temperature, and growth duration, to achieve optimum ZnO nanosheets growth characteristics.
- To employ a comprehensive suite of advanced characterization techniques to thoroughly analyze the structural, morphological, and chemical properties of the synthesized ZnO nanosheets.
- To develop PENGs and TENGs using the synthesized ZnO nanosheets to efficiently convert mechanical energy into electrical energy.

- To measure the output voltage and current and various parameters influencing PENG/TENG nanogenerator performance, including tapping frequency, applied force, spacing, contact surface area.
- To confirm the charge generation and verify the experimental output using COMSOL software.
- To demonstrate and validate the practical utility of ZnO-based nanogenerators in self-powered electronics and sensors, showcasing their versatility in real-world applications.

1.11 Conclusions

This chapter offers a brief introduction highlighting the importance and motivation behind energy harvesting. It explores various energy sources in nature, providing insights into the origin and types of nanogenerators. The literature review focuses on PENG and TENG utilizing diverse functional materials, along with their applications. The goals of the research are derived from this literature review, providing a foundation for the subsequent material selection process.

1.12 References

- [1] Q. Zheng, H. Zhang, B. Shi, X. Xue, Z. Liu, Y. Jin, Y. Ma, Y. Zou, X. Wang, Z. An, W. Tang, W. Zhang, F. Yang, Y. Liu, X. Lang, Z. Xu, Z. Li, Z.L. Wang, In Vivo Self-Powered Wireless Cardiac Monitoring via Implantable Triboelectric Nanogenerator, *ACS Nano*. 10 (2016) 6510–6518. <https://doi.org/10.1021/acsnano.6b02693>.
- [2] S. Moreno, M. Baniasadi, S. Mohammed, I. Mejia, Y. Chen, M.A. Quevedo-Lopez, N. Kumar, S. Dimitrijevich, M. Minary-Jolandan, Biocompatible Collagen Films as Substrates for Flexible Implantable Electronics, *Adv. Electron. Mater.* 1 (2015) 1500154. [https://doi.org/https://doi.org/10.1002aelm.201500154](https://doi.org/10.1002aelm.201500154).
- [3] K. Venugopal, P. Panchatcharam, A. Chandrasekhar, V. Shanmugasundaram, Comprehensive Review on Triboelectric Nanogenerator Based Wrist Pulse Measurement: Sensor Fabrication and Diagnosis of Arterial Pressure, *ACS Sensors*. 6 (2021) 1681–1694. <https://doi.org/10.1021/acssensors.0c02324>.
- [4] A.A. Mathew, V. Shanmugasundaram, Fabrication of Screen-Printed Single-Electrode Triboelectric Nanogenerator-Based Self-Powered Sensor for Pulse Measurement and Its Characterization, *Energy Technol.* 11 (2023) 2300174. <https://doi.org/10.1002ente.202300174>.
- [5] L. Montès, R. Tao, R. Hinchet, G. Ardila, M. Mouis, S. Silveira-Stein, D. Hauser, P. Faucherand, G. Savelli, Energy harvesting from nanostructures, 2014 Int. Symp. Next-

- Generation Electron. ISNE 2014. (2014) 31–32. <https://doi.org/10.1109/ISNE.2014.6839387>.
- [6] H. Hou, W. Lu, B. Liu, Z. Hassanein, H. Mahmood, S. Khalid, Exploring the Role of Fossil Fuels and Renewable Energy in Determining Environmental Sustainability: Evidence from OECD Countries, *Sustainability*. 15 (2023) 2048. <https://doi.org/10.3390/su15032048>.
- [7] N.L. Panwar, S.C. Kaushik, S. Kothari, Role of renewable energy sources in environmental protection: A review, *Renew. Sustain. Energy Rev.* 15 (2011) 1513–1524. <https://doi.org/10.1016/j.rser.2010.11.037>.
- [8] R. Kothari, V. V. Tyagi, A. Pathak, Waste-to-energy: A way from renewable energy sources to sustainable development, *Renew. Sustain. Energy Rev.* 14 (2010) 3164–3170. <https://doi.org/10.1016/j.rser.2010.05.005>.
- [9] Z.L. Wang, G. Zhu, Y. Yang, S. Wang, C. Pan, Progress in nanogenerators for portable electronics, *Mater. Today*. 15 (2012) 532–543. [https://doi.org/10.1016/S1369-7021\(13\)70011-7](https://doi.org/10.1016/S1369-7021(13)70011-7).
- [10] Y. Zi, Z.L. Wang, Nanogenerators: An emerging technology towards nanoenergy, *APL Mater.* 5 (2017) 074103. <https://doi.org/10.1063/1.4977208>.
- [11] Z. Zhang, T. He, M. Zhu, Z. Sun, Q. Shi, J. Zhu, B. Dong, M.R. Yuce, C. Lee, Deep learning-enabled triboelectric smart socks for IoT-based gait analysis and VR applications, *Npj Flex. Electron.* 4 (2020) 1–12. <https://doi.org/10.1038/s41528-020-00092-7>.
- [12] H. Xue, Q. Yang, D. Wang, W. Luo, W. Wang, M. Lin, D. Liang, Q. Luo, A wearable pyroelectric nanogenerator and self-powered breathing sensor, *Nano Energy*. 38 (2017) 147–154. <https://doi.org/https://doi.org/10.1016/j.nanoen.2017.05.056>.
- [13] W. Qin, P. Zhou, X. Xu, C. Huang, G. Srinivasan, Y. Qi, T. Zhang, High-Performance Piezoelectric Nanogenerator Based on Low-Entropy Structured Nanofibers for a Multi-Mode Energy Harvesting and Self-Powered Ultraviolet Photodetector, *ACS Appl. Electron. Mater.* 4 (2022) 2970–2978. <https://doi.org/10.1021/acsaelm.2c00411>.
- [14] Z. Zhou, X. Li, Y. Wu, H. Zhang, Z. Lin, K. Meng, Z. Lin, Q. He, C.C. Sun, J. Yang, Z.L. Wang, Wireless self-powered sensor networks driven by triboelectric nanogenerator for in-situ real time survey of environmental monitoring, *Nano Energy*. 53 (2018) 501–507. <https://doi.org/10.1016/j.nanoen.2018.08.055>.
- [15] G. Min, A. Pullanchiyodan, A.S. Dahiya, E.S. Hosseini, Y. Xu, D.M. Mulvihill, R. Dahiya, Ferroelectric-assisted high-performance triboelectric nanogenerators based on

- electrospun P(VDF-TrFE) composite nanofibers with barium titanate nanofillers, *Nano Energy.* 90 (2021) 106600. <https://doi.org/10.1016/j.nanoen.2021.106600>.
- [16] Y. Wu, Y. Su, J. Bai, G. Zhu, X. Zhang, Z. Li, Y. Xiang, J. Shi, A Self-Powered Triboelectric Nanosensor for PH Detection, *J. Nanomater.* 2016 (2016) 1–6. <https://doi.org/10.1155/2016/5121572>.
- [17] X. Zhang, X. Du, Y. Yin, N.W. Li, W. Fan, R. Cao, W. Xu, C. Zhang, C. Li, Lithium-Ion Batteries: Charged by Triboelectric Nanogenerators with Pulsed Output Based on the Enhanced Cycling Stability, *ACS Appl. Mater. Interfaces.* 10 (2018) 8676–8684. <https://doi.org/10.1021/acsami.7b18736>.
- [18] X. Pu, L. Li, H. Song, C. Du, Z. Zhao, C. Jiang, G. Cao, W. Hu, Z.L. Wang, A Self-Charging Power Unit by Integration of a Textile Triboelectric Nanogenerator and a Flexible Lithium-Ion Battery for Wearable Electronics, *Adv. Mater.* 27 (2015) 2472–2478. <https://doi.org/https://doi.org/10.1002/adma.201500311>.
- [19] S. Rathore, S. Sharma, B.P. Swain, R.K. Ghadai, A Critical Review on Triboelectric Nanogenerator, *IOP Conf. Ser. Mater. Sci. Eng.* 377 (2018) 012186. <https://doi.org/10.1088/1757-899X/377/1/012186>.
- [20] Z.M. Huang, Y.Z. Zhang, M. Kotaki, S. Ramakrishna, A review on polymer nanofibers by electrospinning and their applications in nanocomposites, *Compos. Sci. Technol.* 63 (2003) 2223–2253. [https://doi.org/10.1016/S0266-3538\(03\)00178-7](https://doi.org/10.1016/S0266-3538(03)00178-7).
- [21] Z.L. Wang, J. Song, Piezoelectric nanogenerators based on zinc oxide nanowire arrays, *Science* (80-.). 312 (2006) 242–246. <https://doi.org/10.1126/science.1124005>.
- [22] F.-R. Fan, Z.-Q. Tian, Z. Lin Wang, Flexible triboelectric generator, *Nano Energy.* 1 (2012) 328–334. <https://doi.org/10.1016/j.nanoen.2012.01.004>.
- [23] Z.L. Wang, On Maxwell's displacement current for energy and sensors: the origin of nanogenerators, *Mater. Today.* 20 (2017) 74–82. <https://doi.org/10.1016/j.mattod.2016.12.001>.
- [24] P. Munirathinam, A. Anna Mathew, V. Shanmugasundaram, V. Vivekananthan, Y. Purusothaman, S.J. Kim, A. Chandrasekhar, A comprehensive review on triboelectric nanogenerators based on Real-Time applications in energy harvesting and Self-Powered sensing, *Mater. Sci. Eng. B.* 297 (2023) 116762. <https://doi.org/10.1016/j.mseb.2023.116762>.
- [25] P. Munirathinam, A. Anna Mathew, V. Shanmugasundaram, V. Vivekananthan, Y. Purusothaman, S.J. Kim, A. Chandrasekhar, A comprehensive review on triboelectric nanogenerators based on Real-Time applications in energy harvesting and Self-Powered

- sensing, Mater. Sci. Eng. B. 297 (2023) 116762. <https://doi.org/10.1016/j.mseb.2023.116762>.
- [26] Z.L. Wang, T. Jiang, L. Xu, Toward the blue energy dream by triboelectric nanogenerator networks, Nano Energy. 39 (2017) 9–23. <https://doi.org/10.1016/j.nanoen.2017.06.035>.
- [27] Y. Yang, S. Wang, Y. Zhang, Z.L. Wang, Pyroelectric nanogenerators for driving wireless sensors, Nano Lett. 12 (2012) 6408–6413. <https://doi.org/10.1021/nl303755m>.
- [28] N. Ma, Y. Yang, Enhanced self-powered UV photoresponse of ferroelectric BaTiO₃ materials by pyroelectric effect, Nano Energy. 40 (2017) 352–359. <https://doi.org/10.1016/j.nanoen.2017.08.043>.
- [29] D. Champier, Thermoelectric generators: A review of applications, Energy Convers. Manag. 140 (2017) 167–181. <https://doi.org/10.1016/j.enconman.2017.02.070>.
- [30] Y. Yang, K.C. Pradel, Q. Jing, J.M. Wu, F. Zhang, Y. Zhou, Y. Zhang, Z.L. Wang, Thermoelectric nanogenerators based on single Sb-doped ZnO micro/nanobelts, ACS Nano. 6 (2012) 6984–6989. <https://doi.org/10.1021/nn302481p>.
- [31] N. Jaziri, A. Boughamoura, J. Müller, B. Mezghani, F. Tounsi, M. Ismail, A comprehensive review of Thermoelectric Generators: Technologies and common applications, Energy Reports. 6 (2020) 264–287. <https://doi.org/10.1016/j.egyr.2019.12.011>.
- [32] A.R.M. Siddique, S. Mahmud, B. Van Heyst, A review of the state of the science on wearable thermoelectric power generators (TEGs) and their existing challenges, Renew. Sustain. Energy Rev. 73 (2017) 730–744. <https://doi.org/10.1016/j.rser.2017.01.177>.
- [33] R. Feng, F. Tang, N. Zhang, X. Wang, Flexible, High-Power Density, Wearable Thermoelectric Nanogenerator and Self-Powered Temperature Sensor, ACS Appl. Mater. Interfaces. 11 (2019) 38616–38624. <https://doi.org/10.1021/acsami.9b11435>.
- [34] X. Wang, Piezoelectric nanogenerators-Harvesting ambient mechanical energy at the nanometer scale, Nano Energy. 1 (2012) 13–24. <https://doi.org/10.1016/j.nanoen.2011.09.001>.
- [35] J. Briscoe, S. Dunn, Piezoelectric nanogenerators - a review of nanostructured piezoelectric energy harvesters, Nano Energy. 14 (2014) 15–29. <https://doi.org/10.1016/j.nanoen.2014.11.059>.
- [36] S. Soh, S.W. Kwok, H. Liu, G.M. Whitesides, Contact De-electrification of electrostatically charged polymers, J. Am. Chem. Soc. 134 (2012) 20151–20159. <https://doi.org/10.1021/ja309268n>.

- [37] J. Luo, Z.L. Wang, Recent progress of triboelectric nanogenerators: From fundamental theory to practical applications, *EcoMat.* 2 (2020) 1–22. <https://doi.org/10.1002/eom2.12059>.
- [38] D. Li, C. Wu, L. Ruan, J. Wang, Z. Qiu, K. Wang, Y. Liu, Y. Zhang, T. Guo, J. Lin, T. Whan, Nano Energy Electron-transfer mechanisms for confirmation of contact-electrification in ZnO / polyimide-based triboelectric nanogenerators, *Nano Energy.* 75 (2020) 104818. <https://doi.org/10.1016/j.nanoen.2020.104818>.
- [39] W.R. Salaneck, A. Paton, D.T. Clark, Double mass transfer during polymer-polymer contacts, *J. Appl. Phys.* 47 (2008) 144–147. <https://doi.org/10.1063/1.322306>.
- [40] A.F. Diaz, J. Guay, Contact charging of organic materials: Ion vs. electron transfer, *IBM J. Res. Dev.* 37 (1993) 249–260. <https://doi.org/10.1147/rd.372.0249>.
- [41] M. Kaponig, A. Mölleken, H. Nienhaus, R. Möller, Dynamics of contact electrification, *Sci. Adv.* 7 (2021) 2–7. <https://doi.org/10.1126/sciadv.abg7595>.
- [42] C. P. R. Saunders, A Review of Thunderstorm Electrification Processes, *Science* (80-.). 55 (1992) 642–655. <https://doi.org/10.1126/science.55.1433.636.b>.
- [43] C. Xu, Y. Zi, A.C. Wang, H. Zou, Y. Dai, X. He, P. Wang, Y.-C. Wang, P. Feng, D. Li, Z.L. Wang, On the Electron-Transfer Mechanism in the Contact-Electrification Effect, *Adv. Mater.* 30 (2018) 1706790. <https://doi.org/https://doi.org/10.1002/adma.201706790>.
- [44] Z.L. Wang, A.C. Wang, On the origin of contact-electrification, *Mater. Today.* 30 (2019) 34–51. <https://doi.org/10.1016/j.mattod.2019.05.016>.
- [45] Y. Zhou, W. Deng, J. Xu, J. Chen, Engineering Materials at the Nanoscale for Triboelectric Nanogenerators, *Cell Reports Phys. Sci.* 1 (2020) 100142. <https://doi.org/10.1016/j.xcrp.2020.100142>.
- [46] Y. Zou, L. Bo, Z. Li, Recent progress in human body energy harvesting for smart bioelectronic system, *Fundam. Res.* 1 (2021) 364–382. <https://doi.org/10.1016/j.fmre.2021.05.002>.
- [47] W.D. McArdle, F.I. Katch, V.L. Katch, *Exercise Physiology: Nutrition, Energy, and Human Performance*, Wolters Kluwer Health/Lippincott Williams & Wilkins, 2015. <https://books.google.co.in/books?id=L8UfnQEACAAJ>.
- [48] D. Wan, J. Yang, X. Cui, N. Ma, Z. Wang, Y. Li, P. Li, Y. Zhang, Z.H. Lin, S. Sang, H. Zhang, Human body-based self-powered wearable electronics for promoting wound healing driven by biomechanical motions, *Nano Energy.* 89 (2021) 106465. <https://doi.org/10.1016/j.nanoen.2021.106465>.

- [49] S. Guerin, S.A.M. Tofail, D. Thompson, Organic piezoelectric materials: milestones and potential, *NPG Asia Mater.* 11 (2019) 1–5. <https://doi.org/10.1038/s41427-019-0110-5>.
- [50] T. Nayyar, K. Pubby, S.B. Narang, R. Mishra, Energy harvesting using piezoelectric materials, *Integr. Ferroelectr.* 176 (2016) 268–274. <https://doi.org/10.1080/10584587.2016.1252660>.
- [51] D. Hu, M. Yao, Y. Fan, C. Ma, M. Fan, M. Liu, Nano Energy Strategies to achieve high performance piezoelectric nanogenerators, *Nano Energy.* 55 (2019) 288–304. <https://doi.org/10.1016/j.nanoen.2018.10.053>.
- [52] X. Cao, Y. Xiong, J. Sun, X. Zhu, Q. Sun, Z.L. Wang, Piezoelectric Nanogenerators Derived Self-Powered Sensors for Multifunctional Applications and Artificial Intelligence, *Adv. Funct. Mater.* 31 (2021) 1–31. <https://doi.org/10.1002/adfm.202102983>.
- [53] Y. Guan, M. Bai, Q. Wang, L. Liu, S. Yu, B. Kong, F. Lv, M. Guo, G. Liu, L. Li, L. Zhang, Y. Lin, W. Li, A self-powered wearable piezoelectric nanogenerator for physiological monitoring based on lead zirconate titanate/microfibrillated cellulose@polyvinyl alcohol (PZT/MFC@PVA) composition, *Chem. Eng. J.* 460 (2023) 141598. <https://doi.org/10.1016/j.cej.2023.141598>.
- [54] W.G. Kim, D.W. Kim, I.W. Tcho, J.K. Kim, M.S. Kim, Y.K. Choi, Triboelectric Nanogenerator: Structure, Mechanism, and Applications, *ACS Nano.* 15 (2021) 258–287. <https://doi.org/10.1021/acsnano.0c09803>.
- [55] S.N. Alam, A. Ghosh, P. Shrivastava, U. Shukla, K. Garg, A.C. Edara, N. Sahoo, An introduction to triboelectric nanogenerators, *Nano-Structures and Nano-Objects.* 34 (2023) 100980. <https://doi.org/10.1016/j.nanoso.2023.100980>.
- [56] X. Yin, D. Liu, L. Zhou, X. Li, C. Zhang, P. Cheng, H. Guo, W. Song, J. Wang, Z.L. Wang, Structure and Dimension Effects on the Performance of Layered Triboelectric Nanogenerators in Contact-Separation Mode, *ACS Nano.* 13 (2019) 698–705. <https://doi.org/10.1021/acsnano.8b07935>.
- [57] X. Wang, G. Yin, T. Sun, G. Rasool, K. Abbas, Triboelectric Nanogenerator with a Rotational Freestanding Mode for Multi-directional Vibration Energy Harvesting, *ACS Appl. Energy Mater.* 6 (2023) 7607–7619. <https://doi.org/10.1021/acsaem.3c01042>.
- [58] H. Patnam, S.A. Graham, P. Manchi, M.V. Paranjape, J.S. Yu, Single-Electrode Triboelectric Nanogenerators Based on Ionic Conductive Hydrogel for Mechanical Energy Harvester and Smart Touch Sensor Applications, *ACS Appl. Mater. Interfaces.* 15 (2023) 16768–16777. <https://doi.org/10.1021/acسامي.3c00386>.

- [59] C. Xu, X. Fu, C. Li, G. Liu, Y. Gao, Y. Qi, T. Bu, Y. Chen, Z.L. Wang, C. Zhang, Raindrop energy-powered autonomous wireless hyetometer based on liquid–solid contact electrification, *Microsystems Nanoeng.* 8 (2022) 30. <https://doi.org/10.1038/s41378-022-00362-6>.
- [60] S. Wang, L. Lin, Y. Xie, Q. Jing, S. Niu, Z.L. Wang, Sliding-Triboelectric Nanogenerators Based on In-Plane Charge- Separation Mechanism, (2013).
- [61] P. Bai, G. Zhu, Y. Liu, J. Chen, Q. Jing, W. Yang, J. Ma, G. Zhang, Z.L. Wang, Cylindrical rotating triboelectric nanogenerator, *ACS Nano.* 7 (2013) 6361–6366. <https://doi.org/10.1021/nn402491y>.
- [62] Z.L. Wang, L. Lin, J. Chen, S. Niu, Y. Zi, Triboelectric Nanogenerator: Vertical Contact-Separation Mode, in: *Green Energy Technol.* Springer, Cham., 2016: pp. 23–47. https://doi.org/10.1007/978-3-319-40039-6_2.
- [63] S. Niu, Y. Liu, S. Wang, L. Lin, Y.S. Zhou, Y. Hu, Z.L. Wang, Theory of sliding-mode triboelectric nanogenerators, *Adv. Mater.* 25 (2013) 6184–6193. <https://doi.org/10.1002/adma.201302808>.
- [64] S. Niu, Y. Liu, S. Wang, L. Lin, Y.S. Zhou, Y. Hu, Z.L. Wang, Theoretical investigation and structural optimization of single-electrode triboelectric nanogenerators, *Adv. Funct. Mater.* 24 (2014) 3332–3340. <https://doi.org/10.1002/adfm.201303799>.
- [65] S. Niu, Y. Liu, X. Chen, S. Wang, Y.S. Zhou, L. Lin, Y. Xie, Z.L. Wang, Theory of freestanding triboelectric-layer-based nanogenerators, *Nano Energy.* 12 (2015) 760–774. <https://doi.org/10.1016/j.nanoen.2015.01.013>.
- [66] J.C. Wilcke, Physical Experimental Discussion Concerning Opposite Electricities, Printed by Ioannis Jacobi Adler ... , Rostochii, 1757. <https://books.google.co.in/books?id=2yJTzwEACAAJ>.
- [67] Experiments on Tribo-Electricity, *Nature.* 100 (1917) 336–337. <https://doi.org/10.1038/100336b0>.
- [68] W.D. Greason, Investigation of a test methodology for triboelectrification, *J. Electrostat.* 49 (2000) 245–256. [https://doi.org/10.1016/S0304-3886\(00\)00013-9](https://doi.org/10.1016/S0304-3886(00)00013-9).
- [69] P. Llovera, P. Molinié, A. Soria, A. Quijano, Measurements of electrostatic potentials and electric fields in some industrial applications: Basic principles, *J. Electrostat.* 67 (2009) 457–461. <https://doi.org/10.1016/j.elstat.2009.01.004>.
- [70] A.F.M. Seyam, Y. Cai, W. Oxenham, Devices for measuring electrostatic generation and dissipation on the surfaces of polymeric materials, *J. Text. Inst.* 100 (2009) 338–349. <https://doi.org/10.1080/00405000701819840>.

- [71] R.A. Lodge, B. Bhushan, Effect of physical wear and triboelectric interaction on surface charge as measured by Kelvin probe microscopy, *J. Colloid Interface Sci.* 310 (2007) 321–330. <https://doi.org/10.1016/j.jcis.2007.01.063>.
- [72] T.A.L. Burgo, C.A. Silva, L.B.S. Balestrin, F. Galembeck, Friction coefficient dependence on electrostatic tribocharging, *Sci. Rep.* 3 (2013) 1–8. <https://doi.org/10.1038/srep02384>.
- [73] H. Zou, Y. Zhang, L. Guo, P. Wang, X. He, G. Dai, H. Zheng, C. Chen, A.C. Wang, C. Xu, Z.L. Wang, Quantifying the triboelectric series, *Nat. Commun.* 10 (2019) 1–9. <https://doi.org/10.1038/s41467-019-09461-x>.
- [74] P.Y. Feng, Z. Xia, B. Sun, X. Jing, H. Li, X. Tao, H.Y. Mi, Y. Liu, Enhancing the Performance of Fabric-Based Triboelectric Nanogenerators by Structural and Chemical Modification, *ACS Appl. Mater. Interfaces.* 13 (2021) 16916–16927. <https://doi.org/10.1021/acsami.1c02815>.
- [75] S. Raha, M. Ahmaruzzaman, ZnO nanostructured materials and their potential applications: progress, challenges and perspectives, *Nanoscale Adv.* 4 (2022) 1868–1925. <https://doi.org/10.1039/d1na00880c>.
- [76] Z.L. Wang, Zinc oxide nanostructures: growth, properties and applications, *J. Phys. Condens. Matter.* 16 (2004) R829–R858. <https://doi.org/10.1088/0953-8984/16/25/R01>.
- [77] J.L. Gomez, O. Tigli, Zinc oxide nanostructures: From growth to application, *J. Mater. Sci.* 48 (2013) 612–624. <https://doi.org/10.1007/s10853-012-6938-5>.
- [78] Ü. Özgür, Y.I. Alivov, C. Liu, A. Teke, M.A. Reshchikov, S. Doğan, V. Avrutin, S.J. Cho, H. Morkoç, A comprehensive review of ZnO materials and devices, *J. Appl. Phys.* 98 (2005) 1–103. <https://doi.org/10.1063/1.1992666>.
- [79] Y. Qiu, H. Zhang, L. Hu, D. Yang, L. Wang, B. Wang, J. Ji, G. Liu, X. Liu, J. Lin, F. Li, S. Han, Flexible piezoelectric nanogenerators based on ZnO nanorods grown on common paper substrates, *Nanoscale.* 4 (2012) 6568–6573. <https://doi.org/10.1039/c2nr31031g>.
- [80] S. Wang, H. Tai, B. Liu, Z. Duan, Z. Yuan, H. Pan, Y. Su, G. Xie, X. Du, Y. Jiang, A facile respiration-driven triboelectric nanogenerator for multifunctional respiratory monitoring, *Nano Energy.* 58 (2019) 312–321. <https://doi.org/10.1016/j.nanoen.2019.01.042>.
- [81] B. Liu, S. Wang, Z. Yuan, Z. Duan, Q. Zhao, Y. Zhang, Y. Su, Y. Jiang, G. Xie, H. Tai, Novel chitosan/ZnO bilayer film with enhanced humidity-tolerant property: Endowing triboelectric nanogenerator with acetone analysis capability, *Nano Energy.* 78 (2020)

105256. <https://doi.org/10.1016/j.nanoen.2020.105256>.
- [82] K.H. Kim, B. Kumar, K.Y. Lee, H.K. Park, J.H. Lee, H.H. Lee, H. Jun, D. Lee, S.W. Kim, Piezoelectric two-dimensional nanosheets/anionic layer heterojunction for efficient direct current power generation, *Sci. Rep.* 3 (2013) 1–6. <https://doi.org/10.1038/srep02017>.
- [83] S. Mustapha, M.M. Ndamitso, A.S. Abdulkareem, J.O. Tijani, D.T. Shuaib, A.O. Ajala, A.K. Mohammed, Application of TiO₂ and ZnO nanoparticles immobilized on clay in wastewater treatment: a review, *Appl. Water Sci.* 10 (2020) 1–36. <https://doi.org/10.1007/s13201-019-1138-y>.
- [84] Z.L. Wang, From nanogenerators to piezotronics-A decade-long study of ZnO nanostructures, *MRS Bull.* 37 (2012) 814–827. <https://doi.org/10.1557/mrs.2012.186>.
- [85] N.D. Sharma, R. Maranganti, P. Sharma, On the possibility of piezoelectric nanocomposites without using piezoelectric materials, *J. Mech. Phys. Solids.* 55 (2007) 2328–2350. <https://doi.org/10.1016/j.jmps.2007.03.016>.

Chapter 2

Experimental Methods and Characterization

This chapter summarises the Hot-plate assisted hydrothermal procedure used to synthesis of ZnO nanosheets, over an aluminum substrate, ZnO nanosheets were grown. Emphasized the techniques used for investigating the properties of the materials. Furthermore, PENG and TENG device fabrication steps, advanced instruments utilised to examine the electrical properties of these devices, and ultimately essential parameters have been determined.

2.1 Synthesis process of ZnO nanosheets

Many methods have been investigated for the production of ZnO nanostructures, including electro-deposition, sol-gel method, chemical vapor deposition, chemical methods, pulsed laser detection, and hydrothermal method. In comparison to previous synthesis processes, the hydrothermal approach gained more attention because of environmental concerns, as the water was utilized as the solvent. When compared to other technologies, this process is cost-effective, uses low temperatures, and can manufacture large-scale and well-ordered nanostructures. In addition to this, temperature and pressure can be adjusted to create different kinds of crystallization and nanostructures [1].

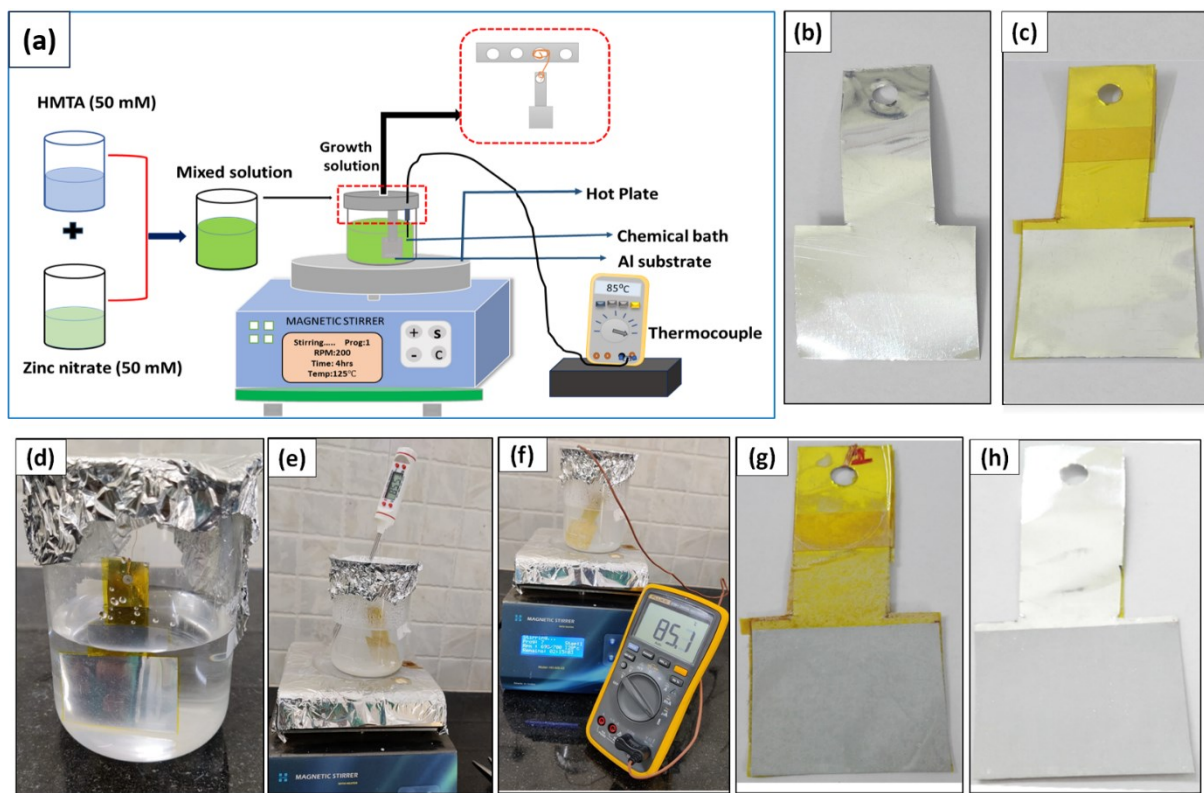
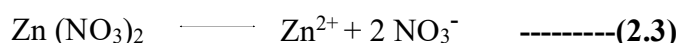
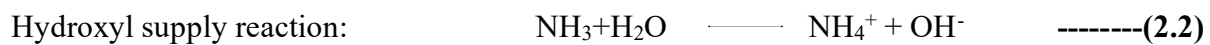
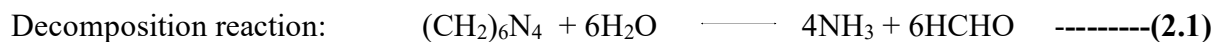


Figure 2.1. (a) Schematic of the preparation steps of ZnO nanosheets and experimental setup of hot plate synthesis of ZnO nanosheets. Real-time images of the preparation steps of ZnO nanosheets (b) bare aluminum substrate, (c) aluminum substrate sealed with Kapton tape (d) substrate suspended in the growth solution in a sealed glass beaker; (e)-(f) growth solution beaker placed over the hot plate and solution temperature observed by using digital thermometer and thermocouple (g)-(h) aluminum substrate after the growth of ZnO nanosheets with the removal of Kapton tape.

Furthermore, hydrothermal procedures often provide a high degree of control over the dimension, shape, and morphological structures of the nanostructures. Owing to these special

advantages, we opted to utilize the hydrothermal approach in our quest to synthesize ZnO nanosheets. The ZnO nanosheet film was synthesized on Al substrates by using hot plate method like shown in schematic Figure 2.1(a). All the chemicals obtained from Sigma Aldrich were and utilised without additional purification, and aluminum foil with a thickness of 0.1 mm was acquired from M/s Special Metals Pvt. Ltd, India, used without further cleaning operations. First, the aluminum substrates were ultrasonically cleaned with acetone and deionized (DI) water for 10 minutes, then dried with a hair blower. Initially, zinc nitrate ($Zn(NO_3)_2 \cdot 6H_2O$, 50 mM) and hexamethylenetetramine ($C_6H_{12}N_4$, HMTA, 50 mM) were dissolved in 100 mL of DI water and stirred for 10 minutes separately at room temperature. These two solutions were mixed in another beaker and stirred up to transparency appeared. One side of the aluminum substrate was sealed with Kapton tape and suspended in the growth solution as shown in Figure 2.1 (b)-(c). The growth solution beaker was covered with aluminum foil. A small opening was made to insert a thermocouple for the temperature monitoring, as shown in Figure 2.1 (d). This small opening in the aluminum foil can be closed or opened depending on the requirement. In the process of synthesis, the growth precursor solution temperature was measured against the applied hot plate temperature by inserting a digital thermometer and thermocouple in the growth precursor solution (Figure 2.1 (e-f)). Finally, the growth precursor beaker was kept over the hotplate at growth temperatures of 85 °C for 4 hrs. After 4 hours of growth, ZnO-coated films on aluminum substrates were taken from the solution, rinsed with DI water, and dried with a hair blower. The real-time images of ZnO nanosheets grown on an aluminum substrate are depicted in Figure 6.1 (g-h). Subsequently, the ZnO nanosheets were further characterized to investigate their properties.

The growth of zinc oxide nanosheets using the hydrothermal method often involves a chemical system that, while widely used, remains not fully understood. According to the literature, the growth mechanism of zinc oxide nanosheets closely resembles that of zinc oxide nanowires [2,3]. The synthesis of ZnO nanosheets involves the combination of zinc nitrate and hexamethylenetetramine in deionized water, with subsequent heating in the temperature range of below 100 °C. The growth of ZnO nanosheets is expected to be influenced by a set of chemical reactions as follows:



Initially, the HMTA decomposes and forming formaldehyde and NH_3 with gradual increase of heat (eqn.2.1). Then, NH_3 reacts with water, producing HO^- ions (eqn.2.2). Afterward the dissolving of zinc nitrate, Zn^{2+} ions are produced (eqn.2.3), resulting in the direct formation of crystals of ZnO (eqn.2.4).

2.2 Characterization techniques

We have used different characterization techniques for surface topography, morphology, roughness, crystallinity, microstructure, elemental composition, optical, chemical and electrical properties. The details of each characterization technique are discussed below.

2.2.1 X-ray diffraction (XRD)

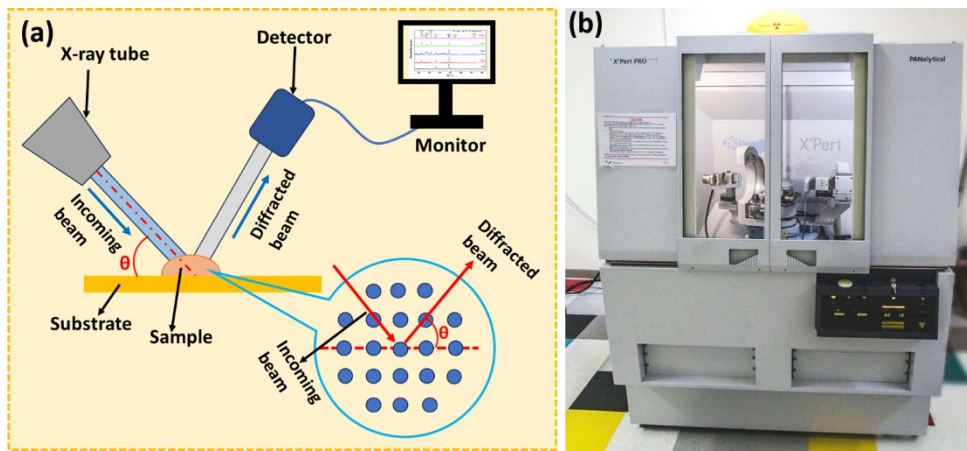


Figure 2.2. (a) Schematic representation of the X-ray diffraction principle, (b) Photograph of PANalytical powder diffractometer instrument (Adopted from) [4].

X-ray diffraction (XRD) is a standard and powerful technique to determine the crystalline structure, composition, identification of different crystalline phase, grain size of poly crystals and interlayer spacing of a sample[5]. XRD creates a diffraction pattern by exposing a sample to X-rays, revealing important information about the material's properties. X-rays are used in XRD because their wavelength ($0.5\text{-}2\text{\AA}$) is approximately equivalent to the spacing between atoms in a crystal lattice. To understand the phenomenon of XRD is aided by the use of constructive interference, which follows the Braggs law (Figure 2.2(a-b)). According to Bragg's law, when monochromatic X-rays are directed at a crystal lattice, scattering occurs as the X-rays interact with the atoms within the lattice. Constructive interference of the scattered waves happens when the angle of incidence satisfies the condition that the path difference between X-rays scattered by successive atomic planes is an integer multiple of the X-ray wavelength. Mathematically expressed formula is $2ds\sin\theta = n\lambda$. Here, d is the distance between lattice

planes, θ is the angle of incidence, n is an integer, and λ is the wavelength. In X-ray diffraction, the interlayer distance is a unique property for each crystal, representing the spacing between lattice planes. The presence of sharp peaks in the XRD pattern signifies a crystalline nature. These peaks result from the diffraction of X-rays by well-defined crystal planes within the material. Conversely, the appearance of broad peaks in the XRD pattern suggests an amorphous or disordered structure. Amorphous materials lack the regular and repeating atomic arrangements characteristic of crystalline substances.

Instrument specifications: The below instruments are used for XRD characterization in this thesis.

Model: XPERT-PRO; **X-ray Source:** Cu-K α radiation ($\lambda = 1.5418 \text{ \AA}$); **Goniometer Configuration:** Horizontal (θ - θ) (XRD, Bruker D8)

Detector: Scan Range: 3° to 136° ; Scanning Angle Rate: 0.01° ; Step Count Time: 1s per step.

2.2.2 Scanning electron microscopy (SEM)

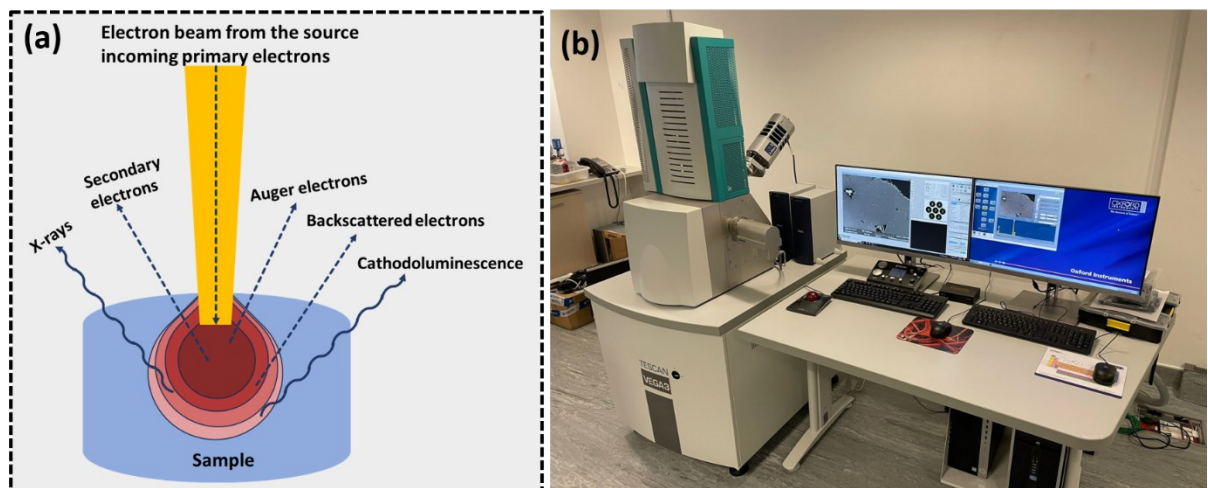


Figure 2.3. (a) Schematic representation of the SEM principle, (b) Photograph of SEM instrument (Adopted from)[6].

Scanning Electron Microscopy (SEM) is one of the sophisticated imaging techniques to characterize the morphology of the materials and compositions with higher resolution. The surface morphology of any material can be provided by the SEM with high-quality images with resolutions of $\sim 5\text{nm}$ [6]. When a higher energy electron beam incident on the sample, the electrons interact with the surface of the sample due the inelastic scattering, generate a spectrum of informative signals include back scattered electrons (BSE), auger electrons, cathodoluminescence, secondary electrons (SE) and X-rays from different depth of the sample, which has shown in Figure 2.3(a). BSE and SE each offering distinct advantages. BSE are

useful for offering compositional insights and due to their shallower penetration depth of SE, provides predominantly the higher resolution image at the nanoscale [6,7].

In the SEM setup, the electrons produced by the electron gun with generating acceleration voltage of 300 V- 30 kV, these electrons traverse through a complex arrangement of electron magnetic lenses to precisely focus the coherent beam over the sample surface. Detectors employed in the SEM serve as crucial components to capture to capture specific facets of the information provided by electrons. Based the detector equipped, SE detectors are optimized to capture high-resolution images of the specimen's topography as well as BSE to understanding the material's composition. The SEM instrument image as shown in the Figure 2.3(b).

Instrument Specifications: The below instruments are used for SEM characterization in this thesis.

Model: TESCAN-VEGA 3LMV attached with Oxford Scanning Electron Microscope; **Electron Source:** pre-centred tungsten hairpin type; **Accelerating voltage:** 300 V to 30 kV; **Resolution:** 3.0 nm; **Magnification:** 5X to 300,000X.

Detector: Secondary electron detector: Everhart-Thornley; Backscattered electron detector: Thin five-segment solid-state detector.

2.2.3 Transmission electron microscopy (TEM)

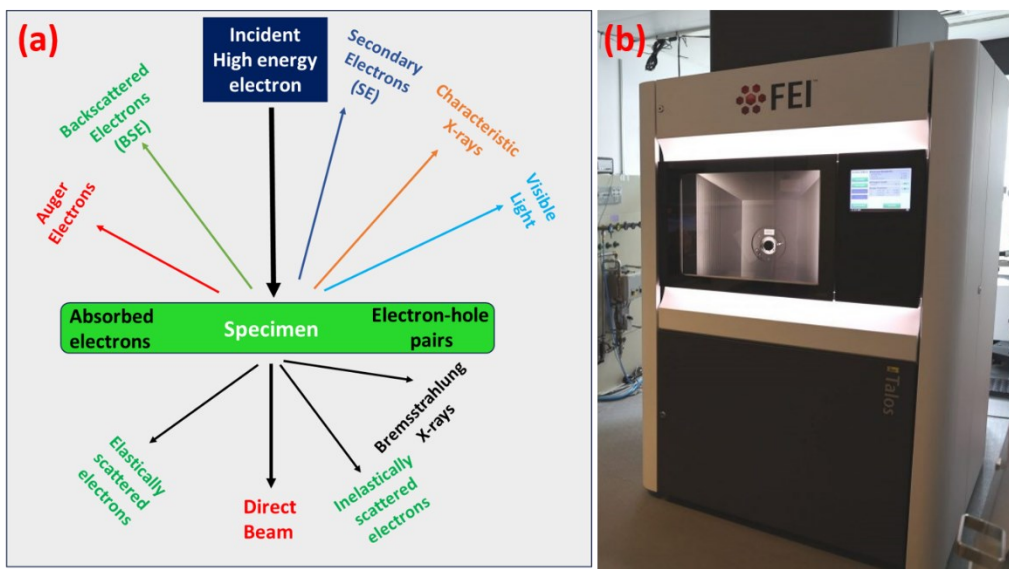


Figure 2.4. (a) Schematic representation of interaction between specimen and electron beam, (b) Photograph of TEM instrument.

Transmission electron microscopy (TEM) is high resolution microscopy technique used to study crystallinity, crystallographic features of point defects, dislocations, crystal structures

and crystal phases, and also morphology of individual nanostructures[8]. TEM generates a high-energy electron beam using cathode tungsten filament source/electron gun. This beam is focused and shaped by an array of electromagnetic lenses before coming into contact with an ultrathin specimen (Figure 2.4). The sample consists of Au/Cu-grids or pellets, which is generally 50-200 nanometers thick. Electrons that travel through the specimen undergo transmission, while those that interact with it help generate an image. On a fluorescent screen or digital detector, the resulting image is detected and visualised. Because of an electron's de-Broglie wavelength is smaller than that of visible light, TEM provides excellent resolution, allowing viewing of structures at the atomic and molecular levels.[9]

Instrument Specifications: The below instruments are used for TEM characterization in this thesis.

Model: Transmission electron microscopic (TEM) images were detected by a TALOS F200S G2 equipped with a CMOS Camera 4K X 4K; operating at a voltage of 200 KV, Total beam current FEG is >150 nA; Resolution- 0.16nm. (TEM, Tecnai G2 20)

2.2.4 Energy dispersive spectroscopy (EDS)

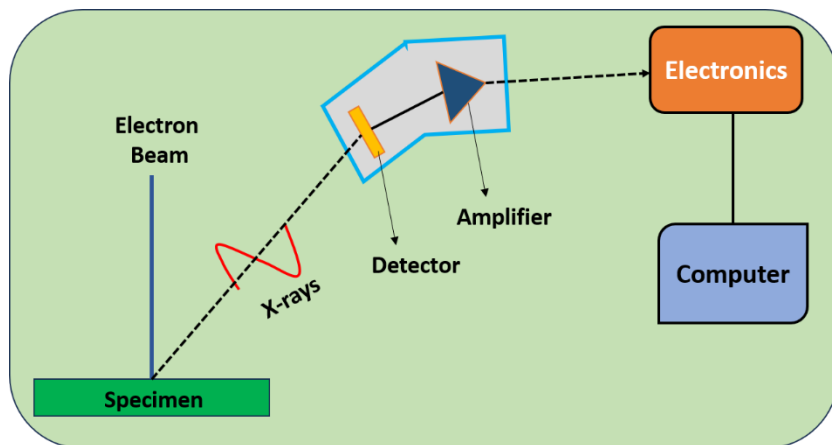


Figure 2.5. Schematic representation of the EDX principle

Energy Dispersive X-ray Spectroscopy (EDX) is an analytical technique useful for chemical composition and the elemental mapping of the sample. Generally, EDX is an additional component or accessory that can be equipped with either an SEM or a TEM. When focused electron beam directed onto the sample surface, the ground state electrons excite to higher energy level, and creates vacancies. Electrons from higher energy levels subsequently fill the vacancies, generating X-rays in the process (Figure 2.5). The emitted X-rays are collected using a solid-state detector, used to analyse the identifying the elements, Mapping the distribution of elements.

2.2.5 Fourier transform infrared spectroscopy (FT-IR)

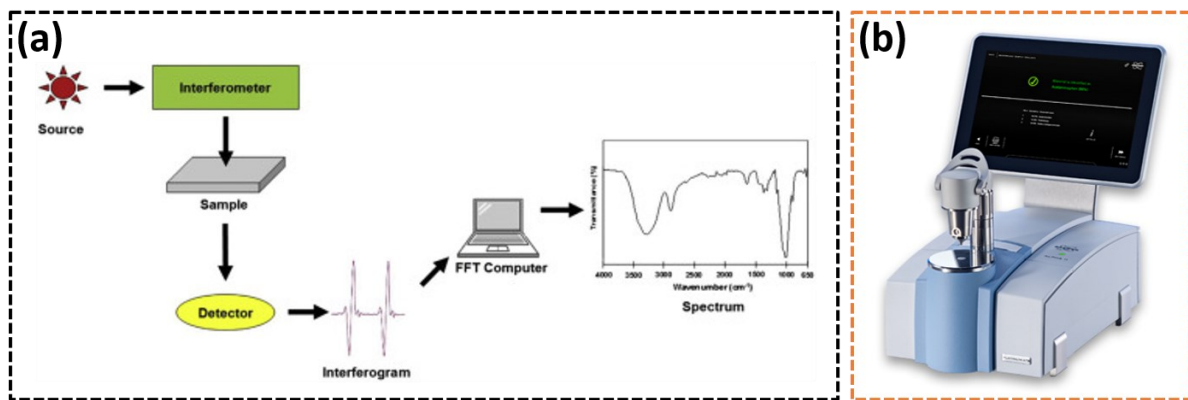


Figure 2.6. (a) Schematic representation of working of FTIR (b) Photograph of FTIR instrument (Reproduced from) [10].

Fourier Transform Infrared (FTIR) spectroscopy is a highly valuable analytical technique employed to examine molecular interactions within a sample[11]. In this method, the sample is exposed to infrared radiation, causing the infrared light to interact with the molecular vibrations of the sample. The resultant response is captured as an interferogram, representing the intensity of the infrared light over time. Utilizing a Fourier transform algorithm, this interferogram is converted from the time domain to the frequency domain (Figure 2.6 (a)). The resulting FTIR spectra reveals the information about the vibrational modes of chemical bonds within a molecule, with peaks in the spectrum correspond to specific vibrational frequencies. This enables the identification of functional groups within the sample. The versatility of FTIR extends to various sample types, including liquids and solids. Key components of an FTIR spectrometer include a radiation source, interferometer, sample compartment, and a detector. Beyond chemical analysis, FTIR spectroscopy contributes to the exploration of material properties such as polymer composition, crystallinity, and the presence of functional groups. FT-IR spectra are recorded using Bruker Fourier transform infrared spectrometer, often employing a KBr pellet, within the range of 4000 to 400 cm^{-1} (Figure 2.6(b)).

Instrument specifications: The below instruments are used for FTIR characterization in this thesis.

Model: Bruker Alpha-II FTIR spectrometer; spectral range 400-4000 cm^{-1} .

2.2.6 Raman spectroscopy

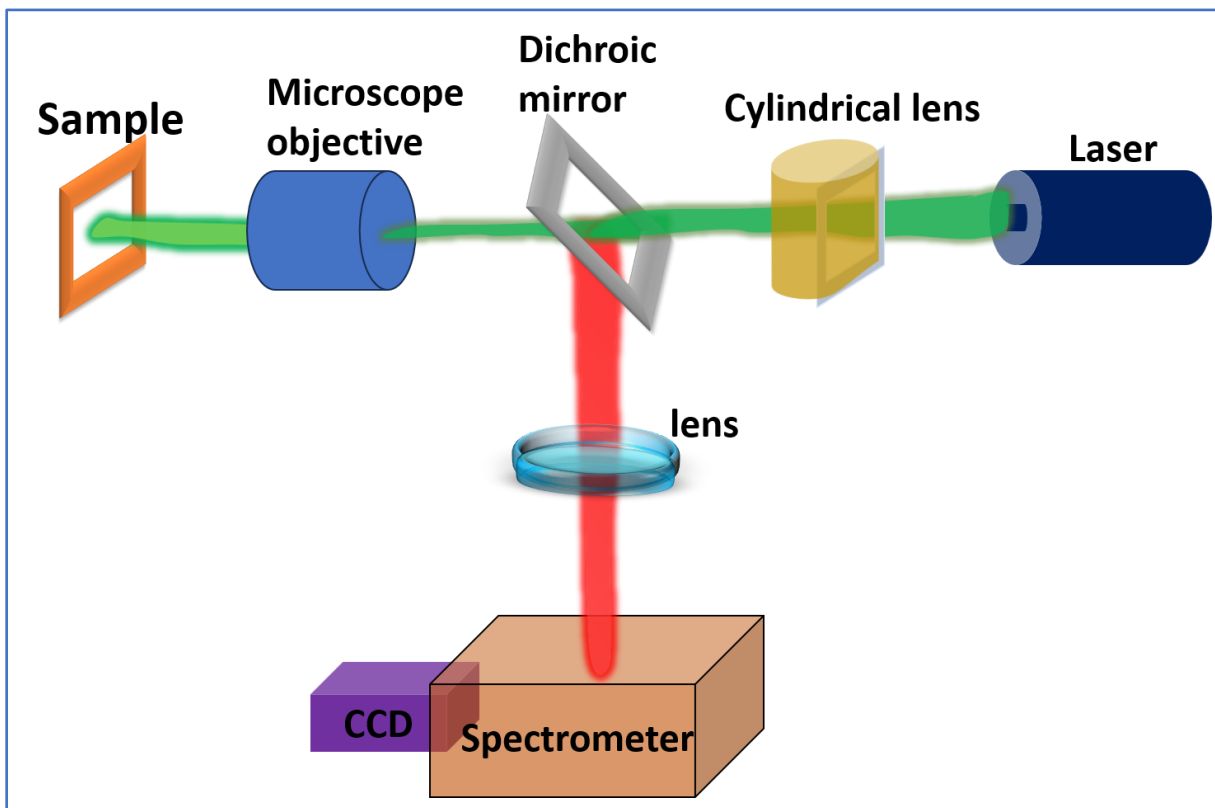


Figure 2.7. Raman spectroscopy instrumentation (Reproduced from) [12]

Raman spectroscopy is non-destructive technique used for studying vibrational, and rotational of the molecules in the sample [12]. Raman spectroscopy works based on Raman effect, in which Raman spectra arises because of inelastic collision of laser beam radiation and the molecules in sample. In Raman spectroscopy, when the monochromatic laser beam interacts with a sample, most of the photons undergo the elastic scattering (Rayleigh scattering), which is having the same frequency to incident beam. The rest of the beam undergo inelastic scattering, which is having the frequency different from the incident beam. The frequency of incident laser beam higher is higher than the frequency scattered will show the stokes line, and the frequency of incident laser beam lower than the frequency scattered will show the Anti-stokes line, in the Raman spectrum. Raman spectra can be recorded over a range of 4000–10 cm^{-1} (Figure 2.7).

Instrument specifications: The below instruments are used for Raman characterization in this thesis.

Model: Renishaw in Via Raman spectrometer, which was equipped with a 785 nm near-IR laser.

2.2.7 Photoluminescence spectroscopy (PL)

The study of photoluminescent or emission properties in materials is conducted using a photoluminescence spectrometer. The study of luminescence proves valuable in discerning the excitation and emission processes, band gap characteristics, and impurity defect levels of materials through analysis of their emission spectra. Photoluminescence is the phenomenon where a material absorbs photons and then re-emits them as light. For the purpose of analyzing the electrical and optical properties of semiconductors, nanomaterials, quantum dots, and other materials that are capable of producing light, this approach is very useful. [13]. Figure 2.8 displays a schematic representation of the components of the PL spectrometer.

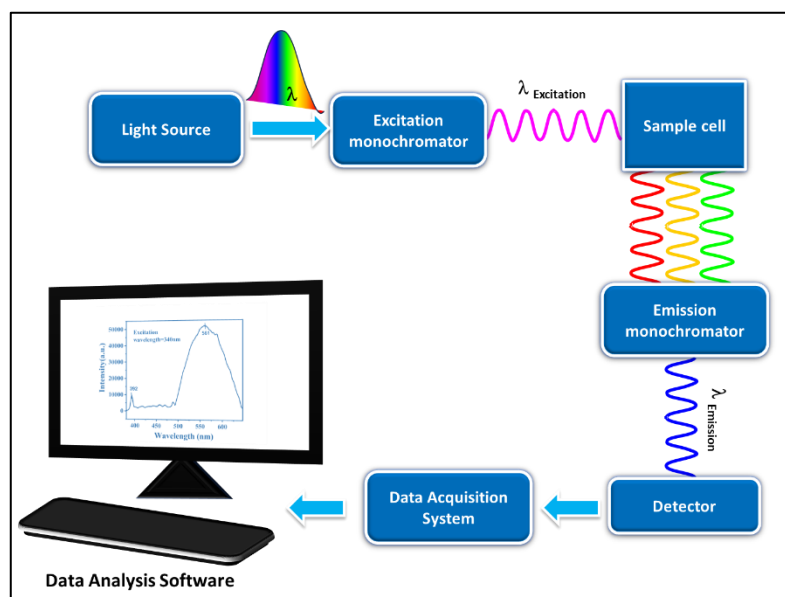


Figure 2.8. Basic instrumentation of Photoluminescence spectrometer

Typically, the spectrometer employs a light source for sample excitation, such as a laser or a light-emitting diode (LED) with a specific wavelength tailored to the material's light absorption characteristics. The sample is enclosed in a stable environment within a box to minimize external influences. Filters are employed to selectively focus on specific photoluminescent emissions of interest by choosing particular wavelengths of emitted light during analysis. The emitted light is captured by a sensitive detector, which then converts it into an electrical signal. Typical detectors utilized in this context include charge-coupled devices (CCDs) and photomultiplier tubes (PMTs). The electrical signal obtained from the detector is processed by the data collection system. This configuration generates a photoluminescence spectrum, capturing information about the intensity and wavelength of the light. Specialized software is employed to analyze the data, providing insights into the material's characteristics. Extraction

of information regarding emission bands, spectral peaks, energy levels, and transition details is achieved through this analysis.

Instrument specifications: The below instruments are used for PL characterization in this thesis.

Model: Fluro log 3-2; Light source: 450 W CW Ozone-free xenon arc lamp (250 to 2500 nm);

Monochromators: Czerny-Turner design with plane gratings for optimized focus at all wavelengths ad minimum stray light.

Sample detector: Photomultiplier R928P, spectral coverage 200 to 870 nm.

Reference detector: UV enhanced silicon photodiode.

2.2.8 Atomic force microscopy (AFM)

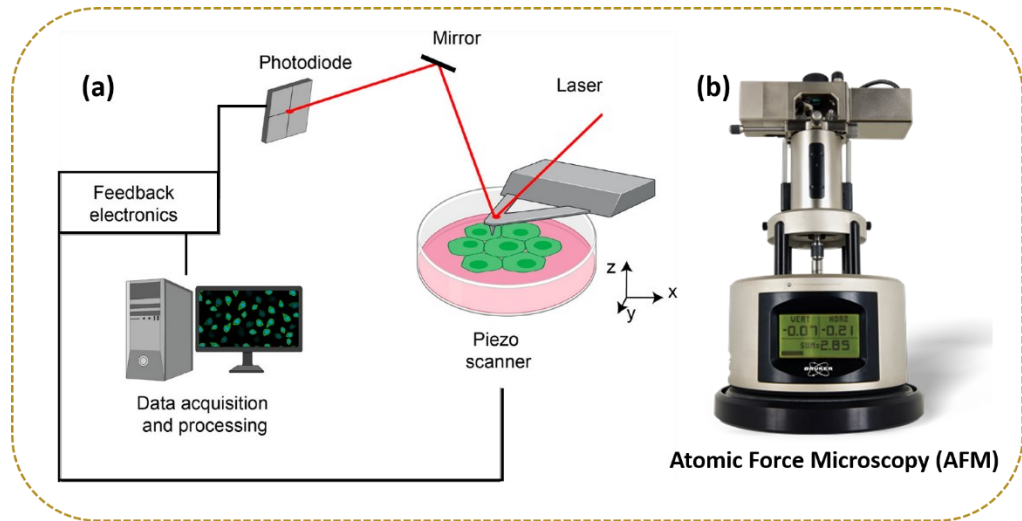


Figure 2.9. (a) the schematic view of the AFM instrumentation (b) AFM instrument
(Reproduced from) [14].

Atomic Force Microscopy (AFM), is powerful instrument for nanoscale surface imaging (Surface roughness, height profile and 3D image) [14]. It is useful to understand their shapes and properties at the tiniest levels. It measures the forces generated between a sharp tip and a sample to produce high-resolution three-dimensional images by scanning the sample's surface. AFM works by interaction forces between a tiny tip and the object/sample being studied. In one common mode, the tip stays in constant touch with the object's surface. As the tip moves across, it adjusts up and down to keep a steady force. These adjustments are recorded to create a detailed map of the object's surface. Another mode, called tapping mode, involves the tip oscillates back and forth as it moves over the object. The size of this Oscillation is kept the same, but changes in the object's surface make the tip oscillation at different rates. These variations help create an image of the object Figure 2.9(a).

Instrumentation:

AFM equipped with a flexible cantilever; AFM features a sharp tip for interacting with the sample surface. A laser beam precisely targets the cantilever's back, while a photodetector captures changes in reflected light intensity as the cantilever moves. The sample, mounted on a piezoelectric scanner, undergoes meticulous movements in the x, y, and z directions for precise scanning. The feedback system operates in a continuous loop, ensuring a constant force or amplitude during scanning. The signals from the photodetector and scanner are sent to a computer, where image processing software transforms the data into high-resolution topographic images, contributing to the detailed analysis of the sample's surface [14] (Figure 2.9(b)).

Instrument specifications: The below instruments are used for AFM characterization in this thesis.

Model: MultiMode 8-HR, SAM6 signal access module, NanoScope COM interface.

2.2.9 Polarizing optical microscope (POM)

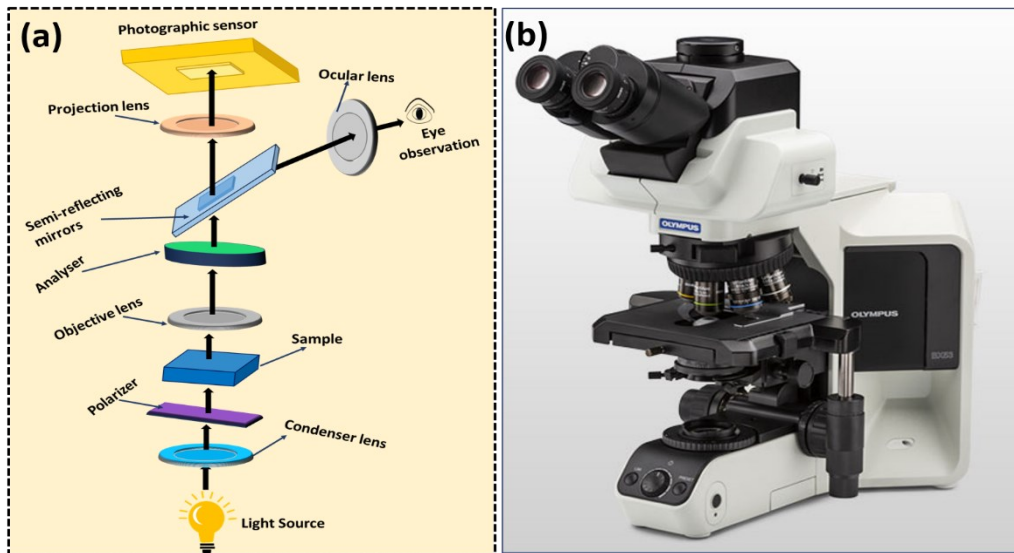


Figure 2.10. (a) Schematic representation of the optical polarizing microscopy instrumentation, (b) Visual depiction of the optical polarizing microscope setup.

Optical microscopy is a valuable technique employed to magnify small objects within the micrometer range, allowing for the in-depth study of their structural details. Optical microscopy relies on key principles such as magnification, resolution, and contrast to visualize small objects using visible light. It employs lenses to enlarge objects, and the total magnification results from multiplying the objective and eyepiece magnifications. Resolution,

determined by the wavelength of light and numerical aperture, dictates the microscope's ability to distinguish adjacent points.

The condenser directs illumination, often equipped with an aperture diaphragm. Objective lenses, with varying magnifications and numerical apertures, magnify the specimen. The stage supports precise specimen positioning, and the focus mechanism ensures accurate focusing. Eyepieces allow for magnified viewing, and binocular microscopes offer stereoscopic images. Additional components include a diaphragm/iris for light control, a magnification changer, filters for fluorescence microscopy, and detectors like cameras for image capture (Figure 2.10).

In our study we did not require polarization and were specifically interested in observing the specimen under bright-field conditions.

Instrument Specifications: The below instruments are used for Optical images in this thesis.

Model: Polarizing optical microscope Olympus BX-53 equipped with a Micropublisher 5.0

RTV camera interfaced to PC software Q-capture pro.

2.2.10 Scanning kelvin probe microscopy (SKP)

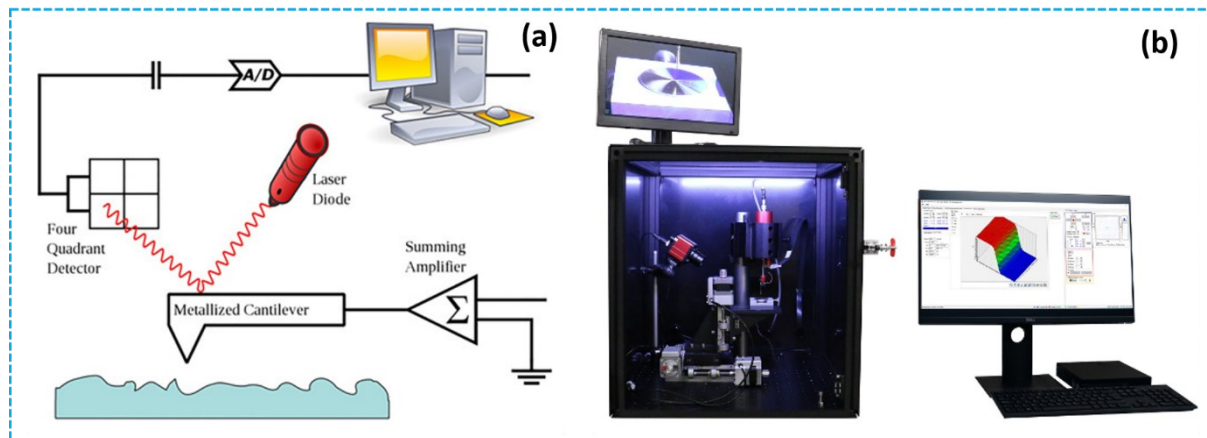


Figure 2.11. (a) schematic of Scanning Kelvin Probe Microscopy instrumentation, (b) Scanning Kelvin Probe Microscopy setup (Reproduced From) [15].

The Scanning Kelvin Probe Microscopy (SKPM) technique provides information on the topography and local electrical characteristics of the sample surface by combining the concepts of Kelvin Probe Microscopy and non-contact AFM. In SKPM, the Atomic Force Microscopy (AFM) system operates in a non-contact mode, wherein a conductive tip attached to a flexible cantilever oscillates just above the sample surface without making physical contact. The oscillation of the conductive AFM tip at the first resonant frequency of the cantilever is pivotal for improved sensitivity and imaging resolution during lateral scanning. The AFM tip's

conductive nature is exploited in SKPM to measure the contact potential difference (CPD) or work function difference between the tip and the sample. As the conductive tip scans laterally over the sample surface, it captures variations in height, thus generating topographic data. Control of the atomic force between the oscillating tip and the sample surface facilitates the acquisition of topography, resulting in a comprehensive three-dimensional representation of the sample (Figure 2.11 (a)) [15].

Instrument Specifications: *The below instruments are used for work function measurement in this thesis.*

Model: Scanning Kelvin Probe (SKP) system (SKP5050, KP Technology Ltd., U.K.) **Tip material / diameter:** Standard 2 mm gold tip (0.05 mm), **Oscilloscope:** Digital TFT oscilloscope for real time signal.

2.3 Nanogenerator device design

In the development of nanogenerator device, we have opted ZnO nanosheets as the source material for both piezoelectric and triboelectric applications, detailed across Chapters 3 to 7. Chapter 3 provides an in-depth look into the piezoelectric nanogenerator, emphasizing the utilization of ZnO nanosheets. Introduces ZnO as one of the key triboelectric layers, while Chapters 3 to 7 incorporate diverse materials as another triboelectric layer including Indium Tin Oxide (ITO), Polyethylene Terephthalate (PET), Overhead Projector (OHP), Poly(methyl methacrylate) (PMMA), and Polydimethylsiloxane (PDMS). The subsequent chapters delve into the electrical characteristics of these unique nanogenerators, offering a comprehensive study of their performance. The focus is on thorough analysis, encompassing experimental measurements and simulations.

2.3.1 Piezoelectric nanogenerator device fabrication

The fabrication of the nanogenerator required two conducting electrodes and piezoelectric nanostructure film. In the thesis we have used ZnO nanosheets as piezoelectric material and ITO/PET one of the electrodes and as explained in the **Section-2.1**. ZnO nanosheets directly coated on aluminum, the uncoated region of aluminium foil shown in Figure 2.12 (a &e) is act as the bottom electrode, and ITO coated PET sheet acts as the top electrode (Sigma Aldrich) (Figure 2.12 (b &f)). The Schematic and real images of the PENG device provided in Figure 2.12 (c-g). The direct growth of ZnO nanosheets on aluminum reduced electrode deposition step. The ITO coated PET sheet was placed over the ZnO nanosheet film without making any short-circuit with a bottom aluminum electrode. This sandwiched (PET:ITO/ZnO

nanosheets/Al) structure is sealed with Kapton tape rigidly to make proper contacts and avoid the triboelectric effect. Two conducting wires were connected to both the electrodes, as shown in Figure 2.12 (d&h). The nanogenerator response against finger tapping was recorded using digital storage oscilloscope (Tektronix TBS1102) with the help of interfacing software (Tekvisa) to the computer.

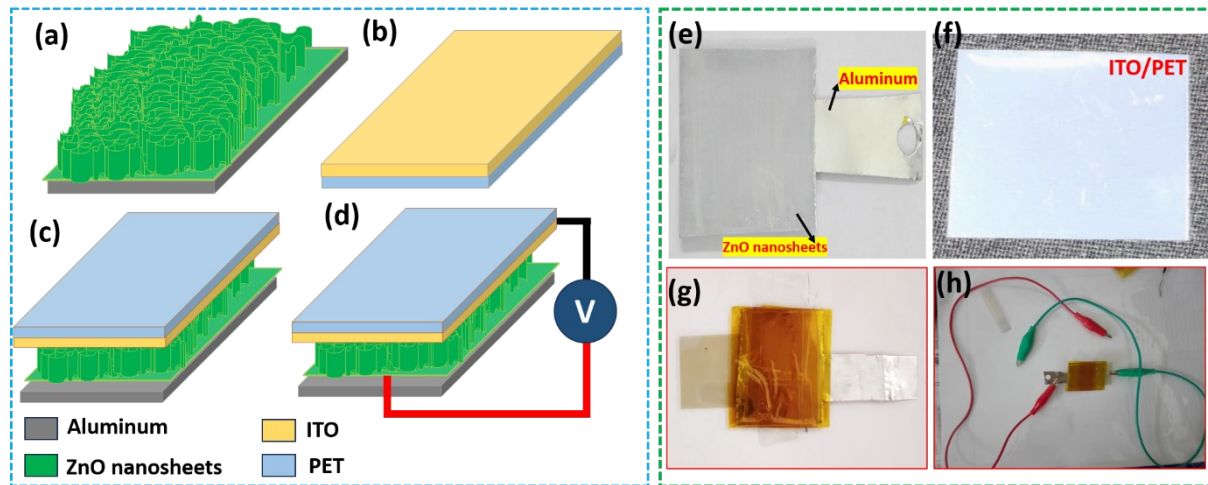


Figure 2.12. Schematic and real time images of (a & e) ZnO coated aluminium (b & f) ITO coated PET (c& g) fabricated PENG device (d & h) the PENG interfaced with connecting wires.

2.3.2 Triboelectric nanogenerator device fabrication

Generally, in TENG fabrication we need two top and bottom electrodes and two dielectric materials/ triboelectric layers. The TENGs involve the use of ZnO nanosheets network film grown on an aluminum substrate. The ZnO serves as one of the triboelectric layer, while other materials include ITO, PET, OHP, PMMA, and PDMS serve as another triboelectric layer. The specific combinations of these materials are carefully chosen to optimize the triboelectric performance of the nanogenerators. In all the working chapters of Chapter 3 to 7 aluminum and ITO used as electrodes. The schematic of the device fabrication is shown in Figure 2.13 (a). The actual pictures of the final TENG device and different fabrication steps are shown in Figure 2.13 (b)-(e). Initially, ZnO coated aluminum substrate with the aluminum side firmly attached to the acrylic sheet/card board of the selected dimension by scotch tape with ZnO nanosheets film facing up like shown in Figure 2.13 (c). Similarly, another triboelectric layer with aluminum/ITO side attached to another acrylic sheet firmly by scotch tape with another triboelectric layer facing up like shown in Figure 2.13 (d). Then, all corners of the lower acrylic sheet/card board were attached with sponge spacers with the application of a strong adhesive.

Next, another acrylic sheet/card board with another triboelectric layer was placed over the spacer and attached with a strong adhesive. Due to the sponge spacer, a finite gap (0.8 to 1.2 cm) exists between the lower ZnO nanosheet triboelectric layer and the upper triboelectric layer. Finally, two electrode lead wires were connected to two electrodes to measure the TENG electrical output, as shown in Figure 2.13 (e). Finally, TENG ($5 \times 5 \text{ cm}^2$) was fully characterized with a distance of 0.8 to 1.2 cm between triboelectric layers and a hand tapping frequency of \sim 3–4 Hz with an applied force of \sim 7 to 9N.

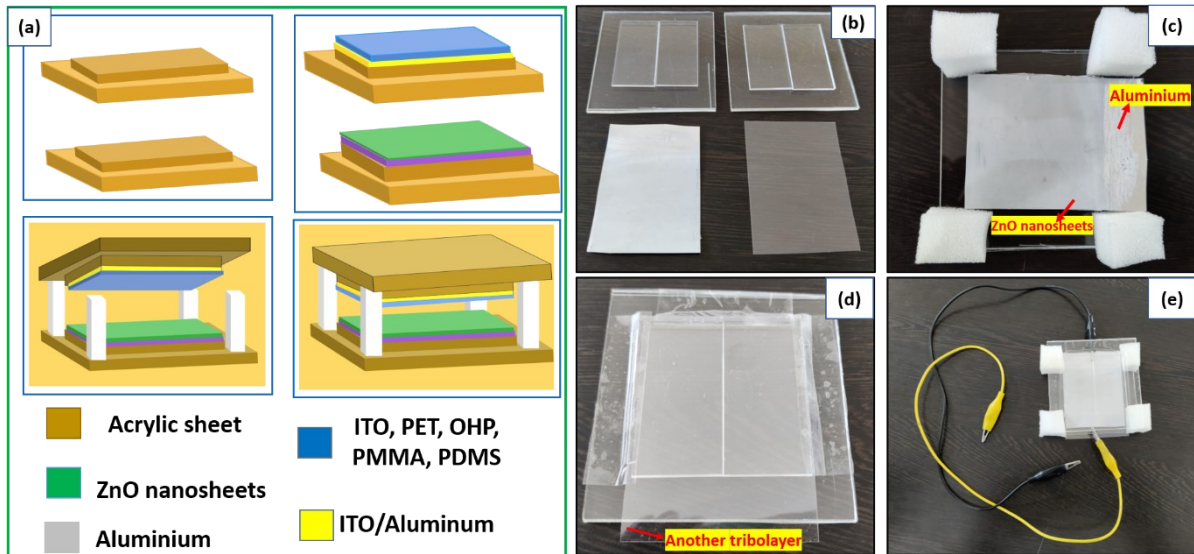


Figure 2.13. (a) Schematic of the TENG fabrication steps, real-time images of TENG device fabrication steps (b) acrylic base sheets, ZnO film, another triboelectric layer, (c) ZnO nanosheet film on aluminum attached to one of the acrylic bases, (d) another triboelectric layer attached to another acrylic base with triboelectric layer facing up, (e) final TENG device with electrode connection for response measurement.

2.4 Instruments used to test nanogenerator device electrical properties

In our study on TENG and PENG, a range of sophisticated instruments are employed to analyze their electrical characteristics. These instruments included digital storage oscilloscopes, multi-meters, and current pre-amplifier, which proved essential for precise measurements of voltage, and current. To gauge the mechanical energy input, we calculated the applied force during both finger tapping and hand tapping, utilizing theoretical equation. Efficiency calculations were performed by comparing the electrical power output to the mechanical power input, providing insights into the overall performance of the TENG. Furthermore, we utilized COMSOL

software to confirm the charge distribution of the TENG, employing simulation-based approaches to validate and understand its electrostatic behavior.

2.4.1 Digital storage oscilloscope



Figure 2.14. Photographs of digital storage oscilloscopes (a) Tektronix TBS1102 (b) GW Insteek GDS-1102B.

The Tektronix TBS1102, a digital storage oscilloscope (DSO), originates from Tektronix, a prominent supplier of test and measurement equipment (see Figure 13(a)). With a bandwidth of 100 MHz, a maximum real-time sampling rate of 2 GS/s, and a record length of up to 2.5K points, it excels in accurately capturing and analysing a diverse range of signals. In terms of connectivity, the TBS1102 is equipped with a USB host port and a USB device port, facilitating data storage, printing, and PC connectivity via TekVisa.

On the other hand, the GW Insteek GDS-1102B, another DSO model, boasts a bandwidth of 200 MHz and a maximum real-time sampling rate of 1 GS/s. Its key features include a generous maximum memory depth of 10M per channel and a 1Mpts FFT frequency domain signal display. Similar to the Tektronix model, the GDS-1102B offers USB host and USB device ports for data storage, printing, and PC connectivity (Figure 2.14 (b)).

2.4.2 Current pre-amplifier

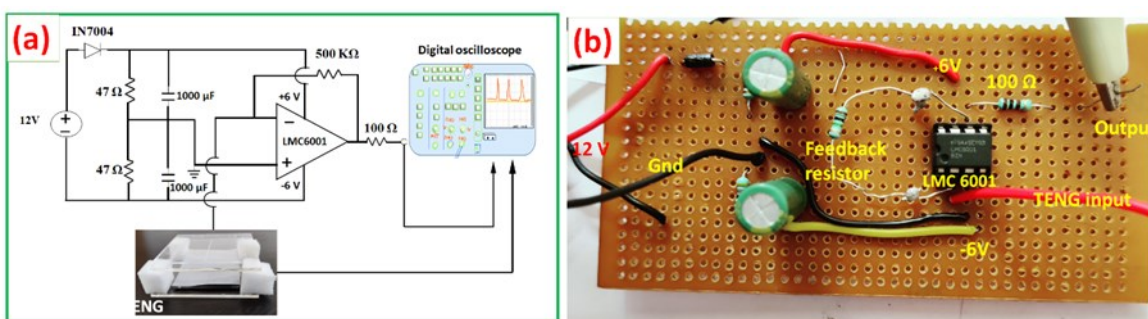


Figure 2.15. (a) Schematic of circuit connections of current to voltage converter circuit, (b) Photograph of the developed circuit on PCB.

Initially we have developed current pre-amplifier to measure output current of nanogenerator similar to the reported literature [16–18]. For that, we have used a current to voltage converter circuit to measure the current produced by the TENG. We adopted the current to voltage converter circuit developed by Clemson University (USA) using ultra-low input current amplifier IC LMC 6001 and named it CNI 570 [16]. The low-noise current preamplifier SR570 has been replaced with current-to-voltage converter electronic circuitry in CNI 570. The current values produced by TENG were verified with CNI 570 and SR570 instruments and found the same[16]. Therefore, we have used CNI570 to measure the current from the voltage drop values. Furthermore, CNI 570 was already demonstrated for TENG current characterization in a few research papers [17–19]. The customized current-to-voltage converter circuit of conversion ratio (500 mV/ μ A or 100 mV/ μ A) has been assembled in-house using a (500 k Ω /100k Ω) feedback resistor. The schematic of the circuit connections and photograph of the developed circuit are shown in Figure 2.15 (a)-(b).

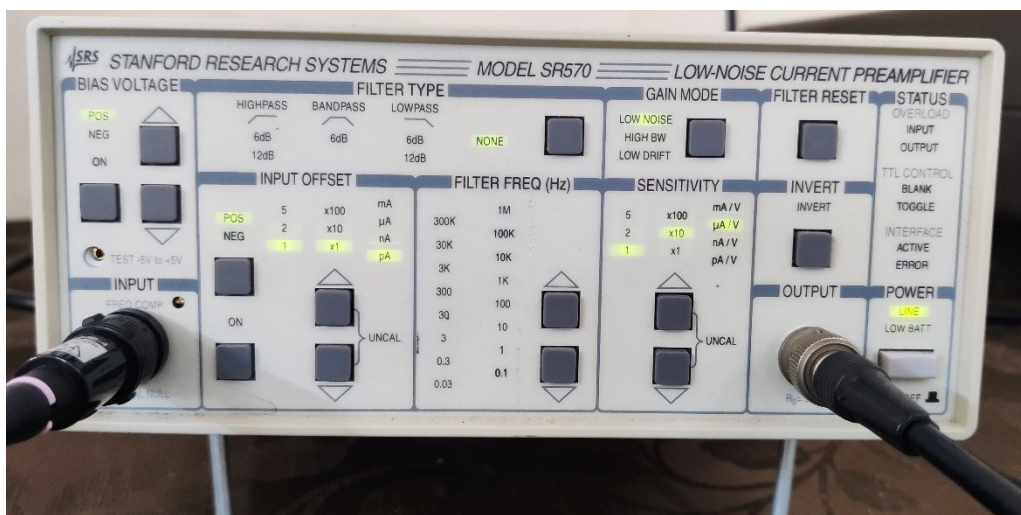


Figure 2.16. Photograph of SR 570 Current pre amplifier.

The SR570, a current pre-amplifier crafted by Stanford Research Systems (SRS), stands as a pinnacle in precision scientific instruments as shown in Figure 2.16. Meticulously designed for the amplification and measurement of electrical currents with low noise, it finds application across diverse settings. It can accurately measure very small current signals thanks to its high sensitivity and performance, including a current gain of up to 10^8 V/A (volts per ampere). One great thing about the SR570 is that it has very low noise, which is very important when working with weak current data. It has an input noise of less than 5 fA/ $\sqrt{\text{Hz}}$. With this feature, even the smallest changes in current can be picked up with a higher signal-to-noise ratio. The preamplifier is even more flexible because it has a wide bandwidth of up to 1 MHz. This lets current signals across a wide frequency range be amplified and analyzed. For example, the

SR570 has a maximum gain of 1 pA/V, an RS-232 interface, two signal filters that can be set up, a changeable input offset current, and line or battery operation.

2.4.3 Tapping machine

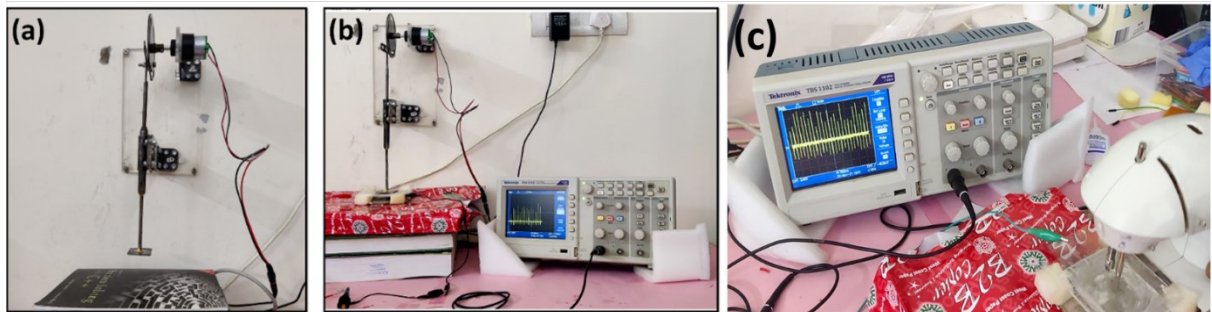


Figure 2.17. (a-b) photograph of developed tapping test set up, (c) Sewing machine tapping. we have developed a proto-type homemade setup for tapping the TENG using a simple DC motor and sewing machine Figure 2.17 (a-c). Furthermore, we have linear motor and sewing machine set up to test the stability of TENG.

2.4.4 Other components

2.4.4.1 Resistance Box

The decade resistance box was used in this thesis ranging from 1 ohm to 100 M ohms, to know the behaviour of the output voltage and current of nanogenerator under different load resistances and also to measure the optimal load resistance of the nanogenerator. Resistance box composed of a group of resistors arranged in a way that is both practical and logical, often in a rotary or switchable arrangement. The user may reach a desired total resistance by manipulating the switches or knobs on the box, since each resistor in the set has a fixed resistance value. When measuring load output voltage, resistance box was connected in parallel to the TENG device meanwhile, when measuring the load output current the resistance box was connected in series. At particular load resistance value, the measured output voltage and current will be optimized, the characteristic behaviour was discussed in the next chapters.



Figure 2.18. Decade resistance box

2.4.4.2 Bridge rectifier and different Capacitors

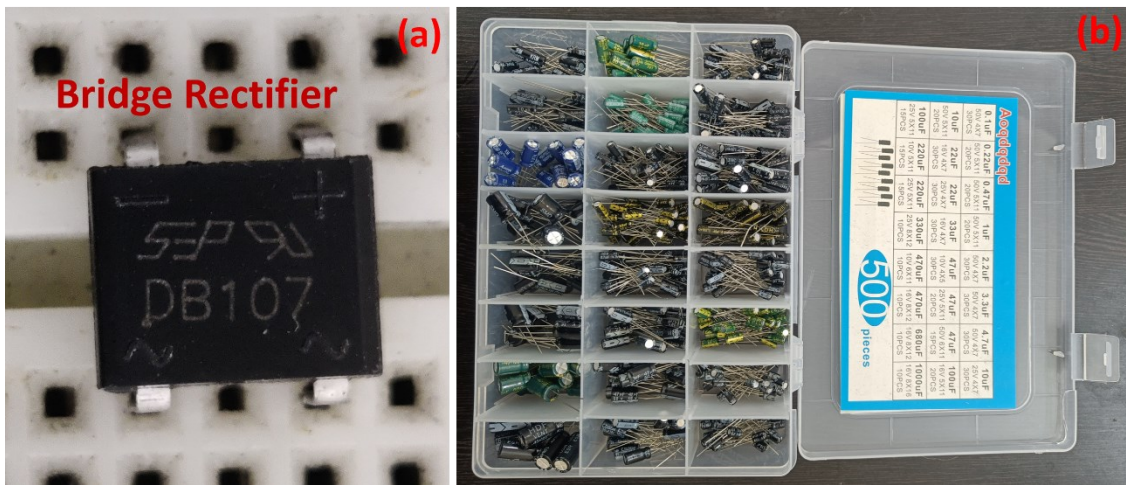


Figure 2.19. (a) Bridge rectifier, (b) capacitor box

In this thesis bridge rectifier model- DB107 (Figure 2.19) was used, which found in single-phase applications. The highest input AC RMS voltage of this IC is 700V, making it appropriate for a variety of applications. This IC can withstand a maximum DC of 1A. This IC has a reverse breakdown voltage of 1000V and a forward voltage drop of 1.1V. It has a 50A surge current capability and is very efficient. PENG and TENG devices were fabricated and utilised to power up small electronic devices, as mentioned in **Section 2.3**. These devices operate on DC power supplies, however TENG produces AC output. The bridge rectifier plays a significant role in this process, connected parallel to the TENG. This rectifier successfully converts the AC output coming from TENG into a steady DC output by employing a bridge configuration of the diode, offering to power up electronic devices.

A capacitor stores electrical energy in an electric field. Its construction involves the isolation of two conductive surfaces by a dielectric, which is an insulating substance. In electrical circuits, capacitors play an important role as energy storage devices, voltage regulators, signal filters, and oscillator timing components. A capacitor acquires and stores energy in reaction to an applied voltage. When the voltage is decreased or eliminated, the capacitor discharges the energy it has stored. For practical applications of TENG, to run the devices continuously it is necessary to store the output coming from TENG, in a capacitor or any energy storage element. In this thesis various range of capacitors for were utilized to store the charge through the nanogenerator. Smaller to larger ($0.1 \mu\text{F}$ to $440 \mu\text{F}$), smaller the capacitance of the capacitor charges fast, when it comes to higher the capacitance of the capacitor charge slowly.

2.4.5 COMSOL multi-physics software

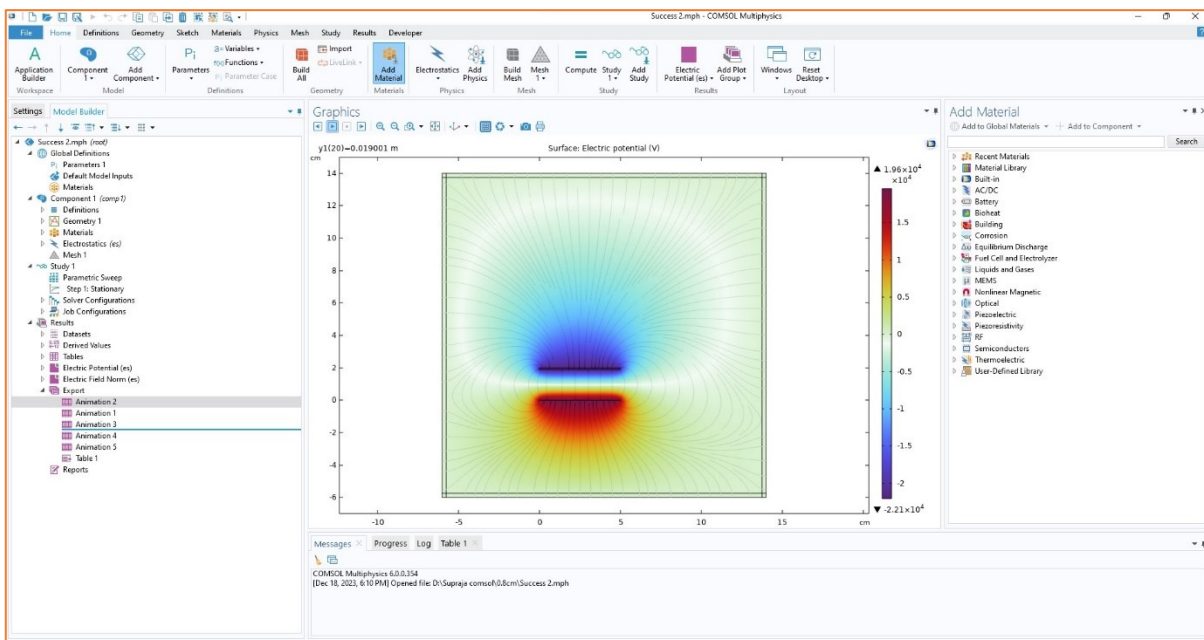


Figure 2.20. Window of the COMSOL software.

COMSOL Multiphysics proves to be a versatile simulation platform applicable to TENG modeling, where it plays a crucial role in converting mechanical energy into electrical energy (Figure 2.20). Users can capitalize on its features to construct precise geometrical representations, articulate material properties, and engage various physics interfaces like Electrostatics and Solid Mechanics to simulate the intricate interplay of mechanical deformation, triboelectric charging, and electrical generation within TENGs. The software's capabilities extend to Multiphysics coupling, boundary condition definition, meshing strategies, and solver configurations, collectively providing a holistic understanding of TENG behavior. We have obtained licence from the I-STEM portal and utilized in this thesis work.

2.4.6 Some of important calculated parameters

2.4.6.1 Force calculation

We don't have any measurement set up to measure the force applied by the hand tapping. However, we have adopted the procedure reported in the literature to calculate the hand tapping force approximately [20,21]. We have done a similar calculation and found the hand tapping force value as ~ 7 N. The calculation details are added below,

Mathematical equation:

The contact pressure caused by a falling object was calculated using a physical model that combined the gravity and pulse terms. When the object falls on the film, there exist two processes:

- 1) initially touching the surface of the film, and
- 2) completely acting on the film.

The object's descending velocity reaches a maximum in the first process and then falls to zero in the second. Therefore, based on the kinetic energy theorem and momentum theorem,

Calculated the force below:

$$m \cdot g \cdot h = \frac{1}{2} m v^2 \quad \text{----- (2.5)}$$

$$(F - m \cdot g) \cdot \Delta t = m \cdot v \quad \text{----- (2.6)}$$

From eqn. (2.1),

$$v = \sqrt{2gh} \quad \text{----- (2.7)}$$

Where, F-force (N), m-mass of the applied force (Kg), v- velocity(m/s), g= 9.8 N/kg, h= height of the spacing (cm), Δt =time period between two consecutive peaks (1/f); where, f is frequency.

From eqn. (2.6),

$$F = \frac{m \cdot v}{\Delta t} + m \cdot g \quad \text{----- (2.8)}$$

2.4.6.2 Efficiency calculation

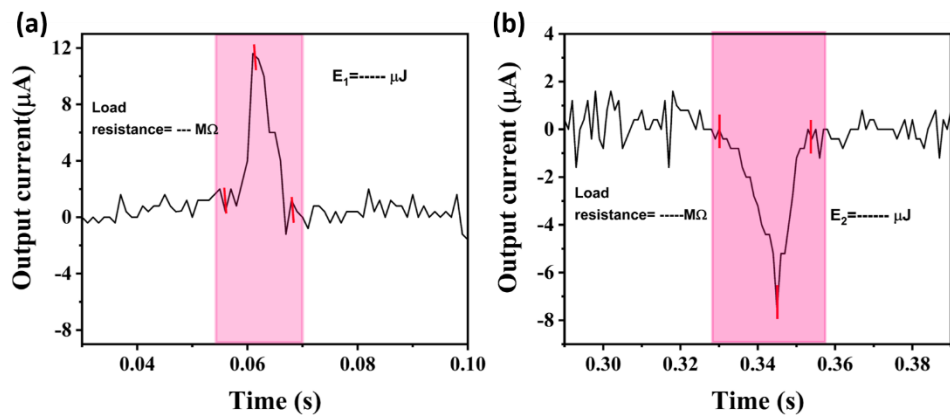


Figure 2.21. Current peak at load resistance of R_L -MΩ in (a) forward (b) reverse.

We have thoroughly searched the literature on TENG's efficiency and found only a few reports discussed it [22–25]. We have adopted the same calculation procedure for finding the efficiency of the TENG. The energy conversion efficiency of TENG is defined as the ratio of the TENG's output electrical energy delivered across the optimal load to its input mechanical energy of the TENG.

$$\text{Electrical Energy} (E_{\text{electrical}}) = \int_{t_1}^{t_2} (I^2 \cdot R) dt \quad \text{----- (2.9)}$$

$$= R_L \cdot \int_{t_1}^{t_2} (I_1^2) dt + R_L \cdot \int_{t_3}^{t_4} (I_2^2) dt \quad \text{----- (2.10)}$$

$$= E_1 \mu J + E_2 \mu J \quad \text{----- (2.11)}$$

Where, t_1 and t_2 , t_3 and t_4 are the time intervals for the positive and negative half cycle of the current at optimal resistance of R_L -MΩ, respectively. I is the output current, ' R_L ' is optimal load resistance.

And, Mechanical energy by moving the top layer is,

$$E_{\text{Mechanical}} = \frac{1}{2} m V^2 \quad \text{----- (2.12)}$$

Here we calculated the 'm' of the top layer using weighing balance (mass of the movable layer).

Consider top layer performing simple harmonic oscillations with frequency.

$$\text{Acceleration} = (2\pi f)^2 x, \text{ then, velocity (v)} = 2\pi f x \quad \text{----- (2.13)}$$

Where, x - maximum distance of the separation (cm)

As a result, the conversion efficiency is,

$$\eta_{\text{actual}} = \frac{E_{\text{electric}}}{E_{\text{kinetic}}} \times 100\% \quad \text{----- (2.14)}$$

2.5 The circuits design used in applications of TENG

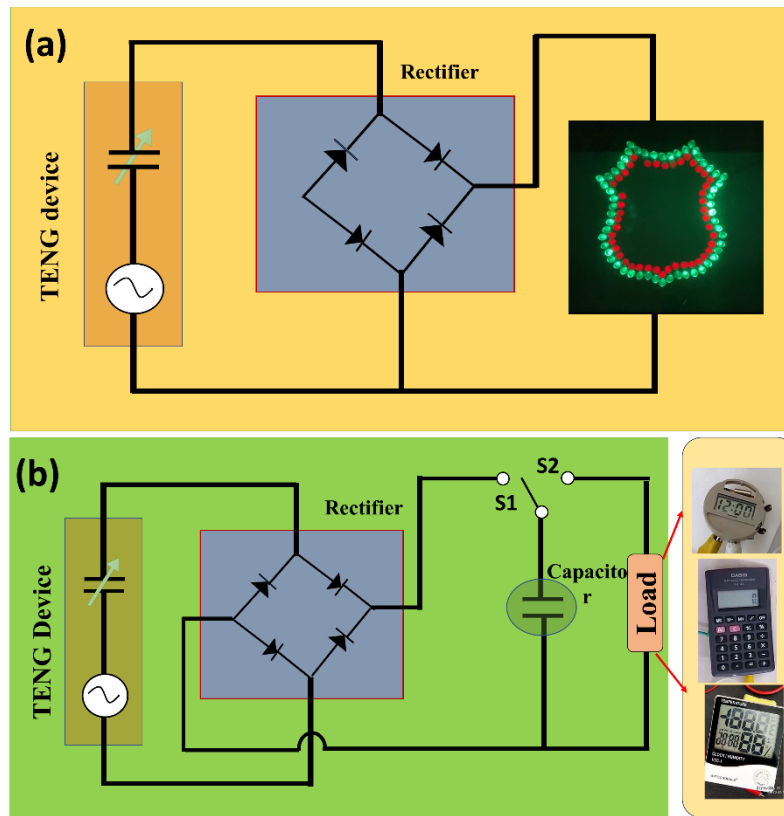


Figure 2.22. schematic of powering electronic devices through the (a) rectifier directly, (b) capacitor integrated to rectifier.

Figure 2.22(a) shows the schematic representation of powering of electronic devices by connecting the rectifier parallel to the rectifier circuit directly. In which, the TENG was connected in parallel to the rectifier, this rectified output directly supplied to electronic devices (LEDs, watch, etc). Figure 2.22(b) shows in which an additional capacitor component added to the circuit in addition to Figure 2.22(a). The rectified output has given to the capacitor (s_1), which is integrated with the electronic devices (s_2). Initially, the connection has given upto s_1 only, once the capacitor gets charged, then the electronic devices integrated with capacitor s_2 get connected. This stored charge can power up the electronic devices till it gets discharged.

2.6 Conclusions

In this chapter, we explore the synthesis of ZnO nanosheets through the use of hotplate assisted hydrothermal method. The exploration of material properties involves an in-depth study employing various characterization techniques. Additionally, we delve into the fabrication of PENG and TENG devices, elucidating the instruments integral to their characterization.

Finally, the chapter provides a comprehensive explanation of the significant parameters derived from our calculations.

2.7 References

- [1] P.M. Aneesh, K.A. Vanaja, M.K. Jayaraj, Synthesis of ZnO nanoparticles by hydrothermal method, in: Z. Gaburro, S. Cabrini (Eds.), Nanophotonic Mater. IV, SPIE, 2007: p. 66390J. <https://doi.org/10.1117/12.730364>.
- [2] R. Parize, J. Garnier, O. Chaix-Pluchery, C. Verrier, E. Appert, V. Consonni, Effects of Hexamethylenetetramine on the Nucleation and Radial Growth of ZnO Nanowires by Chemical Bath Deposition, *J. Phys. Chem. C.* 120 (2016) 5242–5250. <https://doi.org/10.1021/acs.jpcc.6b00479>.
- [3] G. Murillo, E. Leon-Salguero, P.R. Martínez-Alanis, J. Esteve, J. Alvarado-Rivera, F. Güell, Role of aluminum and HMTA in the hydrothermal synthesis of two-dimensional n-doped ZnO nanosheets, *Nano Energy.* 60 (2019) 817–826. <https://doi.org/10.1016/j.nanoen.2019.04.017>.
- [4] C. Zhao, B. Wang, S. Zhong, M. Akhtaruzzaman, W. Liang, H. Chen, Chapter 12 - NDT studies of nanoscale polymeric coatings, in: S. Thomas, J.S. George (Eds.), *Polym. Nanoscale Mater. Surf. Coatings*, Elsevier, 2023: pp. 235–257. <https://doi.org/https://doi.org/10.1016/B978-0-32-390778-1.00019-0>.
- [5] W. Fuller, A. Mahendrasingam, Fibres and Films Studied Using X-Ray Diffraction*, in: J.C. Lindon (Ed.), *Encycl. Spectrosc. Spectrom.* (Second Ed., Second Edi, Academic Press, Oxford, 1999: pp. 589–598. <https://doi.org/https://doi.org/10.1016/B978-0-12-374413-5.00145-7>.
- [6] K. Akhtar, S.A. Khan, S.B. Khan, A.M. Asiri, Scanning Electron Microscopy: Principle and Applications in Nanomaterials Characterization, in: S.K. Sharma (Ed.), *Handb. Mater. Charact.*, Springer International Publishing, Cham, 2018: pp. 113–145. https://doi.org/10.1007/978-3-319-92955-2_4.
- [7] J.I. Goldstein, D.E. Newbury, J.R. Michael, N.W.M. Ritchie, J. Henry, J. Scott, D.C. Joy, *Scanning Electron Microscopy and Associated Techniques: Overview*, 2018.
- [8] W. Zhou, Y.H. Ikuhara, Z. Zheng, K. Wang, B. Cao, J. Chen, 17 - Transmission electron microscopy (TEM) studies of functional nanomaterials, in: V.K. Tewary, Y. Zhang (Eds.), *Model. Charact. Prod. Nanomater.* (Second Ed., Second Edi, Woodhead Publishing, 2023: pp. 467–512. <https://doi.org/https://doi.org/10.1016/B978-0-12-819905-3.00017-8>.

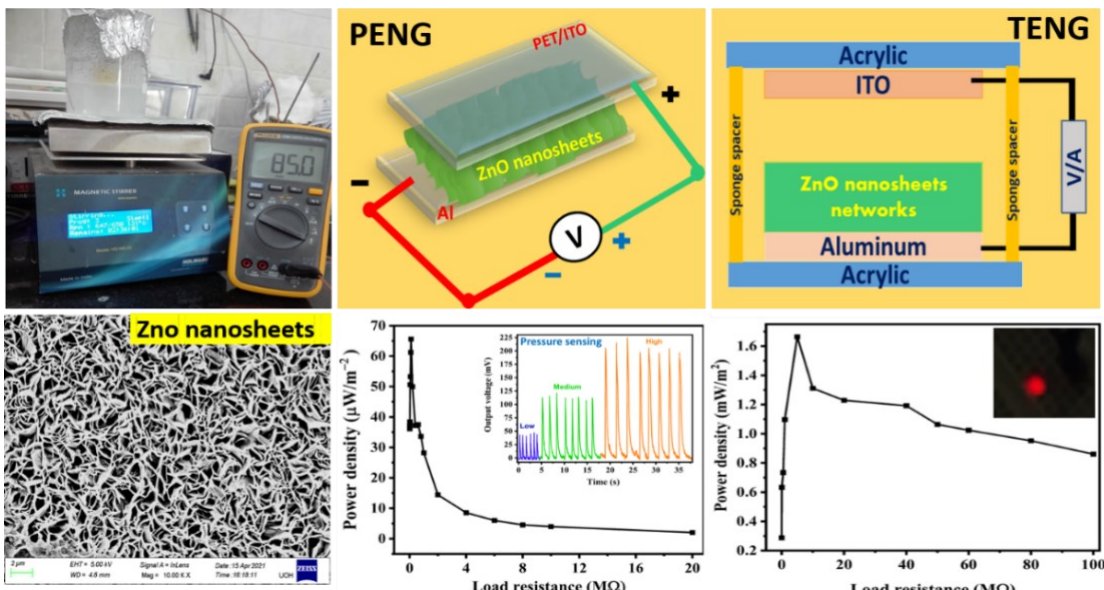
- [9] G.W. Stachowiak, A.W. Batchelor, G.B. Stachowiak, 8 - Surface Micrography and Analysis, in: G.W. Stachowiak, A.W. Batchelor, G.B. Stachowiak (Eds.), *Exp. Methods Tribol.*, Elsevier, 2004: pp. 165–220.
[https://doi.org/https://doi.org/10.1016/S0167-8922\(04\)80024-5](https://doi.org/https://doi.org/10.1016/S0167-8922(04)80024-5).
- [10] V.K. Undavalli, C. Ling, B. Khandelwal, Chapter 6 - Impact of alternative fuels and properties on elastomer compatibility, in: B. Khandelwal (Ed.), *Aviat. Fuels*, Academic Press, 2021: pp. 113–132. <https://doi.org/https://doi.org/10.1016/B978-0-12-818314-4.00001-7>.
- [11] R.A. Spragg, IR Spectrometers, in: J.C. Lindon (Ed.), *Encycl. Spectrosc. Spectrom.*, Elsevier, Oxford, 1999: pp. 1048–1057.
<https://doi.org/https://doi.org/10.1006/rwsp.2000.0130>.
- [12] A. Downes, A. Elfick, Raman spectroscopy and related techniques in biomedicine, *Sensors*. 10 (2010) 1871–1889. <https://doi.org/10.3390/s100301871>.
- [13] I.P. Herman, CHAPTER 14 - Photoluminescence, in: I.P. Herman (Ed.), *Opt. Diagnostics Thin Film Process.*, Academic Press, San Diego, 1996: pp. 619–636.
<https://doi.org/https://doi.org/10.1016/B978-012342070-1/50015-2>.
- [14] D.J. Müller, A.C. Dumitru, C. Lo Giudice, H.E. Gaub, P. Hinterdorfer, G. Hummer, J.J. De Yoreo, Y.F. Dufrêne, D. Alsteens, Atomic Force Microscopy-Based Force Spectroscopy and Multiparametric Imaging of Biomolecular and Cellular Systems, *Chem. Rev.* 121 (2021) 11701–11725. <https://doi.org/10.1021/acs.chemrev.0c00617>.
- [15] D. Thierry, A. Nazarov, D. Persson, Mechanical and chemical coupling in tribocorrosion: In situ and ex situ characterization techniques, *Mech. Electro-Chemical Interact. under Tribocorrosion From Meas. to Model. Build. a Relev. Monit. Approach.* (2021) 29–66. <https://doi.org/10.1016/B978-0-12-823765-6.00003-1>.
- [16] S.S.K. Mallineni, H. Behlow, R. Podila, A.M. Rao, A low-cost approach for measuring electrical load currents in triboelectric nanogenerators, *Nanotechnol. Rev.* 7 (2018) 149–156. <https://doi.org/10.1515/ntrev-2017-0178>.
- [17] A. Sharma, P. Agarwal, Triboelectric Energy Harvester performance enhanced by modifying the tribo-layer with cost-effective fabrication, *Mater. Res. Express.* 6 (2019) 065514. <https://doi.org/10.1088/2053-1591/ab0f64>.
- [18] M.A. Jalili, Z. Khosroshahi, N.R. Kheirabadi, F. Karimzadeh, M.H. Enayati, Green triboelectric nanogenerator based on waste polymers for electrophoretic deposition of titania nanoparticles, *Nano Energy*. 90 (2021) 106581.
<https://doi.org/10.1016/j.nanoen.2021.106581>.

- [19] G. Min, A. Pullanchiyodan, A.S. Dahiya, E.S. Hosseini, Y. Xu, D.M. Mulvihill, R. Dahiya, Ferroelectric-assisted high-performance triboelectric nanogenerators based on electrospun P(VDF-TrFE) composite nanofibers with barium titanate nanofillers, *Nano Energy*. 90 (2021) 106600. <https://doi.org/10.1016/j.nanoen.2021.106600>.
- [20] A. Sultana, M.M. Alam, S. Garain, T.K. Sinha, T.R. Midya, D. Mandal, An Effective Electrical Throughput from PANI Supplement ZnS Nanorods and PDMS-Based Flexible Piezoelectric Nanogenerator for Power up Portable Electronic Devices: An Alternative of MWCNT Filler, *ACS Appl. Mater. Interfaces*. 7 (2015) 19091–19097. <https://doi.org/10.1021/acsami.5b04669>.
- [21] F.R. Fan, L. Lin, G. Zhu, W. Wu, R. Zhang, Z.L. Wang, Transparent triboelectric nanogenerators and self-powered pressure sensors based on micropatterned plastic films, *Nano Lett.* 12 (2012) 3109–3114. <https://doi.org/10.1021/nl300988z>.
- [22] G. Zhu, Z.H. Lin, Q. Jing, P. Bai, C. Pan, Y. Yang, Y. Zhou, Z.L. Wang, Toward large-scale energy harvesting by a nanoparticle-enhanced triboelectric nanogenerator, *Nano Lett.* 13 (2013) 847–853. <https://doi.org/10.1021/nl4001053>.
- [23] C.K. Jeong, K.M. Baek, S. Niu, T.W. Nam, Y.H. Hur, D.Y. Park, G.T. Hwang, M. Byun, Z.L. Wang, Y.S. Jung, K.J. Lee, Topographically-designed triboelectric nanogenerator via block copolymer self-assembly, *Nano Lett.* 14 (2014) 7031–7038. <https://doi.org/10.1021/nl503402c>.
- [24] Y. Xie, S. Wang, S. Niu, L. Lin, Q. Jing, J. Yang, Z. Wu, Z.L. Wang, Grating-Structured Freestanding Triboelectric-Layer Nanogenerator for Harvesting Mechanical Energy at 85% Total Conversion Efficiency, *Adv. Mater.* 26 (2014) 6599–6607. <https://doi.org/10.1002/adma.201402428>.
- [25] A. You, X. Zhang, X. Peng, K. Dong, Y. Lu, Q. Zhang, A Skin-Inspired Triboelectric Nanogenerator with an Interpenetrating Structure for Motion Sensing and Energy Harvesting, *Macromol. Mater. Eng.* 306 (2021) 1–9. <https://doi.org/10.1002/mame.202100147>.

Chapter 3

Synthesis and Fabrication of Zinc Oxide Nanosheet based Piezo and Triboelectric Nanogenerator for Energy Harvesting

The purpose of this chapter was to optimize the growth conditions by synthesizing ZnO nanosheets on the aluminum substrate at different growth temperatures and times. At 85°C and 4 hrs of grown ZnO nanosheets based PENG output reached the maximum. This PENG can be used as a force sensor and photodetector device application. Following that, a TENG device was created employing ITO and ZnO nanosheets as contact triboelectric layers, which produced a higher output voltage than the PENG device. TENG was capable to power LEDs and has potential in a variety of energy-harvesting applications.



Publications:

1. "A Simple and Low-Cost Approach for the Synthesis and Fabrication of ZnO Nanosheet-Based Nanogenerator for Energy Harvesting and Sensing", **Supraja Potu, Rakesh Kumar, Siju Mishra, D Haranath, P Ravi Sankar and K Prakash**, *Engineering Research Express*, Vol 3, No 3, 2021, 035022. <https://doi.org/10.1088/2631-8695/ac184b>.
2. "Triboelectric Nanogenerator Based on ZnO Nanosheet Networks for Mechanical Energy Harvesting", **Supraja Potu, Rakesh Kumar, Siju Mishra, D Haranath**, *IEEE XPLOR*, 2022, <https://doi.org/10.1109/PARC52418.2022.9726684>.

3.1 Introduction

Recently, most of the research focused on energy harvesting due to environmental issues, carbon emissions, and the limited availability of fossil fuels [1,2]. To address these difficulties, a new research field known as ‘nanogenerators’ have emerged, which uses piezoelectric materials to harness mechanical energy [3–5]. The ease with which mechanical energy could be converted to electrical energy utilizing a well-known piezoelectric property makes it even more attractive and potential. The main advantages of mechanical energy are widely and easily available everywhere in nature and all the time. Nanogenerators have been used as actuators, sensors, photodetectors, and self-powered devices [6–9]. Among all piezoelectric materials, Zinc Oxide (ZnO) is selected in this thesis work to fabricate the nanogenerator. ZnO has several advantages viz. non-toxicity, environmental friendly, biocompatibility, and excellent optical and electrical properties [10,11]. The synthesis of ZnO nanostructures is easy, established, and involves a simple process compared to all other materials synthesis. Among different synthesis methods, the hydrothermal synthesis of ZnO nanosheets is a simple, inexpensive, single-step process, and low-temperature ($<100^{\circ}\text{C}$) process [12,13]. The obtained nanosheets exhibited high mechanical durability as well [14]. Hence, hydrothermal synthesis is adopted in this thesis work for the synthesis of ZnO nanosheets.

A hot plate was used in this current work instead of a hot air oven to provide growth temperature to the growth precursor solution. The cost of the process was reduced appreciably by adapting this methodology. It is a simple technique to synthesize nanostructures by direct heating of growth solution at the desired temperature. The hot plate-assisted hydrothermal method can be easily implemented for mass production of ZnO nanosheets films and larger area films for commercial applications. The main advantages of this new method are simple, low cost, rapid growth, catalyst-free, single-step synthesis.

In this chapter, a cost-effective and straightforward method to synthesize ZnO nanosheets using the hot plate-assisted hydrothermal method. Further nanogenerator was fabricated for mechanical energy harvesting and characterized for its electrical characteristics, portable electronic devices and sensors applications.

3.2 Experimental section

3.2.1 Materials

Zinc nitrate hexahydrate ($\text{Zn}(\text{NO}_3)_2 \cdot 6\text{H}_2\text{O}$) and hexamethylenetetramine (HMTA, $\text{C}_6\text{H}_{12}\text{N}_4$) aluminium foil and ITO coated PET sheets (sheet resistance 10 sq^{-1}) were conducting electrodes. These materials were utilized in this chapter.

3.2.2 ZnO nanosheets synthesis

The ZnO nanosheets film was synthesized on Al substrates by following the same method mentioned in Section-2.1. Before performing synthesis, the growth precursor solution temperature was calibrated for 50, 60, 70, 85, 95°C against applied hot plate temperature by inserting a thermocouple in the growth precursor solution. Finally, the beaker containing growth precursor was kept over the hotplate at different growth temperatures for 4 hrs. ZnO coated films on aluminium substrates were taken from the solution after 4 hours of growth, rinsed with DI water, and dried with a hair blower.

Further, ZnO nanosheets growth was performed at different growth durations of 1, 2, 3, 4, 5, and 6 hrs at a one selected optimum temperature of 85°C.

3.2.3 Nanogenerator device fabrication

All the PENG and TENG devices have been fabricated using the same steps, it implies a standardized manufacturing process as mentioned in **Section-2.3**.

3.2.3.1 PENG device fabrication

Several PENG devices-based on the ZnO nanosheets grown at different growth temperatures (50-95°C) and growth duration times (1-6 hrs), were fabricated. An aluminum foil act as the bottom electrode, and ITO coated PET sheet acts as the top electrode. The ITO coated PET sheet was placed over the ZnO nanosheet film without making any short-circuit with a bottom aluminum electrode. The nanogenerator response was also recorded for different finger-tapping pressures, and frequencies.

3.2.3.2 TENG device fabrication

TENG device was fabricated based on ZnO nanosheets grown at optimised temperature and growth duration time (85°C and 4 hrs), in which Al act as one of the electrodes and ITO act as triboelectric layer as well as electrode. TENG output voltage was captured using an oscilloscope against repeated hand tapping. The nanogenerator response was also recorded for different device characterizations under hand tapping force of ~7 N (Chapter-2, Section 2.4.6),

frequency of 3-5 Hz and 0.8 cm of spacing has provided between the triboelectric layers to operate the device under contact separation mode.

3.3 Results and discussion

3.3.1 SEM and EDS analysis

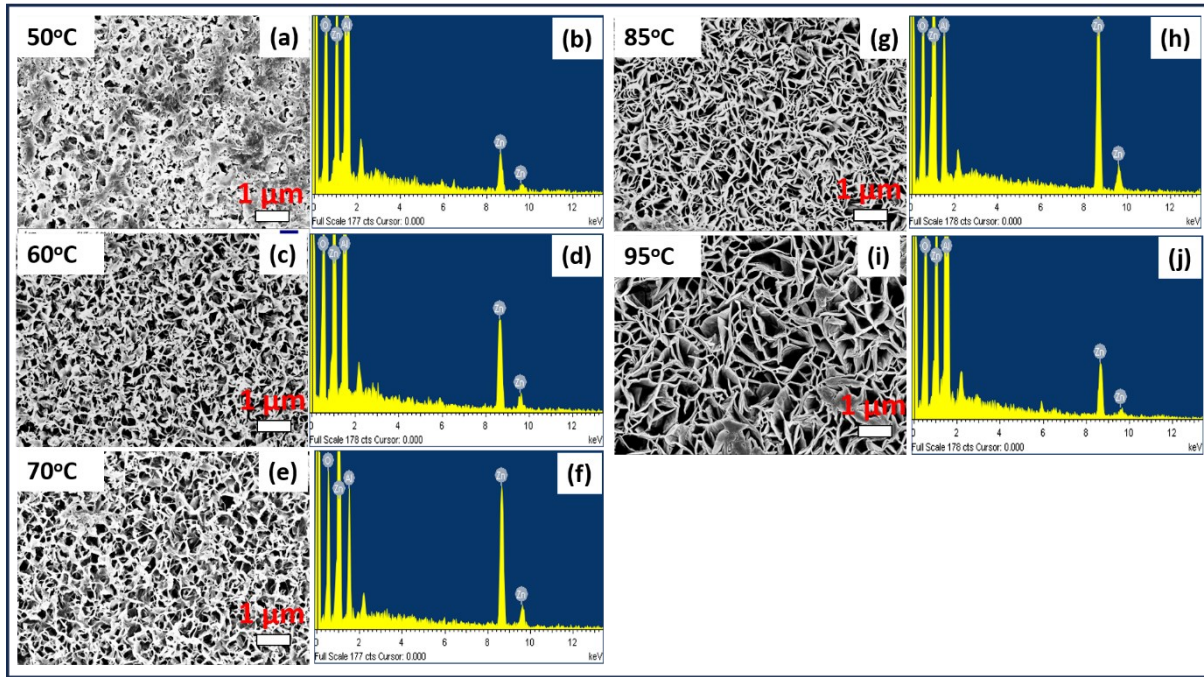


Figure 3.1. (a)-(j) Morphology and EDS spectra of the ZnO films obtained at different temperatures from 50 to 95°C.

Figure 3.1 (a)-(j) shows the surface morphology and elemental analysis of the ZnO thin films prepared at different growth temperatures of 50, 60, 70, 85, and 95°C respectively. In all the cases, ZnO nanosheets are present all over the substrate except at 50°C. These sheets are relatively vertically with respect to the substrate and also randomly distributed. Nanosheets are connected among them in a non-uniform way.

The formation of ZnO nanosheet is similar to the hydrothermal growth of ZnO nanosheets using a hot air oven [15]. Growth temperature plays a significant role in obtaining ZnO nanostructures. At lower temperatures of 50°C and below, growth of nanosheets was not observed due to insufficient thermal energy for the decomposition of HMTA [15] (Figure 3.1(a)). The uniform nanosheets growth was observed from 60°C onwards and continued till 95°C (Figure 3.1(b-j)). The difference in the morphology due to the different densities and length of the nanosheets, which in turn depends on the growth temperature. The growth rate of nanosheets increases with an increase in growth temperature due to sufficient thermal energy.

Further, the purity of prepared films was studied by energy dispersive spectroscopy (EDS), which revealed that all the films show Zn, O, Al, and no other detected elements.

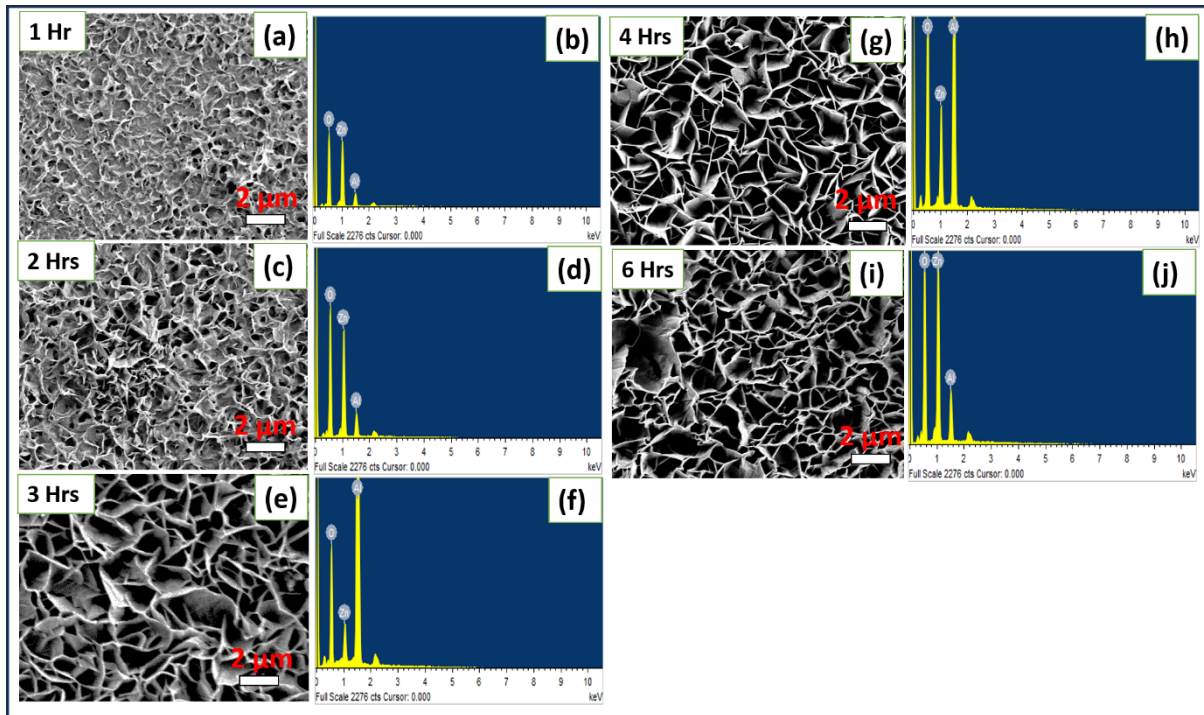


Figure 3.2. (a)-(j) Morphology and EDS spectra of the ZnO films obtained at different growth duration times from 1 hr to 6 hrs.

Figure 3.2 (a)-(j) shows the surface morphology and elemental analysis of the ZnO thin films prepared at different growth times at 1, 2, 3, 4, and 6 hrs, respectively. All of these samples were grown at 85°C, i.e., the temperature that was shown to promote the highest growth rate in the temperature investigation. The ZnO nanosheets on all samples were grown vertically on the aluminum substrate. The ZnO nanosheets length increases with an increase of growth duration from 1 to 4 hrs and saturates after 4 hrs as shown in Figure 3.2(a-j). ZnO nanosheet length saturation with growth time is due to consumption of all the OH^- ions and Zn^{+2} ions in the growth solution. Further, energy dispersive spectroscopy (EDS) revealed that all the films shown Zn, O, Al, and no other elements detected.

3.3.2 XRD analysis

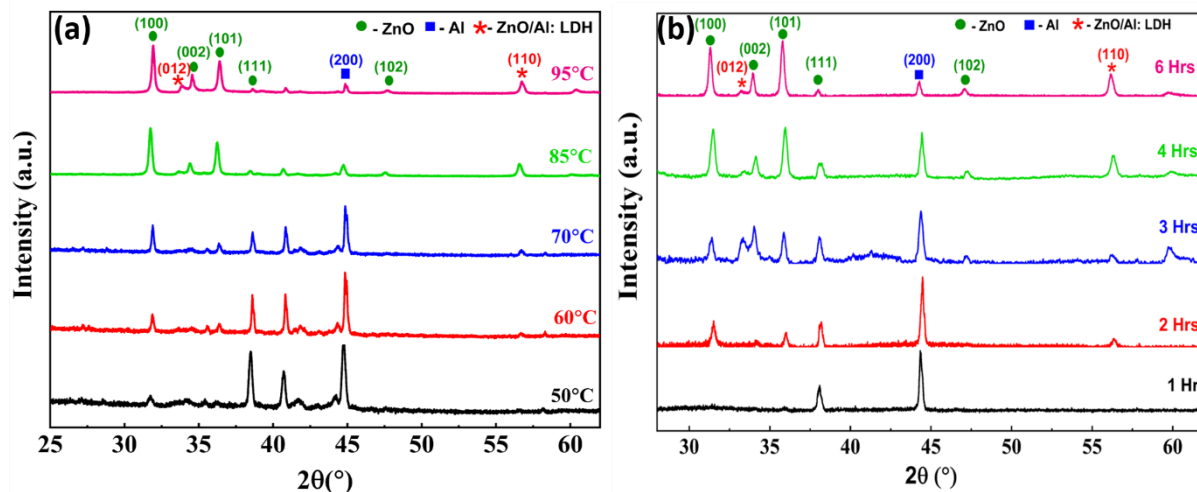


Figure 3.3. (a)-(b) XRD of the ZnO films obtained at different growth temperatures and duration time.

X-ray diffraction (XRD) analysis on ZnO nanosheets grown on aluminum substrate at different temperatures and growth times (Figure 3.3(a-b)). The intense diffraction peak at 44.85° in the XRD corresponding to the (200) plane of cubic bare Al coming directly from the substrate (JCPDS No. #03-0932). The intense diffraction peaks at 31.9° , 34.6° , 36.4° , 38.64° and 47.7° in the XRD corresponding to the (100), (002), (101), (111) and (102), respectively (JCPDS No. #79-0205). The additional diffraction peaks at 33.8° and 56.8° corresponding to (012) and (110) planes confirm the formation of ZnAl: LDH at the interface of ZnO nanostructures and aluminum, which can play a crucial role in the interface properties, such as adhesion, stability to ZnO nanosheets[15]. All ZnO diffraction peaks were identified as belonging to the hexagonal wurtzite structure. This is a common crystal structure for ZnO.

A strong (002) peak intensity at 34.5° suggests that the ZnO nanosheets were grown along the c-axis on the aluminum substrate. This implies a preferential orientation of the crystal growth. The (002) peak intensity was relatively low at low temperatures. This suggests that at very low temperatures, the growth conditions were not optimal for the formation of strong (002) peaks.

The ZnO nanosheets exhibiting a higher intensity had a matching peak at (002)/(100) after 4 hours at 85°C . It suggests that under these conditions, nanosheets improved the crystallinity and aligned well along the c-axis (figure 3.1(g)). As a result, the ZnO nanosheet sample generated at 85°C corresponding peak suggests that the nanosheets have high crystallinity.

Additionally, XRD analysis of ZnO nanosheets obtained at various times of growth provides crucial information about the material's structural characteristics. With increased growth times,

ZnO nanosheets' (002) intensity XRD peak rose. This finding implies that the growth times favored the formation of a higher-order crystal structure, increasing the (002) peak's intensity and leading to enhanced crystallinity in the ZnO nanosheets. The direction of growth of the nanosheets was shown by the peak at (002). As a result, XRD verifies that the nanosheets are displaying good structural characteristics across the wide range of growth temperatures and times that are being studied.

3.3.3 TEM analysis

Figure 3.4(a) shows TEM image of the few nanosheets on the copper grid. The transparent nature of the nanosheets confirms the low thickness of the sample. Further, the selected area electron diffraction (SAED) pattern recorded on ZnO nanosheet exhibited the polycrystalline nature of the ZnO nanosheets. EDX spectrum recorded on ZnO nanosheets further confirms the purity of the nanosheets.

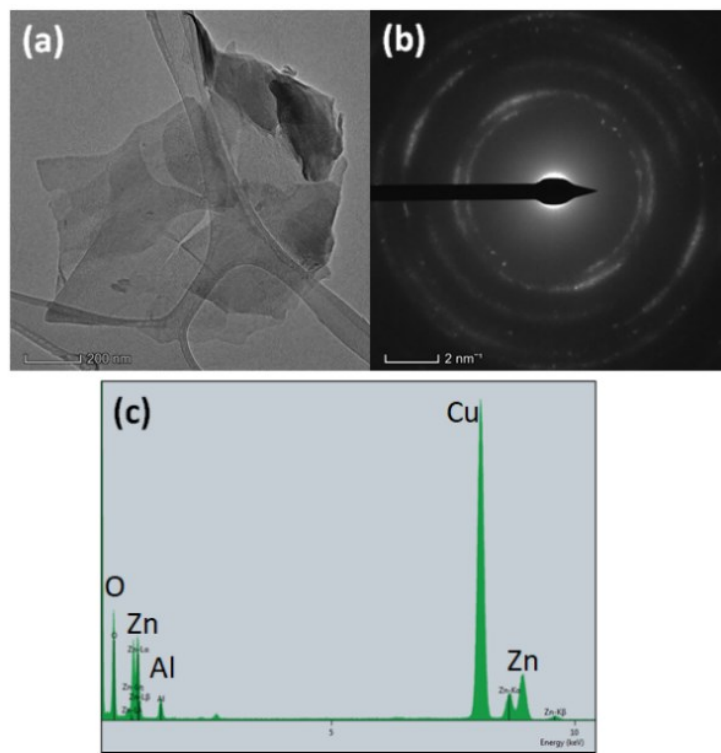


Figure 3.4. (a) TEM image of the ZnO nanosheet, (b) SAED pattern recorded on the ZnO nanosheets, (c) EDX spectrum recorded on the ZnO nanosheet.

3.3.4 Piezoelectric nanogenerator device studies

The response of the nanogenerators fabricated from the ZnO nanosheet films synthesized at different growth temperatures is shown in Figure 3.5(a). This response was recorded at uniform finger tapping pressure on the device under open-circuit conditions. It is clear from Figure 3.5 (a)-(b) that output voltage is increased with an increase in the growth temperature and saturated

above 85°C. The change in the output voltage can be correlated to ZnO nanosheet deformation's magnitude under applied pressure. At lower temperatures films, minor deformation can be expected due to sheet heights were small. At higher growth temperature films, large deformation can be expected due to significant sheet height. The saturation in the output voltage at 85°C and above may be due to the similar thickness of the nanosheet films. Therefore, a growth temperature of 85°C is found to be the optimum growth temperature for higher nanogenerator output voltage. Further, the nanogenerator made up of ZnO nanosheet films synthesized at 85°C were used for all other studies in the following sections.

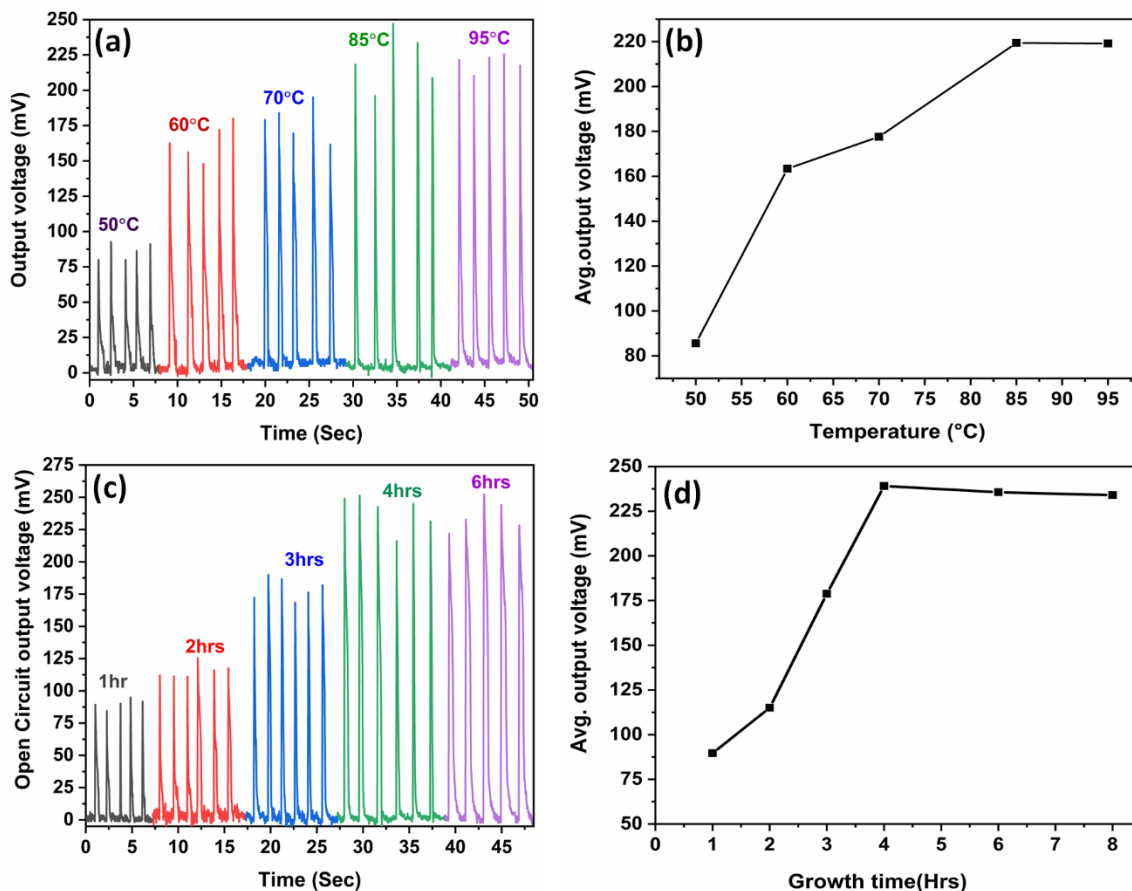


Figure 3.5. Output response of ZnO nanosheets based PENG (a,c) Output voltage, and (b,d) Average output voltage at different growth temperatures and durations, respectively.

Figure 3.5 (c)-(d) shows the typical response of nanogenerators, which were fabricated with ZnO nanosheets films obtained at 85°C for different growth durations of 1-6 hrs. Nanogenerator output is increasing with increasing growth duration and saturated for 4 hrs ZnO nanosheet films onwards. The ZnO nanosheets length increases with an increase of growth duration and saturates after a particular time. ZnO nanosheet length saturation with growth time due to consumption of all the OH^- ions and Zn^{+2} ions in the growth solution

[16]. The saturation of ZnO nanosheet height was observed for 4 hrs of growth and above. The height saturation of ZnO nanosheets resulting in the same deformation under applied pressure and produces the same output.

Figure 3.6 (a)-(b) shows the response of nanogenerators under switching polarity test and linear superposition of voltage test. These tests were performed to confirm the output voltage generated from the nanogenerator alone, not by the oscilloscope or noise in the instrument [17–20]. In the switching polarity test: the forward and reverse connections were established by interchanging nanogenerator connections to the measuring device. The nanogenerator has shown exactly opposite voltage output signal in reverse connection with respect to the forward signal, as shown in Figure 3.6(a) (**See SI Video S3.1**). In both configurations, the output voltage of the nanogenerator is nearly the same. In the second test, the 7-nanogenerator devices were connected in series to add the voltages. The output voltages generated by the series-connected seven nanogenerators are shown in Figure 3.6(b), and an output voltage of ~ 1.2 V was observed (**See SI Video S3.2**). These tests confirmed the output voltage generated from nanogenerator alone not by the oscilloscope or noise in the instrument.

Nanogenerator output voltage was recorded at different load resistances ranging from $10\text{ K}\Omega$ to $100\text{ M}\Omega$ under uniform hand tapping to measure the optimum output power. Figure 3.6(c) shows the variation of output voltage under different load resistances. With an increase in load resistance, the voltage increases and saturates at a value of approximately $\sim 200\text{ mV}$. The saturated output voltage at higher resistance ($>10\text{ M}\Omega$) is close to the open circuit output voltage. Inset of the Figure 3.6 (c) shows the magnified view of output voltage up to $3\text{ M}\Omega$ load resistance. The nanogenerator output voltage behaviour with load resistance can be understood with the help of a simple equivalent model proposed by Z L Wang and other research groups in the literature [21–24]. Now, assume that the nanogenerator device is equivalent to a voltage source, and load resistance (R_L) connected parallel to the device to measure voltage. The voltage drops across the R_L increase until the optimum R_L and saturate at the theoretically infinite load resistance similar to open-circuit voltage [25]. The load resistance dependence of output voltage shows a similar trend as reported in the literature for piezoelectric nanogenerators made of different materials [25–29].

The output power ($Power(P) = \frac{V^2}{(R_L)}$, where, V – output voltage and R_L – load resistance) of the nanogenerator with different load resistances was calculated and depicted in Figure 3.6(d). The maximum output power of 65 nW was observed for the nanogenerator at $100\text{ K}\Omega$

of load resistance R_L . Further, power density of PENG was calculated by considering the area of the devices and found $\sim 77 \mu\text{W}/\text{m}^2$. Inset of the Figure 3.6(d) shows the magnified view of output power up to $5 \text{ M}\Omega$ load resistance. The Output power characteristics of the nanogenerator can be understood from the maximum power transmission theorem [30]. It states that maximum power transmission occurs when the load resistance value equals the source internal resistance. In the present chapter, the peak in output power occurred under impedance matched conditions across a load resistor value $\sim 100 \text{ K}\Omega$. The output power decreased with the load resistance values greater than $100 \text{ K}\Omega$ due to the saturated output voltage. The saturated output voltage at higher load resistance decreases the V^2/R_L ratio (power) value. The dependence of output power with load resistance shows a similar trend as reported in the literature for piezoelectric nanogenerators made of different materials [31–33].

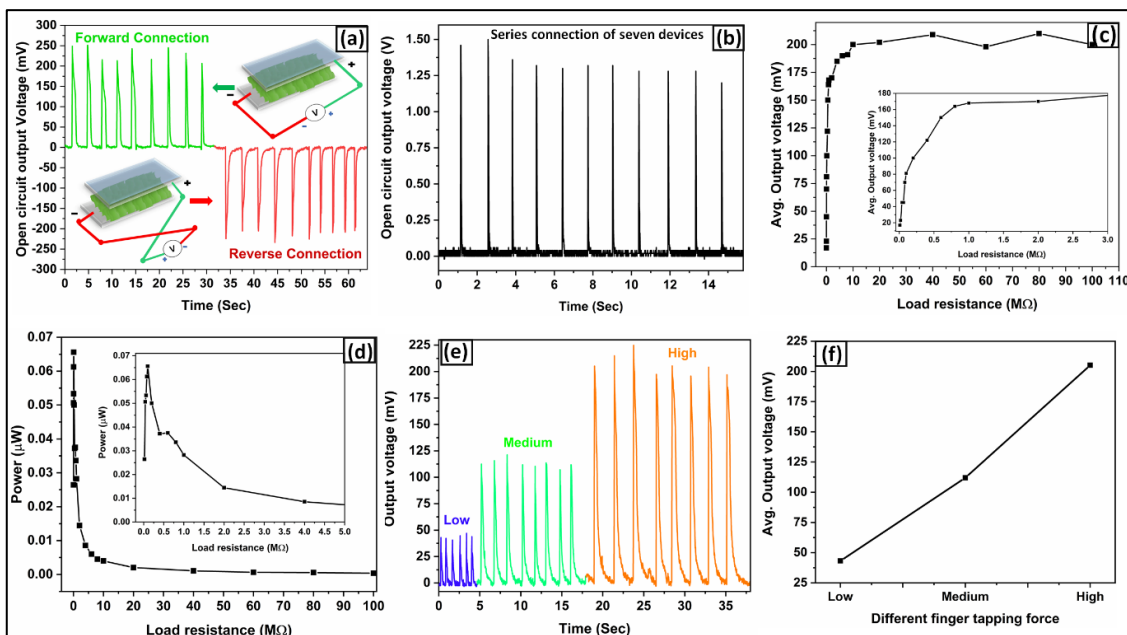


Figure 3.6. Nanogenerator output characteristics against finger tapping (a) Forward and reverse connection response, (b) Output voltage of the series connected seven nanogenerators, (c) Average output voltage of the nanogenerator across different load resistances, (d) Output power variation with variable load resistance, (e) Response of the nanogenerator against different finger tapping pressures, (f) Average output voltage of the nanogenerator as a function of different finger tapping pressures.

Further nanogenerator was explored for pressure sensing application. Figure 3.6(e)-(f) shows the response of the nanogenerator under different finger-tapping pressures of a low, medium, and high. The measured voltages are $\sim 40 \text{ mV}$, 110 mV , and 200 mV for low, medium,

and high tapping pressures. The amount of ZnO nanosheets rises as the pressure acting on the nanosheets increases, resulting in an increase in output voltage.

Further, the response of the nanogenerator tested over 1100 cycles is shown in Figure 3.7(a). Figure 3.7(c)-(d) shows the magnified view of the nanogenerator response of Figure 3.7(a). Further, nanogenerator output voltage at different cycle numbers is plotted and shown in Figure 3.7 (d). It is concluded from Figure 3.7, the nanogenerator has shown high stability and durability similar to the reported literature [34–36].

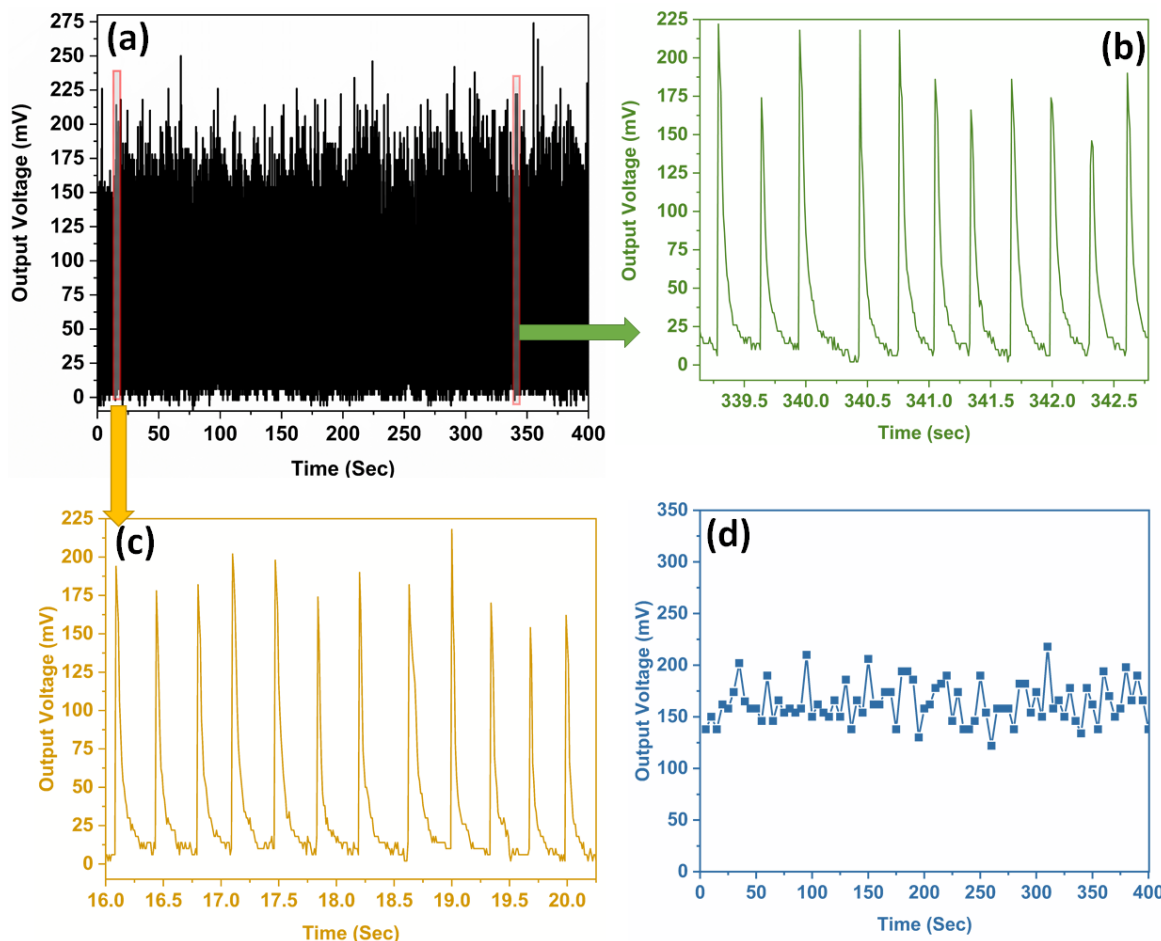


Figure 3.7. (a) Nanogenerator response over 1100 cycles of finger tapping, (b)-(c) Magnified view of the selected region of the cycle test, (d) Nanogenerator output at different cycle numbers.

3.3.5 TENG device studies

TENG's electrical voltage/current generation mechanism based on the coupling of the triboelectric effect and electrostatic induction. At the initial state, the ZnO nanosheet film and ITO are at a certain distance in electrically neutral condition. The ITO surface and aluminum foil acted as two conducting electrodes for device. When the top layer (ITO) is pressed in VCS

mode, the electrode comes to contact with the ZnO dielectric layer and generates a friction. The ZnO nanosheet film that gained electrons became negatively charged, whereas the ITO surface that lost electrons became positively charged. Once the applied force is released, two triboelectric layers get separated. The resulting charge separation will induce an electrical potential difference between the two electrodes and subsequent current flow in the external circuit. As compressed again, the layers come to contact again, electrons flow back through the circuit, reaching equilibrium. The periodic application and removal of force results in alternating current/voltage pulses in the measuring device [37].

The SEM images showing the surface morphology of ITO thin film, as shown in Figure 3.8(a) (ZnO SEM images shown in Figure 3.1(g) and Figure 3.2(g)). Further, the graphic of the fabricated TENG with the aid of sponge spacers and ITO substrate is illustrated in Figure 3.8(b).

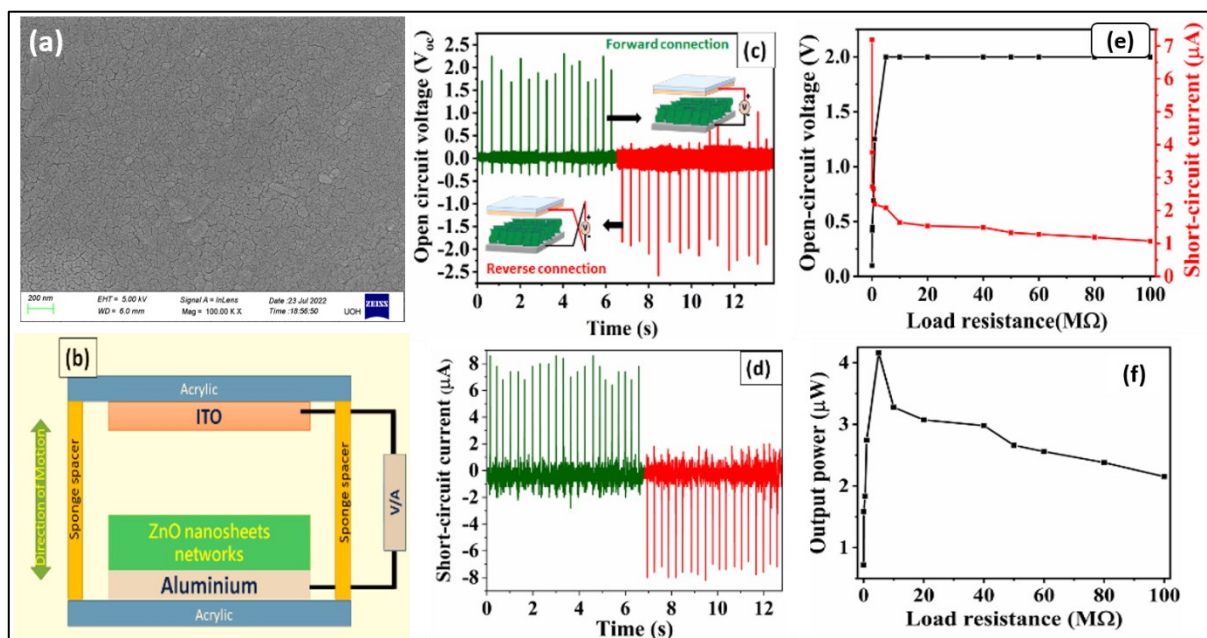


Figure 3.8. (a) SEM image of ITO thin film, (b) schematic view of TENG device, (c) V_{oc} in forward and reverse connection of TENG device, (d) I_{sc} in forward and reverse connection of TENG device. TENG response at different R_L values with (e) Average values of V_{oc} , I_{sc} as a function of different R_L (f) Instantaneous power the TENG device at across different R_L .

Figure 3.8(c) and (d) shows the open-circuit voltage (V_{oc}) and short-circuit current (I_{sc}) against hand tapping in both forward and reverse connections. The V_{oc} is generated due to contact electrification and electrostatic induction between ITO surface and ZnO nanosheet layers under cyclic contact and separation. The V_{oc} and I_{sc} of ~ 2 V and ~ 7 μ A, respectively were produced for hand tapping force for the TENG device. Further switching polarity test (SPT) was performed by reversing inputs to the oscilloscope and found a similar response of the TENG

with opposite polarity. Thus, SPT confirms that the generated electrical output is only from TENG, not from the instrument noise.

In addition, V_{oc} and I_{sc} of TENG were measured at different load resistances (R_L) values of 5 K Ω -100 M Ω range. Further, average values of V_{oc} and I_{sc} at different R_L values are plotted in Figure 3.8(e). The V_{oc} rised with R_L and saturated at ~ 5 M Ω of R_L . As depicted in Figure 3.8(e), the I_{sc} of the TENG showed an obvious drop with increasing the R_L due to ohmic loss[38,39]. Further, the instantaneous output power was calculated using the formula Power (P) =VI (V- output voltage, I- Output current) and presented in Figure 3.8(f) [40]. The maximum output power and power density of 4.15 μ W and 0.16 μ W/cm 2 was obtained at optimum R_L value 5 M Ω . In addition, TENGs exhibited the mechanical-to-electrical energy conversion efficiency of 0.032% (Chapter-2, section-2.4.6, the detailed calculation is provided).

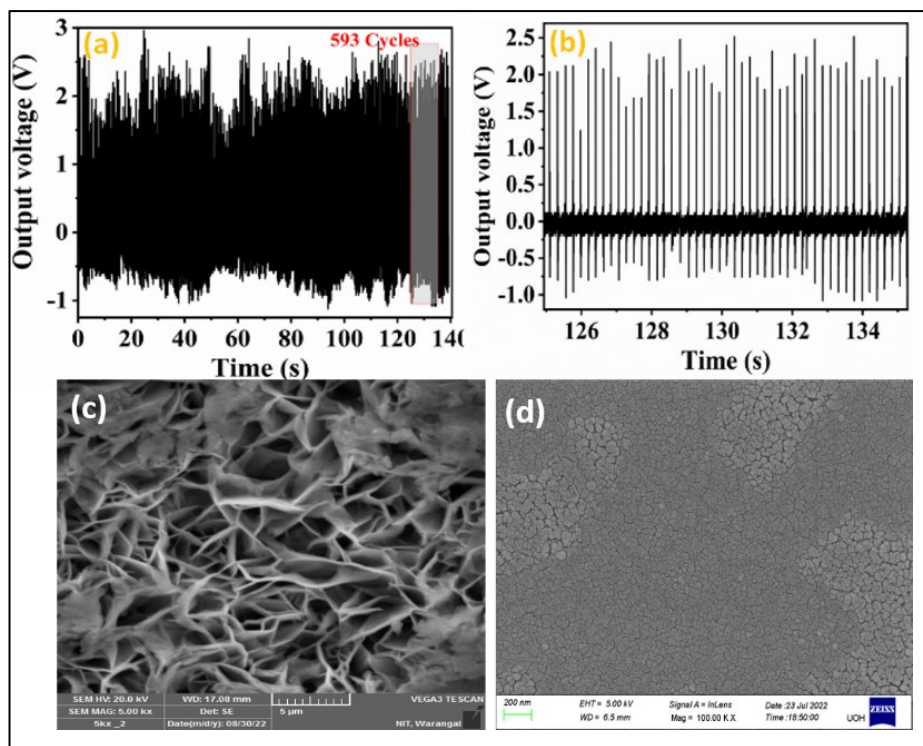


Figure 3.9. (a) Stability of TENG response over 593 cycles, (b) Enlarged view of selected portion of the stability graph. SEM images of (c) ZnO nanosheets (d) ITO thin film after the stability test.

Further, TENG response was tested over 593 energy generation cycles and presented in Figure 3.9(a). The V_{oc} of the TENG did not decrease considerably, which confirms that the excellent stability and durability of the TENG. The minor changes in the V_{oc} are due to the hand tapping force variation. Figure 3.9(b) shows an expanded view of the selected region from the stability

graph. Figure 3.9(c-d) provide a visual insight into the surface morphology following an exhaustive stability test of 593 cycles. Notably, even after this rigorous testing, the films exhibit a commendable maintenance of good morphology.

3.4 Applications of TENG device

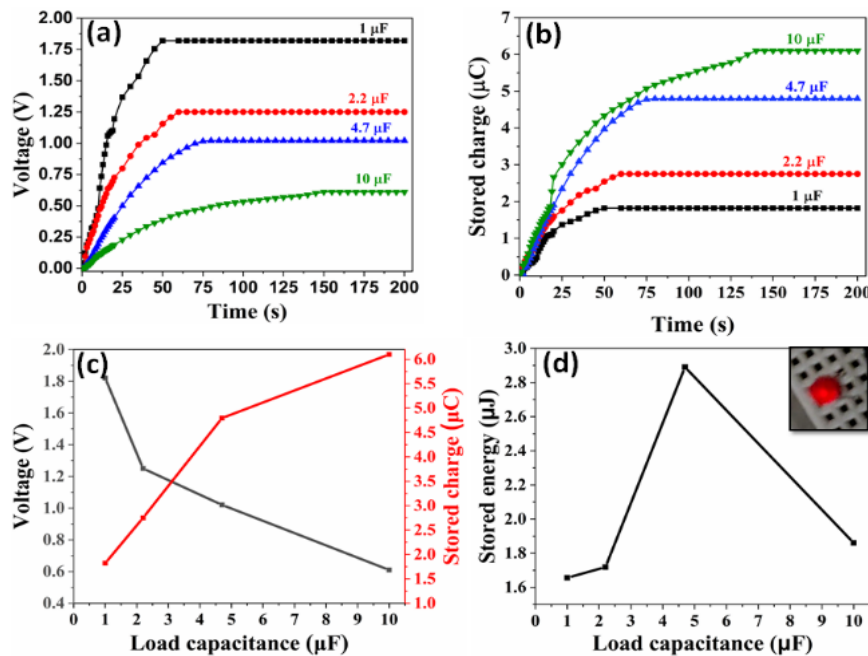


Figure 3.10: Different capacitors (a) Charging curves, b) Stored charge curves as function of time, (c) Charged voltage, and stored charge, (d) Stored energy as a function of load capacitance.

To sustain the continuous operation of electronic devices, the generated AC output from TENG is rectified and used to charge capacitors. These capacitors then store the electrical charge, providing a stable and continuous source of energy that can be efficiently utilized to power various electronic devices. Further, the voltage produced by TENG was used for charging different capacitors (1 μF , 2.2 μF , 4.7 μF and 10 μF) ([See video S3.3](#)). Figure 3.10(a)-(b) shows different load capacitors' charging curves and stored charge curves. Figure 3.10(c) shows the charged voltage and stored charge as a function of load capacitance. Further, energy stored by each load capacitor is presented in Figure 3.10(d), and maximum energy of 2.8 μJ was observed at a 4.7 μF capacitor. Finally, the fabricated TENG was able to power one LED instantaneously without using any charged capacitor, as shown in the inset of Figure 3.10(d) ([See video S3.4](#)).

3.5 Conclusions

In this work, hot plate-assisted hydrothermal growth of ZnO nanosheet networks is reported for the first time. Growth temperature of 85°C and growth duration of 4 hours is optimum for the uniform and dense ZnO nanosheets growth. XRD and TEM study confirms the crystallinity and purity of the ZnO nanosheet films. The PENG is fabricated by placing ITO coated PET on the top of the ZnO nanosheets film, and TENG is fabricated using ITO and ZnO nanosheets film as contact materials. The switching polarity test and linear superposition of voltage tests confirm the generated voltage from nanogenerator. The proposed piezo and triboelectric nanogenerators produced an instantaneous power density of $\sim 77 \mu\text{W/m}^2$ and 10 mW/m^2 , respectively. The proposed PENG exhibits the capability to function as force sensors, while the TENG directly powers a single LED. Additionally, the TENG can efficiently charge multiple capacitors, showcasing its versatility in energy harvesting and storage applications.

3.6 References

- [1] T.R. Anderson, E. Hawkins, P.D. Jones, CO₂, the greenhouse effect and global warming: from the pioneering work of Arrhenius and Callendar to today's Earth System Models, *Endeavour*. 40 (2016) 178–187.
<https://doi.org/10.1016/j.endeavour.2016.07.002>.
- [2] A.M. Omer, Energy use and environmental impacts: A general review, *Adv. Energy Res.* 17 (2014) 1–38. <https://doi.org/10.1063/1.3220701>.
- [3] C. Zhang, W. Fan, S. Wang, Q. Wang, Y. Zhang, K. Dong, Recent Progress of Wearable Piezoelectric Nanogenerators, *ACS Appl. Electron. Mater.* 3 (2021) 2449–2467. <https://doi.org/10.1021/acsaelm.1c00165>.
- [4] Z.L. Wang, J. Song, Piezoelectric nanogenerators based on zinc oxide nanowire arrays, *Science* (80-.). 312 (2006) 242–246. <https://doi.org/10.1126/science.1124005>.
- [5] Y. Hu, L. Lin, Y. Zhang, Z.L. Wang, Replacing a battery by a nanogenerator with 20 v output, *Adv. Mater.* 24 (2012) 110–114. <https://doi.org/10.1002/adma.201103727>.
- [6] Z. Liu, S. Zhang, Y.M. Jin, H. Ouyang, Y. Zou, X.X. Wang, L.X. Xie, Z. Li, Flexible piezoelectric nanogenerator in wearable self-powered active sensor for respiration and healthcare monitoring, *Semicond. Sci. Technol.* 32 (2017) 64004.
<https://doi.org/10.1088/1361-6641/aa68d1>.
- [7] A. Yu, M. Song, Y. Zhang, J. Kou, J. Zhai, Z. Lin Wang, A self-powered AC magnetic

- sensor based on piezoelectric nanogenerator, *Nanotechnology*. 25 (2014) 455503. <https://doi.org/10.1088/0957-4484/25/45/455503>.
- [8] Y. Hu, Z.L. Wang, Recent progress in piezoelectric nanogenerators as a sustainable power source in self-powered systems and active sensors, *Nano Energy*. 14 (2014) 3–14. <https://doi.org/10.1016/j.nanoen.2014.11.038>.
- [9] S.F. Leung, K.T. Ho, P.K. Kung, V.K.S. Hsiao, H.N. Alshareef, Z.L. Wang, J.H. He, A Self-Powered and Flexible Organometallic Halide Perovskite Photodetector with Very High Detectivity, *Adv. Mater.* 30 (2018) 1–8. <https://doi.org/10.1002/adma.201704611>.
- [10] Z.L. Wang, Ten years' venturing in ZnO nanostructures: from discovery to scientific understanding and to technology applications, *Chinese Sci. Bull.* 54 (2009) 4021. <https://doi.org/10.1007/s11434-009-0456-0>.
- [11] J.L. Gomez, O. Tigli, Zinc oxide nanostructures: From growth to application, *J. Mater. Sci.* 48 (2013) 612–624. <https://doi.org/10.1007/s10853-012-6938-5>.
- [12] S. Baruah, J. Dutta, Hydrothermal growth of ZnO nanostructures, *Sci. Technol. Adv. Mater.* 10 (2009) 13001. <https://doi.org/10.1088/1468-6996/10/1/013001>.
- [13] V. Gerbreders, M. Krasovska, E. Sledevskis, A. Gerbreders, I. Mihailova, E. Tamanis, A. Ogurcovs, Hydrothermal synthesis of ZnO nanostructures with controllable morphology change, *CrystEngComm*. 22 (2020) 1346–1358. <https://doi.org/10.1039/c9ce01556f>.
- [14] K.H. Kim, B. Kumar, K.Y. Lee, H.K. Park, J.H. Lee, H.H. Lee, H. Jun, D. Lee, S.W. Kim, Piezoelectric two-dimensional nanosheets/anionic layer heterojunction for efficient direct current power generation, *Sci. Rep.* 3 (2013) 1–6. <https://doi.org/10.1038/srep02017>.
- [15] V. Gaddam, R.R. Kumar, M. Parmar, G.R.K. Yaddanapudi, M.M. Nayak, K. Rajanna, Morphology controlled synthesis of Al doped ZnO nanosheets on Al alloy substrate by low-temperature solution growth method, *RSC Adv.* 5 (2015) 13519–13524. <https://doi.org/10.1039/c4ra14049d>.
- [16] M. Kamruzzaman, J.A. Zapien, Effect of Temperature, Time, Concentration, Annealing, and Substrates on ZnO Nanorod Arrays Growth by Hydrothermal Process

- on Hot Plate, *Crystallogr. Reports.* 63 (2018) 456–471.
<https://doi.org/10.1134/S1063774518030112>.
- [17] R. Yang, Y. Qin, C. Li, L. Dai, Z.L. Wang, Characteristics of output voltage and current of integrated nanogenerators, *Appl. Phys. Lett.* 94 (2009) 92–95.
<https://doi.org/10.1063/1.3072362>.
- [18] K. Il Park, M. Lee, Y. Liu, S. Moon, G.T. Hwang, G. Zhu, J.E. Kim, S.O. Kim, D.K. Kim, Z.L. Wang, K.J. Lee, Flexible nanocomposite generator made of BaTiO 3 nanoparticles and graphitic carbons, *Adv. Mater.* 24 (2012) 2999–3004.
<https://doi.org/10.1002/adma.201200105>.
- [19] M.K. Gupta, J.H. Lee, K.Y. Lee, S.W. Kim, Two-dimensional vanadium-doped ZnO nanosheet-based flexible direct current nanogenerator, *ACS Nano.* 7 (2013) 8932–8939. <https://doi.org/10.1021/nn403428m>.
- [20] A. Yu, H. Li, H. Tang, T. Liu, P. Jiang, Z.L. Wang, Vertically integrated nanogenerator based on ZnO nanowire arrays, *Phys. Status Solidi - Rapid Res. Lett.* 5 (2011) 162–164. <https://doi.org/10.1002/pssr.201105120>.
- [21] Y. Zhou, W. Liu, X. Huang, A. Zhang, Y. Zhang, Z.L. Wang, Theoretical study on two-dimensional MoS2 piezoelectric nanogenerators, *Nano Res.* 9 (2016) 800–807.
<https://doi.org/10.1007/s12274-015-0959-8>.
- [22] Q. Xu, Y. Qin, Theoretical study of enhancing the piezoelectric nanogenerator's output power by optimizing the external force's shape, *APL Mater.* 5 (2017) 074101.
<https://doi.org/10.1063/1.4975772>.
- [23] H.J. Lee, S. Sherrit, L.P. Tosi, P. Walkemeyer, T. Colonius, Piezoelectric energy harvesting in internal fluid flow, *Sensors (Switzerland)*. 15 (2015) 26039–26062.
<https://doi.org/10.3390/s151026039>.
- [24] K. Nadaud, F. Morini, A.S. Dahiya, C. Justeau, S. Boubenia, K.P. Rajeev, K. Nadaud, K.P. Rajeev, D. Alquier, G. Poulin-vittrant, Double buffer circuit for the characterization of piezoelectric nanogenerators based on ZnO nanowires, 063901 (2018) 1–6.
- [25] A. Sultana, M.M. Alam, S. Garain, T.K. Sinha, T.R. Middya, D. Mandal, An Effective Electrical Throughput from PANI Supplement ZnS Nanorods and PDMS-Based

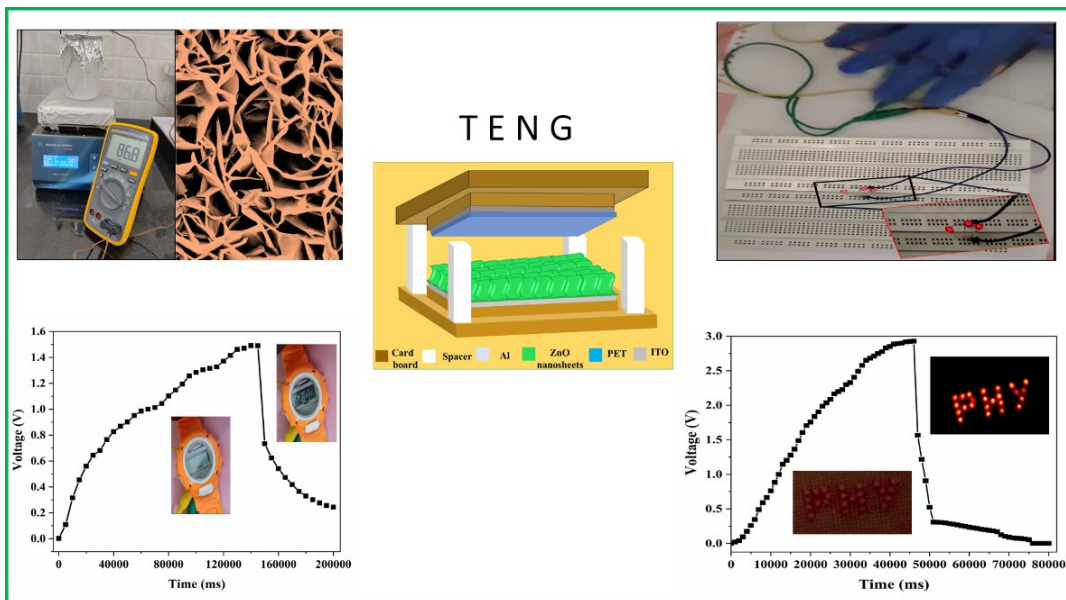
- Flexible Piezoelectric Nanogenerator for Power up Portable Electronic Devices: An Alternative of MWCNT Filler, *ACS Appl. Mater. Interfaces.* 7 (2015) 19091–19097. <https://doi.org/10.1021/acsami.5b04669>.
- [26] S.P. Sensor, X. Li, Z. Lin, G. Cheng, X. Wen, Y. Liu, S. Niu, 3D Fiber-Based Hybrid Nanogenerator for Energy Harvesting and as a, *ACS Nano.* (2014) 10674–10681. <https://doi.org/10.1021/nn504243j>.
- [27] S. Rafique, A.K. Kasi, J.K. Kasi, Aminullah, M. Bokhari, Z. Shakoor, Fabrication of silver-doped zinc oxide nanorods piezoelectric nanogenerator on cotton fabric to utilize and optimize the charging system, *Nanomater. Nanotechnol.* 10 (2020) 1–12. <https://doi.org/10.1177/1847980419895741>.
- [28] S. Stassi, V. Cauda, C. Ottone, A. Chiodoni, C.F. Pirri, G. Canavese, Flexible piezoelectric energy nanogenerator based on ZnO nanotubes hosted in a polycarbonate membrane, *Nano Energy.* 13 (2015) 474–481. <https://doi.org/10.1016/j.nanoen.2015.03.024>.
- [29] S. Ye, C. Cheng, X. Chen, X. Chen, J. Shao, J. Zhang, H. Hu, H. Tian, X. Li, L. Ma, W. Jia, High-performance piezoelectric nanogenerator based on microstructured P(VDF-TrFE)/BNNTs composite for energy harvesting and radiation protection in space, *Nano Energy.* 60 (2019) 701–714. <https://doi.org/10.1016/j.nanoen.2019.03.096>.
- [30] J. Bird, *Electrical Circuit Theory and Technology*, 5th ed, Routledge, 2014. <https://doi.org/10.4324/9781315883342>.
- [31] K. Il Park, J.H. Son, G.T. Hwang, C.K. Jeong, J. Ryu, M. Koo, I. Choi, S.H. Lee, M. Byun, Z.L. Wang, K.J. Lee, Highly-efficient, flexible piezoelectric PZT thin film nanogenerator on plastic substrates, *Adv. Mater.* 26 (2014) 2514–2520. <https://doi.org/10.1002/adma.201305659>.
- [32] C. Luo, S. Hu, M. Xia, P. Li, J. Hu, G. Li, H. Jiang, W. Zhang, A Flexible Lead-Free BaTiO₃/PDMS/C Composite Nanogenerator as a Piezoelectric Energy Harvester, *Energy Technol.* 6 (2018) 922–927. <https://doi.org/10.1002/ente.201700756>.
- [33] S. Garain, S. Jana, T.K. Sinha, D. Mandal, Design of in Situ Poled Ce³⁺-Doped Electrospun PVDF/Graphene Composite Nanofibers for Fabrication of Nanopressure

- Sensor and Ultrasensitive Acoustic Nanogenerator, *ACS Appl. Mater. Interfaces.* 8 (2016) 4532–4540. <https://doi.org/10.1021/acsami.5b11356>.
- [34] D. Yu, Z. Zheng, J. Liu, H. Xiao, G. Huangfu, Y. Guo, Superflexible and Lead-Free Piezoelectric Nanogenerator as a Highly Sensitive Self-Powered Sensor for Human Motion Monitoring, *Nano-Micro Lett.* 13 (2021) 1–12. <https://doi.org/10.1007/s40820-021-00649-9>.
- [35] F. Mokhtari, J. Foroughi, T. Zheng, Z. Cheng, G.M. Spinks, Triaxial braided piezo fiber energy harvesters for self-powered wearable technologies, *J. Mater. Chem. A.* 7 (2019) 8245–8257. <https://doi.org/10.1039/c8ta10964h>.
- [36] S.K. Kim, R. Bhatia, T.H. Kim, D. Seol, J.H. Kim, H. Kim, W. Seung, Y. Kim, Y.H. Lee, S.W. Kim, Directional dependent piezoelectric effect in CVD grown monolayer MoS₂ for flexible piezoelectric nanogenerators, *Nano Energy.* 22 (2016) 483–489. <https://doi.org/10.1016/j.nanoen.2016.02.046>.
- [37] J. Wang, C. Wu, Y. Dai, Z. Zhao, A. Wang, T. Zhang, Z.L. Wang, Achieving ultrahigh triboelectric charge density for efficient energy harvesting, *Nat. Commun.* 8 (2017) 1–7. <https://doi.org/10.1038/s41467-017-00131-4>.
- [38] X. Fan, J. Chen, J. Yang, P. Bai, Z. Li, Z.L. Wang, Ultrathin, rollable, paper-based triboelectric nanogenerator for acoustic energy harvesting and self-powered sound recording, *ACS Nano.* 9 (2015) 4236–4243. <https://doi.org/10.1021/acs.nano.5b00618>.
- [39] T.C. Hou, Y. Yang, H. Zhang, J. Chen, L.J. Chen, Z. Lin Wang, Triboelectric nanogenerator built inside shoe insole for harvesting walking energy, *Nano Energy.* 2 (2013) 856–862. <https://doi.org/10.1016/j.nanoen.2013.03.001>.
- [40] M.L. Seol, J.H. Woo, S.B. Jeon, D. Kim, S.J. Park, J. Hur, Y.K. Choi, Vertically stacked thin triboelectric nanogenerator for wind energy harvesting, *Nano Energy.* 14 (2015) 201–208. <https://doi.org/10.1016/j.nanoen.2014.11.016>.

Chapter 4

A Simple and Low-cost Triboelectric Nanogenerator Based on Two Dimensional ZnO Nanosheets and Its Application in Portable Electronics

This chapter delves into the synthesis and the characteristic properties of ZnO nanosheets and Polyethylene terephthalate (PET). A notable achievement discussed in this chapter is the fabrication of a simple and cost-effective TENG using ZnO nanosheet film and PET as triboelectric layers for the first time. This TENG device demonstrated an impressive output voltage and power density. Further, studied the charging characteristics of various capacitors by utilizing the TENG. This underscores its potential as a promising solution for self-powered sensors and devices.



Publications:

1. "A Simple and Low-Cost Triboelectric Nanogenerator Based on Two Dimensional ZnO Nanosheets and Its Application in Portable Electronics", *Supraja Potu, R. Rakesh Kumar, Siju Mishra, D. Haranath, P. Ravi Sankar, K. Prakash, N. Jayaram babu, T. Venkatappa Rao, K. Uday Kumar, Sensors Actuators A Phys.* 2022, 335, 113368 <https://doi.org/10.1016/J.SNA.2022.113368>.

4.1 Introduction

Several energy harvesting technologies such as photovoltaics, piezoelectric, triboelectric, thermoelectric, and electromagnetic have been developed to provide power to portable electronic devices. The triboelectric energy harvesting phenomenon has many advantages over other methods [1,2]. The triboelectric nanogenerators (TENG) technology is considered suitable for self-powered electronic devices. It has attracted much research interest due to its high output voltage and current with simple structures and easier packaging than piezoelectric nanogenerators (PENG). The TENG device fabrication has a broad choice of materials, and new materials are still being added [2–5]. In addition, TENG could convert almost all forms of mechanical energy such as vibration, rotation, force, pressure, airflow, water flow, raindrops into electricity [1]. TENG can convert both low and high-frequency vibrations into electricity [6,7]. In TENGs, works based on the principle of triboelectrification and electro static induction [8]. Further, TENG can be operated in four modes: sliding, single electrode, free-standing, and contact-separation [9–11]. Among the four modes of TENG, contact separation mode is simple and easy to make and test the device. The performance of TENG is good in contact separation mode with high power densities compared to the other modes [9,10]. In addition, the physical damage to the triboelectric layer is less in contact separation mode than sliding mode and free-standing mode. TENGs vertical contact separation (VCS) mode generally lasts longer due to lesser friction damage. Therefore, TENGs VCS mode is selected in this chapter.

Due to the rapid growth of flexible TENGs, many research groups focused on improving the TENGs performance through a new material synthesis, advanced structural designs, mechanical-coupling effects [11,12]. However, the new triboelectric materials exploration is still a significant research area to reduce the cost and complexity of the TENG device and enhance its energy conversion efficiency. In this chapter, ZnO nanosheets film and polyethylene terephthalate (PET) were used for the first time as a new triboelectric pair in TENG design. The present study is the first work on TENG-based on ZnO nanosheets and PET to the best of our knowledge. In this chapter, ZnO nanosheets synthesized directly on aluminium substrate, PET side of ITO/PET were used as friction layers, eliminating the need to attach the electrodes or depositing electrodes. However, there were reports on TENGs based on ZnO nanorods, ZnO nanowires, ZnO nanolayers, and ZnO nanoripples, but not on ZnO nanosheets. The literature review of all the TENGs based on ZnO nanostructures and the results

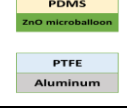
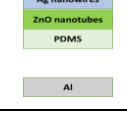
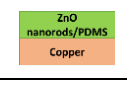
are summarized in terms of the device structure, friction layers, output performance is presented in Table 4.1.

The ZnO is a very promising material, and it has several advantages like non-toxic, cost-effective, bio-compatible, environmentally friendly, and excellent stability [13]. Further, ZnO nanosheets synthesis has several advantages: simple, low cost, rapid growth, seed layer free, single step procedure compared to multiple step and seed layer assisted ZnO nanorods and nanowires [14,15]. In addition, ZnO nanosheets growth is directly obtained on aluminum substrate. Therefore, the substrate act as one of the conducting electrodes for the TENG device and reduces the fabrication steps. Furthermore, the mechanical strength of the ZnO nanosheets is more than nanorods; as a result, the device can withstand high value forces and produce electrical energy [16].

In this work, TENG is fabricated for the first time with ZnO nanosheet film and PET as a novel triboelectric pair for harvesting mechanical energy. The TENG response was studied under load resistance and load capacitance to determine the maximum power and energy generated. In addition, fabricated TENG has been demonstrated for powering the digital watch, 24 LEDs with the help of charged capacitors. Finally, with bio-mechanical energy and tapping machines, TENG stability was tested over many test cycles.

Table 4.1. Literature review of triboelectric nanogenerators based on ZnO nanostructures.

A simple and low-cost TENG.... And its application in portable electronics

Sl. No	Device Structure	Friction Materials	Output Performance	References
1		ZnO nano ripples /polyimide	Output Voltage-80V Current-0.82μA Load resistance-not mentioned	[17]
2		Polyamide/ZnO nanostructure	Output Voltage-20V Current-1.36μA Load resistance-not mentioned	[18]
3		Polyimide/ZnO matrix composite film	Output Voltage-150V (100MΩ) Power density-2.5W/m ² (5 MΩ)	[19]
4		Polyimide/Al doped ZnO	Output Voltage-68V (120MΩ) Current-3.94μA	[20]
5		PDMS/Sb-doped ZnO nanorods	Output Voltage-12V Current density-0.11μAcm ⁻² Load resistance-none	[21]
6		PDMS/ZnO micro balloon/PTFE	Output Voltage-57V (100MΩ) Power density-1105mWm ⁻² (2MΩ)	[22]
7		ZnO nanorods/PDMS	Output Voltage-3.62V Current -112.7nA Load resistance-none	[23]
8		Ag nanowires +ZnO nanotubes +PDMS/Al	Output Voltage-350V (50MΩ) Power density-1.1mWcm ⁻² (20MΩ)	[24]
9		PET/ZnO +PDMS	Output Voltage-3.5V(100 MΩ) Power density-4.8μWcm ⁻² (70MΩ)	[25]
10		Kapton/Zno-Polystene	Output Voltage-7V Power density-0.23mWm ⁻² Load resistance-none	[26]
11		PET/ZnO nanosheets	Output Voltage ~ 4.9V Current-10 μA Power density~ 1 μW/cm ² (5 MΩ)	Present work

4.2 Experimental section

4.2.1 Materials

Zinc nitrate hexahydrate and hexamethylenetetramine (HMTA) and ITO coated PET (60 Ω/sq) sheets. Aluminum foils (thickness $\sim 79.84 \mu\text{m}$) (See SI , Figure S4.1). Acrylic sheets, cardboard, sponges were utilized in this chapter.

4.2.2 ZnO nanosheets synthesis

The ZnO nanosheets film was synthesized on Al substrates by following the same method mentioned in Chapter-2, Section 2.1.

4.2.3 TENG device fabrication

The TENG device have been fabricated using the same steps, it implies a standardized manufacturing process as mentioned in Chapter-2, Section 2.3.2. The ZnO nanosheets network film and PET surface of PET/ITO substrate were the two dielectric materials used to fabricate the TENG device. The ITO surface and the aluminum substrate acted as TENG's top and bottom electrodes, respectively. To study the energy harvesting properties of the TENG devices, they were subjected to a hand tapping force of $\sim 7 \text{ N}$ (Chapter-2, Section 2.4.6), frequency of 3-4 Hz and 1.2 cm of spacing has provided between the triboelectric layers to operate the device under contact separation mode. Finally, two electrode lead wires were connected from the ITO side and the aluminum side to measure the TENG electrical output.

4.3 Results and discussion

4.3.1 SEM and XRD analysis

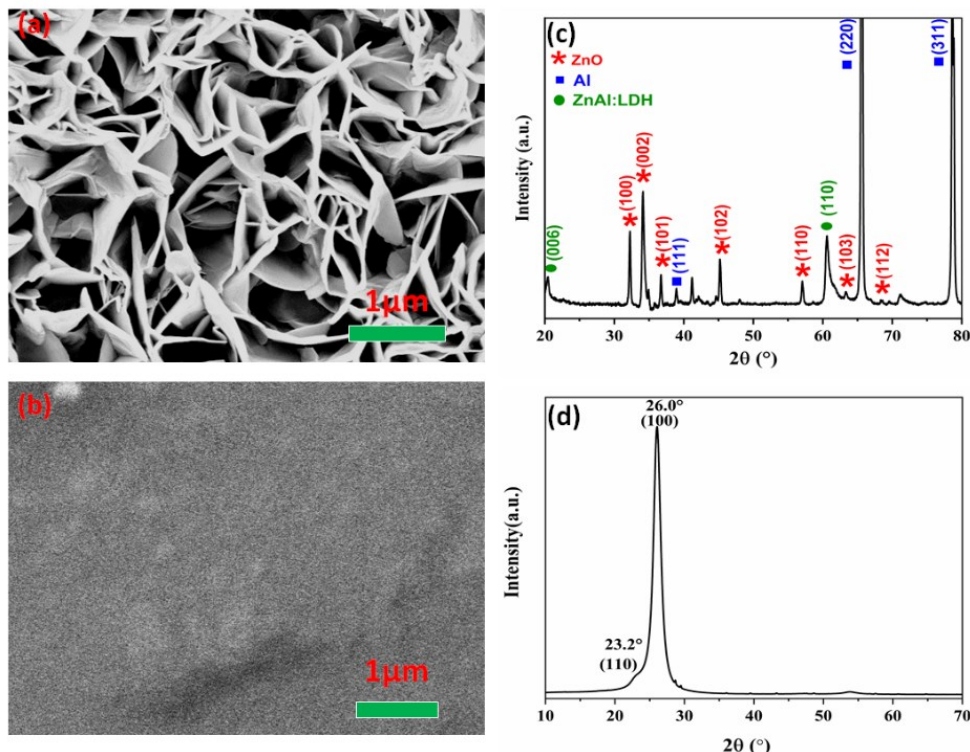


Figure 4.1. SEM images of (a) ZnO nanosheets, (b) PET surface, XRD pattern of (c) ZnO nanosheet film, (d) PET surface.

The surface morphology of the ZnO thin film coated on aluminium and the PET surface of PET/ITO are shown in Figures 4.1(a) and (b). Figure 4.1(a) confirms the vertically grown ZnO nanosheets on the aluminium substrate with uniform density and connectivity among them. The obtained ZnO nanosheets produce a rough topography, and PET surface appears smooth at the macroscopic level, but it also has a rough surface at the microscopic level, as shown in Figure 4.1(b).

Further XRD studies confirm the crystalline nature of the ZnO nanosheet film and the PET surface. The XRD pattern of the ZnO thin film is shown in Figure 4.1(c), and all the ZnO diffraction peaks were indexed with red colour. The ZnO diffraction peaks were in good agreement with the JCPDS card no. 751526 [27]. Similarly, all the diffractions peaks of the aluminium substrate were indexed in blue colour and agreed well with JCPDS card no 040787. In addition, the additional diffraction peaks observed at 20.4° , 60.5° were assigned to the ZnAl:LDH layer that was formed between the ZnO nanosheets and the aluminium substrate [16,28]. The intense diffraction peak observed at 26° in Figure 4.1(d) corresponds to the (100) plane of PET and is in good agreement with the published literature [29,30].

4.3.2 TENG device studies

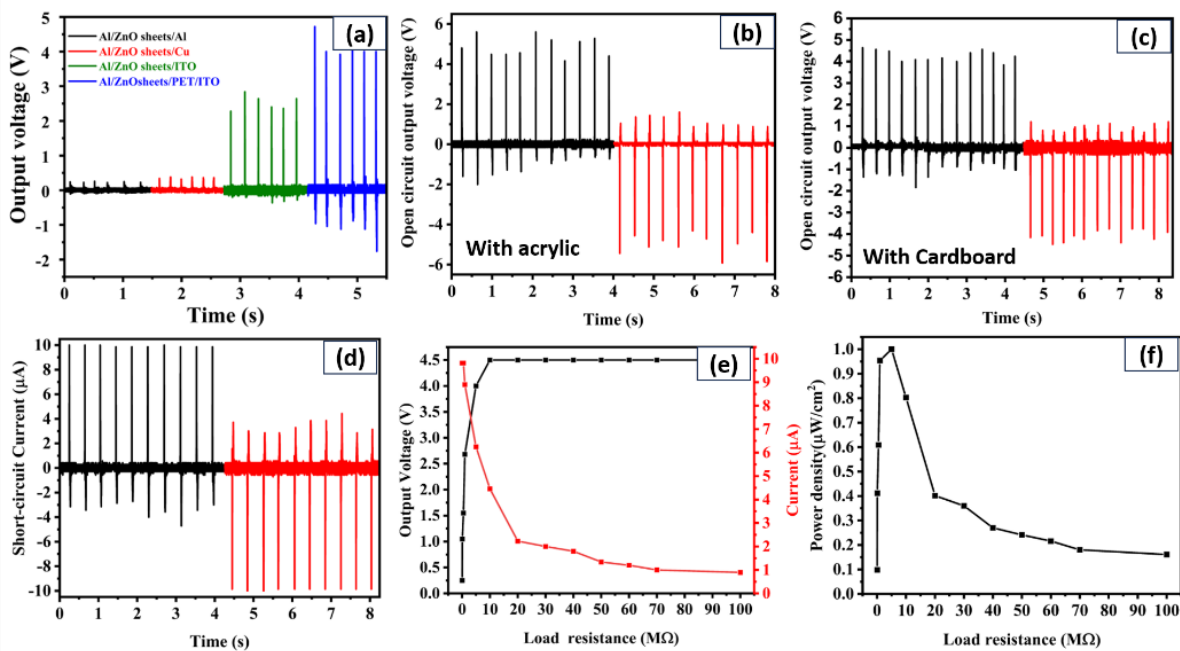


Figure 4.2. (a) V_{oc} of TENG device with different electrodes. V_{oc} of TENG device under switching polarity test of (b) acrylic support, (c) cardboard support, (d) I_{sc} of TENG device under switching polarity test, (e) V_{oc} and I_{sc} measured as a function of different load resistances, (f) instantaneous output power of the TENG device as a function of different load resistances.

The study involves investigating the output response of a ZnO-based TENG with various contact surfaces, including Al, Cu, ITO, and PET/ITO. Figure 4.2(a) illustrates the response of all TENG devices, revealing that the combination of ZnO nanosheets film and PET film as a triboelectric pair produces the maximum open circuit voltage (V_{oc}). Figure 4.2(b) shows the V_{oc} produced by the TENG device (size = $5 \times 5 \text{ cm}^2$, spacing = 1.2 cm) against repeated hand tapping under forward and reverse connections. TENG's forward and reverse connection geometry shows an average V_{oc} of $\sim 4.9 \text{ V}$ ([See SI Video V4.1](#)). The output voltage measurement when the connection to the oscilloscope is reversed is known as the switching polarity test. The switching polarity test verified that the voltage produced by TENG is not from any instrument noise and is given by the TENG device only. To simplify the process and reduce costs, TENG was made with simple cardboard instead of acrylic sheets and tested its response against hand tapping, shown in Figure 4.2(c). TENG made with cardboard also showed a similar response as TENG made with acrylic sheets. The contribution of ZnO nanosheets piezoelectric output voltage was studied separately in piezoelectric device design and found $\sim 300 \text{ mV}$ under the applied hand tapping pressures ([See SI, Figure S4.2](#)). The piezoelectric voltage generated from the ZnO is negligible when compared to the triboelectric

output voltage of \sim 4900 mV.

Further, short-circuit current (I_{sc}) of TENG was measured under repeated hand tapping and responses are shown in Figure 4.2(d) (**Chapter-2, Section-2.4.2**). The maximum value of I_{sc} is approximately 10 μ A, which is related to the transferred charges moving from one electrode to another under a short circuit condition. Asymmetry in the positive and negative peaks (current/voltage) is attributed to the difference between the external force applied on the device and the restoring force of elastic spacers of the device [31–34]. The contact process is done by tapping force, whereas the separation process is due to the elasticity of spacers. Contact and separation process takes different time durations as results charge transfer rates will differ. This asymmetry in voltage and current signals is observed consistently in most literature reports, and more systematic study is required to explain the asymmetry. In conclusion, The V_{oc} and I_{sc} of \sim 4.9 V and 10 μ A were observed for the present TENG.

Further, electrical outputs (V_{oc} , I_{sc}) of TENG device under different load resistances (R_L) were recorded against hand tapping to find out the load characteristics and the instantaneous output power density of the TENG. The I_{sc} and V_{oc} of the TENG under the different load resistance values in the range of 50 K Ω to 100 M Ω are shown in Figure 4.2(e). The V_{oc} increased with external load resistance and saturated at higher load resistance values greater than 10 M Ω . The saturated output voltage (\sim 4.1 V) is close to the open-circuit voltage. At the same time, The I_{sc} decreases with increasing loading resistance due to Ohmic losses as expected. The load resistance dependency of V_{oc} and I_{sc} shows a trend similar to that described in the literature for other TENG's [35–37]. The TENG load resistance can be understood with a simple equivalent model proposed by Z L Wang and other research groups in the literature [38,39]. The TENG is equivalent to a variable capacitor connected to a voltage source. The voltage drops across the R_L increase until the optimum R_L and saturate at the theoretically infinite R_L comparable to V_{oc} [40].

The TENG device's instantaneous output power density ($P = VI/A$, I-current, V-voltage and A-area) was calculated numerically with V_{oc} , I_{sc} at different load resistance values and depicted in Figure 4.2(f). The maximum instantaneous output power and power density of 25 μW and 1 $\mu\text{W}/\text{cm}^2$ were observed at a load resistance value of $\sim 5 \text{ M}\Omega$. The maximum power transmission theorem can explain the nanogenerator's output power characteristics [41]. In the present chapter, instantaneous output power peak under impedance matched conditions across a resistor $\sim 5 \text{ M}\Omega$. The output power decreased with the load resistance values greater than 5 $\text{M}\Omega$. At higher load resistance, the output voltage got saturated as a result, the product ($V_{oc} \times I_{sc}$) value decreased. The behavior of TENG devices under variable resistances illustrates a similar trend that has been described in the literature [42–44]. Further, TENGs exhibited the mechanical-to-electrical energy conversion efficiency of 0.44% (Chapter-2, section- 2.4.6).

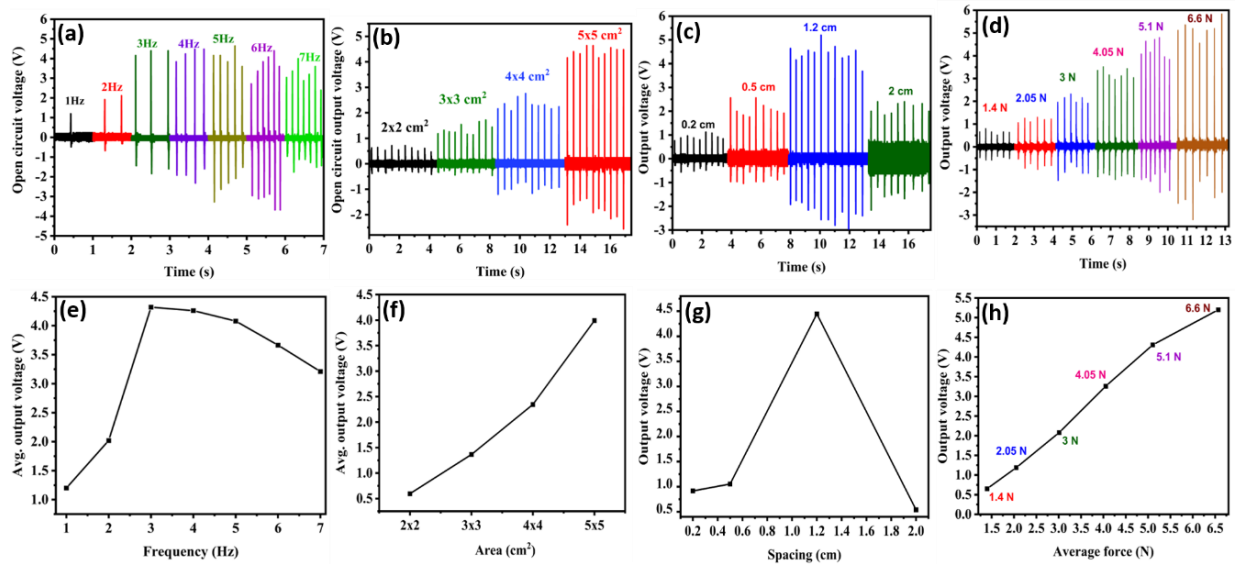


Figure 4.3. TENG output voltage as a function of (a) different frequency, (b) different area, (c) different spacing and, (d) different force, variation of average output voltage with (e) different frequency, (f) different area, (g) different spacing and, (h) different force, respectively.

The V_{oc} of TENG was measured at different frequencies of hand tapping from 1 Hz to 7 Hz to study the frequency response. The response of TENG under different hand tapping frequencies is shown in Figure 4.3(a). The average output voltage of the TENG increased with an increase in the frequency up to 4 Hz and decreased for later frequencies, as shown in Figure 4.3(e). The increased output voltage with the increase in frequency is due to the incomplete neutralization of charges [23,45]. The V_{oc} at high frequencies ($>4 \text{ Hz}$) decreased. If the applied

frequency is too high, the nanogenerator cannot returns to the original position before the next force application results in a low output voltage [46,47].

The influence of triboelectric layer size (device size) on the TENG performance was studied in Figure 4.3(b) shows the TENG response to hand tapping for various device dimensions of 2x2, 3x3, 4x4, and 5x5 cm². Figure 4.3 (f) clearly shows that the TENG average output voltage values were increased from 0.5 V to 4.5 V with an increase in device size. The increased active contact area of the triboelectric layers is responsible for improving the output voltage. A similar trend has also been reported for TENG's in the literature [48,49].

Further, the output performance of the TENG device was measured under different spacing (0.2–2 cm) between the triboelectric layers under the same amount of applied frequency and presented in Figure 4.3 (c) and (g). The experimental findings show that as the separation distance increases, the electrical output of the TENG increases up to 1.2 cm spacing and decreases later. The TENG's V_{oc} is defined with the fundamental equation (i.e., $V_{oc} = rd/e$), where d , r , and e are interlayer spacing, vacuum permittivity and triboelectric charge density on the surface. In accordance with the TENG output equation, the output voltage increases with the spacing. However, the output voltage is decreased at a greater spacing in the present chapter, and similar behaviour is also observed in the literature [50,51]. The reason could be improper contact between the triboelectric layers at such high separation distances [50]. When the spacing is increased at a fixed applied force tapping, the triboelectric layers may not form full contact, as it requires more force at the larger spacing between the triboelectric layers.

To explore the fabricated TENG for force sensor application, the effect of different external applied force on the electrical performance of the TENG device have been studied and presented in Figure 4.3(d and h). From Figure 4.3(g and h), it's clear that TENG output is enhanced with applied force. The V_{oc} changed from ~0.5 V to 5 V. The enhanced output response of TENG with various applied forces is due to increased friction between the triboelectric layers which resulted in the enhanced contact area. A similar trend of TENG response with applied force is reported in the literature [52–54].

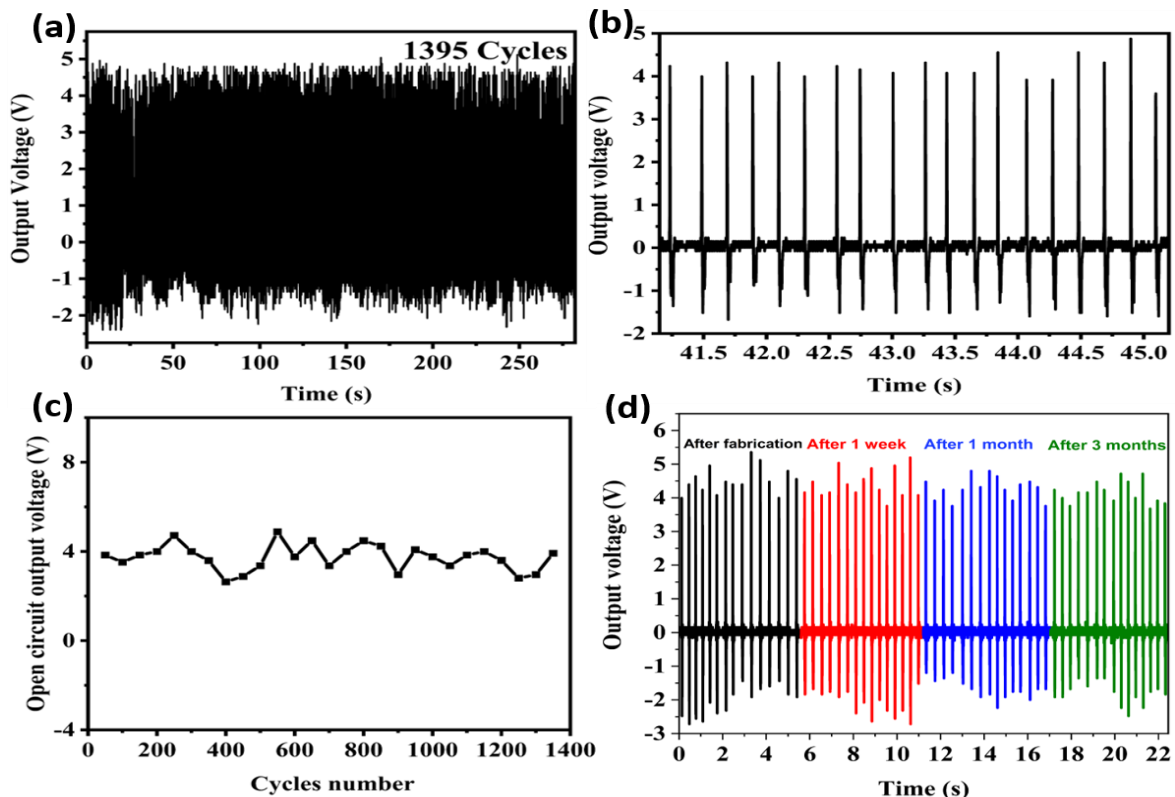


Figure 4.4. (a) TENG stability under 1395 cycles, (b) TENG response of some random cycles selected from the stability graph (c) every 50th cycle number output voltage values from the Figure (a). (d) stability of the TENG at different time points.

The stability and robustness of the TENG were studied to test the TENG for prolonging operation and practical applications. The TENG response was measured for 1395 external hand tapping force cycles, and the response is shown in Figure 4.4(a). In the case of stability analysis, took a gap of a few seconds for every 50–60 cycles TENG response for applying the stable force by hand. In addition, took a gap of a few seconds due to the oscilloscope display limitation. The TENG responses of such 50–60 cycles sets were merged to get the 1396 cycles, which is similar to the reported literature [49]. Figure 4.4(a) shows that the fabricated TENG is highly stable, and a slight deviation in the output voltage was due to the variation in the manual hand tapping force and frequency. Figure 4.4(b) shows the magnified view of some portion of the stability graph. Furthermore, the output voltage of the TENG was noted down for every 50th cycle (ex: 50, 100, 150 etc.) and plotted as shown in Figure 4.4(c). Figure 4.4(c) shows that an average output voltage value of $\sim 4 \pm 0.5$ V was observed. Further, an in-house developed tapping machine setup using a linear motor ([See SI Video V4.2](#)) and sewing machine tested the TENG stability over many cycles (~ 5000 cycles) and found it stable ([See, SI, Figure S4.3](#)) ([See SI Video V4.3](#)). Figure 4.4(d) represents the TENG response at different

times, for example, immediately after fabrication, one week, one month, and three months. The stable output response of the TENG was observed in all cases.

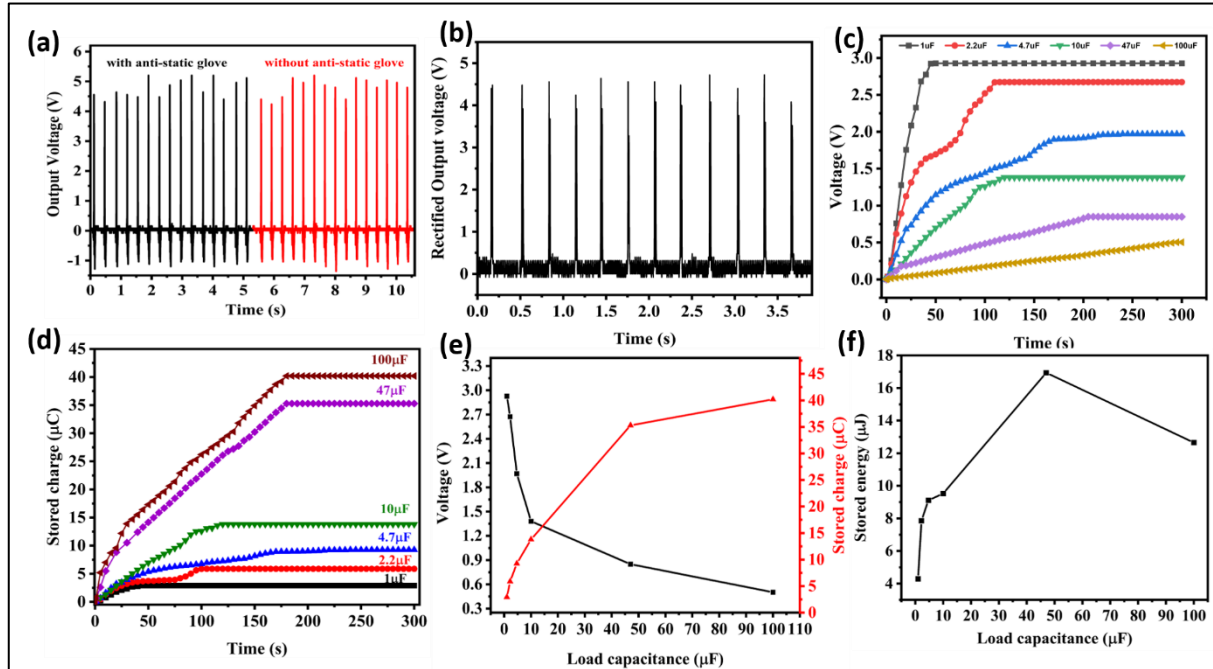


Figure 4.5. (a) response of the TENG against hand tapping with (black) and without (red) antistatic gloves, (b) TENG open-circuit voltage after rectification, (c) Different load capacitors charging curves as a function of time, (d) stored charge curves of different load capacitors as a function of time, (e) the charged voltage and stored charges as a function of load capacitance (C_L), (f) the stored energy as a function of C_L .

In addition, the TENG response was recorded with and without anti-static gloves and confirmed that the contribution of static charge by hand is not there in the TENG output as shown in the Figure 4.5(a). For practical applications, it is necessary to convert the TENG AC output into a DC output and store it in a capacitor or any energy storage element. The output voltage of the TENG device was rectified using a DB 107 IC rectifier to produce the DC voltage, and the DC output voltage graph is presented in Figure 4.5(b). Further, the charging characteristics of various capacitors and the stored voltage, charge, energy as a function of the load capacitor were investigated. Figure 4.5(c) shows the charging voltages on different load capacitors (C_L) of 1, 2.2, 4.7, 10, 47, and 100 μ F. The charging speed is greater for smaller C_L , and the time until the voltage is reached the saturation is shorter. The charge stored on these various capacitors was calculated by the product of the charged voltage (V) and capacitance C_L , as shown in Figure 4.5(d). It is evident from Figure 4.5(d) that an increment in the load capacitor value results in increased charge storage. The values of charged voltage and stored charge as a

function of various load capacitance values were plotted as shown in Figure 4.5(e). The behavior of charged voltage and stored charge with respect to the load capacitor is opposite. Figure 4.5(f) illustrates the variation of the maximum stored energy as a function of the C_L . The maximum stored energy of $16.9 \mu\text{J}$ was observed at the optimal C_L of $47 \mu\text{F}$. The behavior of TENG across different load capacitance values is similar to the reported literature [55,56].

4.4 Applications

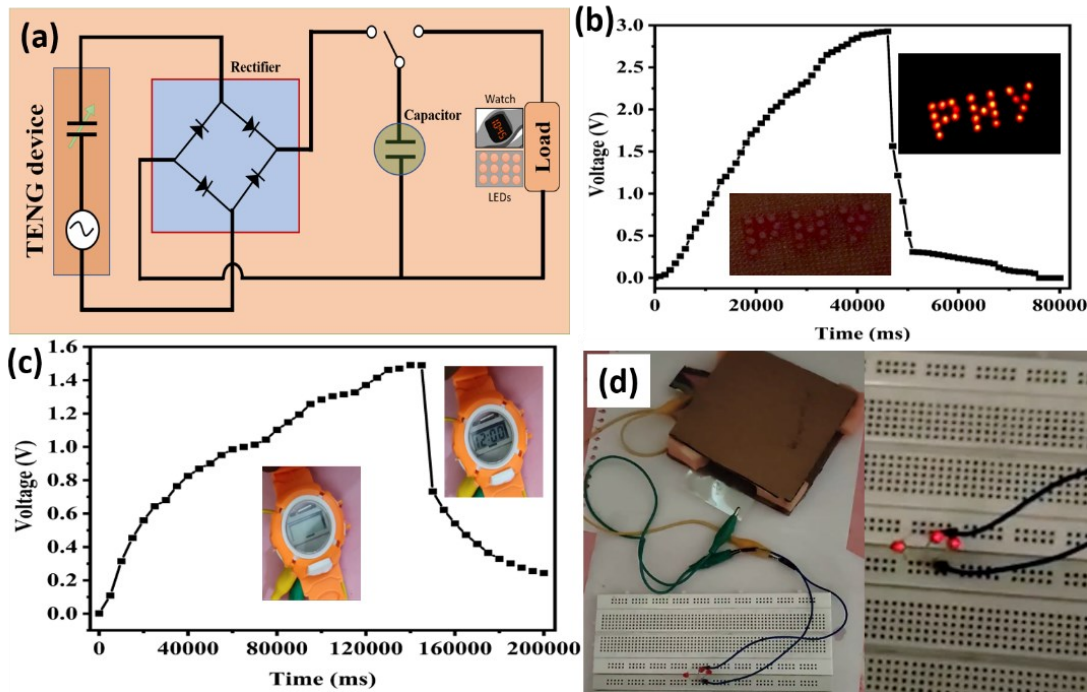


Figure 4.6. (a) Schematic connections for charging of capacitor using TENG and powering electronic devices, capacitor charging and discharging curves before and after power up the electronic devices (b) 24 red LEDs, (c) digital watch, (d) snapshot of the continuous switching on 3 LEDs under cyclic application of force.

Further, TENG was explored for powering digital watch, and 24 commercial LEDs with the help of 2.2 and $1 \mu\text{F}$ charged capacitors, respectively, as shown in Figure 4.6 (a). The charging and discharging curves of capacitors switching on digital watch and 24 LEDs are shown in Figure 4.6(b)-(c). The inset of Figure 4.6(b) and (c) shows photographs of the off and on status of the digital watch ([See SI, Video V4.4](#)). and LEDs ([See SI, Video V4.5](#)). Further, TENG can directly power up 3 LEDs continuously in response to hand tapping, as shown in Figure 4.6 (d) ([See SI, Video V4.6](#)).

4.5 Conclusions

In summary, triboelectric nanogenerator is fabricated with a new triboelectric pair and its characteristics were studied. For the first time, the ZnO nanosheets film and the PET surface were acted as a friction layer for the triboelectric nanogenerator. The fabricated TENG operated in vertical-contact separation mode and produced an open-circuit voltage, short circuit current and instantaneous power density of ~ 4.9 V, $10\ \mu\text{A}$ and $1\ \mu\text{W}/\text{cm}^2$, respectively. The TENG can directly drive 3 LEDs simultaneously, and with the help of an energy storage element, it can switch on a digital watch and 24 LEDs. In addition, TENG shows exceptional structural durability and stability of electrical output over a large number of cycles. The TENG in this work offers a simple design since no additional electrode deposition step is required and is cost-effective as ZnO nanosheets synthesis done by low-temperature hot plate assisted hydrothermal method. Furthermore, the TENG device fabrication can easily be scaled to large areas for higher performance. Therefore, fabricated TENG is a prospective candidate for self-powered sensors and devices.

4.6 References

- [1] C. Wu, A.C. Wang, W. Ding, H. Guo, Z.L. Wang, Triboelectric Nanogenerator: A Foundation of the Energy for the New Era, *Adv. Energy Mater.* 9 (2019) 1–25. <https://doi.org/10.1002/aenm.201802906>.
- [2] D.W. Kim, J.H. Lee, J.K. Kim, U. Jeong, Material aspects of triboelectric energy generation and sensors, *NPG Asia Mater.* 12 (2020) 6. <https://doi.org/10.1038/s41427-019-0176-0>.
- [3] P. Bai, G. Zhu, Z.H. Lin, Q. Jing, J. Chen, G. Zhang, J. Ma, Z.L. Wang, Integrated multilayered triboelectric nanogenerator for harvesting biomechanical energy from human motions, *ACS Nano.* 7 (2013) 3713–3719. <https://doi.org/10.1021/nn4007708>.
- [4] J. Zhong, Y. Zhang, Q. Zhong, Q. Hu, B. Hu, Z.L. Wang, J. Zhou, Fiber-based generator for wearable electronics and mobile medication, *ACS Nano.* 8 (2014) 6273–6280. <https://doi.org/10.1021/nn501732z>.
- [5] Z. Zhao, L. Zhou, S. Li, D. Liu, Y. Li, Y. Gao, Y. Liu, Y. Dai, J. Wang, Z.L. Wang, Selection rules of triboelectric materials for direct-current triboelectric nanogenerator, *Nat. Commun.* 12 (2021) 1–8. <https://doi.org/10.1038/s41467-021-25046-z>.
- [6] Z.L. Wang, Triboelectric nanogenerators as new energy technology and self-powered

- sensors - Principles, problems and perspectives, *Faraday Discuss.* 176 (2014) 447–458. <https://doi.org/10.1039/c4fd00159a>.
- [7] R. Hinchet, W. Seung, S.W. Kim, Recent Progress on Flexible Triboelectric Nanogenerators for SelfPowered Electronics, *ChemSusChem.* 8 (2015) 2327–2344. <https://doi.org/10.1002/cssc.201403481>.
- [8] F.-R. Fan, Z.-Q. Tian, Z. Lin Wang, Flexible triboelectric generator, *Nano Energy.* 1 (2012) 328–334. <https://doi.org/10.1016/j.nanoen.2012.01.004>.
- [9] B. Yang, W. Zeng, Z. Peng, S. Liu, K. Chen, X. Tao, A Fully Verified Theoretical Analysis of Contact-Mode Triboelectric Nanogenerators as a Wearable Power Source, *Adv. Energy Mater.* 6 (2016) 1–8. <https://doi.org/10.1002/aenm.201600505>.
- [10] H. Zhang, L. Quan, J. Chen, C. Xu, C. Zhang, S. Dong, C. Lü, J. Luo, A general optimization approach for contact-separation triboelectric nanogenerator, *Nano Energy.* 56 (2019) 700–707. <https://doi.org/10.1016/j.nanoen.2018.11.062>.
- [11] R. Zhang, H. Olin, Material choices for triboelectric nanogenerators: A critical review, *EcoMat.* 2 (2020) 1–13. <https://doi.org/10.1002/eom2.12062>.
- [12] H. Yang, F.R. Fan, Y. Xi, W. Wu, Design and engineering of high-performance triboelectric nanogenerator for ubiquitous unattended devices , *EcoMat.* 3 (2021) 1–36. <https://doi.org/10.1002/eom2.12093>.
- [13] Z.L. Wang, Zinc oxide nanostructures: growth, properties and applications, *J. Phys. Condens. Matter.* 16 (2004) R829–R858. <https://doi.org/10.1088/0953-8984/16/25/R01>.
- [14] D. Sakai, K. Nagashima, H. Yoshida, M. Kanai, Y. He, G. Zhang, X. Zhao, T. Takahashi, T. Yasui, T. Hosomi, Y. Uchida, S. Takeda, Y. Baba, T. Yanagida, Substantial Narrowing on the Width of “Concentration Window” of Hydrothermal ZnO Nanowires via Ammonia Addition, *Sci. Rep.* 9 (2019) 1–10. <https://doi.org/10.1038/s41598-019-50641-y>.
- [15] H. Qi, E.R. Glaser, J.D. Caldwell, S.M. Prokes, Growth of Vertically Aligned ZnO Nanowire Arrays Using Bilayered Metal Catalysts, *J. Nanomater.* 2012 (2012) 1–7. <https://doi.org/10.1155/2012/260687>.
- [16] K.H. Kim, B. Kumar, K.Y. Lee, H.K. Park, J.H. Lee, H.H. Lee, H. Jun, D. Lee, S.W.

- Kim, Piezoelectric two-dimensional nanosheets/anionic layer heterojunction for efficient direct current power generation, *Sci. Rep.* 3 (2013) 1–6.
<https://doi.org/10.1038/srep02017>.
- [17] Y.P. Jeon, J.H. Park, T.W. Kim, Highly-enhanced triboelectric nanogenerators based on zinc-oxide nanoripples acting as a triboelectric layer, *Appl. Surf. Sci.* 445 (2018) 50–55. <https://doi.org/10.1016/j.apsusc.2018.03.125>.
- [18] Y.P. Jeon, J.H. Park, T.W. Kim, Highly flexible triboelectric nanogenerators fabricated utilizing active layers with a ZnO nanostructure on polyethylene naphthalate substrates, *Appl. Surf. Sci.* 466 (2019) 210–214.
<https://doi.org/10.1016/j.apsusc.2018.09.249>.
- [19] D. Li, C. Wu, L. Ruan, J. Wang, Z. Qiu, K. Wang, Y. Liu, Y. Zhang, T. Guo, J. Lin, T.W. Kim, Electron-transfer mechanisms for confirmation of contact-electrification in ZnO/polyimide-based triboelectric nanogenerators, *Nano Energy.* 75 (2020) 104818.
<https://doi.org/10.1016/j.nanoen.2020.104818>.
- [20] Y.P. Jeon, C. Wu, K.H. Yoo, T.W. Kim, Enhancement of the output voltage for triboelectric nanogenerators due to Al doping in the zinc oxide layer, *J. Alloys Compd.* 831 (2020) 154913. <https://doi.org/10.1016/j.jallcom.2020.154913>.
- [21] S.N. Chen, C.H. Chen, Z.H. Lin, Y.H. Tsao, C.P. Liu, On enhancing capability of tribocharge transfer of ZnO nanorod arrays by Sb doping for anomalous output performance improvement of triboelectric nanogenerators, *Nano Energy.* 45 (2018) 311–318. <https://doi.org/10.1016/j.nanoen.2018.01.013>.
- [22] W. Deng, B. Zhang, L. Jin, Y. Chen, W. Chu, H. Zhang, M. Zhu, W. Yang, Enhanced performance of ZnO microballoon arrays for a triboelectric nanogenerator, *Nanotechnology.* 28 (2017) 135401. <https://doi.org/10.1088/1361-6528/aa5f34>.
- [23] Y.H. Ko, G. Nagaraju, S.H. Lee, J.S. Yu, PDMS-based triboelectric and transparent nanogenerators with ZnO nanorod arrays, *ACS Appl. Mater. Interfaces.* 6 (2014) 6631–6637. <https://doi.org/10.1021/am5018072>.
- [24] X. Yue, Y. Xi, C. Hu, X. He, S. Dai, L. Cheng, G. Wang, Enhanced output-power of nanogenerator by modifying PDMS film with lateral ZnO nanotubes and Ag nanowires, *RSC Adv.* 5 (2015) 32566–32571. <https://doi.org/10.1039/c5ra02098k>.

- [25] A. Dos Santos, F. Sabino, A. Rovisco, P. Barquinha, H. Águas, E. Fortunato, R. Martins, R. Igreja, Optimization of zno nanorods concentration in a micro-structured polymeric composite for nanogenerators, *Chemosensors*. 9 (2021) 1–13. <https://doi.org/10.3390/chemosensors9020027>.
- [26] A.K. Gupta, C. Hsu, S.-N. Lai, C. Lai, ZnO-Polystyrene Composite as Efficient Energy Harvest for Self-Powered Triboelectric Nanogenerator, *ECS J. Solid State Sci. Technol.* 9 (2020) 115019. <https://doi.org/10.1149/2162-8777/aba7fa>.
- [27] N. Bi, L. Zhang, Q. Zheng, F. Zhuge, J. Li, X.P.A. Gao, J. Du, Control of ZnO nanowire growth and optical properties in a vapor deposition process, *J. Mater. Sci. Technol.* 33 (2017) 850–855. <https://doi.org/10.1016/j.jmst.2017.03.024>.
- [28] V. Gaddam, R.R. Kumar, M. Parmar, G.R.K. Yaddanapudi, M.M. Nayak, K. Rajanna, Morphology controlled synthesis of Al doped ZnO nanosheets on Al alloy substrate by low-temperature solution growth method, *RSC Adv.* 5 (2015) 13519–13524. <https://doi.org/10.1039/c4ra14049d>.
- [29] Y.A. Stetsiv, M.M. Yatsyshyn, D. Nykypanchuk, S.A. Korniy, I. Saldan, O. V. Reshetnyak, T.J. Bednarchuk, Characterization of polyaniline thin films prepared on polyethylene terephthalate substrate, *Polym. Bull.* 78 (2021) 6251–6265. <https://doi.org/10.1007/s00289-020-03426-7>.
- [30] C. Guillén, J. Herrero, Comparison study of ITO thin films deposited by sputtering at room temperature onto polymer and glass substrates, *Thin Solid Films*. 480–481 (2005) 129–132. <https://doi.org/10.1016/j.tsf.2004.11.040>.
- [31] S. Paria, R. Bera, S.K. Karan, A. Maitra, A.K. Das, S.K. Si, L. Halder, A. Bera, B.B. Khatua, Insight into Cigarette Wrapper and Electroactive Polymer Based Efficient TENG as Biomechanical Energy Harvester for Smart Electronic Applications, *ACS Appl. Energy Mater.* 1 (2018) 4963–4975. <https://doi.org/10.1021/acsaem.8b00951>.
- [32] A. Ahmed, Design, Modelling and Analysis of Triboelectric Nanogenerators, (2018). <https://hdl.handle.net/1807/93154>.
- [33] M.L. Seol, J.H. Woo, D. Il Lee, H. Im, J. Hur, Y.K. Choi, Nature-replicated nano-in-micro structures for triboelectric energy harvesting, *Small*. 10 (2014) 3887–3894. <https://doi.org/10.1002/smll.201400863>.

- [34] J. Chen, G. Zhu, W. Yang, Q. Jing, P. Bai, Y. Yang, T.C. Hou, Z.L. Wang, Harmonic-resonator-based triboelectric nanogenerator as a sustainable power source and a self-powered active vibration sensor, *Adv. Mater.* 25 (2013) 6094–6099. <https://doi.org/10.1002/adma.201302397>.
- [35] J. Qian, X. Wu, D.S. Kim, D.W. Lee, Seesaw-structured triboelectric nanogenerator for scavenging electrical energy from rotational motion of mechanical systems, *Sensors Actuators, A Phys.* 263 (2017) 600–609. <https://doi.org/10.1016/j.sna.2017.07.021>.
- [36] I. Kim, H. Roh, J. Yu, H. Jeon, D. Kim, A triboelectric nanogenerator using silica-based powder for appropriate technology, *Sensors Actuators, A Phys.* 280 (2018) 85–91. <https://doi.org/10.1016/j.sna.2018.07.013>.
- [37] X. Fan, J. Chen, J. Yang, P. Bai, Z. Li, Z.L. Wang, Ultrathin, rollable, paper-based triboelectric nanogenerator for acoustic energy harvesting and self-powered sound recording, *ACS Nano.* 9 (2015) 4236–4243. <https://doi.org/10.1021/acsnano.5b00618>.
- [38] S. Niu, Z.L. Wang, Theoretical systems of triboelectric nanogenerators, *Nano Energy.* 14 (2014) 161–192. <https://doi.org/10.1016/j.nanoen.2014.11.034>.
- [39] C. Fang, T. Tong, T. Bu, Y. Cao, S. Xu, Y. Qi, C. Zhang, Overview of Power Management for Triboelectric Nanogenerators, *Adv. Intell. Syst.* 2 (2020) 1900129. <https://doi.org/10.1002/aisy.201900129>.
- [40] S. Niu, Y.S. Zhou, S. Wang, Y. Liu, L. Lin, Y. Bando, Z.L. Wang, Simulation method for optimizing the performance of an integrated triboelectric nanogenerator energy harvesting system, *Nano Energy.* 8 (2014) 150–156. <https://doi.org/10.1016/j.nanoen.2014.05.018>.
- [41] J. Bird, *Electrical Circuit Theory and Technology*, 5th ed, Routledge, 2014. <https://doi.org/10.4324/9781315883342>.
- [42] H. Zhang, L. Quan, Theoretical Prediction and Optimization Approach to Triboelectric Nanogenerator, in: *Electrost. Disch. - From Electr. Break. Micro-Gaps to Nano-Generators*, IntechOpen, 2019. <https://doi.org/10.5772/intechopen.86992>.
- [43] K. Xia, Z. Zhu, H. Zhang, Z. Xu, A triboelectric nanogenerator as self-powered temperature sensor based on PVDF and PTFE, *Appl. Phys. A Mater. Sci. Process.* 124

- (2018) 1–7. <https://doi.org/10.1007/s00339-018-1942-5>.
- [44] J. Peng, S.D. Kang, G.J. Snyder, Optimization principles and the figure of merit for triboelectric generators, *Sci. Adv.* 3 (2017) 1–7.
<https://doi.org/10.1126/sciadv.aap8576>.
- [45] F.R. Fan, Z.Q. Tian, Z. Lin Wang, Flexible triboelectric generator, *Nano Energy*. 1 (2012) 328–334. <https://doi.org/10.1016/j.nanoen.2012.01.004>.
- [46] X.S. Zhang, M. Di Han, R.X. Wang, F.Y. Zhu, Z.H. Li, W. Wang, H.X. Zhang, Frequency-multiplication high-output triboelectric nanogenerator for sustainably powering biomedical microsystems, *Nano Lett.* 13 (2013) 1168–1172.
<https://doi.org/10.1021/nl3045684>.
- [47] C. Xue, J. Li, Q. Zhang, Z. Zhang, Z. Hai, L. Gao, R. Feng, J. Tang, J. Liu, W. Zhang, D. Sun, A novel arch-shape nanogenerator based on piezoelectric and triboelectric mechanism for mechanical energy harvesting, *Nanomaterials*. 5 (2014) 36–46.
<https://doi.org/10.3390/nano5010036>.
- [48] Q. Wang, M. Chen, W. Li, Z. Li, Y. Chen, Y. Zhai, Size effect on the output of a miniaturized triboelectric nanogenerator based on superimposed electrode layers, *Nano Energy*. 41 (2017) 128–138. <https://doi.org/10.1016/j.nanoen.2017.09.030>.
- [49] T. Kamilya, P.K. Sarkar, S. Acharya, Unveiling Peritoneum Membrane for a Robust Triboelectric Nanogenerator, *ACS Omega*. 4 (2019) 17684–17690.
<https://doi.org/10.1021/acsomega.9b01963>.
- [50] T.C. Hou, Y. Yang, H. Zhang, J. Chen, L.J. Chen, Z. Lin Wang, Triboelectric nanogenerator built inside shoe insole for harvesting walking energy, *Nano Energy*. 2 (2013) 856–862. <https://doi.org/10.1016/j.nanoen.2013.03.001>.
- [51] P. Ravi Sankar, P. Supraja, S. Mishra, K. Prakash, R. Rakesh Kumar, D. Haranath, A novel triboelectric nanogenerator based on only food packaging aluminium foils, *Mater. Lett.* 310 (2022) 131474. <https://doi.org/10.1016/j.matlet.2021.131474>.
- [52] S. Zhao, A Triboelectric Nanogenerator Based on MgSiO₃ Powder for a Human Motion Counter, *J. Electron. Mater.* 50 (2021) 6836–6843.
<https://doi.org/10.1007/s11664-021-09245-4>.
- [53] V. Vivekananthan, A. Chandrasekhar, N.R. Alluri, Y. Purusothaman, S.J. Kim, A

highly reliable, impervious and sustainable triboelectric nanogenerator as a zero-power consuming active pressure sensor, *Nanoscale Adv.* 2 (2020) 746–754.
<https://doi.org/10.1039/c9na00790c>.

- [54] B. Dudem, R.D.I.G. Dharmasena, R. Riaz, V. Vivekananthan, K.G.U. Wijayantha, P. Lugli, L. Petti, S.R.P. Silva, Wearable Triboelectric Nanogenerator from Waste Materials for Autonomous Information Transmission via Morse Code, *ACS Appl. Mater. Interfaces.* 14 (2022) 5328–5337. <https://doi.org/10.1021/acsami.1c20984>.
- [55] Y. Yao, T. Jiang, L. Zhang, X. Chen, Z. Gao, Z.L. Wang, Charging System Optimization of Triboelectric Nanogenerator for Water Wave Energy Harvesting and Storage, *ACS Appl. Mater. Interfaces.* 8 (2016) 21398–21406.
<https://doi.org/10.1021/acsami.6b07697>.
- [56] S. Niu, Y. Liu, Y.S. Zhou, S. Wang, L. Lin, Z.L. Wang, Optimization of triboelectric nanogenerator charging systems for efficient energy harvesting and storage, *IEEE Trans. Electron Devices.* 62 (2015) 641–647.
<https://doi.org/10.1109/TED.2014.2377728>.

4.7 Supporting Information

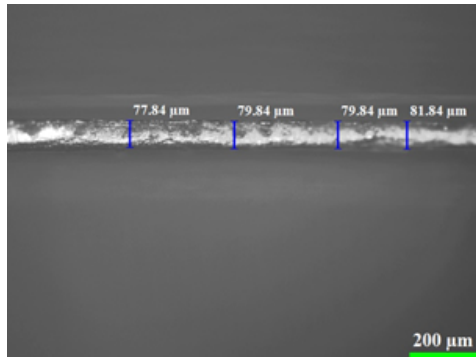


Figure S4.1. Cross-sectional view of the aluminum substrate in the Optical microscope for the thickness measurement.

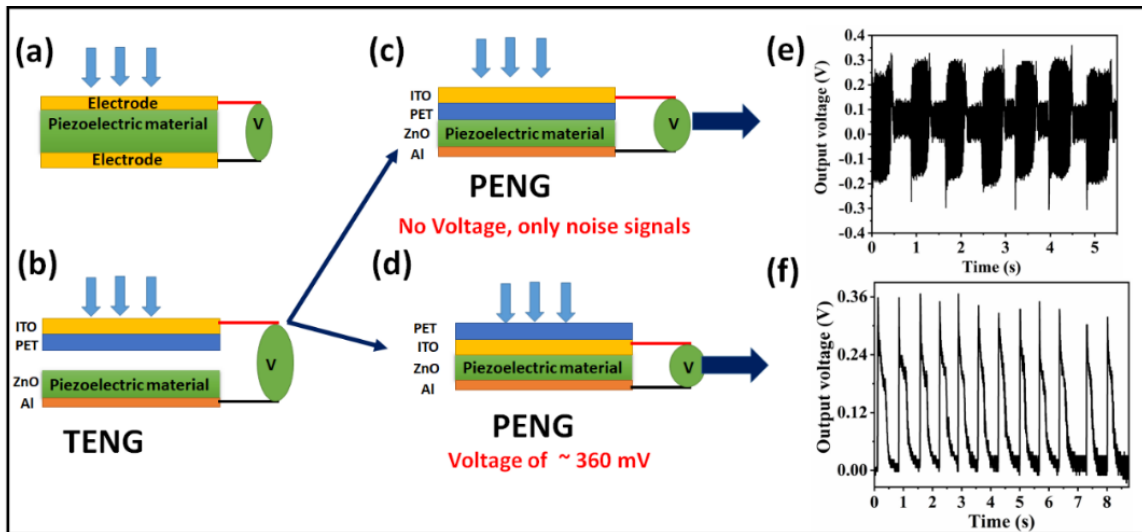


Figure S4.2. (a) Schematic of general piezoelectric nanogenerator device, (b) present TENG design, (c) TENG converted to piezo-geometry with PET surface above the ZnO nanosheets, (d) TENG converted to piezo-geometry with ITO surface above the ZnO nanosheets, (e) open circuit piezo voltage of the fabricated PENG (Figure 3(c)) against hand tapping, (f) open circuit piezo voltage of the fabricated PENG (Figure 3(d)) against hand tapping.

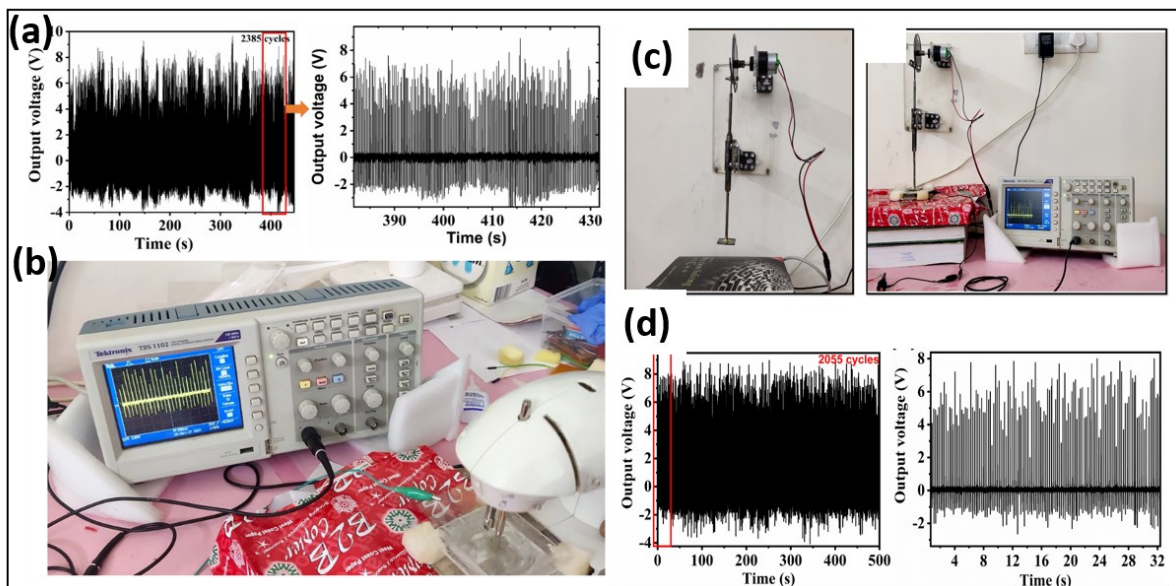
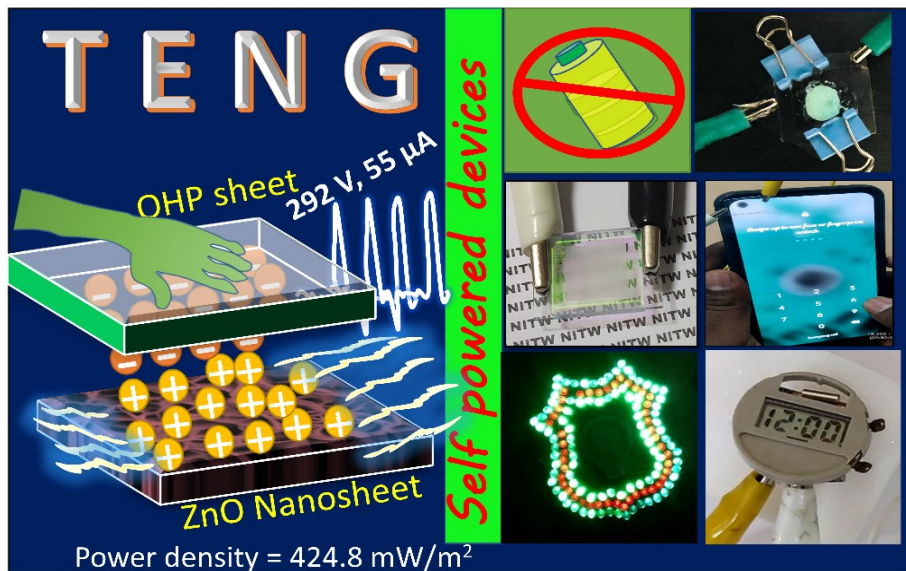


Figure S4.3. (a) Stability response of TENG with Sewing machine tapping and magnified view of few cycles from the stability graph, (b) photograph of TENG response during the stability testing, (c) Developed tapping test set up and photograph of the TENG response during the measurement, (d) response of TENG for 2055 cycles and magnified view of few cycles from the stability graph.

Chapter 5

High-Performance and Low-Cost Overhead Projector Sheet-Based Triboelectric Nanogenerator for Self-Powered Cholesteric Liquid Crystal, Electroluminescence, and Portable Electronic Devices

This chapter delves into the inventive use of (Overhead projector) OHP sheets as a distinctive triboelectric layer, capitalizing on their transparent PET composition and inherent pre-charged properties. This unique feature enhances their efficiency in receiving ink particles, significantly reducing the surface ion injection step. The charged nature of one side of the OHP sheet is responsible for improving the TENG's output performance. The TENG device is fabricated with ZnO nanosheets and OHP sheets as frictional layers. A detailed electrical characterization of the TENG device is conducted. Further, demonstrated self-powered cholesteric liquid crystal (CLC), electroluminescence and portable electronic devices.



Publications:

- ❖ “High-Performance and Low-Cost Overhead Projector Sheet-Based Triboelectric Nanogenerator for Self-Powered Cholesteric Liquid Crystal, Electroluminescence, and Portable Electronic Devices”. *Supraja Potu, Navaneeth M, Rakesh Kumar R, Buchaiah G, Jayalakshmi V, Siju Mishra, Haranath D, Anjaly Babu, Uday Kumar K, and Prakash K, ACS Applied Energy Materials.* 2022. <https://doi.org/10.1021/acsaem.2c02359>.

5.1 Introduction

In recent years, triboelectric nanogenerators (TENG) have gained intense attention owing to their diverse applications in energy harvesting [1] self-powered sensors [2], self-powered medical devices [3], self-powered health monitoring [3], electrochromic devices [4], electroluminescent devices [5], optical modulation [6], electromechanical systems [7], and e-paper [8]. TENGs convert a variety of mechanical energies in our daily life into electricity by utilizing the combined effect of contact electrification and the electrostatic induction phenomenon. Until the discovery of TENG in 2012, contact electrification was treated as an undesirable effect [9]. After that, the field of TENGs is rapidly progressed due to their high output voltages, high energy conversion efficiency, broad material availability, low cost, easy device fabrication, high flexibility, and environmental friendliness [10]. However, there are significant challenges encountered by TENGs; (1) low output power, (2) applications of TENGs in limited fields due to low output power, and (3) no product commercialization due to the use of complex TENG designs. Specific strategies have been proposed in the literature to overcome the above challenges and enhance the TENG's output power. These strategies were proposed based on the governing equations of TENG's output voltage, current, and charge [11–13].

The first strategy attempts to increase the surface charge density as it is directly related to the current, voltage, output energy, and power of TENGs. The surface charge density can be increased by selecting new materials which have high surface charge density from the triboelectric series [14] or any materials (e.g.: oxides, nitrides) from the periodic table and polymers [15–17]. In addition, surface modification, which includes physical modification [18,19], chemical surface functionalization [20–23], and surface ion injection [24–26] is also considered for the surface charge density increment. Furthermore, the performance of TENGs output can also be improved by filling some special fillers into the triboelectric layers [27–29]. The optimization of particulate fillers can effectively improve the charge trapping ability and improve TENG's output. In other strategies, increasing the effective contact area between the frictional layers enhances the TENG charge output. Increasing the effective contact area includes the use of liquid/gel electrodes and soft structures [30].

In this work, the pre-charged triboelectric layer was used for a high-performance triboelectric nanogenerator with cost-effective materials and explored applications of TENG in new fields. This study introduced a new triboelectric pair of over-head projector (OHP) sheets

A simple and low-cost TENG.... And its application in CLC, EL, and portable electronics

and ZnO nanosheet arrays on aluminium foil to fabricate the TENG device. The OHP sheet is a transparent material made up of PET and it has a pre-charge on one side to receive the ink particles. The existence of charge on the OHP sheets greatly enhances the TENG performance and also reduces the surface ion injection step [24]. The cost of OHP sheets is very low compared to the other triboelectric layers such as PTFE, PVDF, silicone, and FEP. A simple test has been performed to confirm the charged nature of the OHP (PET) sheets in contrast to normal PET sheets. In the test, small paper pieces were placed on a table, and the OHP sheet and PET sheet were placed close to the paper pieces. The OHP attracted paper pieces, whereas the PET sheet did not attract any paper pieces, as shown in **SI Figure S5.1 (a-b)**. Further, both sides of the OHP sheet were tested to confirm the presence of a charge on them. It was clear from the test that one side of the OHP is strongly attracting a large number of paper pieces, whereas another side does not attract many, as shown in **SI Figure S5.1(c-d)**. Therefore, high output voltage and current from only one side of the OHP sheet can be expected. Table 5.1 shows the existing ZnO-based TENGs with different triboelectric layers, their output performance, and applications. The ZnO-OHP-based TENG and its application in self-powered cholesteric liquid crystal (CLC) and electroluminescence devices have not been reported in the literature so far. The present investigation is the first of its kind, and it opens up new possibilities with the ZnO-based TENG. The self-powered liquid crystal displays and electroluminescence devices have received limited attention in the literature due to the high power required to turn on these devices. In the present work, the optical responses of electroluminescent and CLC devices in various applications using AC voltage produced by the fabricated TENG devices were studied.

Recently, the research group of Wang et al. reported TENG-driven cholesteric liquid crystal devices and their application in information security, smart windows, optical switches, e-paper displays, and wireless sensors [31–34]. To the best of the author's knowledge, these are the only four reports available in the literature on TENG-driven cholesteric liquid crystals. The present chapter also reports a similar application using TENG-driven cholesteric liquid crystal devices but with additional advantages. The advantages include the simple design of TENG without any additional modifications to the conventional design process such as patterning of triboelectric layers. The aluminium foil, ZnO, OHP sheets, cardboards, and sponge spacers involved in the TENG fabrications make it a cost-effective design. The vertical contact separation mode is selected among the four working modes due to its high output power density

A simple and low-cost TENG.... And its application in CLC, EL, and portable electronics

compared to the other working modes and less physical damage to the triboelectric layers than the lateral sliding and free-standing mode [35,36].

This chapter studied a high-performance TENG using ZnO nanosheet film and OHP sheet as frictional layers. The fabricated TENG has been characterized by its output current, voltage, power, and stability. The TENG performance has been studied with different device sizes, under the different frequencies of applied force and magnitudes of applied force. In addition, TENG has been explored for self-powered device applications.

Table 5.1. List of pairing materials that formed TENG with ZnO nanostructure films and their output voltage, and power/power density, and explored applications.

Sl.No	ZnO Triboelectric layer	Pairing Triboelectric layer	Output Performance (V_{oc} , I_{sc} , P)	Demonstrated Applications	Ref
1	PVDF+ ZnO Nanowires	Nylon+ ZnO	330 V, 10 μ A, 150nc 3 W/m ²	168 series LEDs directly, power up thermometer with a charged capacitor	[37]
2	PDMS+ Ag+ZnO Nanotubes	Aluminum	1.1 mWcm ⁻² , 10 μ Acm ⁻²	Switched on 99 LEDs	[38]
⁴²	Al doped ZnO+Graphene oxide	Polyimide	105V, 2.85 μ Acm ⁻² , 5.61nccm ⁻² , 2.5 W/m ²	Switched on 60 series-connected LEDs	[39]
4	ZnO nanorods	PDMS	5.34 V, 181.4 nA	No application	[40]
5	Chitosan+ ZnO	PDMS	24.5 nW, 0.9 V	Acetone sensing	[41]
6	ZnO nanorods+ Polystyrene	Kapton	7 V, 0.99 nA,230 μ Wcm ⁻²	No application	[42]
7	ZnO nanosheets	PET	4.9V, 10 μ A, 1 μ Wcm ⁻²	power up watch, 24 LEDs with a charged capacitor	[43]
8	Bacterial Cellulose + ZnO	Teflon	57.6V, 5.78 μ A, 42mWm ⁻²	No Applications	[44]
9	ZnO nanoparticles	Kapton	57V, 1.21 μ A ,1.34nc 2.8 1 μ Wcm ⁻²	power up watch, calculator with a charged capacitor	[45]
⁴⁹	ZnO nanosheets	ITO	~2V,~6 μ A, 4.15 μ W	No applications	[46]
⁵⁰	ZnO+ PVDF	PTFE	24.5 μ Wcm ⁻² , 78V, 0.46 μ Acm ⁻²	No applications	[47]
12	ZnO nanostrctures	Polymide	31.6 V, 5.43 μ A	No applications	[48]

13	ZnO nanoripples	Polymide	~80 V, 0.8 μ A 1.13W/m ²	No applications	[49]
14	Sb-doped ZnO	PDMS	12 V, 20 nAcm ⁻²	No applications	[50]
15	PDMS+ ZnO	PTFE	64.2V, 6.1 mAm-2, 1105 mWm-2	Switched on 30 LEDs	[51]
16	ZnO+PDMS	ITO/PET	6V, 4.8 μ Wcm ⁻²	power up thermometer with a charged capacitor	[52]
17	ZnO Nanosheets	Overhead Projector (OHP) sheet	~424.8 mWm⁻² ~292V, ~55 μA	Self-powered CLC, EL, portable electronic devices	Present Work

5.2 Experimental section

5.2.1 Materials

Zinc nitrate hexahydrate ($Zn(NO_3)_2 \cdot 6H_2O$), hexamethylenetetramine (HMTA), ITO/PET, aluminum foils, Overhead projector (OHP) sheets/slides (thickness~100 μ m) (**SI, S2**) and the nematic liquid crystal E7($n_e = 1.741$, $n_o = 1.517$ at 589 nm; $T_{NI} = 59$ °C), right-handed chiral dopant R5011(HCCH, helical twisting power $HTP = 107$ μ m⁻¹) were utilized in the present chapter.

5.2.2 ZnO nanosheets synthesis

The ZnO nanosheets film was synthesized on Al substrates by following the same method mentioned in Section-2.1.

5.2.3 Triboelectric nanogenerator device fabrication

The TENG device have been fabricated using the same steps, it implies a standardized manufacturing process as mentioned in Section-2.3.2. In the TENG, ZnO nanosheets array and OHP sheet (charged side) were used as frictional layers, and ITO, aluminum substrates were used as conductive electrodes. OHP sheet was attached to the conducting side of ITO with charged side facing up. Two electrical connections were made from the bottom aluminum and top ITO electrode to record the TENG response. The fabricated TENG was tested periodically under vertical contact separation mode by applying hand slap force of ~6.12 N (Chapter-2, Section 2.4.6), frequency of 3-5 Hz and 0.8 cm of spacing (Figure 5.1(a)). The hand slapping force was calculated approximately using the reported procedure in the literature [19,53].

5.2.4 Preparation of different color CLC devices and testing with TENG

A simple and low-cost TENG.... And its application in CLC, EL, and portable electronics

The nematic LC material (E7) was mixed with the chiral dopant R5011 to obtain mixtures with different concentrations of the dopant in dichloromethane as a solvent. Chiral dopant concentrations of 2.1, 2.6, and 3.2 wt% were used, allowing the CLC cells to reflect red (R), green (G), and blue (B) regions, respectively. In order to obtain homogeneous mixtures, these mixtures were stirred on a magnetic stirrer at a temperature of 80 °C (above the isotropic temperature) for 8 hours. The mixtures were filled into the as-purchased LC cells by capillary action in the isotropic phase above a clearing point of E7 (~ 59 °C). The LC cell comprises two ITO-coated glass substrates treated with a polyimide layer and rubbed in antiparallel directions. The gap between two substrates is 5 μm with an active electrode area of 0.6 × 0.6 cm². The schematic of the fabrication process and photographs of the fabricated CLC devices are shown in Figure 5.1(b)-(c). Initially, CLC cells were placed on a black background. They exhibited the reflection colors of red, green, and blue with the wavelengths 630 nm, 532 nm, and 465 nm corresponding to the added chiral dopant concentrations, as shown in Figure 5.1(c).

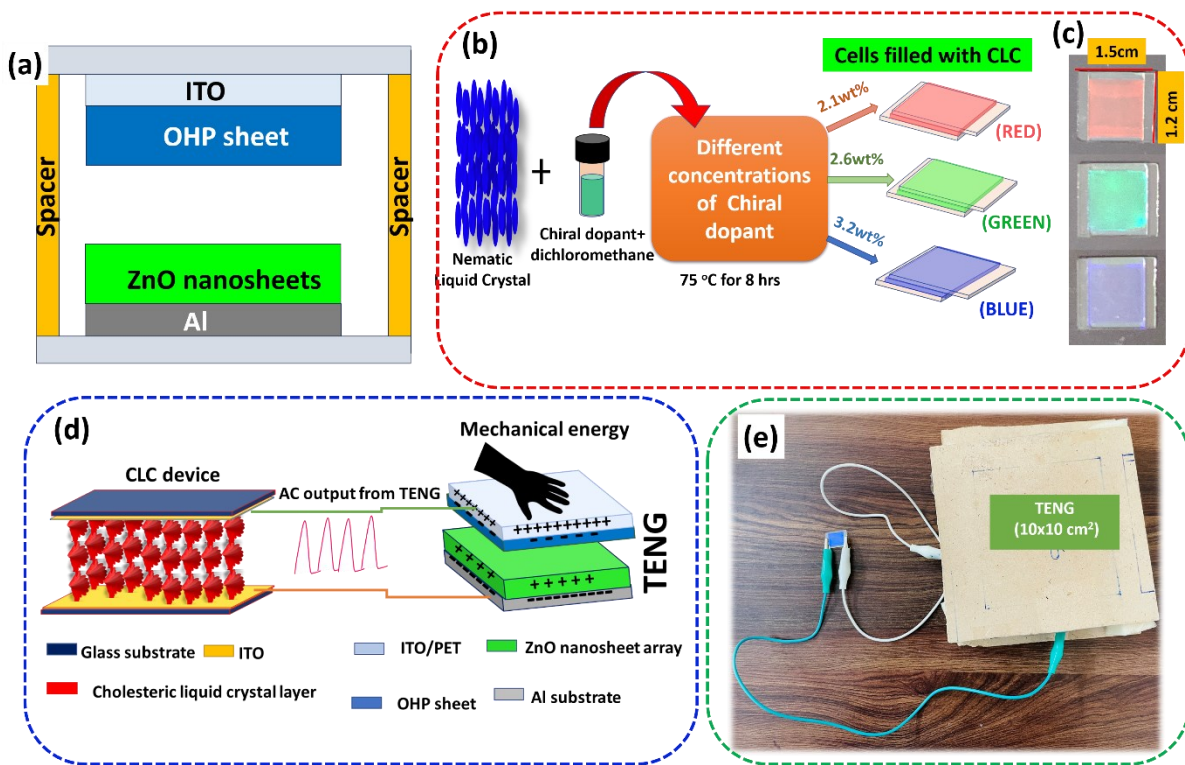


Figure 5.1. (a) Schematic of TENG device, (b) schematic view of the fabrication of the different colored CLC devices, (c) photographs of the original CLC devices on a black background, (d) schematic view of the TENG integrated CLC device, (e) Photograph of actual CLC device integrated in TENG.

A simple and low-cost TENG.... And its application in CLC, EL, and portable electronics

The schematic of the TENG connected to the CLC device is shown in Figure 5.1(d). The AC output of the TENG device is used for the molecular reorientation in the CLC device to change its optical properties. The AC signal generated by the TENG device upon the application of mechanical force is given as an input to the CLC device to transform its state. Depending on the magnitude of the AC signal, the CLC device may transform to more than one state. The photograph of the TENG ($10 \times 10 \text{ cm}^2$) device integrated with the CLC is shown in Figure 5.1(e).

5.3 Results and discussion

5.3.1 SEM, EDAX, and AFM analysis

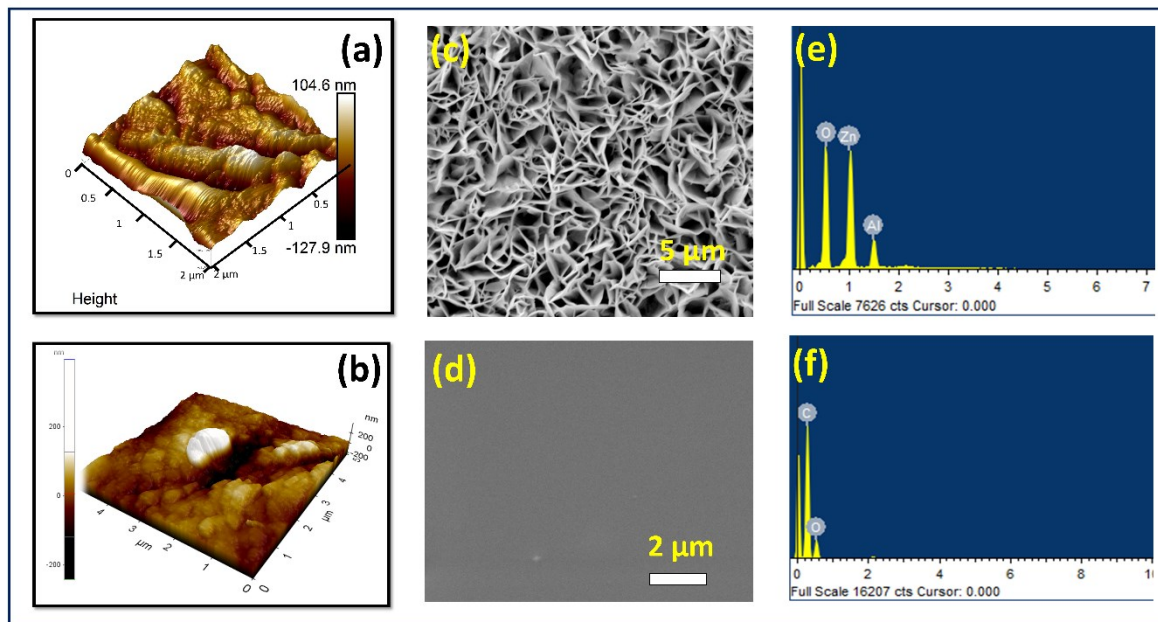


Figure 5.2. Topographical images of the (a) ZnO nanosheet film, (b) OHP sheet, and morphological images of the (c) ZnO nanosheet film, (d) OHP sheet, and EDX spectrum of the (e) ZnO nanosheet film and, (f) OHP sheet.

Figure 5.2 (a) and (b) show the AFM images of the ZnO nanosheet film and the OHP sheet surfaces, respectively. The surface of the ZnO film has greater roughness than the OHP sheet due to the presence of the ZnO nanosheets. This rough surface of ZnO film forms a more effective contact area to get the high output power to the TENG. In addition, the surface of frictional layers with SEM was carried out, and the corresponding images were analyzed and shown in Figure 5.2 (c-d). The SEM images corroborate the AFM results of the low and high roughness of the OHP sheet and the ZnO nanosheet film. EDX spectra recorded from ZnO

nanosheet film and OHP sheet are shown in Figures 5.2 (e) and (f). The EDX spectrum confirms the existence of Zn, O, Al in the case of ZnO nanosheets on aluminium foil and C, O in the OHP sheet.

5.3.2 XRD, FTIR, PL, and TEM analysis

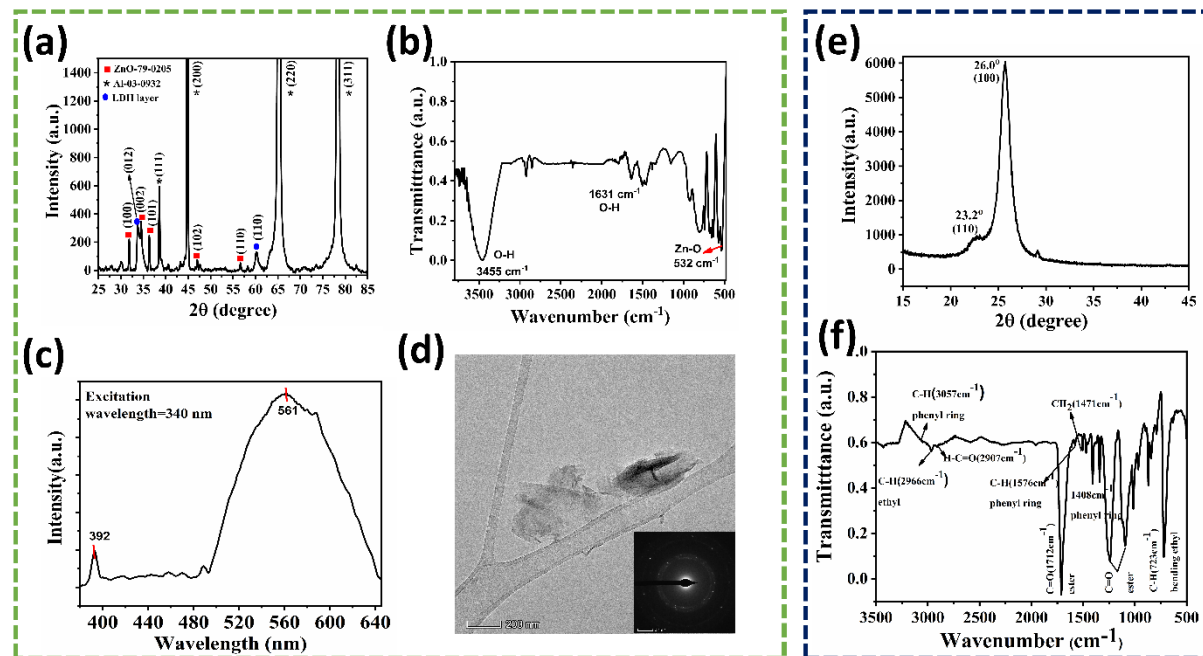


Figure 5.3. ZnO nanosheet film (a) XRD pattern, (b) FT-IR spectrum, (c) PL spectrum of ZnO nanosheet powder, (d) TEM image of the ZnO nanosheet (inset SAED pattern), OHP sheet (e) XRD pattern, (f) FT-IR spectrum.

Figure 5.3 (a) shows the XRD pattern of the ZnO nanosheets film and OHP sheet. ZnO film displayed typical diffraction peaks at $2\theta = 31.8, 34.49, 36.33, 47.04$, and 56.67° , which were ascribed to (100), (002), (101), (102), and (110) planes of the ZnO crystal structure, respectively. All the peaks were well matched with the standard data of the hexagonal phase of zinc oxide (JCPDF card no. 79-0205). The diffraction peaks at $2\theta = 38.55, 44.84, 65.19, 78.29^\circ$, which corresponds to (111), (200), (220), and (311) planes of the aluminum, respectively, and matched with JCPDF card no.03-0932. The additional peaks 33.74 and 60.13° corresponds to (012) and (110) of the ZnO: Al/LDH layer, respectively. Figure 5.3 (b) shows FTIR spectra of ZnO nanosheets, the absorption ranging from 450 to 550 cm^{-1} is due to the stretching vibration of ZnO. The broad bands were seen at 3455 cm^{-1} and 1631 cm^{-1} , corresponding to the hydroxyl groups of stretching and bending vibrations, respectively.

The room-temperature PL spectra of ZnO nanosheets powder was measured using excitation of the 340 nm shown in Figure 5.3 (c). The observed broad emission is considered as having been caused by electron transitions from the shallow donor levels of oxygen vacancies and zinc interstitials to the valence band [54] UV emission (392 nm) is the near band edge emission of ZnO's wide band gap. Figure 5.3 (d) shows the individual ZnO nanosheets TEM images and inset SAED pattern confirmed the polycrystalline nature of the ZnO nanosheets.

Figure 5.3(e) and (f) shows the XRD and FTIR spectra of OHP(PET) sheet. The diffraction peaks observed at $2\theta = 23.2$ and 26.0° corresponds to the (110) and (100) planes of PET crystalline structure [55]. The monomer of PET film consists of four functional groups: two ester groups, one aromatic ring and one ethyl group. These functional groups consist of many bonds which are as follows: C–C, C–H, C–O, C= O, and aromatic ring. The identified vibrational groups are summarized in the Table 5.2. The bands are in good agreement with the previous literature reports [56].

Table 5.2: Functional groups and their absorption bands observed for PET sheet.

Absorption bands (cm⁻¹)	Bands
1094 and 1240	C–O stretching bond
1712	stretching vibration of the C=O bond of the ester group.
2966	C–H stretching bond of ethyl group
723	C–H bending bond of ethyl group
3057	C–H stretching band of the aromatic ring
1576	C–H bond stretching vibration of the phenyl ring.
1408	C–C phenyl ring stretching band
1471	CH ₂ bending bond of ethylene glycol

5.3.3 Triboelectric nanogenerator device studies

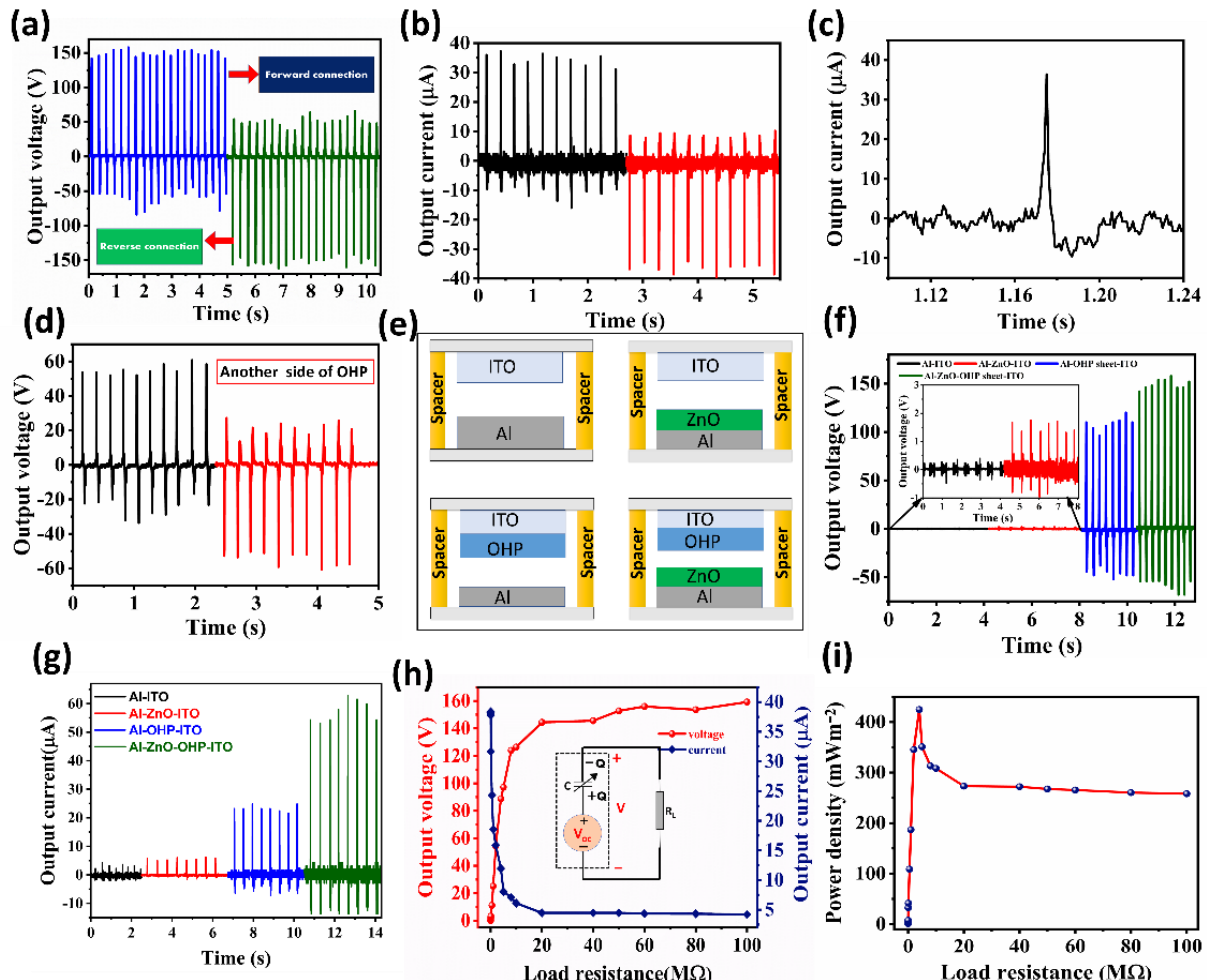


Figure 5.4. Electrical characteristics of TENG ($5 \times 5 \text{ cm}^2$) (a) open-circuit voltage, and (b) short circuit current in forward and reverse connections, (c) magnified view of short circuit current of TENG response in one cycle, (d) TENG response with another side of OHP sheet surface, (e) schematic of TENGs with different tribo-pairs, (f-g) TENG responses with different tribo-pairs of Al-ITO, ZnO-ITO, OHP-Al, ZnO-OHP (h) plot of output voltage and current with different load resistances, (i) Instantaneous power density with the load resistance.

A simple hand slapping force was used on TENG devices ($5 \times 5 \text{ cm}^2$) to investigate mechanical energy harvesting. The open-circuit voltage (V_{oc}) and short circuit current (I_{sc}) of TENG against repeated hand slapping pressure were recorded and presented in Figures 5.4 (a) and (b), respectively. The V_{oc} and I_{sc} of the TENG device are $\sim 150 \text{ V}$ and $\sim 34.5 \mu\text{A}$, respectively. The observed values are significantly higher than ZnO-PET-based TENG [43]. This enhancement is due to the pre-charged nature of the OHP sheets compared to the normal PET sheets. The V_{oc} and I_{sc} of the six TENG devices fabricated under identical conditions and found the same response were verified. The V_{oc} and I_{sc} were measured as part of the switching

polarity test to confirm the origin of the electrical signal [57]. In the switching polarity test, the V_{oc} and I_{sc} were measured under reversed electrical connections to the measuring device. From the switching polarity test (Figures 5.4 (a)-(b)), it appears that V_{oc} and I_{sc} come from the TENG devices, not from noise. The magnified view of short circuit current of TENG response in one cycle is presented in Figure 5.4 (c).

Another TENG fabricated by keeping another side (non-charged) of the OHP as a frictional layer to understand the effect of the ink-receiving layer (charged) side on the TENG performance. The response of this new TENG is shown in Figure 5.4(d) and the output voltage is reduced to ~ 55 V, indicating that the charged side of OHP significantly affects the output voltage. Figure 5.4(e-g) shows the measured V_{oc} of different TENG devices: (i) without ZnO and OHP (ITO-Al) (ii) without OHP (ITO-ZnO), (iii) without ZnO nanosheet layer (OHP-Al), (iv) with ZnO and OHP (ZnO-OHP). It is evident from Figure 5.4(g) that OHP and ZnO frictional layers play a significant role in enhancing the output voltage and current.

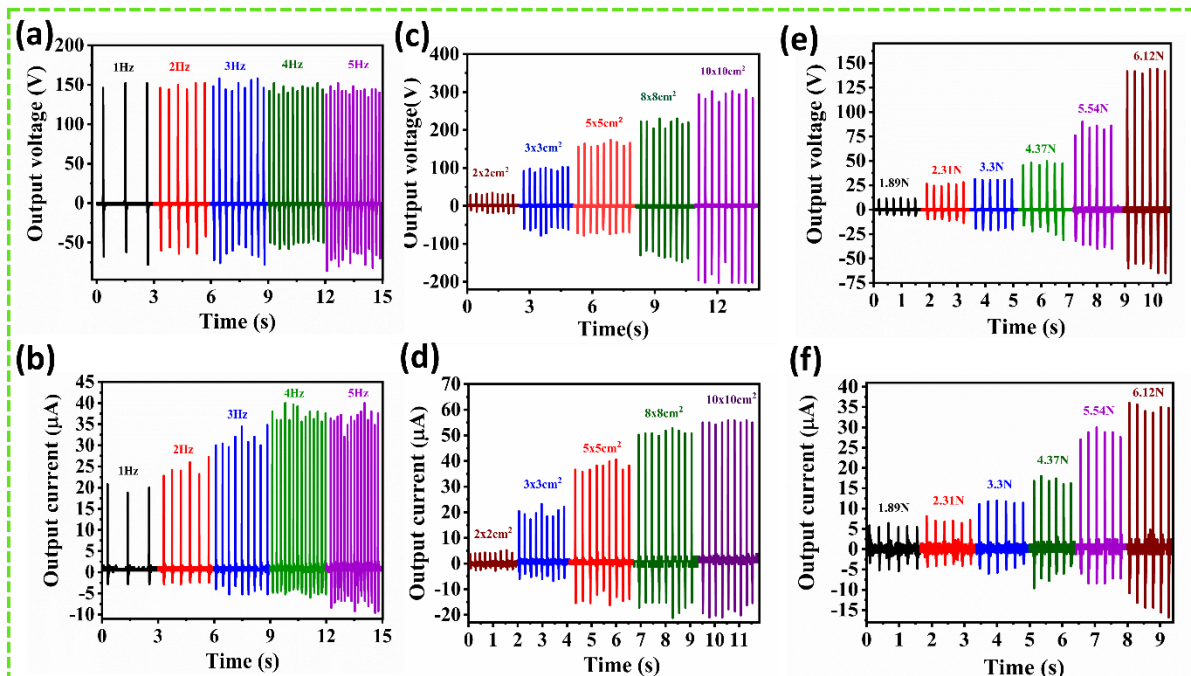
The working mechanism of the contact separation mode TENG is very well elucidated in the literature based on triboelectrification and electrostatic induction [1,58]. A similar mechanism is adopted for the proposed TENG and presented in Chapter-2, Section-3. This model consists of an OHP sheet as a one triboelectric layer and ZnO nanosheet film as another a triboelectric layer attached with ITO/PET and aluminum electrodes, respectively. The TENG is in equilibrium in the initial state, since there is no contact between ZnO and the OHP sheet. When these layers contact each other under external force, they exchange electrons based on their electron affinities. The ZnO and OHP sheet carries the same quantity of opposite charges, resulting in equilibrium. When the external force is removed, the electrical potential is induced between the top and bottom electrodes. This potential difference drives the electrons (current) from one electrode to another until an equilibrium is reached. The induced electrostatic charges flow back (current) in the reverse direction when the external force is reapplied. The repeated application and removal of force produce an AC electrical output. Therefore, an alternating current is generated by continuous contact and separation movements

To study the instantaneous output power of the TENG device ($5 \times 5 \text{ cm}^2$), the V_{oc} and I_{sc} were measured at different load resistance values ranging from $1 \text{ K}\Omega$ to $100 \text{ M}\Omega$. With increasing load resistance, the average value of V_{oc} increases and I_{sc} decreases, as shown in Figure 5.4(h). From Figure 5.4(h), instantaneous power density was measured using $P = \frac{VI}{A}$

A simple and low-cost TENG.... And its application in CLC, EL, and portable electronics

where I and V are current, and voltage at different loads, and A is the active contact area. The output power density of TENG is initially increased, reaches the maximum value at optimal load resistance ($\sim 4 \text{ M}\Omega$), and is decreased for later load resistances, as shown in Figure 5.4(i). TENG exhibits the highest power density when the external load is equivalent to the device's internal resistance. The maximum power density of 424.8 mW/m^2 is observed at the optimal load resistance of $4 \text{ M}\Omega$. The energy conversion efficiency of the TENG was calculated using the calculation procedure reported in the literature [59–61]. The efficiency of the TENG device is defined as ratio of electrical energy delivered by the TENG to the applied mechanical energy. The energy conversion efficiency of $\sim 6.3\%$ was obtained with the fabricated TENG (In Chapter 2, Section-2.4.6).

Figure 5.5. Comparative study of TENG V_{oc} and I_{sc} with (a)-(b) different frequencies of the



applied force, (c)-(d) different active areas of the devices, and (e)-(f) different magnitudes of applied forces.

Figure 5.5 (a)-(b) represents the variation of TENG output voltage and the current with different frequencies of applied force. The output voltage did not change much with frequency, and this may be due to the open circuit voltage does not involve any dynamic charge process under open circuit conditions [62,63]. On the other hand, the current increased with frequency and stabilized after 4 Hz. The output current is increased due to the fast transferring of charges at high frequency of contact and separation [62]. To know the best performance of TENG, the

A simple and low-cost TENG.... And its application in CLC, EL, and portable electronics

effect of the different active areas of devices, different frequencies of applied force, and different magnitudes of applied forces were studied. Figure 5 represents a comparative study of TENG's V_{oc} and I_{sc} under the effect of different parameters. Figures 5.5(c)-(d) shows the variation of TENG output voltage and current with different active areas of 2×2 , 3×3 , 5×5 , 8×8 , and $10 \times 10 \text{ cm}^2$. It is clear from Figure 5.5(c)-(d) that the TENG output voltage and current are increased with active area of the devices. As the active area of the device increases, the effective contact electrification also increases proportionally, which results in the increase of voltage and current. The reported literature well supports the observed behavior of TENG with the area of the TENG devices [64,65]. Further, the effect of applied hand slapping force on TENG output was studied and presented in Figure 5.5 (e)-(f). The TENG output voltage and the current are increased gradually with the applied force. This could be due to the increased friction area between the triboelectric layers with applied force, resulting in more charges. A similar dependence of TENG performance with applied force is observed for other TENGs in the literature [65,66].

The stability of the fabricated TENG has been tested over a large number of cycles with hand slapping (4300 cycles) and also with linear motor ($>10,000$ cycles). The TENG output voltage responses are presented in Figures 5.6 (a) and (b) for hand slapping and linear motor. In the case of hand slapping, sets of ~ 30 -40 cycles of responses were recorded with a gap of a few seconds and all such data sets merged to make 4300 cycles. In the case of linear motor, the TENG device was continuously tested for 60 minutes (a frequency of ~ 3 Hz), and responses were collected at different time intervals such as 10, 20, 30, 40, 50, and 60th minute. The different output voltages in the stability test (Figure 5.6 (a) and (b)) are due to the difference in the magnitude of the force applied by the hand slapping and liner motor tapping

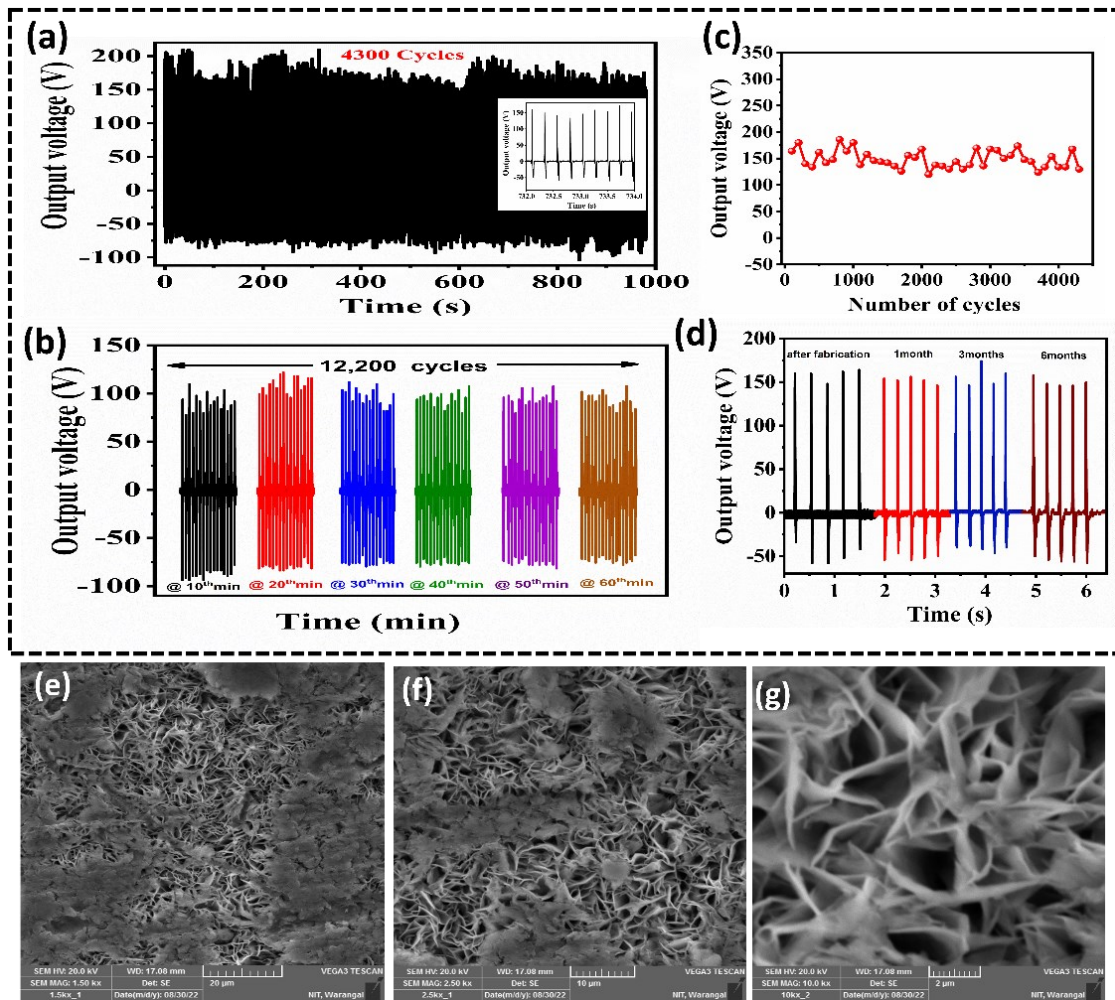


Figure 5.6. Stability of TENG (a) 4300 cycles with hand tapping (inset few cycles from stability graph), (b) 12,220 cycles with linear motor, (c) TENG output voltage vs number of cycles, and (d) Stability test of TENG over a period of 6 months. (e-g) SEM images of ZnO nanosheets after stability test of 10,000 cycles.

Figure 5.6 (c) shows the variation of output voltage as a function of cycle number (every 100th cycle). Furthermore, the TENG's stability was tested over 6 months, as shown in Figure 5.6 (d), and was found stable. SEM images of ZnO nanosheets film after 10,000 cycles test to check the stability of the ZnO nanosheets were studied. The SEM images of ZnO nanosheets at different magnifications are shown in Figure 5.6 (e-g). The important observations from SEM images are: (1) ZnO nanosheets are intact with the substrate, (2) no significant changes in the morphology of ZnO nanosheets, and (3) at a few places, ZnO nanosheets merged themselves, and this needs a detailed systematic study for better understanding. The stability tests show that the TENG showed a highly stable output over a long period of time.

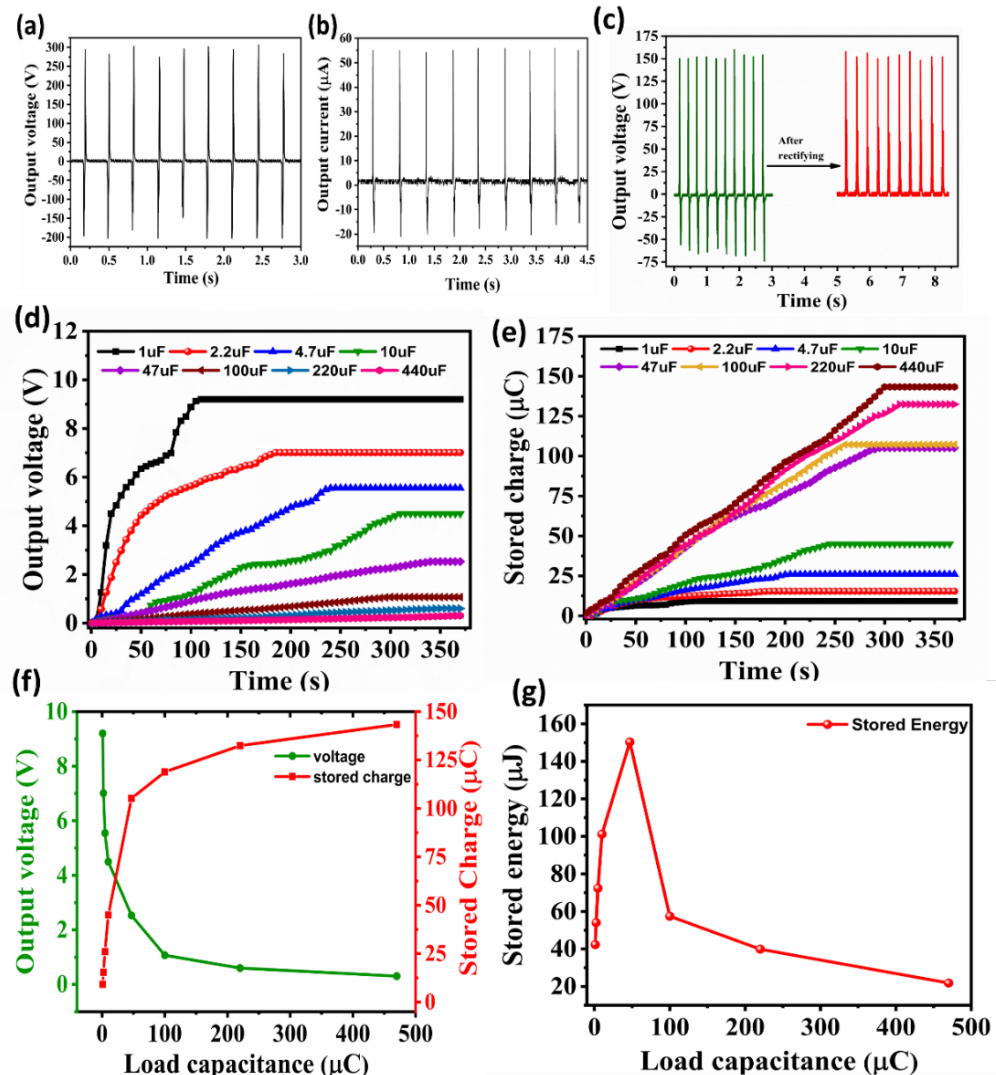


Figure 5.7. Response $10 \times 10 \text{ cm}^2$ TENG (a) open circuit voltage, (b) short circuit current. (c) TENG output voltage before and after rectification. (d) Charging curves different load capacitors, (e) stored charge at different load capacitances, (f) output voltage and stored charges behaviour as a function of the load capacitance, (g) the maximum stored energy as a function of the load capacitance.

The open circuit voltage and short circuit current of $\sim 292 \text{ V}$ and $55 \mu\text{A}$ were observed for $10 \times 10 \text{ cm}^2$ TENG is shown Figure 5.7 (a-b). TENG output was rectified using full wave rectifier (DB107) and rectified output is shown in Figure 5.7 (c). The rectified TENG output was used for charging the capacitors. Figure 5.7 (d-g) shows the charging curves of different load capacitors (1- 440 μF) by continuous operation of TENG for ~ 380 sec. From the charging curves, it is concluded that the capacitors are charged in the range of 0.2 - 9 V in 380 sec. The charging speed is higher for a smaller load capacitor, and quickly reaches the saturation voltage

A simple and low-cost TENG.... And its application in CLC, EL, and portable electronics

(V). On the other hand, the charging speed is slow for a higher load capacitor, and it may reach saturation voltage at a longer time duration (Figure 5.7(d)). From the charge and potential difference relationship equation $Q=C_L V$, the stored charge was calculated and presented in Figure 5.7(e). As expected, the stored charge in the capacitor increased with the load capacitor values. The $440 \mu\text{F}$ load capacitor held the maximum charges of $\sim 150 \mu\text{C}$ in 300 seconds. The output voltage and stored charge were plotted as a function of the load capacitance, which is shown in Figure 5.7(f). It indicates an inverse relationship between the output voltage and the stored charge with respect to the load capacitance.

In addition, the stored energy(E) was calculated from $E=\frac{1}{2}CV^2$ and shown in Figure 5.7(g).

The maximum stored energy is observed at an optimal load capacitance value of $47 \mu\text{F}$, where the impedance between the TENG and the capacitive load matches. The load capacitance behavior of TENG is similar to the existing literature.

5.4 Applications

5.4.1 Self-powered electroluminescence and portable electronic devices application

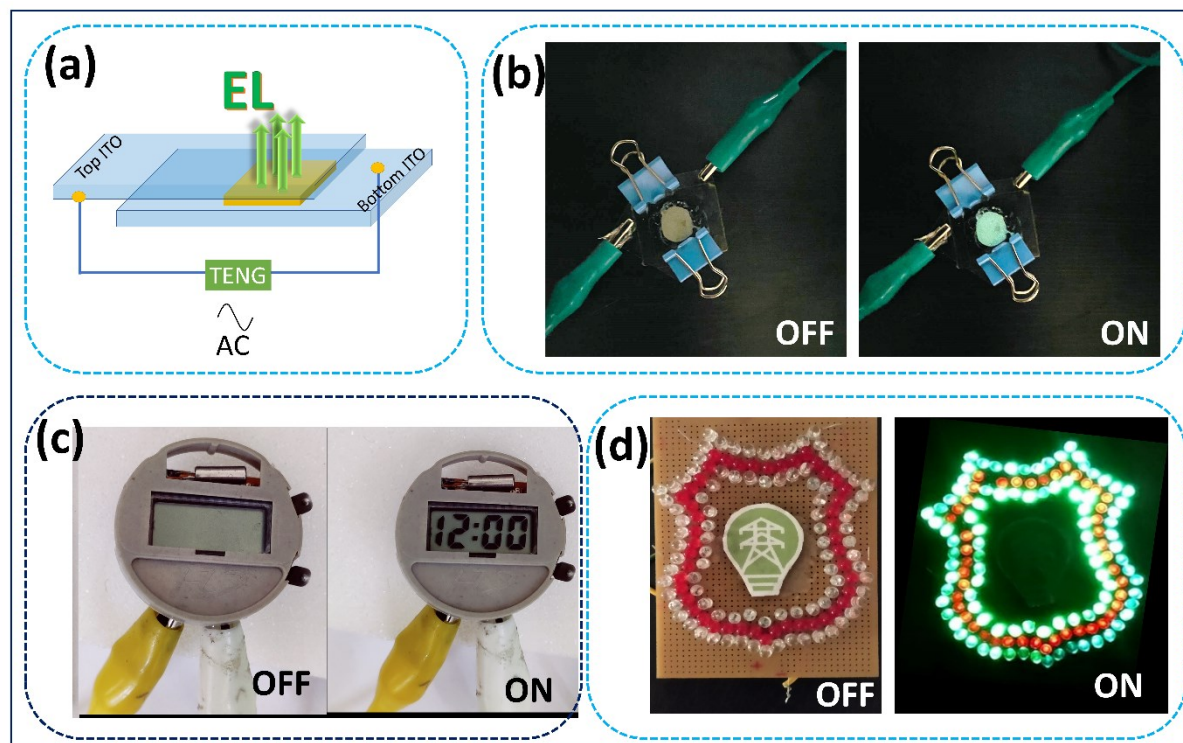


Figure 5.8. (a) Schematic of the electroluminescence device and its components, on and off state photographs of (b) electroluminescence, (c) digital watch, (d) LEDs.

A simple and low-cost TENG.... And its application in CLC, EL, and portable electronics

Further, the TENG AC output has been used for powering electroluminescence (EL) devices. Figure 5.8(a) shows the schematic structure of the electroluminescence device in which luminescent powder (ZnS-Cu, Al) is sandwiched between two ITO electrodes without any short circuit. The output of the TENG device was given directly to the EL device's top and bottom ITO electrodes. Figure 5.8(b) shows the photographs of the electroluminescence device before and after applying a TENG output ([SI, Video S5.1](#)). A very high electric field (10^6 - 10^7 V/m) is required to obtain AC-EL emission from ZnS:Cu, Al phosphor material. The phosphor with a particle size of less than 20 μ m can induce such a local field when a potential difference of more than 100 V_{PP} (peak to peak) is applied across the EL device. In practical phosphors, the radiative emission is not caused by direct recombination, but by transitions taking place via energy levels of activators introduced as impurities. In ZnS: Cu, Al phosphor, the excess doping of copper (\sim 1000-1500 ppm) is a prerequisite for the phosphor to exhibit EL. This has the dual functionality of primarily forming electrically conducting Cu_xS needles inside the ZnS grain and secondly, creating the luminescence centers required in the ZnS host lattice [67,68]. When a high voltage is applied, the Cu_xS needles provide an enhanced local electric field in the ZnS grains, thus producing EL. The field emission of electrons from the sharp ends of Cu-rich conducting Cu_xS needles occurs at alternate ends as the field reverses. These electrons are trapped at some short distance from the inclusion. They are then released from the traps when the field is sufficiently high and accelerated towards the inclusion where the field enhancement causes impact ionization leaving behind a hole. These electrons can drift through the bulk and subsequently recombine radiatively within the trapped holes. Finally, radiative relaxation results in AC-EL. The fabricated TENG is capable of producing visible electroluminescence from the EL device. In addition, self-powered electroluminescence signboards/ text displays using large area TENG devices were designed.

The fabricated TENG further directly power the digital watch ([SI Video S5.2](#)) and 135 series-connected LEDs ([SI Video S5.3](#)). Figures 5.8 (c) and (d) show the photographs of the digital watch and LEDs before and after applying the TENG output to them.

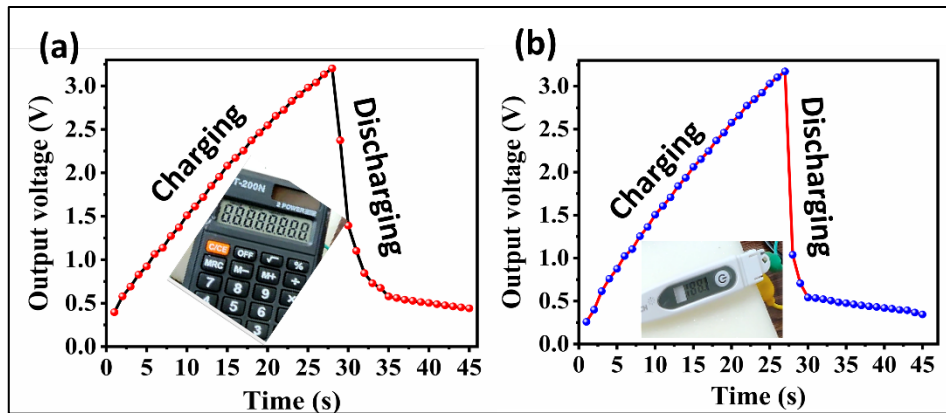


Figure 5.9. Capacitor charging and discharging curves before and after power up the electronic devices (a) calculator, (b) digital thermometer.

Further, TENG powered the electronic Calculator ([SI Video S5.4](#)) and digital Thermometer ([SI Video S5.5](#)). by utilizing the charged voltage of $4.7 \mu\text{F}$ capacitor in less than 30 seconds. The charging and discharging of the capacitor before and after the load are connected is shown in Figure 5.9 (a)-(b).

5.4.2 Self-powered CLC device applications

Figure 5.10 (a) illustrates the switching mechanism of the CLC device between planar and focal conic textures induced by the AC electrical signal from TENG. The applied AC signal can change the orientation of the molecules and thus affect their optical properties. In this chapter, CLC devices are driven directly by the AC output of TENG, which affects their optical properties. It is essential to have a higher input voltage to switch the CLC device from a planar to a focal conic state. Therefore, a $10 \times 10 \text{ cm}^2$ TENG device was used for this application (Figure 5.1(e)).

Initially, CLCs are in the planar (P) state, in which they exhibit a partially transparent state. In this state, only a particular wavelength of light in the width of the CLCs photonic bandgap is transmitted, and the rest is reflected. When the TENG's electrical pulse is applied, the CLCs are changed from a planar (P) to a focal conic (FC) state, in which the helicoidal CLC structure is randomly orientated, scattering incident light and causing the display to become opaque ([SI Video S5.6](#)). The CLC FC state can be changed back to the planar state after the applied force on the TENG device is released. The polarized microscope images and real time photographs of the CLC devices are shown in Figure 5.10 (b)-(c), which depicts the transformation of CLC devices from the P to FC when the AC output of TENG is applied. Figure 5.10 (d) shows the

A simple and low-cost TENG.... And its application in CLC, EL, and portable electronics

transmission spectra of the CLC devices in the planar state and focal conic state triggered by TENG. It is clear that the transmitted light intensity has decreased in the FC state.

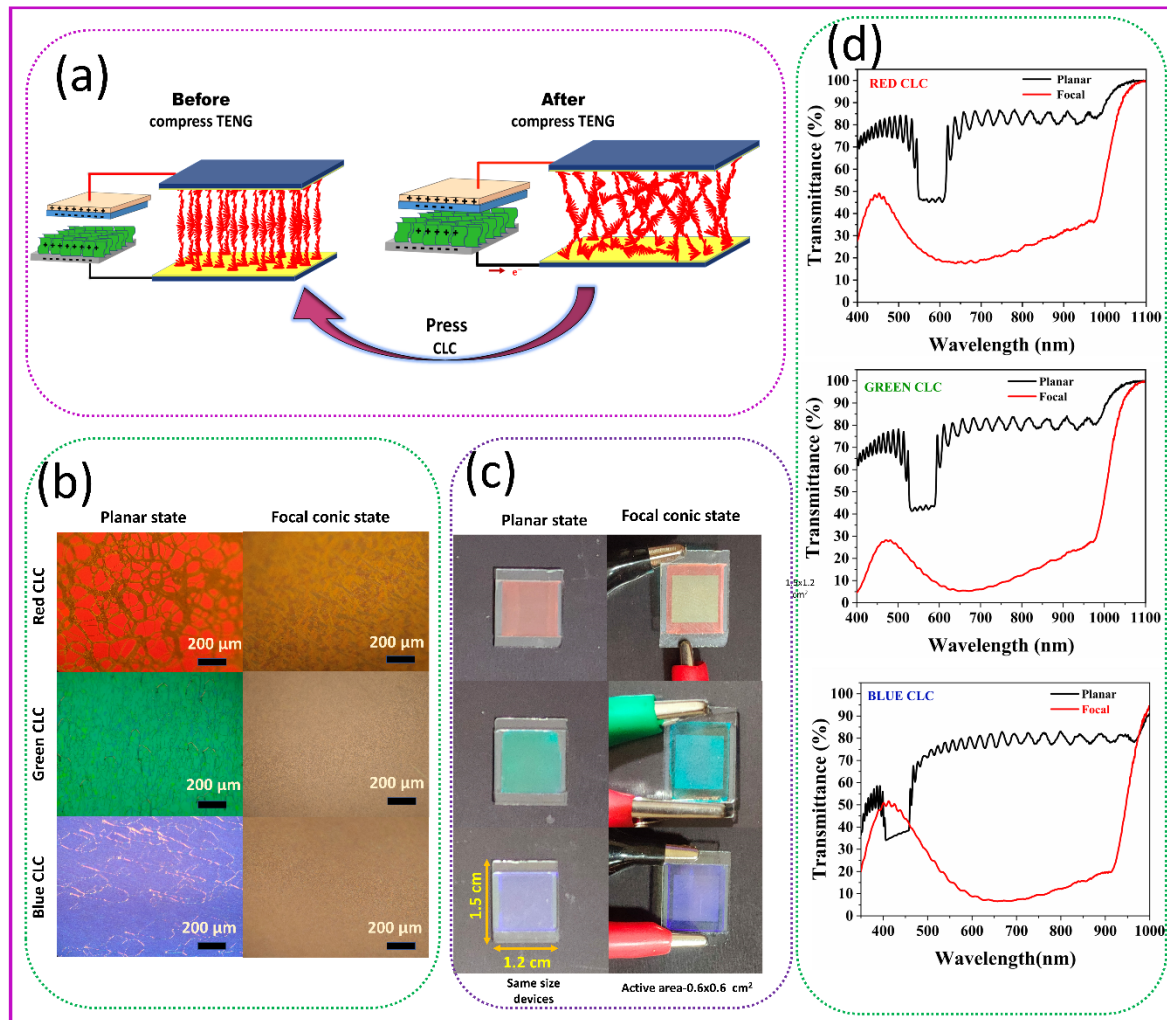


Figure 5.10. (a) Working principle of self-powered CLC device driven with TENG device before and after applying force on TENG, (b) Polarizing optical microscopy images of different CLC's in red, blue, green cells driven from planar to focal conic by TENG device, (c) Real-time images of different CLC's in red, blue, green cells driven from planar to focal conic by TENG device, (d) transmission spectra of CLC devices in planar and focal conic state.



Figure 5.11. (a) switching action of CLC, (b) photograph of the CLC device integrated with mobile phone camera, practical applications of CLC devices integrated with TENG are (c) switchable smart windows, (d) optical switches, (e) secured/ authenticated or unauthenticated QR codes, (f) mobile phone face lock security, and (g) display of patterned of "LC" letters of CLC connected to TENG device.

The arrangement of the LC molecules inside the cell determines their collective optical properties. For example, when the molecules are arranged in a planar (P) alignment that is

A simple and low-cost TENG.... And its application in CLC, EL, and portable electronics

parallel to the substrate, the layer reflects light of specific wavelengths depending on the pitch and is transparent for the rest of the wavelengths. Therefore, when no voltage is applied, the planar state is semi-transparent to light. The intermolecular forces are rather weak and can be perturbed by an applied electric field. Because the molecules are polar, they interact with an electric field, which causes them to change their orientation slightly [69–71]. When an electric field was applied to the CLC cell, the helical pitch and direction of the LC were changed from their initial states because of the compromise between the dielectric and elastic torques. When the planar state is subjected to an AC voltage, it changes to the focal conic state. If the applied voltage is not enough to unwind the helix, the LC molecules try to align in the direction of the applied electric field. As a result, the helices tilt away from the substrate without unwinding the helix. Since the helix is randomly oriented, it scatters light [70,71]. Therefore, the focal conic state is opaque to light.

To investigate real-time applications by exploiting the partial transmittance in the P state and opaqueness in the FC state of the CLC device were tested. Secure authentication devices (facial unlocking in mobile phones, QR code scanning, etc.), smart windows, and a CLC display to show letters are all real-time applications (optical switch).

The primary switching action of a self-powered CLC device is shown in Figure 5.11(a). The CLC device was placed over a text printed on a paper, and the visibility of text through the CLC device in the P and FC state clearly demonstrates the switching action ([SI Video S5.7](#)). To exemplify the potential of CLC devices for smart window applications, installed CLC device on top of the smartphone camera, as shown in Figure 5.11(b), and captured images. A smartphone camera has used to photograph the landscape of a building before and after applying the TENG pulse to it using a CLC device as shown in Figure 5.11(c) ([SI Video S5.8](#)). When the CLC device is in the P state, the scenery of a building is clear; nevertheless, when the CLC device is converted to the FC state by the TENG electrical pulse, the scenery of a building is not apparent. To demonstrate the CLC device as an optical switch, and captured the text (NITW) printed on a paper through the CLC device via a smartphone camera before and after applying the TENG pulse as shown in Figure 5.11(d). Further, scanned the QR code before applying the TENG pulse to the CLC device, and the QR code has been scanned successfully and shows the encoded picture with "NITW" letters, as shown in Figure 5.11(e). When the TENG output was applied to the CLC device, the QR code could not be scanned due to the CLC device's transition to the FC state. This results in other misleading results on the Google

A simple and low-cost TENG.... And its application in CLC, EL, and portable electronics

lens (mobile)app, as shown in Figure 5.11(e) (**SI Video S5.9**). In a similar way, to unlock a smartphone by the face recognition unlock method was tried. When the TENG device was pressed, the smartphone was locked, but before applying the TENG the smartphone was unlocked successfully, as shown in Figure 5.11(f) (**SI Video S5.10**). In this way, this self-powered CLC-TENG is helpful as a security device.

In addition, Self-powered CLC for text display applications were demonstrated. Next, patterned "LC" letters on the ITO plate by using a simple etching procedure, as shown in Figure 5.11(g). Initially, mask the pattern "LC" using a Kapton tape, and the un-patterned area can be etched out using a concentrated solution of HCl and zinc dust. Later, the ITO plates were washed thoroughly, spin-coated with PVA solution, and baked at 200°C for 2 h. The cell was made by maintaining a gap of 5 μ m using PET films and CLC was filled through capillary action. The CLC cell exhibited green reflection shown in Figure 5.11(g), however when the TENG pulse was applied, the display showed "LC" letters in the transparent state (whitish color) owing to the change of CLC to FC state, but the etched region still showed green reflection (**SI Video S5.11**).

5.4. Conclusions

In conclusion, a novel and high-performance TENG has been utilized for self-powered cholesteric liquid crystal, electroluminescence, and portable electronic devices. The cost-effective TENG was fabricated using ZnO nanosheets films and OHP sheets. The fabricated TENG produced a high output voltage, current, and power density of \sim 292 V, \sim 55 μ A, and \sim 424.8 mW/m², respectively. The self-powered CLC is used for security, display, and smart window applications. The self-powered electroluminescence devices and LEDs can be used for e-paper/digital billboard applications. This real-time proof of concept study showed the combination of TENG with CLC and EL for intelligent mechanical responsive devices, and this area offers a lot of room for growth.

5.5 References

- [1] C. Wu, A.C. Wang, W. Ding, H. Guo, Z.L. Wang, Triboelectric Nanogenerator: A Foundation of the Energy for the New Era, *Adv. Energy Mater.* 9 (2019) 1–25. <https://doi.org/10.1002/aenm.201802906>.
- [2] A. Yu, P. Jiang, Z. Lin Wang, Nanogenerator as self-powered vibration sensor, *Nano Energy*. 1 (2012) 418–423. <https://doi.org/10.1016/j.nanoen.2011.12.006>.
- [3] H. Wang, J. Cheng, Z. Wang, L. Ji, Z.L. Wang, Triboelectric nanogenerators for

A simple and low-cost TENG.... And its application in CLC, EL, and portable electronics

- human-health care, *Sci. Bull.* 66 (2021) 490–511.
<https://doi.org/10.1016/j.scib.2020.10.002>.
- [4] M.H. Yeh, L. Lin, P.K. Yang, Z.L. Wang, Motion-driven electrochromic reactions for self-powered smart window system, *ACS Nano.* 9 (2015) 4757–4765.
<https://doi.org/10.1021/ACSNANO.5B00706>.
- [5] H.J. Park, S. Kim, J.H. Lee, H.T. Kim, W. Seung, Y. Son, T.Y. Kim, U. Khan, N.M. Park, S.W. Kim, Self-Powered Motion-Driven Triboelectric Electroluminescence Textile System, *ACS Appl. Mater. Interfaces.* 11 (2019) 5200–5207.
<https://doi.org/10.1021/acsami.8b16023>.
- [6] X. Chen, Y. Wu, A. Yu, L. Xu, L. Zheng, Y. Liu, H. Li, Z. Lin Wang, Self-powered modulation of elastomeric optical grating by using triboelectric nanogenerator, *Nano Energy.* 38 (2017) 91–100. <https://doi.org/10.1016/j.nanoen.2017.05.039>.
- [7] D. Jiang, Z. Fan, H. Wang, M. Xu, G. Chen, Y. Song, Z.L. Wang, Triboelectric nanogenerator powered electrowetting-on-dielectric actuator for concealed aquatic microbots, *ACS Nano.* 14 (2020) 15394–15402.
<https://doi.org/10.1021/acsnano.0c05901>.
- [8] Y. Gu, T. Hou, P. Chen, J. Cao, C. Pan, W. Hu, B.-R. Yang, X. Pu, Z.L. Wang, Self-powered electronic paper with energy supplies and information inputs solely from mechanical motions, *Photonics Res.* 8 (2020) 1496.
<https://doi.org/10.1364/prj.394044>.
- [9] F.R. Fan, Z.Q. Tian, Z. Lin Wang, Flexible triboelectric generator, *Nano Energy.* 1 (2012) 328–334. <https://doi.org/10.1016/j.nanoen.2012.01.004>.
- [10] B. Saravanakumar, K. Thiagarajan, N.R. Alluri, S. SoYoon, K. Taehyun, Z.H. Lin, S.J. Kim, Fabrication of an eco-friendly composite nanogenerator for self-powered photosensor applications, *Carbon N. Y.* 84 (2015) 56–65.
<https://doi.org/10.1016/j.carbon.2014.11.041>.
- [11] J.J. Shao, T. Jiang, Z.L. Wang, Theoretical foundations of triboelectric nanogenerators (TENGs), *Sci. China Technol. Sci.* 63 (2020) 1087–1109.
<https://doi.org/10.1007/s11431-020-1604-9>.
- [12] S. Pan, Z. Zhang, Fundamental theories and basic principles of triboelectric effect: A review, *Friction.* 7 (2019) 2–17. <https://doi.org/10.1007/s40544-018-0217-7>.
- [13] S. Niu, S. Wang, L. Lin, Y. Liu, Y.S. Zhou, Y. Hu, Z.L. Wang, Theoretical study of contact-mode triboelectric nanogenerators as an effective power source, *Energy*

A simple and low-cost TENG.... And its application in CLC, EL, and portable electronics

- Environ. Sci. 6 (2013) 3576–3583. <https://doi.org/10.1039/c3ee42571a>.
- [14] H. Zou, L. Guo, H. Xue, Y. Zhang, X. Shen, X. Liu, P. Wang, X. He, G. Dai, P. Jiang, H. Zheng, B. Zhang, C. Xu, Z.L. Wang, Quantifying and understanding the triboelectric series of inorganic non-metallic materials, *Nat. Commun.* 11 (2020) 1–7. <https://doi.org/10.1038/s41467-020-15926-1>.
- [15] Z. Zhao, L. Zhou, S. Li, D. Liu, Y. Li, Y. Gao, Y. Liu, Y. Dai, J. Wang, Z.L. Wang, Selection rules of triboelectric materials for direct-current triboelectric nanogenerator, *Nat. Commun.* 12 (2021) 1–8. <https://doi.org/10.1038/s41467-021-25046-z>.
- [16] J. Kaur, H. Singh, Fabrication of composite material based nanogenerator for electricity generation enhancement of food waste by-product, *Mater. Chem. Phys.* 256 (2020) 123331. <https://doi.org/10.1016/j.matchemphys.2020.123331>.
- [17] R. Zhang, H. Olin, Material choices for triboelectric nanogenerators: A critical review, *EcoMat.* 2 (2020) 1–13. <https://doi.org/10.1002/eom2.12062>.
- [18] L. Zhao, Q. Zheng, H. Ouyang, H. Li, L. Yan, B. Shi, Z. Li, A size-unlimited surface microstructure modification method for achieving high performance triboelectric nanogenerator, *Nano Energy.* 28 (2016) 172–178. <https://doi.org/10.1016/j.nanoen.2016.08.024>.
- [19] F.R. Fan, L. Lin, G. Zhu, W. Wu, R. Zhang, Z.L. Wang, Transparent triboelectric nanogenerators and self-powered pressure sensors based on micropatterned plastic films, *Nano Lett.* 12 (2012) 3109–3114. <https://doi.org/10.1021/nl300988z>.
- [20] Z.H. Lin, Y. Xie, Y. Yang, S. Wang, G. Zhu, Z.L. Wang, Enhanced triboelectric nanogenerators and triboelectric nanosensor using chemically modified TiO₂ nanomaterials, *ACS Nano.* 7 (2013) 4554–4560. <https://doi.org/10.1021/nn401256w>.
- [21] G. Song, Y. Kim, S. Yu, M.O. Kim, S.H. Park, S.M. Cho, D.B. Velusamy, S.H. Cho, K.L. Kim, J. Kim, E. Kim, C. Park, Molecularly Engineered Surface Triboelectric Nanogenerator by Self-Assembled Monolayers (METS), *Chem. Mater.* 27 (2015) 4749–4755. <https://doi.org/10.1021/acs.chemmater.5b01507>.
- [22] S.H. Shin, Y.H. Kwon, Y.H. Kim, J.Y. Jung, M.H. Lee, J. Nah, Triboelectric charging sequence induced by surface functionalization as a method to fabricate high performance triboelectric generators, *ACS Nano.* 9 (2015) 4621–4627. <https://doi.org/10.1021/acsnano.5b01340>.
- [23] A.N. Ravichandran, M. Ramuz, S. Blayac, Increasing surface charge density by effective charge accumulation layer inclusion for high-performance triboelectric

- nanogenerators, MRS Commun. 9 (2019) 682–689.
<https://doi.org/10.1557/mrc.2019.64>.
- [24] S. Wang, Y. Xie, S. Niu, L. Lin, C. Liu, Y.S. Zhou, Z.L. Wang, Maximum surface charge density for triboelectric nanogenerators achieved by ionized-air injection: Methodology and theoretical understanding, *Adv. Mater.* 26 (2014) 6720–6728.
<https://doi.org/10.1002/adma.201402491>.
- [25] W. Kim, T. Okada, H.W. Park, J. Kim, S. Kim, S.W. Kim, S. Samukawa, D. Choi, Surface modification of triboelectric materials by neutral beams, *J. Mater. Chem. A* 7 (2019) 25066–25077. <https://doi.org/10.1039/c9ta09990e>.
- [26] H.Y. Li, L. Su, S.Y. Kuang, C.F. Pan, G. Zhu, Z.L. Wang, Significant Enhancement of Triboelectric Charge Density by Fluorinated Surface Modification in Nanoscale for Converting Mechanical Energy, *Adv. Funct. Mater.* 25 (2015) 5691–5697.
<https://doi.org/10.1002/adfm.201502318>.
- [27] J. Chen, H. Guo, X. He, G. Liu, Y. Xi, H. Shi, C. Hu, Enhancing Performance of Triboelectric Nanogenerator by Filling High Dielectric Nanoparticles into Sponge PDMS Film, *ACS Appl. Mater. Interfaces*. 8 (2016) 736–744.
<https://doi.org/10.1021/acsami.5b09907>.
- [28] D. Ali, B. Yu, X. Duan, H. Yu, M. Zhu, Enhancement of output performance through post-poling technique on BaTiO₃ /PDMS-based triboelectric nanogenerator, *Nanotechnology*. 28 (2017) 075203. <https://doi.org/10.1088/1361-6528/aa52b7>.
- [29] X. He, H. Guo, X. Yue, J. Gao, Y. Xi, C. Hu, Improving energy conversion efficiency for triboelectric nanogenerator with capacitor structure by maximizing surface charge density, *Nanoscale*. 7 (2015) 1896–1903. <https://doi.org/10.1039/c4nr05512h>.
- [30] P. Cheng, H. Guo, Z. Wen, C. Zhang, X. Yin, X. Li, D. Liu, W. Song, X. Sun, J. Wang, Z.L. Wang, Largely enhanced triboelectric nanogenerator for efficient harvesting of water wave energy by soft contacted structure, *Nano Energy*. 57 (2019) 432–439. <https://doi.org/10.1016/j.nanoen.2018.12.054>.
- [31] J. Wang, C. Meng, C.T. Wang, C.H. Liu, Y.H. Chang, C.C. Li, H.Y. Tseng, H.S. Kwok, Y. Zi, A fully self-powered, ultra-stable cholesteric smart window triggered by instantaneous mechanical stimuli, *Nano Energy*. 85 (2021) 105976.
<https://doi.org/10.1016/j.nanoen.2021.105976>.
- [32] Y.H. Chen, P.Y. Lin, T.W. Wang, N. Tiwari, S.C. Lin, H.S. Wu, D. Choi, W. Wu, D. Choi, Y.C. Hsiao, Z.H. Lin, Dynamics of Electrically Driven Cholesteric Liquid

A simple and low-cost TENG.... And its application in CLC, EL, and portable electronics

- Crystals by Triboelectrification and Their Application in Self-Powered Information Securing and Vision Correcting, *ACS Energy Lett.* 6 (2021) 3185–3194.
<https://doi.org/10.1021/acsenergylett.1c01619>.
- [33] J. Wang, C. Meng, Q. Gu, M.C. Tseng, S.T. Tang, H.S. Kwok, J. Cheng, Y. Zi, Normally Transparent Tribo-Induced Smart Window, *ACS Nano.* 14 (2020) 3630–3639. <https://doi.org/10.1021/acsnano.0c00107>.
- [34] H. Liu, Z.H. Guo, F. Xu, L. Jia, C. Pan, Z.L. Wang, X. Pu, Triboelectric-optical responsive cholesteric liquid crystals for self-powered smart window, E-paper display and optical switch, *Sci. Bull.* 66 (2021) 1986–1993.
<https://doi.org/10.1016/j.scib.2021.05.016>.
- [35] B. Yang, W. Zeng, Z.H. Peng, S.R. Liu, K. Chen, X.M. Tao, A Fully Verified Theoretical Analysis of Contact-Mode Triboelectric Nanogenerators as a Wearable Power Source, *Adv. Energy Mater.* 6 (2016) 1–8.
<https://doi.org/10.1002/aenm.201600505>.
- [36] H. Zhang, L. Quan, J. Chen, C. Xu, C. Zhang, S. Dong, C. Lü, J. Luo, A general optimization approach for contact-separation triboelectric nanogenerator, *Nano Energy.* 56 (2019) 700–707. <https://doi.org/10.1016/j.nanoen.2018.11.062>.
- [37] X. Pu, J.W. Zha, C.L. Zhao, S.B. Gong, J.F. Gao, R.K.Y. Li, Flexible PVDF/nylon-11 electrospun fibrous membranes with aligned ZnO nanowires as potential triboelectric nanogenerators, *Chem. Eng. J.* 398 (2020) 125526.
<https://doi.org/10.1016/j.cej.2020.125526>.
- [38] X. Yue, Y. Xi, C. Hu, X. He, S. Dai, L. Cheng, G. Wang, Enhanced output-power of nanogenerator by modifying PDMS film with lateral ZnO nanotubes and Ag nanowires, *RSC Adv.* 5 (2015) 32566–32571. <https://doi.org/10.1039/c5ra02098k>.
- [39] D. Li, C. Wu, L. Ruan, J. Wang, Z. Qiu, K. Wang, Y. Liu, Y. Zhang, T. Guo, J. Lin, T.W. Kim, Electron-transfer mechanisms for confirmation of contact-electrification in ZnO/polyimide-based triboelectric nanogenerators, *Nano Energy.* 75 (2020) 104818.
<https://doi.org/10.1016/j.nanoen.2020.104818>.
- [40] Y.H. Ko, G. Nagaraju, S.H. Lee, J.S. Yu, PDMS-based triboelectric and transparent nanogenerators with ZnO nanorod arrays, *ACS Appl. Mater. Interfaces.* 6 (2014) 6631–6637. <https://doi.org/10.1021/am5018072>.
- [41] B. Liu, S. Wang, Z. Yuan, Z. Duan, Q. Zhao, Y. Zhang, Y. Su, Y. Jiang, G. Xie, H. Tai, Novel chitosan/ZnO bilayer film with enhanced humidity-tolerant property:

A simple and low-cost TENG.... And its application in CLC, EL, and portable electronics

- Endowing triboelectric nanogenerator with acetone analysis capability, Nano Energy. 78 (2020) 105256. <https://doi.org/10.1016/j.nanoen.2020.105256>.
- [42] A.K. Gupta, C.-H. Hsu, S.-N. Lai, C.-S. Lai, ZnO-Polystyrene Composite as Efficient Energy Harvest for Self-Powered Triboelectric Nanogenerator, ECS J. Solid State Sci. Technol. 9 (2020) 115019. <https://doi.org/10.1149/2162-8777/aba7fa>.
- [43] P. Supraja, R.R. Kumar, S. Mishra, D. Haranath, P.R. Sankar, K. Prakash, N. Jayarambabu, T.V. Rao, K.U. Kumar, A simple and low-cost triboelectric nanogenerator based on two dimensional ZnO nanosheets and its application in portable electronics, Sensors Actuators A Phys. 335 (2022) 113368. <https://doi.org/10.1016/j.sna.2022.113368>.
- [44] S. Jakmuangpak, T. Prada, W. Mongkolthanaruk, V. Harnchana, S. Pinitsoontorn, Engineering Bacterial Cellulose Films by Nanocomposite Approach and Surface Modification for Biocompatible Triboelectric Nanogenerator, ACS Appl. Electron. Mater. 2 (2020) 2498–2506. <https://doi.org/10.1021/acsaelm.0c00421>.
- [45] M. Sahu, S. Šafranko, S. Hajra, A.M. Padhan, P. Živković, S. Jokić, H.J. Kim, Development of triboelectric nanogenerator and mechanical energy harvesting using argon ion-implanted kapton, zinc oxide and kapton, Mater. Lett. 301 (2021) 1–5. <https://doi.org/10.1016/j.matlet.2021.130290>.
- [46] P. Supraja., R. Rakesh Kumar., S. Mishra, D. Haranath., Triboelectric Nanogenerator Based on ZnO Nanosheet Networks for Mechanical Energy Harvesting, 2022 2nd Int. Conf. Power Electron. IoT Appl. Renew. Energy Its Control. PARC 2022. (2022) 1–4. <https://doi.org/10.1109/PARC52418.2022.9726684>.
- [47] H.H. Singh, N. Khare, Flexible ZnO-PVDF/PTFE based piezo-tribo hybrid nanogenerator, Nano Energy. 51 (2018) 216–222. <https://doi.org/10.1016/j.nanoen.2018.06.055>.
- [48] Y.P. Jeon, J.H. Park, T.W. Kim, Highly flexible triboelectric nanogenerators fabricated utilizing active layers with a ZnO nanostructure on polyethylene naphthalate substrates, Appl. Surf. Sci. 466 (2019) 210–214. <https://doi.org/10.1016/j.apsusc.2018.09.249>.
- [49] Y.P. Jeon, J.H. Park, T.W. Kim, Highly-enhanced triboelectric nanogenerators based on zinc-oxide nanoripples acting as a triboelectric layer, Appl. Surf. Sci. 445 (2018) 50–55. <https://doi.org/10.1016/j.apsusc.2018.03.125>.
- [50] S.N. Chen, C.H. Chen, Z.H. Lin, Y.H. Tsao, C.P. Liu, On enhancing capability of

A simple and low-cost TENG.... And its application in CLC, EL, and portable electronics

- tribocharge transfer of ZnO nanorod arrays by Sb doping for anomalous output performance improvement of triboelectric nanogenerators, *Nano Energy*. 45 (2018) 311–318. <https://doi.org/10.1016/j.nanoen.2018.01.013>.
- [51] W. Deng, B. Zhang, L. Jin, Y. Chen, W. Chu, H. Zhang, M. Zhu, W. Yang, Enhanced performance of ZnO microballoon arrays for a triboelectric nanogenerator, *Nanotechnology*. 28 (2017) 135401. <https://doi.org/10.1088/1361-6528/aa5f34>.
- [52] A. Dos Santos, F. Sabino, A. Rovisco, P. Barquinha, H. Águas, E. Fortunato, R. Martins, R. Igreja, Optimization of zno nanorods concentration in a micro-structured polymeric composite for nanogenerators, *Chemosensors*. 9 (2021) 1–13. <https://doi.org/10.3390/chemosensors9020027>.
- [53] A. Sultana, M.M. Alam, S. Garain, T.K. Sinha, T.R. Midya, D. Mandal, An Effective Electrical Throughput from PANI Supplement ZnS Nanorods and PDMS-Based Flexible Piezoelectric Nanogenerator for Power up Portable Electronic Devices: An Alternative of MWCNT Filler, *ACS Appl. Mater. Interfaces*. 7 (2015) 19091–19097. <https://doi.org/10.1021/acsami.5b04669>.
- [54] S. Kim, R.M.D.S. Somaratne, J.E. Whitten, Effect of Adsorption on the Photoluminescence of Zinc Oxide Nanoparticles, *J. Mater. Chem. C*. 122 (2018) 18982–18994. <https://doi.org/10.1021/acs.jpcc.8b04715>.
- [55] Y.A. Stetsiv, M.M. Yatsyshyn, D. Nykypanchuk, S.A. Korniy, I. Saldan, O. V. Reshetnyak, T.J. Bednarchuk, Characterization of polyaniline thin films prepared on polyethylene terephthalate substrate, *Polym. Bull.* 78 (2021) 6251–6265. <https://doi.org/10.1007/s00289-020-03426-7>.
- [56] A.A. El-Saftawy, A. Elfalaky, M.S. Ragheb, S.G. Zakhary, Electron beam induced surface modifications of PET film, *Radiat. Phys. Chem.* 102 (2014) 96–102. <https://doi.org/10.1016/j.radphyschem.2014.04.025>.
- [57] R. Yang, Y. Qin, C. Li, L. Dai, Z.L. Wang, Characteristics of output voltage and current of integrated nanogenerators, *Appl. Phys. Lett.* 94 (2009) 92–95. <https://doi.org/10.1063/1.3072362>.
- [58] F.-R. Fan, Z.-Q. Tian, Z. Lin Wang, Flexible triboelectric generator, *Nano Energy*. 1 (2012) 328–334. <https://doi.org/10.1016/j.nanoen.2012.01.004>.
- [59] G. Zhu, Z.H. Lin, Q. Jing, P. Bai, C. Pan, Y. Yang, Y. Zhou, Z.L. Wang, Toward large-scale energy harvesting by a nanoparticle-enhanced triboelectric nanogenerator, *Nano Lett.* 13 (2013) 847–853. <https://doi.org/10.1021/nl4001053>.

- [60] C.K. Jeong, K.M. Baek, S. Niu, T.W. Nam, Y.H. Hur, D.Y. Park, G.T. Hwang, M. Byun, Z.L. Wang, Y.S. Jung, K.J. Lee, Topographically-designed triboelectric nanogenerator via block copolymer self-assembly, *Nano Lett.* 14 (2014) 7031–7038. <https://doi.org/10.1021/nl503402c>.
- [61] A. You, X. Zhang, X. Peng, K. Dong, Y. Lu, Q. Zhang, A Skin-Inspired Triboelectric Nanogenerator with an Interpenetrating Structure for Motion Sensing and Energy Harvesting, *Macromol. Mater. Eng.* 306 (2021) 1–9. <https://doi.org/10.1002/mame.202100147>.
- [62] R. Pan, W. Xuan, J. Chen, S. Dong, H. Jin, X. Wang, H. Li, J. Luo, Fully biodegradable triboelectric nanogenerators based on electrospun polylactic acid and nanostructured gelatin films, *Nano Energy.* 45 (2018) 193–202. <https://doi.org/10.1016/j.nanoen.2017.12.048>.
- [63] S. Wang, L. Lin, Z.L. Wang, Nanoscale triboelectric-effect-enabled energy conversion for sustainably powering portable electronics, *Nano Lett.* 12 (2012) 6339–6346. <https://doi.org/10.1021/nl303573d>.
- [64] T. Kamilya, P.K. Sarkar, S. Acharya, Unveiling Peritoneum Membrane for a Robust Triboelectric Nanogenerator, *ACS Omega.* 4 (2019) 17684–17690. <https://doi.org/10.1021/acsomega.9b01963>.
- [65] Y. Lu, H. Tian, J. Cheng, F. Zhu, B. Liu, S. Wei, L. Ji, Z.L. Wang, Decoding lip language using triboelectric sensors with deep learning, *Nat. Commun.* 13 (2022) 1–12. <https://doi.org/10.1038/s41467-022-29083-0>.
- [66] S.M.S. Rana, M.T. Rahman, M. Salauddin, S. Sharma, P. Maharjan, T. Bhatta, H. Cho, C. Park, J.Y. Park, Electrospun PVDF-TrFE/MXene Nanofiber Mat-Based Triboelectric Nanogenerator for Smart Home Appliances, *ACS Appl. Mater. Interfaces.* 13 (2021) 4955–4967. <https://doi.org/10.1021/acsami.0c17512>.
- [67] H. Chander, V. Shanker, D. Haranath, S. Dudeja, P. Sharma, Characterization of ZnS:Cu, Br electroluminescent phosphor prepared by new route, *Mater. Res. Bull.* 38 (2003) 279–288. [https://doi.org/10.1016/S0025-5408\(02\)01027-9](https://doi.org/10.1016/S0025-5408(02)01027-9).
- [68] D. Haranath, S. Sahai, S. Mishra, M. Husain, V. Shanker, Fabrication and electro-optic properties of a MWCNT driven novel electroluminescent lamp, *Nanotechnology.* 23 (2012) 435704. <https://doi.org/10.1088/0957-4484/23/43/435704>.
- [69] A. Ryabchun, A. Bobrovsky, Cholesteric Liquid Crystal Materials for Tunable Diffractive Optics, *Adv. Opt. Mater.* 6 (2018) 1800335.

<https://doi.org/https://doi.org/10.1002/adom.201800335>.

- [70] H.K. Bisoyi, Q. Li, Liquid Crystals: Versatile Self-Organized Smart Soft Materials, *Chem. Rev.* 122 (2022) 4887–4926. <https://doi.org/10.1021/acs.chemrev.1c00761>.
- [71] S.W. Oh, J.M. Baek, S.H. Kim, T.H. Yoon, Optical and electrical switching of cholesteric liquid crystals containing azo dye, *RSC Adv.* 7 (2017) 19497–19501. <https://doi.org/10.1039/C7RA01507K>.

5.6 Supporting information

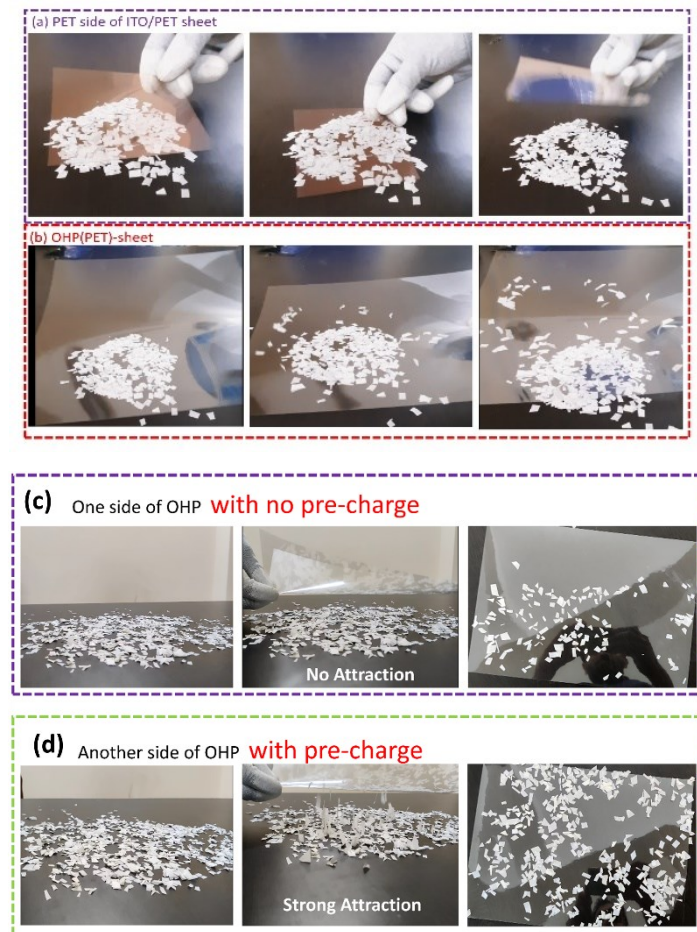


Figure. S5.1 (a)-(b) Photographs of PET and OHP sheets. Photographs of the different sides of the OHP sheet during the test, (c) non-charged side of OHP, (d) charged side of OHP.

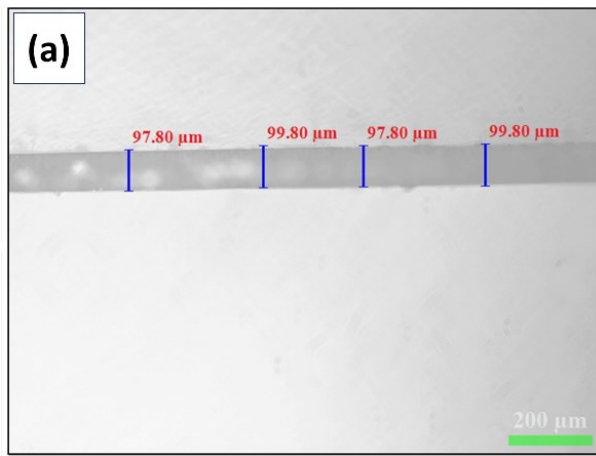
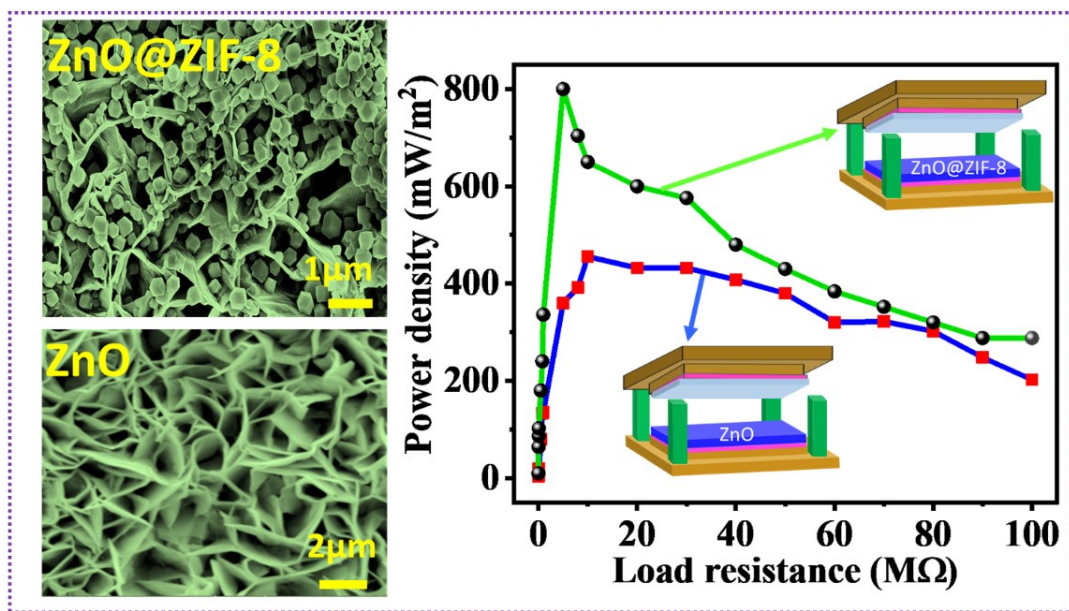


Figure S5.2. (a) cross-sectional view of OHP sheet in the optical microscope to measure the thickness.

Chapter 6

Enhancing Triboelectric Nanogenerator Performance with Metal-Organic Framework Modified ZnO Nanosheets for Self-Powered Electronic Devices and Energy Harvesting

This chapter provides surface modification as a viable approach to improve the TENG's performance. ZIF-8 particles have been introduced on the ZnO nanosheet film's surface to modify it. In the TENG device's fabrication process, poly (methyl methacrylate) (PMMA) is used as a frictional layer and Zeolitic Imidazolate Framework (ZIF-8) particles are added to ZnO nanosheets. Based on pure and ZIF-8 modified ZnO films as a fixed tri-layer, two TENG devices were constructed. Additionally, a measurement of the TENG's output response shows an impressive rise in the output of ZnO-modified ZIF-8 particles. TENG additionally demonstrates the applications of self-powered electrical devices.



1. "Enhancing Triboelectric Nanogenerator Performance with Metal-Organic Framework Modified ZnO Nanosheets for Self-Powered Electronic Devices and Energy Harvesting". *Supraja Potu, M. Navaneeth, Anshika Bhadriya, Arbacheena Bora, Yuvaraj Sivalingam, Anjaly Babu, Mahesh Velpula, Buchaiah Gollapelli, Rakesh Kumar Rajaboina*, Uday Kumar Khanapuram, Haranath Divi, Prakash Kodali, and Lakshakoti Bochu, ACS Applied Nano Materials, 2023, <https://doi.org/10.1021/acsanm.3c03430>.*

6.1 Introduction

The development of nanogenerators for energy harvesting has advanced significantly, as the TENG discussed in previous chapters (3, 4, and 5). Since 2012, TENGs have found numerous potential applications that require long-term sustainability, including smart homes [1], wireless sensor networks [2], security systems [3], health [4,5], gas [6,7], motion detection [8], powering electronic [9,10] and robotics [11]. TENG operates in four different modes, namely contact separation, single electrode mode, relative sliding mode, and free-standing mode, which allow their adaptation to diverse applications utilizing various types of mechanical motions [12,13].

Researchers across the globe put much effort to enhance the output performance of TENGs by focusing on improving charge generation during contact electrification. Charge generation further depends on the number of contact points or contact area between the frictional layers. Several approaches have been explored, including different TENG designs [14–17], surface morphology modifications [18–20], surface treatments [21–24], materials introduction [25–29] and the charge pumping method [30]. Surface morphology modification is an easy and efficient way to improve the TENG output performance.

The current study introduces a novel surface modification approach using Metal-organic frameworks (MOFs) to improve the performance of TENG devices. MOFs attracted lot of attention in the TENG field after the first report on MOF-based TENG [31]. MOFs offer several benefits such as unique morphology, high specific surface area, adjustable pore sizes, structural diversity, and high thermal and chemical stabilities. In this chapter, zeolitic imidazolate framework-8 (ZIF-8) utilized in surface modification of ZnO. ZIF-8 is a type of MOF material and is composed of metal ions (Zn^{2+}) and organic linkers (imidazolate), giving it distinct properties, and it has been used in TENGs applications [32–34]. This method involves the synthesis of ZIF-8 particles on the surface of ZnO nanosheets in a two-step hydrothermal method. This unique modification increased the contact points between triboelectric materials, altered the work function and improved the output performance of TENGs. Further, previous studies investigated the various forms of ZnO, including nanosheets, nanorods, nanowires, nano ripples, and films, for TENG [35–38]. The detailed literature review of MOFs-based TENGs is presented in Table-6.1 for a comparison of performances. It is clear from the literature review that the obtained power density is on par with the reported literature. Further, ZIF-8@ZnO composite films were previously prepared in the literature and used in

applications other than TENGs [39–42]. Therefore, exploring the combination of ZnO with ZIF-8 particle composite film for TENG applications is novel and opens new avenues. Additionally, ZnO has several advantages such as low cost, non-toxic, low-temperature synthesis, and multifunctional properties compared to other triboelectric materials.

In the present chapter, synthesizing ZnO nanosheets on an aluminum substrate, followed by the growth of ZIF-8 particles directly on the surface of the ZnO nanosheets. This ZIF-8@ZnO configuration resulted in a notable improvement in the performance of the TENG device when compared to TENGs based on ZnO alone. Specifically, achieved a 1.39-fold increase in output voltage, a 1.44-fold boost in output current, and an elevation of output power density from 455 mW/m² to 800 mW/m². This enhanced performance of the TENG device could power approximately 180 commercial LEDs through continuous hand tapping. Furthermore, demonstrated the practical applicability of the fabricated TENG device in self-powered devices and biomechanical energy harvesting scenarios.

Table 6.1. MOF based TENGs and its output performance

Sl.no	MOF Triboelectric layer	Pairing Triboelectric layer	Voltage, Current, Power density	Ref
1	ZIF-8	Kapton	164 V, 7 μ A, 392 mW/m ²	[32]
2	PDMS-HKUST-1	Cu	205 V, 37 μ A, 7.92 W/m ²	[43]
3	ZIF-7, ZIF-9, ZIF-11, ZIF-12 (ZIF-7 Best)	Kapton/ethyl cellulose	60 V, 1.1 μ A, 7.7 mW/m ²	[44]
4	ZIF-62	Teflon	70 V, 1.9 μ A, 9.68 mW/m ²	[45]
5	MIL-88A	FEP (fluorinated ethylene propylene)	90 V, 2.5 μ A , 16.2 mW/m ²	[46]
6	ZIF-67	Teflon	118 V, 1.7 μ A, 150 mW/m ²	[47]
7	Cyclodextrin-MoF	Teflon	152 V, 1.2 μ A, 80 mW/m ²	[48]
8	ZUT-8(C=C)	PVDF	600 V , 80 μ A, 2.21 W/m ²	[49]
9	UiO-66-NH ₂ /PDMS	Al	375 V, 8 μ A , 1.69 W/m ²	[50]
10	UiO-66: with NO ₂	Cu	23.79 V, 0.29 μ A	[51]
11	ZIF-8HG	Kapton	150 V, 4.95 μ A , 1.04 μ W	[33]
12	MOF-5	PTFE	484 V, 40 μ A, 5.08 W/m ²	[52]

MOF Modified ZnO Nanosheets based TENG... Self-Powered Electronic Devices

13	Polyvinylidene Fluoride/UiO-66	Cu	52.8 V, 4.29 μ A, 1.41 W/m ²	[53]
14	Co/Zn bimetal organic framework	PTFE	47 V, 7 μ A, 1.1 mW/m ²	[54]
15	Co-NPC/Ecoflex MXene/Ecoflex and Co-NPC/Ecoflex	Human skin	21 V, 9.85 μ A/m ² , 16 mW/m ² 30.64 V, 13.33 μ A/ m ²	[55]
16	ZIF-8/MO-PPy@CelF	PTFE	129 V, 6.8 μ A, 33.3 mW/m ²	[56]
17	ZUT-75(Co))	PVDF	565.67 V, 90.72 μ A, 3.28 W/m ²	[57]
18	Co-NPC/PVDF	Nylon-11	710 V, 210.96 mA/m ² , 19.71 W/m ²	[58]
19	MOFs flakes in Silk nanofibers	PDMS	215 V, 10 μ A, 2.63 W/m ²	[59]
20	Zn/Co-MOF	PVDF	623.34 V, 68.82 μ A, 17.16 W/m ²	[60]
21	NH ₂ -MIL-101(Fe,Cu) partciles with CNF	FEP	194 V, 14 μ A, 203 mW/m ²	[61]
22	LC-MXene/ZrF-67 nanocomposites with CGL	Hand	1340V,435mA/ m ² , 65 W/m ²	[62]
23	MOF-525@Ecoflex	Hand	1665 V, 111 mA/m ² , 25.7 W/m ²	[63]
24	PAN@ZIF-8	PTFE	260 V, 24.5 μ A, 1.91 W/m ²	[64]
25	PVA@ZIF-67	PMMA	300 V, 47.5 μ A, 593 mW/m ²	[65]
26	Metal-biomolecule frameworks (MBIOFs)	Teflon	200 V, 6 μ A, 260 mW/m ²	[66]
27	MIL-100 (Fe)	FEP	75 V, 5 μ A, 15mW/m ²	[67]
28	UiO-66-4F@PDMS	Al	937.4 V, 30.6 μ A, 38.7 W/m ²	[68]
29	Cu-BHT	Tap water	28 V, 7.8 μ A, 340 μ W	[69]
30	MIL-101(Cr)-PY	PTFE	825 V, 11 μ A, 25.03 W/m ²	[70]
31	UiO-66-Br	Al	110.41 V, 92.93 mW /m ²	[71]
32	UiO-66-NO ₂ @PDMS	Cu	191 V, 17.3 μ A	[72]
37	ZIF-8@ ZnO Nanosheets	PMMA	200.5 V, 41.5 μA, 800 mW/m²	This work

6.2 Experimental section

6.2.1 Materials

Zinc nitrate hexahydrate, Hexamethylenetetramine (HMTA), Dimethylformamide (DMF), 2-methylimidazole, polymethyl methacrylate (PMMA) sheets, Aluminum foils(thickness ~0.1 mm) , cardboards, sponges, and LEDs were utilized in the present chapter.

6.2.2 ZnO nanosheets synthesis

The ZnO nanosheets film was synthesized on Al substrates by following the same method mentioned in Section-2.1.

6.2.3 Synthesis of ZIF-8@ZnO

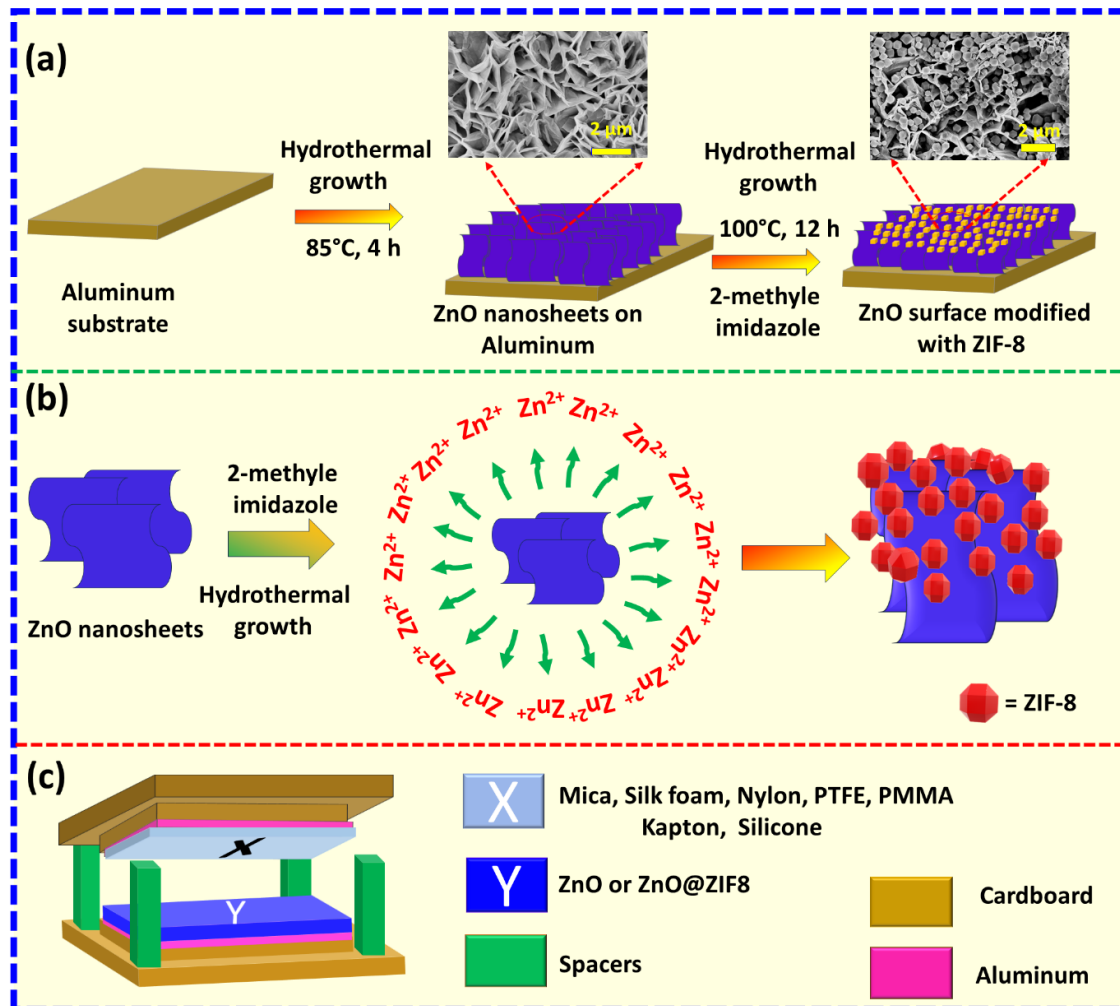
All chemicals are analytical-grade reagents used in the experiment without additional purification. ZnO nanosheets were grown directly on the surface of the aluminum substrate, as illustrated in Figure 6.1(a).

The synthesis process of ZIF-8@ZnO is shown in Figure 6.1(a). ZIF-8 synthesis typically involves a metal source such as Zn ions, an organic linker (imidazole or other ligands), and suitable solvents. It is important to choose a solvent that is compatible with both ZIF-8 and ZnO. In the present chapter, the ZIF-8 directly grown on the surface of the ZnO nanosheets. For that, the grown ZnO nanosheets already on the aluminum substrate were immersed in the precursor solution, which contains 6 mL of DMF, mixed with 2 mL of water containing 100 mg of 2-methylimidazole, and stirred for 30 minutes until obtaining the white color solution. To get ZIF-8, the solution containing ZnO nanosheet film was kept in the oven at 100°C for 12 hrs. After the completion of the reaction time, the substrate was carefully removed from the growth solution, thoroughly washed with deionized water, and then left to dry.

The mechanism behind the growth of ZIF-8 particles on ZnO nanosheets involves the interaction between the ZIF-8 precursor components and the ZnO nanosheet surface, leading to the nucleation and subsequent growth of ZIF-8 crystals. In the literature, the mechanism of ZIF-8 synthesis using ZnO nanorods and nanoparticles is well-reported, and a similar mechanism can be applied to ZIF-8 synthesis using ZnO nanosheets [39–42]. Initially, the ZnO film surface needs to be activated to provide suitable sites for the nucleation of ZIF-8. The activated surface should have exposed reactive sites, such as Zn or oxygen vacancies, which can facilitate the attachment of ZIF-8 precursor species. When the ZIF-8 precursor solution is in contact with the ZnO thin film surface. The Zn^{+2} ions adsorb from ZnO surface, and the

imidazolate linkers can interact with the activated sites on the surface, as shown in Figure 6.1(b). The adsorbed Zn ions and organic linkers on the ZnO surface can undergo chemical reactions, which lead to the formation of small ZIF-8 nuclei. Once the nuclei are formed, further ZIF-8 growth occurs through the continuous attachment of Zn^{2+} ions from ZnO surface and organic linkers from the precursor solution onto the existing nuclei. These nuclei act as the starting points for the growth of larger ZIF-8 crystals [42,73,74]. The obtained ZnO, ZIF-8@ZnO films were characterized for their surface morphology, crystallinity, and surface work function.

Figure 6.1. (a) Schematic synthesis procedure of the ZnO and ZIF-8@ZnO, (b) Mechanism of ZIF-8 particles growth on ZnO nanosheets, (c) Schematic diagram of the ZnO, ZIF-8@ZnO based TENG



devices and its components.

6.2.4 TENG device fabrication

In this work, fabricated two types of TENG devices using ZnO and ZIF-8@ZnO films as the frictional layers. The schematic of the TENG device is illustrated in Figure 6.1(c). In the first type, ZnO nanosheets on an aluminum foil served as one frictional layer, while various opposite frictional layers such as Mica sheet, Silk foam, Nylon, Kapton, PTFE, Silicone, and PMMA were attached to another aluminum foil. This device is referred to as Z-TENG. In the second type, ZIF-8@ZnO film on an aluminum foil acted as one frictional layer and similar opposite frictional layers were attached to the other aluminum foil. This device is denoted as Z8-TENG. A total of 14 TENG devices were fabricated for this study. The active area of each TENG device was $5 \times 5 \text{ cm}^2$, applied force $\sim 7\text{N}$ (Chapter-2, Section 2.4.6), frequency was 4-5Hz and the spacing between the frictional layers was measured as 0.8 cm.

6.3 Results and discussion

6.3.1 SEM studies

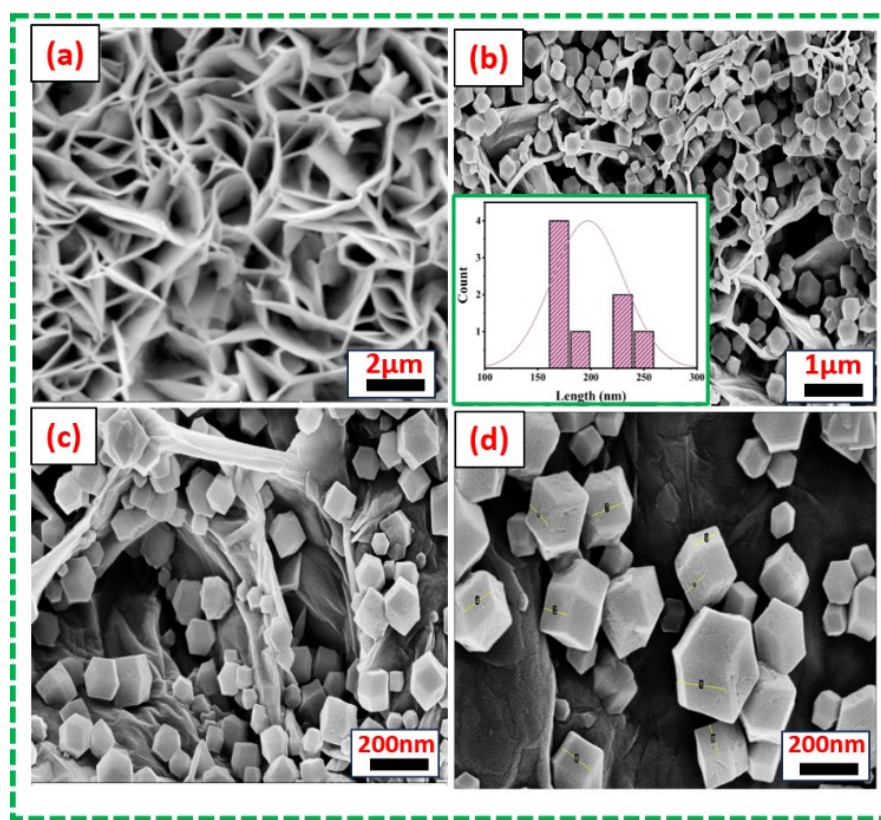


Figure 6.2. SEM images of (a) ZnO nanosheets (b)-(d) ZIF-8@ZnO.

Figure 6.2(a-d) presents SEM images of the ZnO and ZIF-8@ZnO films, showcasing their structure and surface morphology. In Figure 6.2(a), the ZnO nanosheets are observed, exhibiting a sheet-like structure grown uniformly on an aluminum substrate. Moving on to

Figures 6.2(b-d), shows the morphology of the ZIF-8@ ZnO film, where ZIF-8 poly hydron-shaped crystals have uniformly grown on the ZnO sheets. This uniform growth results in an increased effective surface contact area during the TENG operation. The average size of the ZIF-8 particles was determined to be approximately ~ 214 nm, as indicated in the inset of Figure 6.2(b).

6.3.2 XRD and Raman analysis

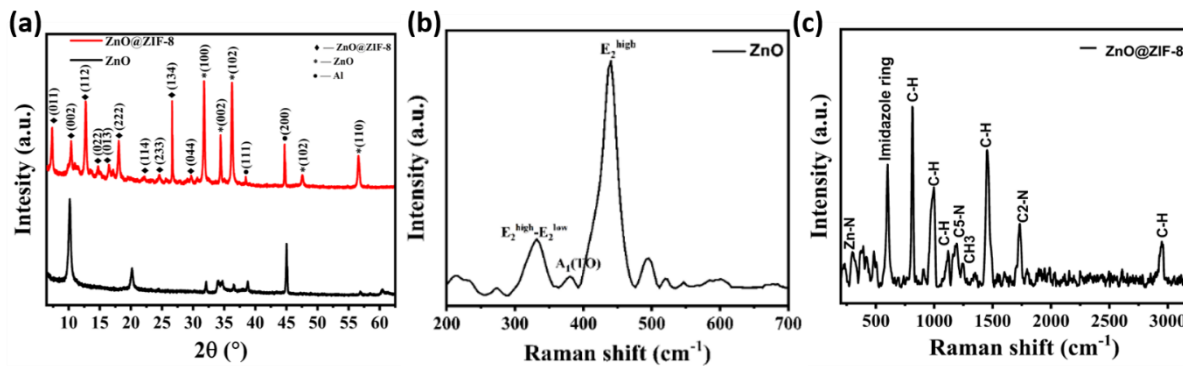


Figure 6.3. (a) XRD pattern of ZnO nanosheets and ZIF-8@ZnO, (b-c) Raman spectra of the ZnO nanosheets and ZIF-8@ZnO.

Additionally, Figure 6.3(a) depicts the XRD pattern of both the ZnO nanosheets and ZIF-8@ZnO samples. The diffraction peaks observed in the XRD spectrum affirm the crystalline nature of the synthesized samples. Furthermore, the characteristic peaks of aluminum and ZnO match well with the JCPDS numbers 03-0932 and 75-0576, respectively, providing further evidence of the sample's crystallinity. The successful synthesis of both ZnO and ZIF-8@ZnO has been corroborated by previous reports [41,74]. In conclusion, Figure 6.2(a-d) and the corresponding analysis demonstrate the well-defined structure and surface morphology of the ZnO and ZIF-8@ZnO films, highlighting the formation of ZIF-8 poly hydron shaped crystals on the ZnO sheets and their potential impact on enhancing the effective surface contact area during TENG operation.

Raman spectroscopy was employed to investigate the vibrational properties of both synthesized ZnO and ZIF-8@ZnO samples. The Raman spectra of the ZnO nanosheets revealed characteristic peaks corresponding to a wurtzite ZnO structure. Specifically, the peaks detected were E_2 high– E_2 low, A_1 (TO), and E_2 high, located at 332 cm^{-1} , 381 cm^{-1} , and 439 cm^{-1} , respectively (Figure 6.3(b))[75,76]. Figure 6.3(c) illustrates the Raman spectra of ZIF-8@ZnO, which exhibited peaks at various wavenumbers denoting distinct vibrational modes and molecular interactions. The observed peaks and their corresponding assignments are as

follows: (1) 299 cm^{-1} and 601 cm^{-1} : Correspond to Zn–N stretching and imidazolium ring puckering, respectively, (2) 812 cm^{-1} , 903 cm^{-1} , and 993 cm^{-1} : Correspond to δH (out of plane), bending C–H (out of plane) ($\text{C}_4\text{–C}_5$), and bending C–H (out of plane) ($\text{C}_2\text{–H}$), (3) 1116 cm^{-1} , 1192 cm^{-1} , 1348 cm^{-1} , and 1453 cm^{-1} : Correspond to stretching of C–N, bending of CH_3 , stretching of $\text{C}_2\text{–N}_1$, and stretching of C–H (methyl), respectively[77–79].

6.3.3 TENG output performance

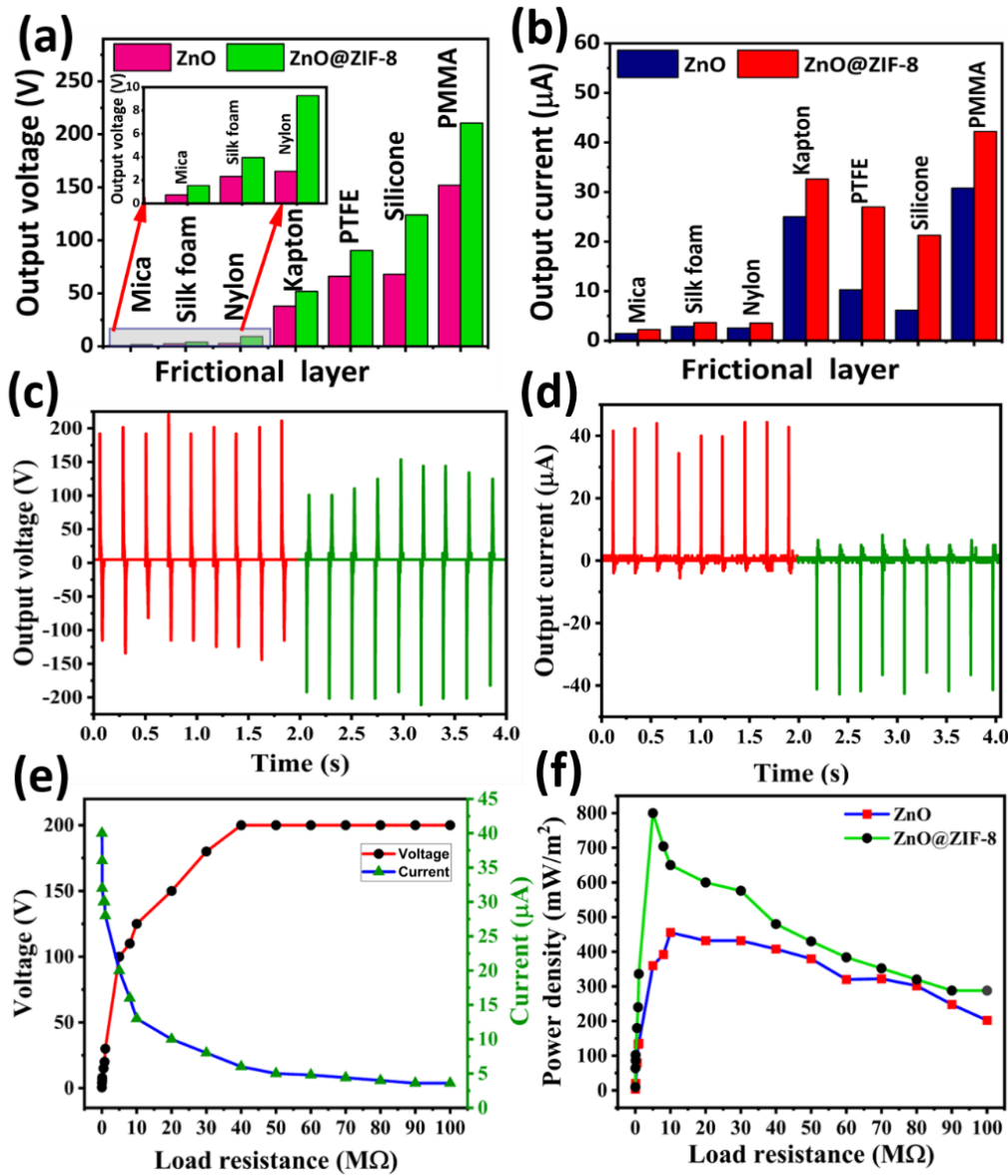


Figure 6.4. The electrical response bar diagrams of the ZnO and ZIF-8@ ZnO based TENG devices with different opposite triboelectric layers (a) open circuit voltage (b) short circuit current. The ZIF-8@ ZnO based TENG output response with PMMA (c) open circuit voltage

(d) short circuit current, (e) The behavior of the ZIF-8@ZnO TENG under the external load resistance, (f) instantaneous power density of the ZnO and ZIF-8@ZnO TENG.

Initially, Z-TENG and Z8-TENG devices' electrical responses were studied with different opposite triboelectric layers such as Mica, Silk form, Nylon, Kapton, PTFE, Silicone rubber, and PMMA. Figure 6.4 (a)-(b) shows a bar chart of the maximum voltage and current obtained for each device with different opposite triboelectric layers, and the waveform graphs for each pair's output responses are provided in **SI Figure S6.1**. The results clearly showed that all Z8-TENG devices performed better than Z-TENG devices. This enhanced output can be explained by the change in the work function and surface morphology of the ZIF-8@ZnO film compared to ZnO nanosheet film.

The Z8-TENG devices output terminals were connected to current and voltage measuring devices to study complete electrical performance characteristics. Figure 6.4 (c)-(d) displays the output voltage and current responses of Z8-TENG under repeated hand tapping. The Z8-TENG demonstrated a maximum output voltage of approximately 200.5 V and a maximum output current of about 41.5 μ A under open circuit and short circuit conditions, respectively. These values were 1.39 and 1.44 times higher than the corresponding values of Z-TENG, highlighting the superior performance of the Z8-TENG (**SI Figure S6.2**).

To confirm that the signals were solely generated by the TENG, the connections at the measurement instruments were reversed, and as a result, the output voltage and current signals were inverted. This observation confirms that the signals were indeed generated exclusively by the TENG. Figure 6.4(e) illustrates the behavior of voltage and current characteristics of the Z8-TENG under various external load resistances. It is evident from the graph that the TENG's output voltage increased with an increase in resistance, whereas the current exhibited an inverse trend. At higher load resistances, both the voltage and current reached saturation levels, with the TENG displaying the highest voltage and the lowest current. The power density of the TENG calculated by the following formula

$$P_{max} = \frac{VI}{Area} \quad \text{-----(1)}$$

Where V and I represents output voltage and current, respectively.

The maximum power density of Z and Z8-TENG were calculated from the load characteristic graphs data and presented in Figure 6.4 (f). It is found that Z8-TENG exhibited maximum power of 800 mW/m² at an optimum load resistance of 10 M Ω , which is 1.76 times higher than

the Z-TENG. As observed from the load characteristic graphs, both TENG devices exhibited a gradual increase in power density as the load resistance was increased until it reached the optimal value. However, beyond the optimum load resistance, the power density declined with a further increase in resistance [80]. In addition, TENGs exhibited the mechanical-to-electrical energy conversion efficiency of 41.36% (Chapter-2, section- 2.4.6).

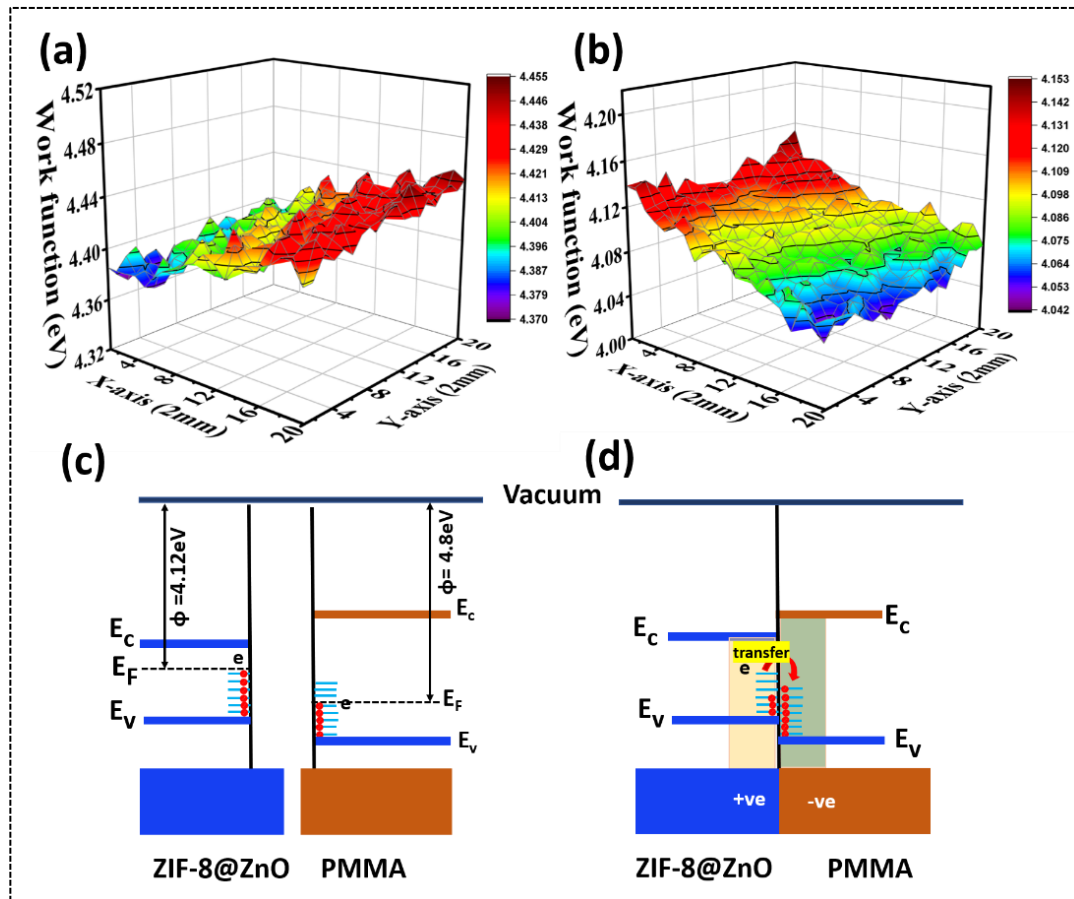


Figure 6.5. 2D work function mapping of (a) ZnO, (b) ZIF-8@ ZnO; (c)-(d) Electron transfer mechanism between ZIF-8@ZnO and PMMA during the contact electrification.

In Figure 6.5(a)-(b), presents the 3D mapping images depicting the work function distribution for the ZnO and ZIF-8@ZnO samples. In the context of TENGs operating in vertical contact separation mode, the output response relies on the difference in work functions between the two triboelectric layers. A larger difference in work functions leads to increased charge transfer during contact electrification, resulting in a higher output voltage. The measurements reveal that the work functions of ZnO and ZIF-8@ ZnO are 4.40 eV and 4.12 eV, respectively, indicating a decrease in the work function for the ZIF-8@ ZnO film compared to the ZnO film. A lower work function indicates that the material has a better tendency to lose electrons during

the triboelectric process. The evidence for enhanced performance of TENG with work function tuning was well reported in the literature [81].

The origin of the electron transfer mechanism can be explained on the basis of contact potential arising from the work function difference between ZIF-8@ZnO and PMMA, as illustrated in Figure 6.5. Figure 6.5(c-d) illustrates fermi energy levels for ZIF-8@ZnO and PMMA based on their respective work function values. Since the work function of ZIF-8@ZnO is lower (4.12 eV) than that of PMMA (4.8 eV), electron transfer occurs from ZIF-8@ZnO to PMMA during the contact electrification process, aimed at equalizing the Fermi levels. This results in ZIF-8@ZnO becoming positively charged and PMMA acquiring a negative charge. An alternative way to explain this phenomenon is through the electron cloud model. When both materials are initially in separated state, electrons are confined within their respective potential wells and cannot move freely. However, when the two materials come into contact, their individual electron clouds partially overlap, creating an asymmetric double-well potential. Consequently, electrons transfer from ZIF-8@ZnO, with its lower work function, to PMMA, which has a higher work function. After the separation, the electrons transferred to PMMA remain within the potential well, resulting in ZIF-8@ZnO acquiring a positive charge and PMMA obtaining a negative charge polarity.

In this chapter, a reference work function value for PMMA of 4.8 eV was taken from, the reported literature [82]. The significant difference in work functions between ZIF-8@ ZnO and PMMA facilitated a more pronounced transfer of electrons from ZIF-8@ZnO to PMMA during the contact electrification process. This enhanced electron transfer led to more transferred charges, consequently enhancing the output performance of the Z8-TENG compared to the Z-TENG. Furthermore, the SEM images revealed that the number of contact points during the contact electrification process may be higher for ZIF-8@ ZnO compared to pure ZnO. The increased number of contact points between the two materials during the triboelectric interaction can be attributed to the presence of ZIF-8 particles on the ZnO nanosheets. These combined effects resulted in a substantial boost in the output performance of the Z8-TENG compared to the conventional Z-TENG, making the modified ZIF-8@ZnO-based TENG a more effective energy harvesting device.

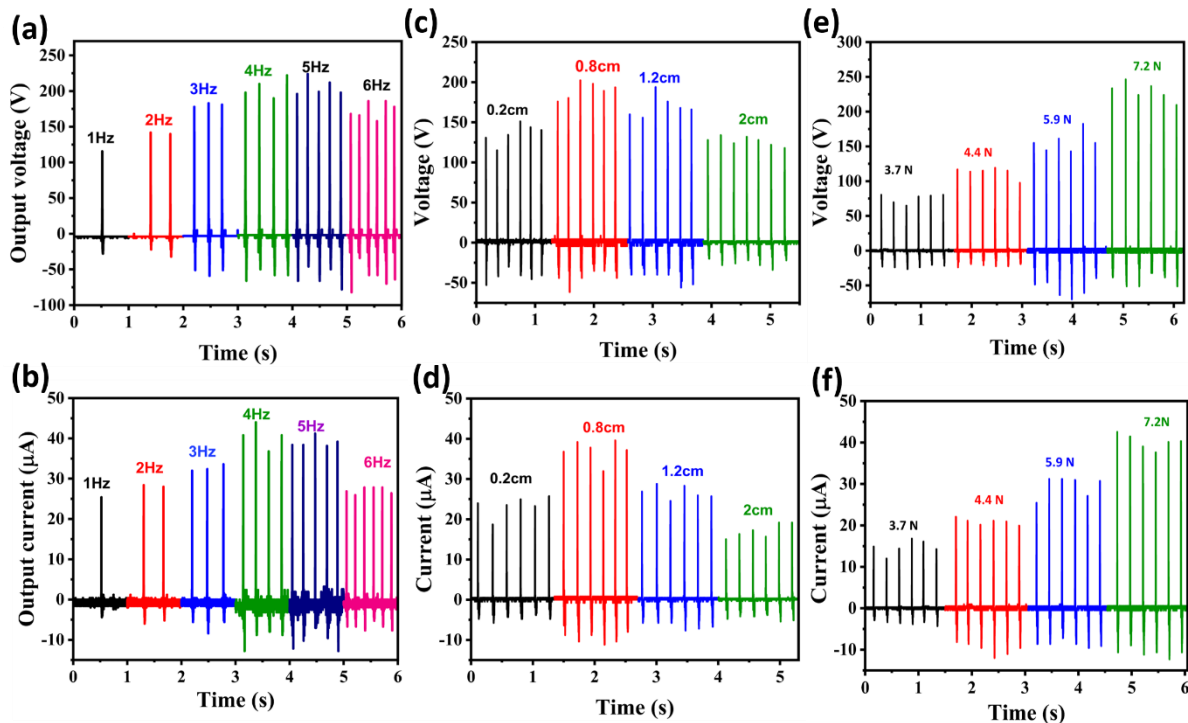


Figure 6.6. Z8-TENG responses as a function of (a-b) different frequencies of applied force(c-d) different spacing (e-f) different impact of the forces.

Furthermore, the output voltage and current for Z8-TENG at various frequencies of applied force were conducted. Figure 6.6(a-b) presents the output performance of the TENGs as a function of the applied frequency. As the frequency increases, the electron flow through the external circuit responds more rapidly, leading to higher output signals. At lower frequencies, the output voltage and current show a linear increase with the frequency due to the increased response time of the TENG to the applied force. This behavior aligns with previous findings reported in the literature [83–85]. However, as the frequency continues to increase, the output voltage and current start to decrease. This phenomenon occurs because the applied force is applied too rapidly at higher frequencies and the TENG cannot fully recover its original position before the next impact of the force occurs [85].

The study investigates the performance of a TENG under varied spacing conditions and external applied forces. The TENG's electrical output was examined with spacing ranging from 0.2 to 2 cm between triboelectric layers as shown in Figure 6.6(c-d). Surprisingly, the experimental results reveal an initial increase in output up to a 1.2 cm spacing, followed by a decline at larger distances, contrary to theoretical expectations. This deviation is attributed to potential improper contact between the triboelectric layers at higher separation distances. The TENG's V_{oc} is defined by the equation $V_{oc} = rd/e$, where d is interlayer spacing, r is vacuum

permittivity, and e is triboelectric charge density. However, the output voltage and current is decreased at a greater spacing in the present chapter, and similar behavior is also observed in the literature [86,87].

Furthermore, the device was assessed for force sensor applications, demonstrating an enhanced output response with increased applied forces (Figure 6.6(e-f)). The augmented output is ascribed to heightened friction between the triboelectric layers, leading to an expanded contact area. This observation aligns with similar trends reported in the literature [88–90]. Overall, the study underscores the critical influence of spacing and applied force on the TENG's electrical performance, emphasizing the need for optimal conditions for effective energy generation.

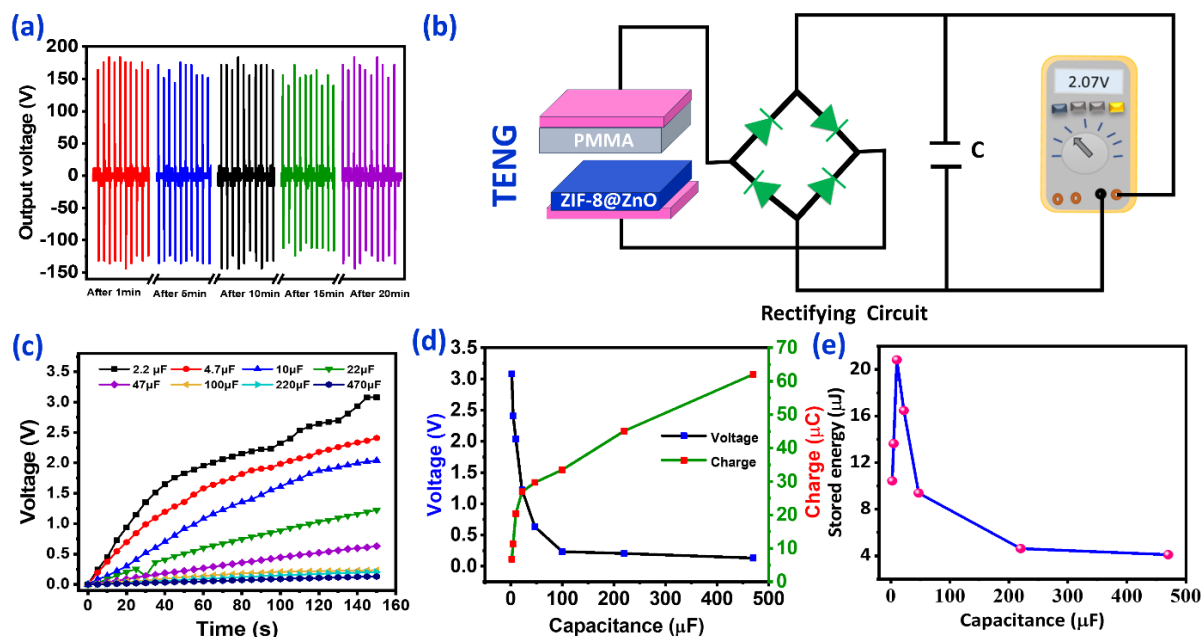


Figure 6.7. (a) Stability of the ZIF-8@ZnO based TENG; (b) Schematic of circuit diagram used for rectification of TENG output and charging capacitors, (c) charged voltage vs time for various capacitors; (d) Saturated stored voltage and charge as function capacitive load; (e) calculated stored energy as function of capacitive load.

To assess the practical applicability of the TENG, its repeatability and stability were crucial factors. In order to evaluate the TENG's stability, continuous tests were performed, and the output voltage was monitored for 20 minutes using an in-house designed tapping machine at a consistent frequency of 4 to 5 Hz. As depicted in Figure 6.7(a), the TENG's output voltage remained constant throughout the entire duration of the test, confirming its excellent stability. For efficient energy storage, a rectifier circuit (schematic representation shown in Figure

6.7(b)) was implemented to capture and store the electrical energy generated by the TENG. This rectifier circuit converted the AC output signal from the TENG into a DC signal suitable for charging capacitors. The TENG's applicability was further validated through charging capacitors and powering electronic gadgets in real-time, which both demonstrated the TENG's reliability in practical applications. During the capacitor charging process, capacitors with various capacitances (2.2, 4.7, 10, 22, 47, 100, 220, and 470 μF) were connected to the rectifier circuit, and their charging behavior was observed over 120 seconds, as shown in Figure 6.7(c). It was observed that capacitors with lower capacitance charged faster, while capacitors with higher capacitance charged more slowly [28,91]. The graph in Figure 6.7(d) represents each capacitor's maximum charged voltage and stored charge. The total energy stored in each capacitor was calculated using the formula $E = 1/2 CV^2$, where C and V are the capacitance and voltage, respectively. Notably, the optimal load capacitance resulted in the maximum stored energy of 20.82 μJ , as depicted in Figure 6.7(e). This indicates that the TENG's impedance and capacitance load are optimally matched at the maximum stored energy point.

6.4 Applications

6.4.1 Self-powered and portable electronic devices application

The Z8-TENG has demonstrated its capability to power multiple small electronic devices. With a contact area of $5 \times 5 \text{ cm}^2$, the Z8-TENG could power a series of 180 red LEDs with each manual tap, as depicted in Figure 6.8(a) ([SI, Video V6.1](#)). This successful demonstration underscores the TENG's effectiveness as a device for converting mechanical energy into electrical energy. To make practical use of this electrical energy, the AC output from the TENG was converted into DC using a bridge rectifier. The electrical energy generated by the TENG through continuous tapping was stored in various capacitors. Once the desired energy level was reached, it was utilized to momentarily power electronic devices.

Figure 6.8(b-d) shows the photographs of LEDs and electronic devices powered by the TENG for brief periods, typically around 1-2 seconds. In just 30 seconds of manual tapping at a frequency of 3 to 4 Hz on the TENG, a 4.7 μF capacitor was charged to a voltage of 2-3 V. This stored energy proved sufficient to momentarily turn on small electronic gadgets like electronic watches ([SI, Video V6.2](#)), calculators ([SI, Video V6.3](#)), and thermometers ([SI](#),

Video V6.4), as depicted in Figure 6.8(b-d). Furthermore, for continuous device operation, the TENG can be attached to a mechanical source with continuous mechanical motion.

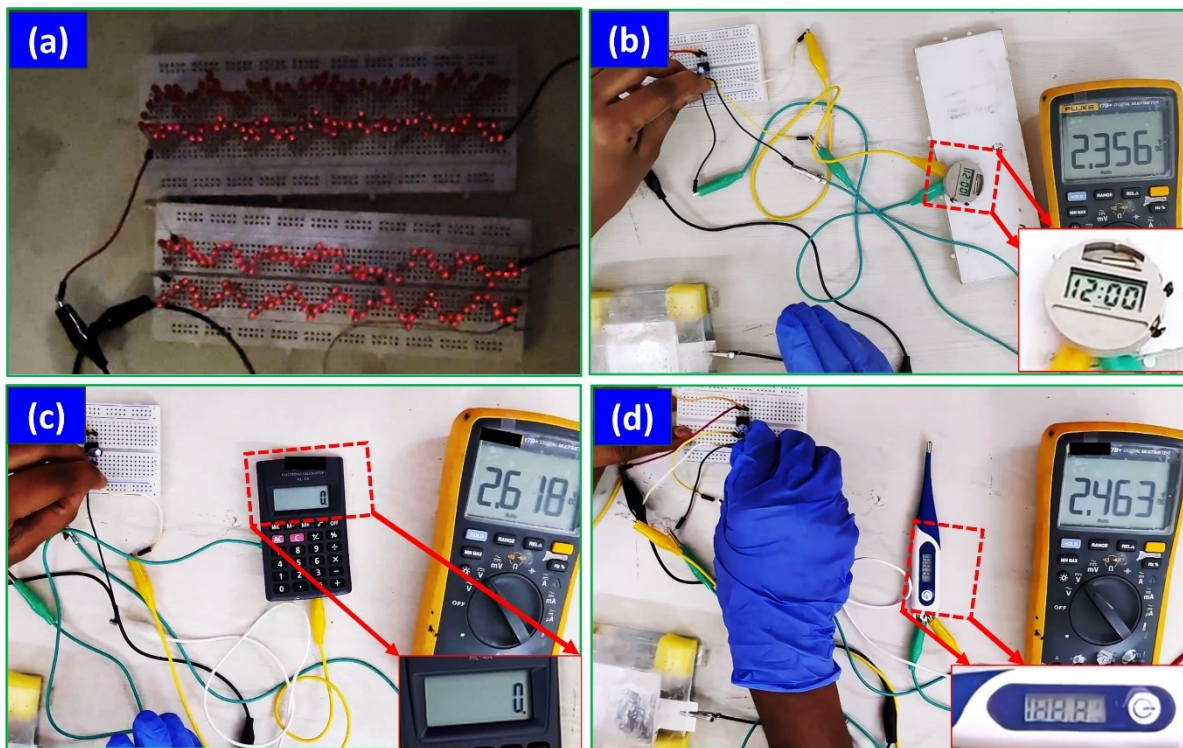


Figure 6.8. Real time photographs of powering LEDs and electronic devices by TENG (a) real time image of the 180 LEDs lighting up by TENG; powering electronic devices momentarily using charged capacitor of $4.7 \mu\text{F}$ (b) wrist watch, (c) calculator and (d) thermometer.

6.5 Conclusions

This study introduced an innovative surface modification approach by synthesizing zeolitic imidazolate framework-8 (ZIF-8) particles on ZnO nanosheets using a straightforward hydrothermal process. The surface modification of ZnO with ZIF-8 substantially modified the work function, number of contact points between the triboelectric materials, leading to remarkable improvements in the output performance of the TENG. The TENG device based on the ZIF-8@ ZnO configuration demonstrated significant enhancements in output voltage, current, and power density by 1.39, 1.44, and 1.76 times, respectively, compared to the ZnO-TENG. Additionally, the practical usability of the ZIF-8@ZnO TENG was successfully demonstrated by charging capacitors and powering small electronic devices. Furthermore, the ZIF-8@ZnO TENG exhibited stable output and outstanding repeatability during continuous testing, further supporting its potential for real-world applications. The combination of ZnO

and ZIF-8 particles offers exciting prospects for advancing TENG devices and driving progress in the field of energy harvesting. This research opens new avenues for enhancing the performance of TENGs using MOFs, making them highly promising for various energy harvesting and self-powered applications.

6.6 References

- [1] S.M.S. Rana, M.T. Rahman, M. Salauddin, S. Sharma, P. Maharjan, T. Bhatta, H. Cho, C. Park, J.Y. Park, Electrospun PVDF-TrFE/MXene Nanofiber Mat-Based Triboelectric Nanogenerator for Smart Home Appliances, *ACS Appl. Mater. Interfaces*. 13 (2021) 4955–4967. <https://doi.org/10.1021/acsami.0c17512>.
- [2] Z. Zhou, X. Li, Y. Wu, H. Zhang, Z. Lin, K. Meng, Z. Lin, Q. He, C.C. Sun, J. Yang, Z.L. Wang, Wireless self-powered sensor networks driven by triboelectric nanogenerator for in-situ real time survey of environmental monitoring, *Nano Energy*. 53 (2018) 501–507. <https://doi.org/10.1016/j.nanoen.2018.08.055>.
- [3] P. Munirathinam, A. Chandrasekhar, Self-Powered Triboelectric Nanogenerator for Security Applications, *Micromachines*. 14 (2023) 592. <https://doi.org/10.3390/mi14030592>.
- [4] H. Wang, J. Cheng, Z. Wang, L. Ji, Z.L. Wang, Triboelectric nanogenerators for human-health care, *Sci. Bull.* 66 (2021) 490–511. <https://doi.org/10.1016/j.scib.2020.10.002>.
- [5] A.S. Dahiya, J. Thireau, J. Boudaden, S. Lal, U. Gulzar, Y. Zhang, T. Gil, N. Azemard, P. Ramm, T. Kiessling, C. O'Murchu, F. Sebelius, J. Tilly, C. Glynn, S. Geary, C. O'Dwyer, K.M. Razeeb, A. Lacampagne, B. Charlot, A. Todri-Sanial, Review—Energy Autonomous Wearable Sensors for Smart Healthcare: A Review, *J. Electrochem. Soc.* 167 (2020) 037516. <https://doi.org/10.1149/2.0162003jes>.
- [6] K. Zhao, G. Gu, Y. Zhang, B. Zhang, F. Yang, L. Zhao, M. Zheng, G. Cheng, Z. Du, The self-powered CO₂ gas sensor based on gas discharge induced by triboelectric nanogenerator, *Nano Energy*. 53 (2018) 898–905. <https://doi.org/10.1016/j.nanoen.2018.09.057>.
- [7] D. Wang, D. Zhang, J. Guo, Y. Hu, Y. Yang, T. Sun, H. Zhang, X. Liu, Multifunctional poly(vinyl alcohol)/Ag nanofibers-based triboelectric nanogenerator for self-powered MXene/tungsten oxide nanohybrid NO₂ gas sensor, *Nano Energy*. 89 (2021) 106410. <https://doi.org/10.1016/j.nanoen.2021.106410>.
- [8] G.H. Lim, S.S. Kwak, N. Kwon, T. Kim, H. Kim, S.M. Kim, S.W. Kim, B. Lim, Fully

- stretchable and highly durable triboelectric nanogenerators based on gold-nanosheet electrodes for self-powered human-motion detection, *Nano Energy.* 42 (2017) 300–306. <https://doi.org/10.1016/j.nanoen.2017.11.001>.
- [9] G.M. Rani, C.M. Wu, K.G. Motora, R. Umapathi, Waste-to-energy: Utilization of recycled waste materials to fabricate triboelectric nanogenerator for mechanical energy harvesting, *J. Clean. Prod.* 363 (2022) 132532. <https://doi.org/10.1016/j.jclepro.2022.132532>.
- [10] G.M. Rani, C.M. Wu, K.G. Motora, R. Umapathi, C.R.M. Jose, Acoustic-electric conversion and triboelectric properties of nature-driven CF-CNT based triboelectric nanogenerator for mechanical and sound energy harvesting, *Nano Energy.* 108 (2023) 108211. <https://doi.org/10.1016/j.nanoen.2023.108211>.
- [11] Z. Yuan, G. Shen, C. Pan, Z.L. Wang, Flexible sliding sensor for simultaneous monitoring deformation and displacement on a robotic hand/arm, *Nano Energy.* 73 (2020) 104764. <https://doi.org/10.1016/j.nanoen.2020.104764>.
- [12] S. Niu, Z.L. Wang, Theoretical systems of triboelectric nanogenerators, *Nano Energy.* 14 (2014) 161–192. <https://doi.org/10.1016/j.nanoen.2014.11.034>.
- [13] S. Wang, L. Lin, Z.L. Wang, Triboelectric nanogenerators as self-powered active sensors, *Nano Energy.* 11 (2015) 436–462. <https://doi.org/10.1016/j.nanoen.2014.10.034>.
- [14] X. Wang, S. Niu, Y. Yin, F. Yi, Z. You, Z.L. Wang, Triboelectric Nanogenerator Based on Fully Enclosed Rolling Spherical Structure for Harvesting Low-Frequency Water Wave Energy, *Adv. Energy Mater.* 5 (2015) 1–9. <https://doi.org/10.1002/aenm.201501467>.
- [15] T.X. Xiao, X. Liang, T. Jiang, L. Xu, J.J. Shao, J.H. Nie, Y. Bai, W. Zhong, Z.L. Wang, Spherical Triboelectric Nanogenerators Based on Spring-Assisted Multilayered Structure for Efficient Water Wave Energy Harvesting, *Adv. Funct. Mater.* 28 (2018) 1–8. <https://doi.org/10.1002/adfm.201802634>.
- [16] Z. Zhang, J. Cai, High output triboelectric nanogenerator based on PTFE and cotton for energy harvester and human motion sensor, *Curr. Appl. Phys.* 22 (2021) 1–5. <https://doi.org/10.1016/j.cap.2020.11.001>.
- [17] K. Li, Y.S. Wu, Q. Liu, G.G. Cheng, Z.Q. Zhang, L.Q. Guo, Y. Wang, J.N. Ding, Rotational Triboelectric Nanogenerator Based on a PDMS@CS Composite Material, *J. Phys. Chem. C.* 122 (2018) 24578–24584. <https://doi.org/10.1021/acs.jpcc.8b08361>.

- [18] Y. Zou, J. Xu, K. Chen, J. Chen, Advances in Nanostructures for High-Performance Triboelectric Nanogenerators, *Adv. Mater. Technol.* 6 (2021) 1–16. <https://doi.org/10.1002/admt.202000916>.
- [19] M.A.P. Mahmud, J.J. Lee, G.H. Kim, H.J. Lim, K.B. Choi, Improving the surface charge density of a contact-separation-based triboelectric nanogenerator by modifying the surface morphology, *Microelectron. Eng.* 159 (2016) 102–107. <https://doi.org/10.1016/j.mee.2016.02.066>.
- [20] V. Kumar, P. Kumar, R. Deka, Z. Abbas, S.M. Mobin, Recent Development of Morphology-Controlled Hybrid Nanomaterials for Triboelectric Nanogenerator: A Review, *Chem. Rec.* 22 (2022) e202200067. <https://doi.org/10.1002/tcr.202200067>.
- [21] L. Zhao, Q. Zheng, H. Ouyang, H. Li, L. Yan, B. Shi, Z. Li, A size-unlimited surface microstructure modification method for achieving high performance triboelectric nanogenerator, *Nano Energy.* 28 (2016) 172–178. <https://doi.org/10.1016/j.nanoen.2016.08.024>.
- [22] F.R. Fan, L. Lin, G. Zhu, W. Wu, R. Zhang, Z.L. Wang, Transparent triboelectric nanogenerators and self-powered pressure sensors based on micropatterned plastic films, *Nano Lett.* 12 (2012) 3109–3114. <https://doi.org/10.1021/nl300988z>.
- [23] Z.H. Lin, Y. Xie, Y. Yang, S. Wang, G. Zhu, Z.L. Wang, Enhanced triboelectric nanogenerators and triboelectric nanosensor using chemically modified TiO₂ nanomaterials, *ACS Nano.* 7 (2013) 4554–4560. <https://doi.org/10.1021/nn401256w>.
- [24] S.H. Shin, Y.H. Kwon, Y.H. Kim, J.Y. Jung, M.H. Lee, J. Nah, Triboelectric charging sequence induced by surface functionalization as a method to fabricate high performance triboelectric generators, *ACS Nano.* 9 (2015) 4621–4627. <https://doi.org/10.1021/acsnano.5b01340>.
- [25] R. Zhang, H. Olin, Material choices for triboelectric nanogenerators: A critical review, *EcoMat.* 2 (2020) 1–13. <https://doi.org/10.1002/eom2.12062>.
- [26] Y. Dong, S.S.K. Mallineni, K. Maleski, H. Behlow, V.N. Mochalin, A.M. Rao, Y. Gogotsi, R. Podila, Metallic MXenes: A new family of materials for flexible triboelectric nanogenerators, *Nano Energy.* 44 (2018) 103–110. <https://doi.org/10.1016/j.nanoen.2017.11.044>.
- [27] S. Kim, M.K. Gupta, K.Y. Lee, A. Sohn, T.Y. Kim, K.S. Shin, D. Kim, S.K. Kim, K.H. Lee, H.J. Shin, D.W. Kim, S.W. Kim, Transparent flexible graphene triboelectric nanogenerators, *Adv. Mater.* 26 (2014) 3918–3925.

<https://doi.org/10.1002/adma.201400172>.

- [28] M.K. Kim, M.S. Kim, H.B. Kwon, S.E. Jo, Y.J. Kim, Wearable triboelectric nanogenerator using a plasma-etched PDMS-CNT composite for a physical activity sensor, *RSC Adv.* 7 (2017) 48368–48373. <https://doi.org/10.1039/c7ra07623a>.
- [29] M. Shanbedi, H. Ardebili, A. Karim, Polymer-based triboelectric nanogenerators: Materials, characterization, and applications, *Prog. Polym. Sci.* 144 (2023) 101723. <https://doi.org/10.1016/j.progpolymsci.2023.101723>.
- [30] L. Xu, T.Z. Bu, X.D. Yang, C. Zhang, Z.L. Wang, Ultrahigh charge density realized by charge pumping at ambient conditions for triboelectric nanogenerators, *Nano Energy*. 49 (2018) 625–633. <https://doi.org/10.1016/j.nanoen.2018.05.011>.
- [31] Z. Shao, J. Chen, Q. Xie, L. Mi, Functional metal/covalent organic framework materials for triboelectric nanogenerator, *Coord. Chem. Rev.* 486 (2023) 215118. <https://doi.org/10.1016/j.ccr.2023.215118>.
- [32] G. Khandelwal, A. Chandrasekhar, N.P. Maria Joseph Raj, S.J. Kim, Metal–Organic Framework: A Novel Material for Triboelectric Nanogenerator–Based Self-Powered Sensors and Systems, *Adv. Energy Mater.* 9 (2019) 1–8. <https://doi.org/10.1002/aenm.201803581>.
- [33] S. Hajra, M. Sahu, R. Sahu, A.M. Padhan, P. Alagarsamy, H.G. Kim, H. Lee, S. Oh, Y. Yamauchi, H.J. Kim, Significant effect of synthesis methodologies of metal-organic frameworks upon the additively manufactured dual-mode triboelectric nanogenerator towards self-powered applications, *Nano Energy*. 98 (2022) 107253. <https://doi.org/10.1016/j.nanoen.2022.107253>.
- [34] S. Hajra, M. Sahu, A.M. Padhan, J. Swain, B.K. Panigrahi, H.G. Kim, S.W. Bang, S. Park, R. Sahu, H.J. Kim, A new insight into the ZIF-67 based triboelectric nanogenerator for self-powered robot object recognition, *J. Mater. Chem. C*. 9 (2021) 17319–17330. <https://doi.org/10.1039/d1tc04729a>.
- [35] S. Potu, M. Navaneeth, R.K. Rajaboina, B. Gollapelli, J. Vallamkondu, S. Mishra, H. Divi, A. Babu, K. Uday Kumar, P. Kodali, High-Performance and Low-Cost Overhead Projector Sheet-Based Triboelectric Nanogenerator for Self-Powered Cholesteric Liquid Crystal, Electroluminescence, and Portable Electronic Devices, *ACS Appl. Energy Mater.* 5 (2022) 13702–13713. <https://doi.org/10.1021/acsam.2c02359>.
- [36] W. Deng, B. Zhang, L. Jin, Y. Chen, W. Chu, H. Zhang, M. Zhu, W. Yang, Enhanced performance of ZnO microballoon arrays for a triboelectric nanogenerator,

- Nanotechnology. 28 (2017) 135401. <https://doi.org/10.1088/1361-6528/aa5f34>.
- [37] Y.P. Jeon, J.H. Park, T.W. Kim, Highly-enhanced triboelectric nanogenerators based on zinc-oxide nanoripples acting as a triboelectric layer, *Appl. Surf. Sci.* 445 (2018) 50–55. <https://doi.org/10.1016/j.apsusc.2018.03.125>.
- [38] Y.P. Jeon, J.H. Park, T.W. Kim, Highly flexible triboelectric nanogenerators fabricated utilizing active layers with a ZnO nanostructure on polyethylene naphthalate substrates, *Appl. Surf. Sci.* 466 (2019) 210–214. <https://doi.org/10.1016/j.apsusc.2018.09.249>.
- [39] Y. Li, C. Ma, P. Nian, H. Liu, X. Zhang, Green synthesis of ZIF-8 tubular membranes from a recyclable 2-methylimidazole water-solvent solution by ZnO nanorods self-converted strategy for gas separation, *J. Memb. Sci.* 581 (2019) 344–354. <https://doi.org/10.1016/j.memsci.2019.03.069>.
- [40] H. Kim, W. Kim, J. Park, N. Lim, R. Lee, S.J. Cho, Y. Kumaresan, M.K. Oh, G.Y. Jung, Surface conversion of ZnO nanorods to ZIF-8 to suppress surface defects for a visible-blind UV photodetector, *Nanoscale*. 10 (2018) 21168–21177. <https://doi.org/10.1039/c8nr06701e>.
- [41] D. Ju, H. Xu, Z. Qiu, J. Guo, J. Zhang, B. Cao, Highly sensitive and selective triethylamine-sensing properties of nanosheets directly grown on ceramic tube by forming NiO/ZnO PN heterojunction, *Sensors Actuators, B Chem.* 200 (2014) 288–296. <https://doi.org/10.1016/j.snb.2014.04.029>.
- [42] X. Wang, J. Liu, S. Leong, X. Lin, J. Wei, B. Kong, Y. Xu, Z.X. Low, J. Yao, H. Wang, Rapid Construction of ZnO@ZIF-8 Heterostructures with Size-Selective Photocatalysis Properties, *ACS Appl. Mater. Interfaces*. 8 (2016) 9080–9087. <https://doi.org/10.1021/acsami.6b00028>.
- [43] R. Wen, J. Guo, A. Yu, J. Zhai, Z. lin Wang, Humidity-Resistive Triboelectric Nanogenerator Fabricated Using Metal Organic Framework Composite, *Adv. Funct. Mater.* 29 (2019) 1–9. <https://doi.org/10.1002/adfm.201807655>.
- [44] G. Khandelwal, N.P. Maria Joseph Raj, S.J. Kim, Zeolitic Imidazole Framework: Metal–Organic Framework Subfamily Members for Triboelectric Nanogenerators, *Adv. Funct. Mater.* 30 (2020) 1–8. <https://doi.org/10.1002/adfm.201910162>.
- [45] G. Khandelwal, N.P. Maria Joseph Raj, S.J. Kim, ZIF-62: a mixed linker metal-organic framework for triboelectric nanogenerators, *J. Mater. Chem. A*. 8 (2020) 17817–17825. <https://doi.org/10.1039/d0ta05067a>.

- [46] G. Khandelwal, N.P. Maria Joseph Raj, V. Vivekananthan, S.J. Kim, Biodegradable metal-organic framework MIL-88A for triboelectric nanogenerator, *IScience*. 24 (2021) 102064. <https://doi.org/10.1016/j.isci.2021.102064>.
- [47] S. Hajra, M. Sahu, A.M. Padhan, J. Swain, B.K. Panigrahi, H.G. Kim, S.W. Bang, S. Park, R. Sahu, H.J. Kim, A new insight into the ZIF-67 based triboelectric nanogenerator for self-powered robot object recognition, *J. Mater. Chem. C*. 9 (2021) 17319–17330. <https://doi.org/10.1039/d1tc04729a>.
- [48] S. Hajra, M. Sahu, A.M. Padhan, I.S. Lee, D.K. Yi, P. Alagarsamy, S.S. Nanda, H.J. Kim, A Green Metal–Organic Framework-Cyclodextrin MOF: A Novel Multifunctional Material Based Triboelectric Nanogenerator for Highly Efficient Mechanical Energy Harvesting, *Adv. Funct. Mater.* 31 (2021) 1–11. <https://doi.org/10.1002/adfm.202101829>.
- [49] Z. Shao, J. Chen, K. Gao, Q. Xie, X. Xue, S. Zhou, C. Huang, L. Mi, H. Hou, A Double-Helix Metal-Chain Metal-Organic Framework as a High-Output Triboelectric Nanogenerator Material for Self-Powered Anticorrosion., *Angew. Chem. Int. Ed. Engl.* 61 (2022) e202208994. <https://doi.org/10.1002/anie.202208994>.
- [50] Y. Wang, X. Zhang, D. Yang, L. Wu, J. Zhang, T. Lei, R. Yang, Highly stable metal-organic framework UiO-66-NH₂ for high-performance triboelectric nanogenerators, *Nanotechnology*. 33 (2022) 065402. <https://doi.org/10.1088/1361-6528/ac32f8>.
- [51] R. Wen, R. Feng, B. Zhao, J. Song, L. Fan, J. Zhai, Controllable design of high-efficiency triboelectric materials by functionalized metal—organic frameworks with a large electron-withdrawing functional group, *Nano Res.* 15 (2022) 9386–9391. <https://doi.org/10.1007/s12274-022-4731-6>.
- [52] R.A. Shaukat, Q.M. Saqib, J. Kim, H. Song, M.U. Khan, M.Y. Chougale, J. Bae, M.J. Choi, Ultra-robust tribo- and piezo-electric nanogenerator based on metal organic frameworks (MOF-5) with high environmental stability, *Nano Energy*. 96 (2022) 107128. <https://doi.org/10.1016/j.nanoen.2022.107128>.
- [53] Y. Hu, Y. Wang, S. Tian, A. Yu, L. Wan, J. Zhai, Performance-Enhanced and Washable Triboelectric Air Filter Based on Polyvinylidene Fluoride/UiO-66 Composite Nanofiber Membrane, *Macromol. Mater. Eng.* 306 (2021) 1–8. <https://doi.org/10.1002/mame.202100128>.
- [54] N. Jayababu, D. Kim, Co/Zn bimetal organic framework elliptical nanosheets on flexible conductive fabric for energy harvesting and environmental monitoring via

- triboelectricity, *Nano Energy*. 89 (2021) 106355.
<https://doi.org/10.1016/j.nanoen.2021.106355>.
- [55] S.M.S. Rana, M.A. Zahed, M.T. Rahman, M. Salauddin, S.H. Lee, C. Park, P. Maharjan, T. Bhatta, K. Shrestha, J.Y. Park, Cobalt-Nanoporous Carbon Functionalized Nanocomposite-Based Triboelectric Nanogenerator for Contactless and Sustainable Self-Powered Sensor Systems, *Adv. Funct. Mater.* 31 (2021) 1–12.
<https://doi.org/10.1002/adfm.202105110>.
- [56] Q. Li, X. An, X. Qian, Methyl Orange-Doped Polypyrrole Promoting Growth of ZIF-8 on Cellulose Fiber with Tunable Tribopolarity for Triboelectric Nanogenerator, *Polymers (Basel)*. 14 (2022) 332. <https://doi.org/10.3390/polym14020332>.
- [57] J. Chen, Z. Shao, Y. Zhao, X. Xue, H. Song, Z. Wu, S. Cui, L. Zhang, C. Huang, L. Mi, H. Hou, Metal-Ion Coupling in Metal-Organic Framework Materials Regulating the Output Performance of a Triboelectric Nanogenerator, *Inorg. Chem.* 61 (2022) 2490–2498. <https://doi.org/10.1021/acs.inorgchem.1c03338>.
- [58] M.T. Rahman, S.S. Rana, M.A. Zahed, S. Lee, E.-S. Yoon, J.Y. Park, Metal-organic framework-derived nanoporous carbon incorporated nanofibers for high-performance triboelectric nanogenerators and self-powered sensors, *Nano Energy*. 94 (2022) 106921. <https://doi.org/10.1016/j.nanoen.2022.106921>.
- [59] Z. Chen, Y. Cao, W. Yang, L. An, H. Fan, Y. Guo, Embedding in-plane aligned MOF nanoflakes in silk fibroin for highly enhanced output performance of triboelectric nanogenerators, *J. Mater. Chem. A*. 10 (2022) 799–807.
<https://doi.org/10.1039/d1ta08605g>.
- [60] C. Huang, G. Lu, N. Qin, Z. Shao, D. Zhang, C. Soutis, Y.Y. Zhang, L. Mi, H. Hou, Enhancement of Output Performance of Triboelectric Nanogenerator by Switchable Stimuli in Metal-Organic Frameworks for Photocatalysis, *ACS Appl. Mater. Interfaces*. 14 (2022) 16424–16434. <https://doi.org/10.1021/acsami.2c01251>.
- [61] T. Wang, Q. Zhu, Q. Zhu, Q. Yang, S. Wang, L. Luo, A highly stable bimetallic organic framework for enhanced electrical performance of cellulose nanofiber-based triboelectric nanogenerators, *Nanoscale Adv.* 4 (2022) 4314–4320.
<https://doi.org/10.1039/d2na00379a>.
- [62] M. Salauddin, S.S. Rana, M. Sharifuzzaman, S.H. Lee, M.A. Zahed, Y. Do Shin, S. Seonu, H.S. Song, T. Bhatta, J.Y. Park, Laser-carbonized MXene/ZrF-67 nanocomposite as an intermediate layer for boosting the output performance of fabric-

- based triboelectric nanogenerator, *Nano Energy.* 100 (2022) 107462. <https://doi.org/10.1016/j.nanoen.2022.107462>.
- [63] S.M.S. Rana, M.T. Rahman, M.A. Zahed, S.H. Lee, Y. Do Shin, S. Seonu, D. Kim, M. Salauddin, T. Bhatta, K. Sharstha, J.Y. Park, Zirconium metal-organic framework and hybridized Co-NPC@MXene nanocomposite-coated fabric for stretchable, humidity-resistant triboelectric nanogenerators and self-powered tactile sensors, *Nano Energy.* 104 (2022) 107931. <https://doi.org/10.1016/j.nanoen.2022.107931>.
- [64] P. Pandey, K. Thapa, G.P. Ojha, M.K. Seo, K.H. Shin, S.W. Kim, J.I. Sohn, Metal-organic frameworks-based triboelectric nanogenerator powered visible light communication system for wireless human-machine interactions, *Chem. Eng. J.* 452 (2023) 139209. <https://doi.org/10.1016/j.cej.2022.139209>.
- [65] S. Barsiwal, A. Babu, U.K. Khanapuram, S. Potu, N. Madathil, R.K. Rajaboina, S. Mishra, H. Divi, P. Kodali, R. Nagapuri, T. Chinthakuntla, ZIF-67-Metal–Organic-Framework-Based Triboelectric Nanogenerator for Self-Powered Devices, *Nanoenergy Adv.* 2 (2022) 291–302. <https://doi.org/10.3390/nanoenergyadv2040015>.
- [66] G. Khandelwal, M.K. Ediriweera, N. Kumari, N.P. Maria Joseph Raj, S.K. Cho, S.J. Kim, Metal-Amino Acid Nanofibers based Triboelectric Nanogenerator for Self-Powered Thioacetamide Sensor, *ACS Appl. Mater. Interfaces.* 13 (2021) 18887–18896. <https://doi.org/10.1021/acsami.1c03075>.
- [67] J. Mo, Y. Liu, Q. Fu, C. Cai, Y. Lu, W. Wu, Z. Zhao, H. Song, S. Wang, S. Nie, Triboelectric nanogenerators for enhanced degradation of antibiotics via external electric field, *Nano Energy.* 93 (2022) 106842. <https://doi.org/10.1016/j.nanoen.2021.106842>.
- [68] Y.M. Wang, X. Zhang, C. Liu, L. Wu, J. Zhang, T. Lei, Y. Wang, X.B. Yin, R. Yang, Remarkable improvement of MOF-based triboelectric nanogenerators with strong electron-withdrawing groups, *Nano Energy.* 107 (2023) 108149. <https://doi.org/10.1016/j.nanoen.2022.108149>.
- [69] Y. Wu, Y. Luo, P.K. Chu, C. Menon, Revealing the conductivity stability of 2D Cu-MOFs as flexible electrodes: demonstration of triboelectric nanogenerators, *Nano Energy.* 111 (2023) 108427. <https://doi.org/10.1016/j.nanoen.2023.108427>.
- [70] Y. Zhang, T. Kang, X. Han, W. Yang, W. Gong, K. Li, Y. Guo, Molecular-functionalized metal-organic frameworks enabling contact-electro-catalytic organic decomposition, *Nano Energy.* 111 (2023) 108433.

- <https://doi.org/10.1016/j.nanoen.2023.108433>.
- [71] Y.D. More, S. Saurabh, S. Mollick, S.K. Singh, S. Dutta, S. Fajal, A. Prathamshetti, M.M. Shirolkar, S. Panchal, M. Wable, S. Ogale, S.K. Ghosh, Highly Stable and End-group Tuneable Metal–Organic Framework/Polymer Composite for Superior Triboelectric Nanogenerator Application, *Adv. Mater. Interfaces*. 9 (2022) 2201713. <https://doi.org/10.1002/admi.202201713>.
- [72] R. Wen, B. Zhao, L. Fan, J. Guo, J. Zhai, Controlling the Output Performance of Triboelectric Nanogenerator Through Filling Isostructural Metal–Organic Frameworks With Varying Functional Groups, *Adv. Mater. Technol.* 8 (2023) 2201330. <https://doi.org/https://doi.org/10.1002/admt.202201330>.
- [73] C. Ying-Bo, Z. Lin-Fei, W. Biao, H. Xiao-Yu, L. Dong-Qing, Z. Feng-Xiao, Z. Yu-Feng, Structural evolution of zeolitic imidazolate framework-8(ZIF-8), *J. Tianjin Polytech. Univ.* 35 (2016) 1–4. <https://doi.org/10.3969/j.issn.1671-024x.2016.05.001>.
- [74] J. Park, J.B. Ju, W. Choi, S.O. Kim, Highly reversible ZnO@ZIF–8-derived nitrogen-doped carbon in the presence of fluoroethylene carbonate for high-performance lithium-ion battery anode, *J. Alloys Compd.* 773 (2019) 960–969. <https://doi.org/10.1016/j.jallcom.2018.09.298>.
- [75] S. Chen, Y. Liu, C. Shao, R. Mu, Y. Lu, J. Zhang, D. Shen, X. Fan, Structural and optical properties of uniform ZnO nanosheets, *Adv. Mater.* 17 (2005) 586–590. <https://doi.org/10.1002/adma.200401263>.
- [76] A. Aljaafari, Size Dependent Photocatalytic Activity of ZnO Nanosheets for Degradation of Methyl Red, *Front. Mater.* 7 (2020) 1–7. <https://doi.org/10.3389/fmats.2020.562693>.
- [77] B. Olaniyan, B. Saha, Comparison of Catalytic Activity of ZIF-8 and Zr/ZIF-8 for Greener Synthesis of Chloromethyl Ethylene Carbonate by CO₂ Utilization, *Energies*. 13 (2020) 521. <https://doi.org/10.3390/en13030521>.
- [78] A. Awadallah-F, F. Hillman, S.A. Al-Muhtaseb, H.K. Jeong, On the nanogate-opening pressures of copper-doped zeolitic imidazolate framework ZIF-8 for the adsorption of propane, propylene, isobutane, and n-butane, *J. Mater. Sci.* 54 (2019) 5513–5527. <https://doi.org/10.1007/s10853-018-03249-y>.
- [79] X. He, C. Yang, D. Wang, S.E. Gilliland, D.R. Chen, W.N. Wang, Facile synthesis of ZnO@ZIF core-shell nanofibers: Crystal growth and gas adsorption, *CrystEngComm*. 19 (2017) 2445–2450. <https://doi.org/10.1039/c7ce00368d>.

- [80] S. Mishra, P. Supraja, D. Haranath, R.R. Kumar, S. Pola, Effect of surface and contact points modification on the output performance of triboelectric nanogenerator, *Nano Energy*. 104 (2022) 107964. <https://doi.org/10.1016/j.nanoen.2022.107964>.
- [81] S. Bayan, D. Bhattacharya, R.K. Mitra, S.K. Ray, Two-dimensional graphitic carbon nitride nanosheets: A novel platform for flexible, robust and optically active triboelectric nanogenerators, *Nanoscale*. 12 (2020) 21334–21343. <https://doi.org/10.1039/d0nr03879b>.
- [82] C.F. Gallo, W.L. Lama, W.L. Lama, Classical Electrostatic Description of the Work Function and Ionization Energy of Insulators, *IEEE Trans. Ind. Appl. IA-12* (1976) 7–11. <https://doi.org/10.1109/TIA.1976.349379>.
- [83] P. Supraja, R.R. Kumar, S. Mishra, D. Haranath, P.R. Sankar, K. Prakash, N. Jayarambabu, T.V. Rao, K.U. Kumar, A simple and low-cost triboelectric nanogenerator based on two dimensional ZnO nanosheets and its application in portable electronics, *Sensors Actuators A Phys.* 335 (2022) 113368. <https://doi.org/10.1016/j.sna.2022.113368>.
- [84] C. Xue, J. Li, Q. Zhang, Z. Zhang, Z. Hai, L. Gao, R. Feng, J. Tang, J. Liu, W. Zhang, D. Sun, A novel arch-shape nanogenerator based on piezoelectric and triboelectric mechanism for mechanical energy harvesting, *Nanomaterials*. 5 (2014) 36–46. <https://doi.org/10.3390/nano5010036>.
- [85] X.S. Zhang, M. Di Han, R.X. Wang, F.Y. Zhu, Z.H. Li, W. Wang, H.X. Zhang, Frequency-multiplication high-output triboelectric nanogenerator for sustainably powering biomedical microsystems, *Nano Lett.* 13 (2013) 1168–1172. <https://doi.org/10.1021/nl3045684>.
- [86] T.C. Hou, Y. Yang, H. Zhang, J. Chen, L.J. Chen, Z. Lin Wang, Triboelectric nanogenerator built inside shoe insole for harvesting walking energy, *Nano Energy*. 2 (2013) 856–862. <https://doi.org/10.1016/j.nanoen.2013.03.001>.
- [87] P. Ravi Sankar, P. Supraja, S. Mishra, K. Prakash, R. Rakesh Kumar, D. Haranath, A novel triboelectric nanogenerator based on only food packaging aluminium foils, *Mater. Lett.* 310 (2022) 131474. <https://doi.org/10.1016/j.matlet.2021.131474>.
- [88] S. Zhao, A Triboelectric Nanogenerator Based on MgSiO₃ Powder for a Human Motion Counter, *J. Electron. Mater.* 50 (2021) 6836–6843. <https://doi.org/10.1007/s11664-021-09245-4>.
- [89] V. Vivekananthan, A. Chandrasekhar, N.R. Alluri, Y. Purusothaman, S.J. Kim, A

highly reliable, impervious and sustainable triboelectric nanogenerator as a zero-power consuming active pressure sensor, *Nanoscale Adv.* 2 (2020) 746–754. <https://doi.org/10.1039/c9na00790c>.

- [90] B. Dudem, R.D.I.G. Dharmasena, R. Riaz, V. Vivekananthan, K.G.U. Wijayantha, P. Lugli, L. Petti, S.R.P. Silva, Wearable Triboelectric Nanogenerator from Waste Materials for Autonomous Information Transmission via Morse Code, *ACS Appl. Mater. Interfaces*. 14 (2022) 5328–5337. <https://doi.org/10.1021/acsami.1c20984>.
- [91] S. Niu, Y. Liu, Y.S. Zhou, S. Wang, L. Lin, Z.L. Wang, Optimization of triboelectric nanogenerator charging systems for efficient energy harvesting and storage, *IEEE Trans. Electron Devices*. 62 (2015) 641–647. <https://doi.org/10.1109/TED.2014.2377728>.

6.7 Supporting information

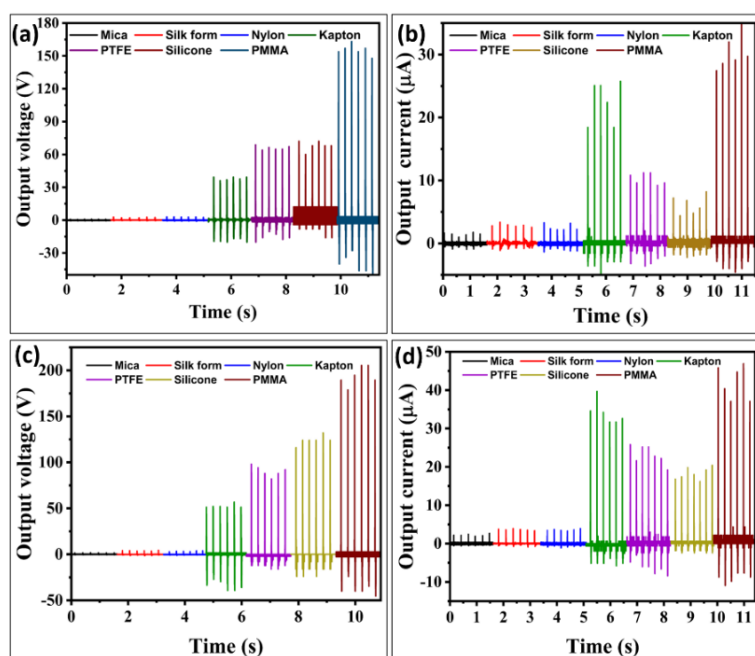


Figure. S6.1 Waveform representation of different dielectrics with fixed triboelectric layer of (a-b) ZnO (c-d) ZnO@ZIF-8.

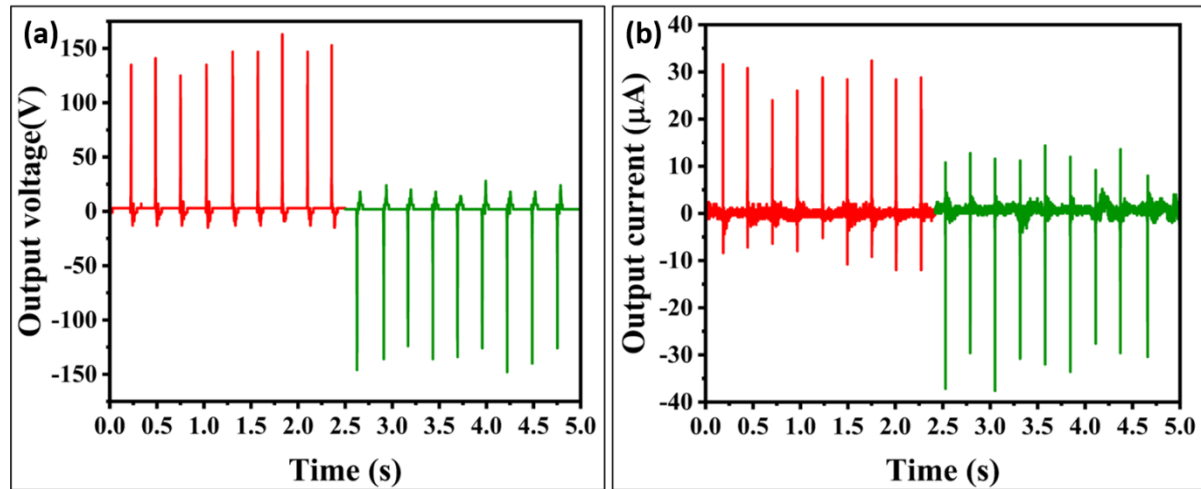
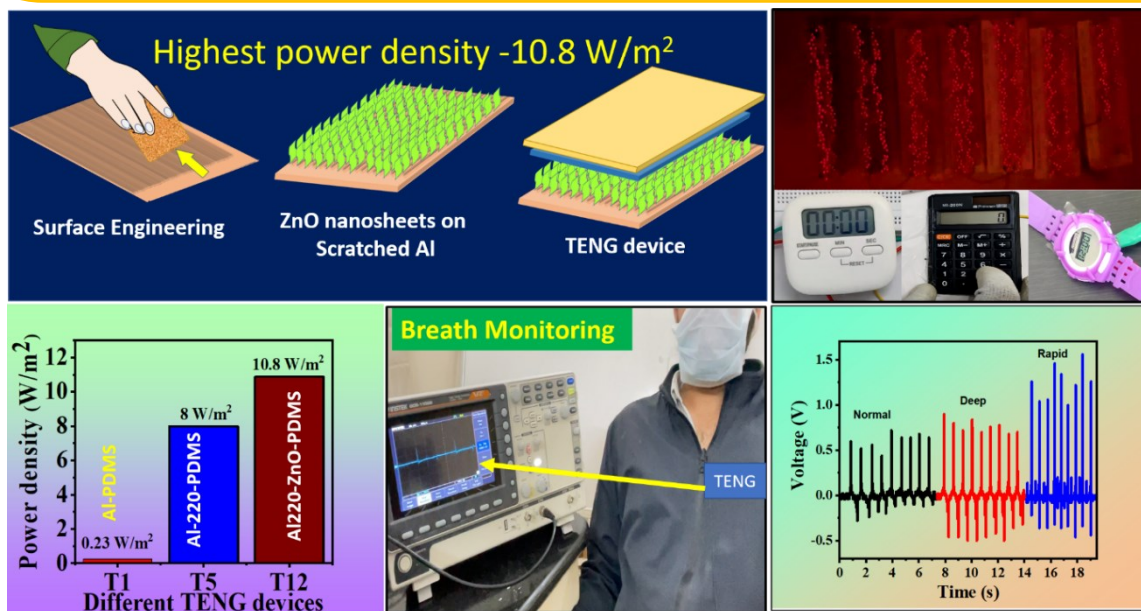


Figure S6.2. The output (a) voltage and (b) current of the ZnO-based TENG with PMMA as an opposite triboelectric layer.

Chapter 7

Surface-Engineered High-Performance Triboelectric Nanogenerator for Self-Powered Health Monitoring and Electronics

This chapter discusses the application of surface engineering on one of the triboelectric layers in the fabrication of the high performance TENG. To modify the surface of the aluminum, sandpapers with grit sizes ranging from P80 to P400 were used, which increased the contact area and resulted in improved output. Furthermore, the ZnO nanosheets were grown on an aluminum substrate and used to create the TENG device both before and after the surface modification. After the modification, the TENG output power was significantly enhanced. Surface engineering not only improves the output of the TENG but also increases the sensitivity, which has major applications in multifunctional wearable devices and health monitoring gadgets.



Publications:

1. "Surface-Engineered High-Performance Triboelectric Nanogenerator for Self-Powered Health Monitoring and Electronics", *Supraja Potu, Navaneeth Madathil, Siju Mishra, Arbacheena Bora, Yuvaraj Sivalingam, Anjaly Babu, Mahesh Velpula, Lakshakoti Bochu, Balaji Ketharachapalli, Anu Kulandaivel, Rakesh Kumar Rajaboina**, *Uday Kumar Khanapuram, Haranath Divi, Prakash Kodali, Banavoth Murali, and Ravi Ketavath, CS Applied Engineering Materials*, 2023, 1, 10, 2663–2675, <https://doi.org/10.1021/acsadmat.3c00416>.

7.1 Introduction

In recent years, there has been increased interest in the development of personal self-powered health monitoring systems, which have the potential to improve human health [1,2]. Wearable electronic devices and sensors are capable of tracking a variety of human physiological signals, including blood pressure, breathing rate, body temperature, pulse detection, heartbeat rate, and oxygen saturation levels. By detecting the monitored signals, these devices/sensors will provide information about the patient's health before they get critically sick. Various technologies, such as pyroelectric nanogenerators [3,4] piezoelectric [5–7], and triboelectric nanogenerators [8–10], have been established depending on the requirements in the application of health care monitoring. Among these, triboelectric nanogenerators (TENGs) have emerged as a promising option due to their high sensitivity to mechanical vibration, ability to generate high output voltages, low-frequency operation, variety of working modes, and wide range of material options.

TENGs have been considered to be one of the most successful methods for extracting low-frequency mechanical energy for sensor development. By wearing a TENG device on the body respirator, cardiovascular, and physical activity can be monitored. Therefore, the TENG is undoubtedly one of the best wearable and self-powered health monitoring device options. TENGs have already been used in health monitoring applications such as respiration sensing [11], heartbeat detection [12], pulse detection [13], joint motion sensing [14], electroacupuncture [15], throat phone [16], neural [17], CO₂ detection [18], sweat [19], and gait monitoring [20]. However, higher power density and high-sensitivity TENGs are needed for health monitoring, primarily driven by the size and weight constraints of wearable and implantable devices. Therefore, improving the power density of TENGs is crucial for enhancing their sensing capabilities and powering portable electronic devices.

In recent years, there have been significant efforts to increase the TENG output, with the developments focused on various strategies such as selecting different triboelectric materials with large work function differences, [21,22] increasing the surface contact area of the triboelectric layers, [23–25] optimizing the external circuit, and combining TENGs with other energy harvesting technologies [26–28]. Among these methods, increasing the surface contact area is particularly attractive, as it can significantly enhance the charge transfer and power output. However, the existing techniques, such as chemical etching [23], grafting [29], grating-electrode-enabled surface plasmon excitation [30], polymer coating [31], plasma

treatment [32], physical surface modification [33], ultrasonic, and X-ray radiation and ion injection [34], are expensive, time-consuming, and may have environmental hazards. Therefore, it is crucial to develop an ecofriendly, inexpensive, and time efficient surface modification technique.

In this chapter, a cost-effective physical surface modification technique utilized [33]. This method has many advantages over existing methods, such as being relatively inexpensive and being a straightforward technique that does not require specialized equipment or extensive training. It can be performed manually, and using this method not only increases the surface area but also increases the contact points, which enhances the output of the TENG. Other literature output performances of TENG employing various surface modification methods compared in tabular form [33,35–40] (**SI Table S7.1**).

The surface modification method involves using sandpapers to scratch against the triboelectric layer (Aluminum), increasing its surface area and improving the output performance and sensitivity of the TENG. Furthermore, ZnO nanosheets were synthesized on surface-modified aluminum substrates, resulting in a higher density of ZnO nanosheets than those grown on a flat aluminum substrate.

Table 7.1. Comparison of electrical output performance of ZnO nanostructures-PDMS based TENG as in the literature with present work.

S.No	ZnO nanostructures	PDMS as triboelectric layer	Another triboelectric layer	Output voltage and current	Power/Power density	Applications	Ref.
1	Al-doped ZnO: GO films	-	PI	105 V, 2.85 μ A/cm ²	2.5W/m ²	power up of LEDs	[41]
2	Chitosan +ZnO bilayer film	PDMS	-	0.8V, ~40nA	27.2 μ W/ m ²	acetone sensing and non-invasive diabetes diagnosis	[42]
3	Porous PDMS covered carbon fibers yarns with aligned ZnO nanorods	-	-	72V, 10 μ A	741mW/ m ²	Power up 28 LEDs and thermometer and hygrometer	[43]
4	Ce-doped ZnO-PANI nanocomposite film	PDMS	-	0.4V	-	human health monitoring	[44]
5	Ga doped ZnO nanorods	PDMS		27V, 0.119 μ A/cm ²	-	-	[45]
6	ZnO	PDMS	-	350 V, 4 μ A	-	-	[46]
7	Ga-doped ZnO nanowire	PDMS	-	65 V, 225nA/cm ²	36.5mW/m ²	-	[47]
8	polyacrylonitrile (PAN) nanofiber/ZnO Nanorods	PDMS	-	166 V, 37 μ A	1.85W/m ²	Power up light-emitting diodes (LEDs), calculator, and hygrothermograph and blue energy harvesting	[48]

Surface-Engineered High-Performance TENG.... Health Monitoring and Electronics

9	PDMS+ZnO microballoon	-	PTFE	57 V, 59 mA m ⁻²	1.1W/m ²	Powered up 30 commercial LEDs,	[49]
10	surface-embossed PDMS on ZnO nanoflakes	-	Al coated fabric	166.6 V, 113.3μA	229.28μW	-	[50]
11	yttrium (Y)-doped ZnO microflowers//PDMS	-	Tissue paper	247 V, 7μA	~6W/m ²	powering various portable electronics and biomechanical sensors	[51]
12	ZnO nanoflowers/ PDMS	-	Al	260 V, 11.21μA	0.26W /m ²	20 commercial light-emitting diodes and	[52]
13	ZnO nanorods	PDMS	-	5.34 V, 181.4nA	-	-	[53]
14	ZnO nanorods	PDMS	-	11V, 3.5μA	246mW/ m ²	-	[54]
15	ZnO nanorods/PDMS	-	PET	7.7 V	48mW/ m ²	powering of small electronic devices	[55]
16	ZnO nanowires/PDMS	-	Al	150 V, 14μA	2.1W/ m ²	-	[56]
17	ZnO nanorods/PDMS	-	Ag coated textile	170 V, 120μA	1.1mW	self-powered smart clothes and personal electronics	[57]
18	ZnO ellipse/PDMS	-	Al	120V, 29.8μA	1.04W/m ²	-	[58]
19	ZnO pyramid/PDMS	-	Al	160 V, 14.6μA	0.6 W/m ²	-	[58]
20	ZnO nanospheres/Porous PDMS	-	Graphene	271 V, 7.8μA	0.975W/m ²	-	[59]
21	ZnO+ PAA ionogel/PDMS	-	Skin	189 V, 6.2μA	2.17W/m ²	Wearable power technology and self-driven sensing.	[60]
22	GQD-reinforced ZnO nanosheets	PDMS	-	40V, 2μA/cm ²	-	Self-powered UV sensors	[61]
23	ZnO nanosheets	PDMS	-	1442V, 155μA	10.8 W/m ²	Portable electronic devices, wearable devices, and self-powered healthcare sensors.	This work

Further, TENG devices were fabricated using ZnO nanosheets synthesized on a surface-modified aluminum with PDMS films as an opposite triboelectric layer. It was observed that the power density (10.8 W/m²) of the surface-modified device with ZnO is 46 and 1.36 times higher than the plane aluminum-PDMS and scratched aluminum-PDMS TENGs, respectively. The addition of ZnO nanosheets greatly enhanced the power density. So far, the power density in this work is the highest value for the ZnO nanosheets-based TENGs, the detailed literature review presented in **Table 7.1**.

The fabricated TENG is able to turn on electric devices of the digital watch, stopwatch, and calculator, and also illuminates 824 LEDs directly without using any storage element. The designed TENG is also utilized for respiratory monitoring in real time. This chapter, experimentally proved that the fabricated TENG has significant potential in the field of wearable sensors and offers for patient's greater convenience to those who are dealing with respiratory health problems.

7.2 Experimental section

7.2.1 Materials

Zinc nitrate hexahydrate ($\text{Zn}(\text{NO}_3)_2 \cdot 6\text{H}_2\text{O}$) and hexamethylenetetramine (HMTA), aluminum substrates (thickness ~ 0.1 mm), poly (dimethylsiloxane) (PDMS), and sandpapers with different grit sizes of 80, 120, 180, 220, 320, and 400 were utilized in the present chapter.

7.2.2 Surface modification of aluminum substrates using sandpapers

The contact surface area needs to be increased to obtain a high-output performance TENG. This was achieved by scratching aluminum substrates using sandpapers with different grit sizes (80, 120, 180, 220, 320, and 400) [33]. The surface of the sandpapers was examined using an optical microscope, and real time images are presented in Figure 7.1. In one group of samples, the aluminum substrate was scratched in one direction repeatedly for 5 min to increase surface roughness, and this process was repeated with different grit size sandpapers (**SI, Figure S7.1(a-g)**). After conducting several experiments, it was observed that the aluminum substrate scratched with a 220-grit size sandpaper (220) exhibited the maximum TENG output response. In another group of samples, the effect of scratching time on TENG output was investigated by scratching the aluminum substrate with a 220-grit size for different durations ranging from 1 to 9 min (**SI, Figure S7.2(a-f)**).

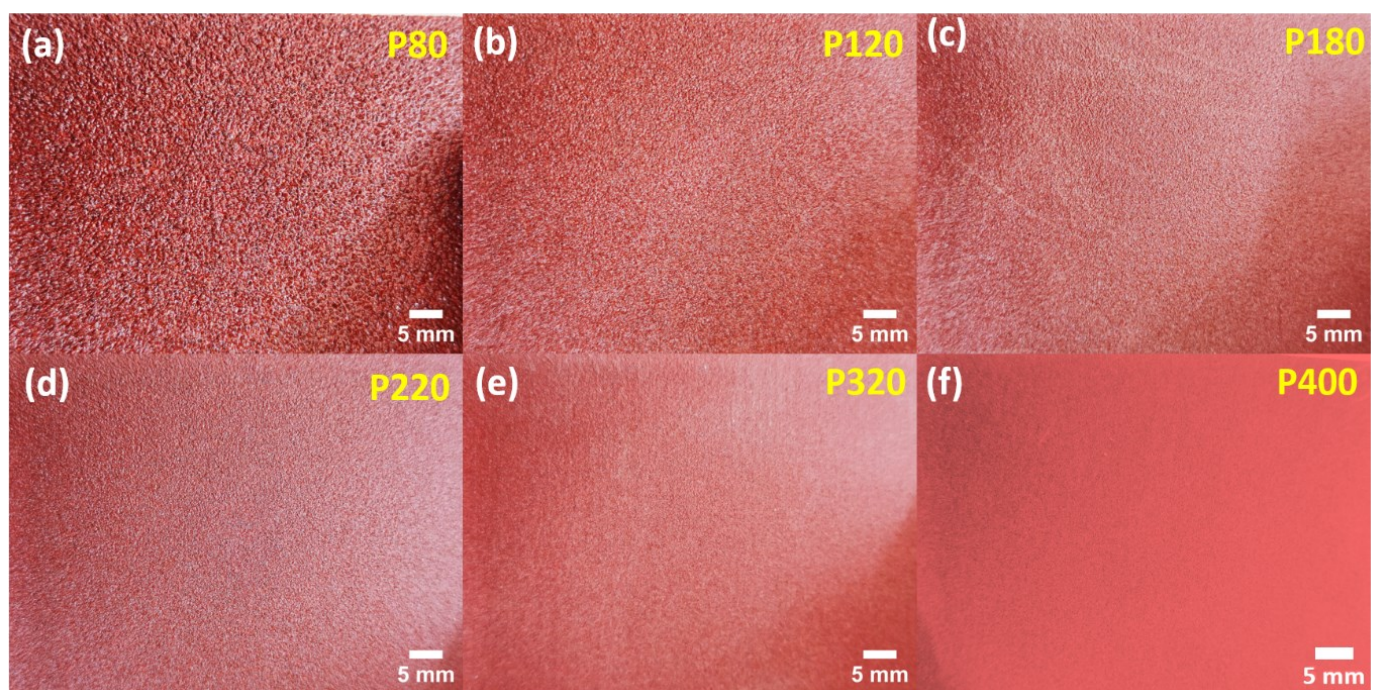


Figure 7.1. Real-time images of sand papers with different grit sizes of P80, 120, 180, 220, 320, and 400, respectively.

7.2.3 ZnO nanosheets synthesis

The ZnO nanosheet film was synthesized on Al substrates by following the same method mentioned in Chapter-2, Section-2.1.

7.2.4 Preparation of the PDMS film

In Figure 7.2(a), a schematic diagram of the PDMS film preparation process is presented. To prepare the PDMS solution, and the curing agent and elastomer were mixed in a ratio of 1:10 (w/w). The mixture was stirred mechanically for 15 min to ensure a homogeneous solution. The mixture was then poured into a clean Petri dish and allowed to settle for 5 min to remove any bubbles. Subsequently, the Petri dish was placed in an oven at 100 °C for 2 h. The thin and flexible self-standing PDMS film was gently removed from the Petri dish after the process was complete. This process was repeated to produce PDMS films of varying thicknesses. The original photographs of the prepared PDMS and its flexible nature can be found in, Figure 7.2(b-d).

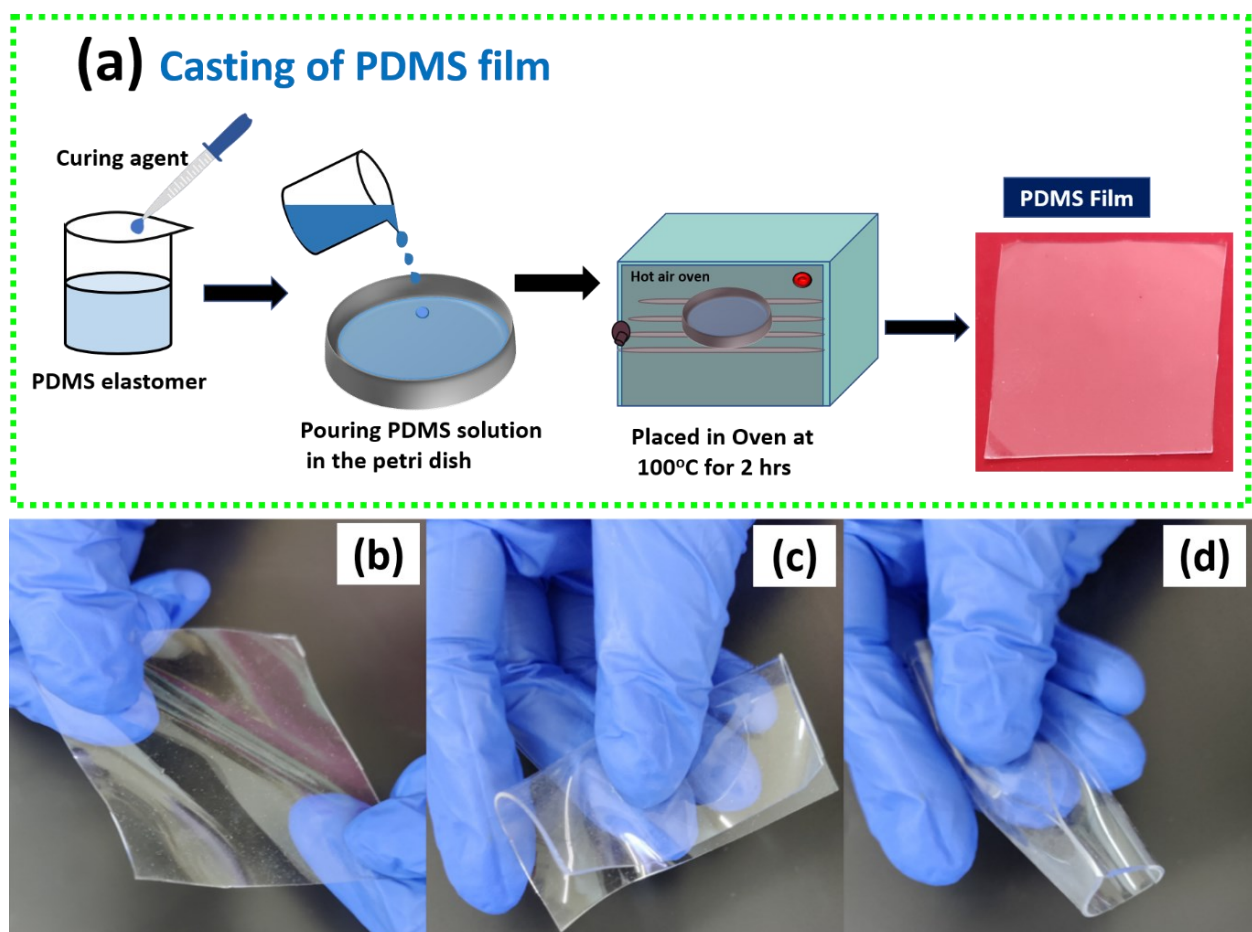


Figure 7.2. (a) Schematic view of the fabrication of PDMS film and photographs of prepared PDMS. Real time images of PDMS film, (b) elongated, (c) folded, and (d) twisted.

7.2.5 TENG device fabrication

Two sets of TENG devices were fabricated in this study. The first set involved using plane/scratched Al and PDMS as the triboelectric pair without a ZnO coating on Al. The second set of devices included ZnO nanosheets grown on the plane/scratched Al and PDMS as the triboelectric pair. The detailed list of devices and their geometry are presented in **SI, Table S7.2**. The TENG devices T1–T7 are made of plane aluminum/surface-modified aluminum with fixed PDMS as the opposite triboelectric layer. In the case of T8–T15 devices, ZnO nanosheets were grown on plane aluminum/surface-modified aluminum with a fixed PDMS as an opposite triboelectric layer. The fabrication process for TENG device is detailed in Section-2.3.2, and their structure details are listed in **SI, Table S7.2**. In the present chapter, Aluminum substrates were used as top and bottom conducting electrodes, and PDMS and ZnO nanosheets acted as the top and bottom frictional layers, respectively. To study the energy harvesting properties of the TENG devices, they were subjected to a hand tapping force of ~ 7 N (Chapter-2, Section 2.4.6), frequency of 3-5 Hz and 0.8 cm of spacing has provided between the triboelectric layers to operate the device under contact separation mode.

7.3 Results and discussion

7.3.1 SEM and optical microscopic studies

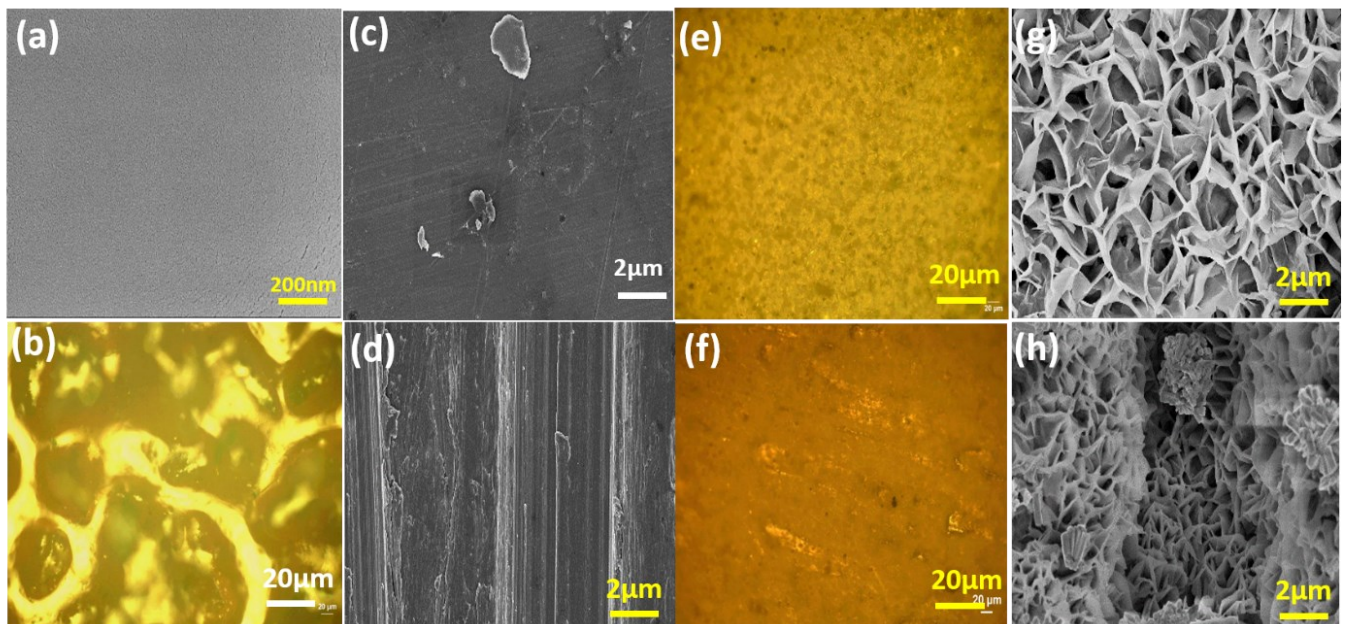


Figure 7.3. (a) Surface morphology of PDMS; (b) optical images of sandpaper with a grit size of 220; SEM images of (c) Plane Al, (d) scratched Al; optical images of ZnO nanosheets

film on (e) plane, (f) scratched aluminum; SEM images of ZnO nanosheets on (g) Plane Al and (h) scratched Al, respectively.

The TENG performance is strongly influenced by the contact surface area, which is, in turn, affected by the morphology of the frictional layers. SEM and optical microscopy were used to examine the surface morphology of the ZnO and PDMS film surfaces. Figure 7.3(a) shows the surface morphology of the PDMS (~0.2 mm thickness) film, and it can be seen that the PDMS film has a smooth surface. In addition, Figure 7.3(b) presents an optical microscopy image of sandpaper with a grit size of P220. The optical images of the other samples, consisting of scratched aluminum with various grit sizes (80, 120, 180, 320, and 400) and scratching times (1, 3, 5, 7, and 9 min) at a fixed grit size of 220, were provided in **SI, Figure S7.1 and S7.2**. The surface of aluminum exhibits a distinct morphology when scratched with sandpaper, creating valleys and hill-like structures compared to the plane aluminum surface, as shown in Figure 7.3(c,d). Optical microscopy images in Figure 7.3(e,f) depict the grown ZnO nanosheets on both plane and scratched aluminum substrates (grit size, 220, and scratching time, 5 min). Here, we can observe the uniform growth of the ZnO film across both substrates, as confirmed by the microscopy images. However, SEM images in Figure 7.3(g,h) revealed that the density of ZnO nanosheets was higher on the scratched aluminum substrate compared to the plane aluminum substrate. The increased density of ZnO nanosheet growth is attributed to the increased surface area of the scratched aluminum surface. This increased surface area and density of ZnO nanosheets significantly enhance the performance of the TENG.

7.3.2 AFM and XRD studies

Further support for the SEM observations was provided by studying the surface topography of ZnO nanosheets grown on the scratched aluminum substrate and PDMS film using atomic force microscopy (AFM). Figures 7.4(a) and (b) show AFM analysis of ZnO and PDMS films, which shows that the surface roughness of PDMS is greater than that of the ZnO film, which is employed to enhance the surface area. The root-mean-square (RMS) surface roughness of the ZnO nanosheet film and PDMS films are 74 and 56.5 nm, respectively.

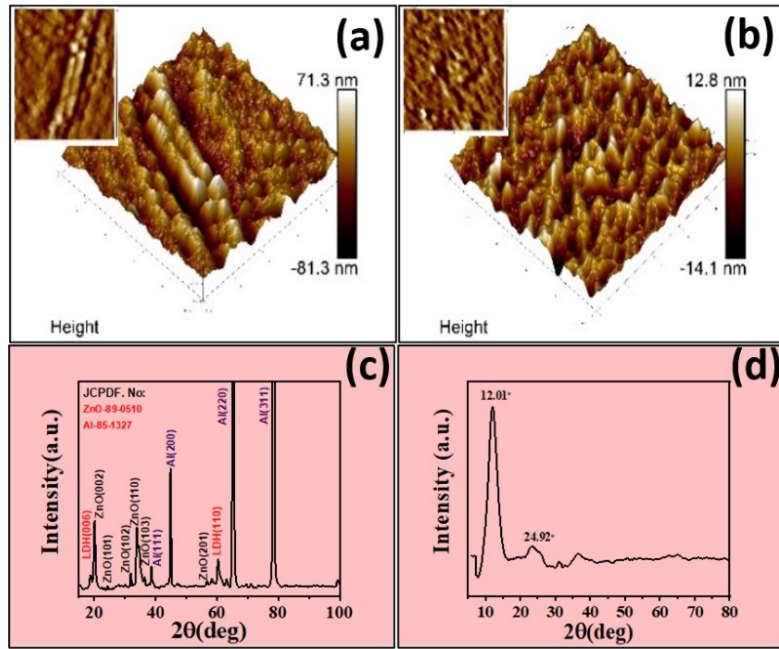


Figure 7.4. ZnO nanosheets on Al substrate and PDMS films (a-b) AFM images, (c-d) XRD pattern.

In Figure 7.4(c), all detectable peaks at $20.2^\circ, 24.38^\circ, 31.96^\circ, 33.95^\circ, 36.39^\circ$ and 56.86° belong to (002), (101), (102), (110), (103) and (201) planes of ZnO wurtzite structure (JCPDF No.89-0510). The diffraction peaks at 18.8° and 60.3° peaks correspond to the planes of ZnO: LDH layer[62,63].The obtained peaks of the aluminum sheet were well matched with JCPDF no.85-1327, and these crystallographic planes are similar to the peaks appearing at $38.6, 44.9, 65.3$ and 78.5° , which corresponds to the (111), (200), (220) and (311), respectively. Meanwhile, in Figure 7.4(d), the peaks at 12.01° and 24.92° corresponds to PDMS film.

7.3.3 FTIR and Raman analysis

Further, from FTIR analysis (Figure 7.5(a)), the absorption peak at 3364 and 2922 cm^{-1} were stretching vibrations of O-H amide group and C-H groups, the absorption peaks at 1636 and 1385 cm^{-1} corresponds to C=C stretching vibration of the alkane group and C=O group asymmetric vibration. The peaks at 1034 and 880 cm^{-1} corresponds to stretching vibration of C-N and C-H groups. The absorption peak at 581 cm^{-1} due to stretching vibration of ZnO hexagonal phase[64,65] (Figure 7.5(a)). The absorption peak at 2962 cm^{-1} reflects the stretching vibration of CH_3 group. The absorption peaks near 1256 cm^{-1} are the symmetric deformation of the Si- CH_3 group and the high-intensity peaks at 1010, 843, and 783 cm^{-1} stretching vibrations of Si-O-Si, Si-C and Si-O groups, respectively[66] (Figure 7.5(b)).

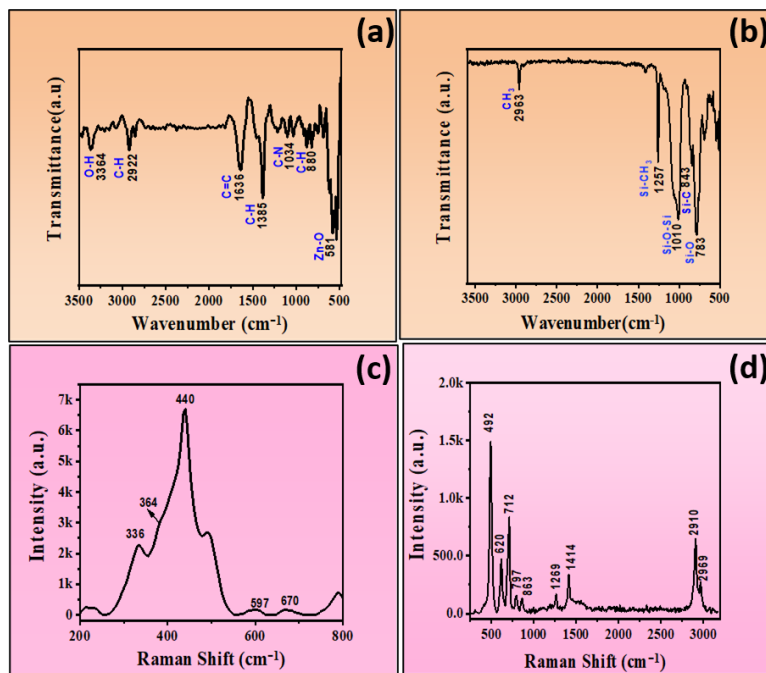


Figure 7.5. ZnO nanosheets on Al substrate and PDMS films, (a-b) IR spectra range from 400-4000 cm^{-1} , and (c-d) Raman spectra, respectively.

Figure 7.5(c), Raman spectra of ZnO nanosheets show that the detected peaks correspond to a wurtzite ZnO structure[67]. The peaks correspond to E_2 high- E_2 low, $\text{A}1$ (TO), and E_2 high, at 332 cm^{-1} , 381 cm^{-1} , and 439 cm^{-1} , respectively. The peaks at 597 and 670 cm^{-1} corresponds to E_1 low and E_2 high- E_2 low. These results are consistent with the XRD results. PDMS shows two prominent peaks at 2905 and 2960 cm^{-1} , which correspond to symmetric and antisymmetric $-\text{CH}_3$ stretching vibrations, respectively. The peak 492 cm^{-1} corresponds to the symmetric stretching of Si-O-Si (Figure 7.5(d)).

The obtained vibrational modes of the Raman spectra of PDMS have given[68,69] below.

Table 7.2. vibrational modes of the Raman spectra of PDMS

S. No.	Wavenumber (cm ⁻¹)	Vibrational mode
1.	492	Stretch Si–O –Si
2.	620	Stretch asymmetric Si–C
3.	712	Stretch symmetrical Si–C
4.	797	Stretch Si–C
5.	863	Stretch asymmetric CH ₃
6.	1269	Bending symmetrical Si-CH ₃
7.	1414	Bending asymmetric CH ₃
9.	2910 & 2969	Symmetric and antisymmetric – CH ₃ stretching vibrations

7.3.4 SKP characterization of frictional layers

Further, SKP was used to measure the work function of plane Al, scratched Al (grit 220), plane Al-ZnO, scratched Al-ZnO (grit 80), scratched Al-ZnO (grit 220), scratched Al-ZnO (grit 400), and the corresponding work function graphs are shown in Figure 7.6(a-e). The calculated work functions of plane Al, scratched Al (grit 220), Plane Al-ZnO, scratched Al-ZnO (grit 80), scratched Al-ZnO (grit 220), and scratched Al-ZnO (grit 400) were 4.22, 4.14, 4.48, 4.29, 4.08, and 4.26 eV, respectively. The work function difference significantly impacts the triboelectric charge density of tested materials. If the work function difference is higher between the contacting layers, more electrons will be transferred, resulting in higher charge density. As PDMS layer is constant for all the devices fabricated in this work, its work function value is 4.58 eV [70].

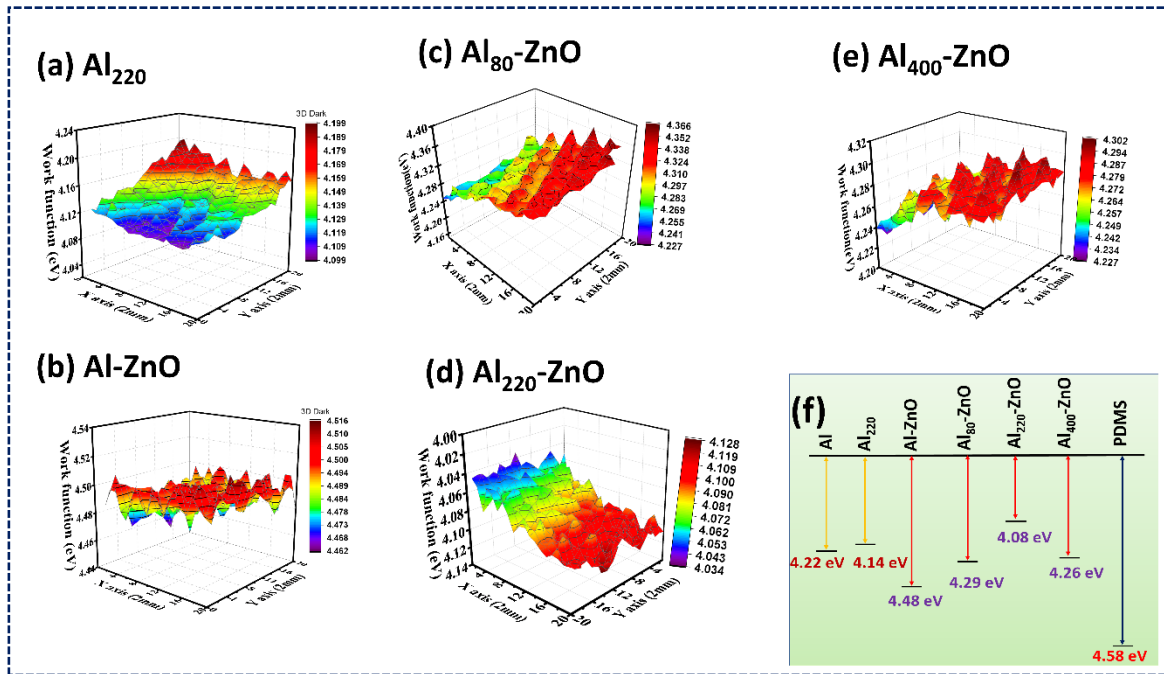


Figure 7.6. SKP raster scan images of samples (a) Scratched Al with 220 grit sandpaper; ZnO nanosheet film on (b) Plan aluminum, (c) Scratched Al with 80 grit size (d) Scratched Al with 220 grit size (e) Scratched Al with 400 grit size (f) comparison of work functions of all films.

According to the theory of work function, the amount of surface charges is related to the work function and the amount of the dielectric layers, which satisfy the following equation:[71,72]

$$Q_s = \alpha S \Delta \phi = \alpha S (\phi_1 - \phi_2)$$

Where Q_s , S , ϕ_1 , and ϕ_2 are the number of tribo-charges formed on the dielectric surface, contact area (areal size), and work function of the dielectric materials, respectively. The work function difference is higher for Al₂₂₀-ZnO and PDMS pair from Figure 7.6(f). Therefore, the TENG made up of Al₂₂₀-ZnO and PDMS pair is expected to have higher electrical output compared to other devices.

7.3.5 TENG output performance

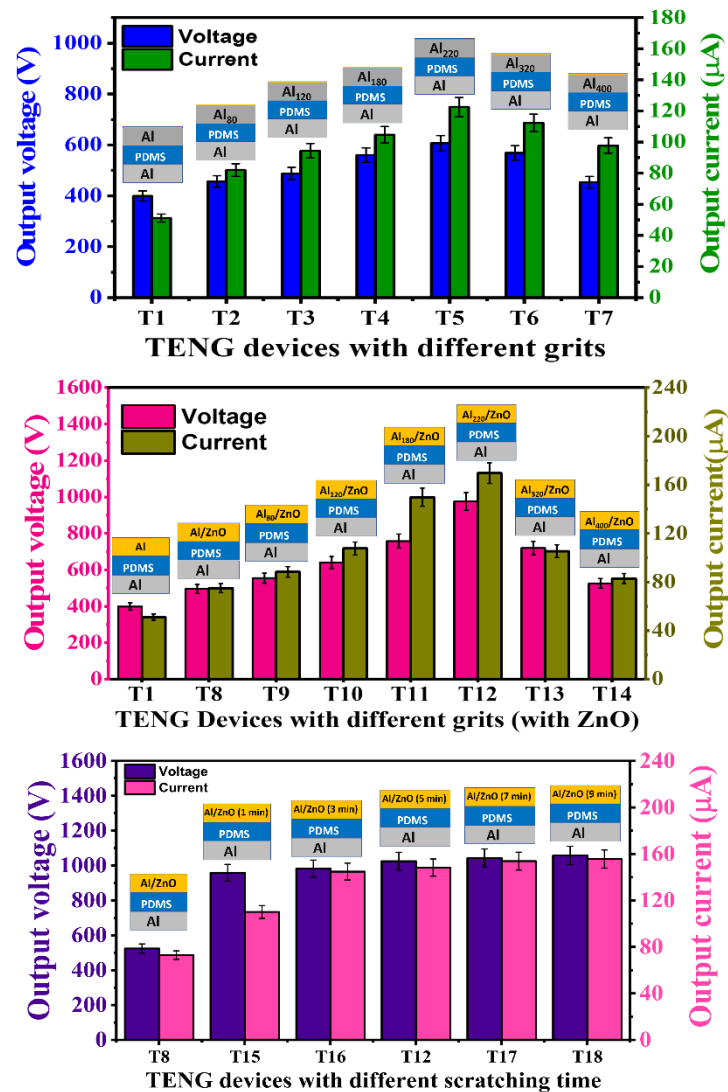


Figure 7.7. The average output voltage and current of the TENGs using, (a) plane aluminum and scratched aluminum with different grit sizes of sandpapers, (b) plane aluminum, ZnO deposited plane aluminum and ZnO deposited scratched aluminum with different grit sizes of sandpapers, and, (c) ZnO deposited scratched aluminum at different scratching time with fixed grit size (P220).

The electrical output of TENG devices (T1-T7) made of plane aluminum and surface-modified aluminum with fixed PDMS are shown in Figure 7.7(a). The results demonstrate that the open circuit output voltage (V_{oc}) and short-circuit current (I_{sc}) increased up to device T5 (220 grit size) and then decreased. The waveform representation of responses is shown in **SI, Figure S7.3 (a-b)**. This behavior is attributed to the effective surface modification of aluminum using

sandpaper. The particle size on smaller grit sizes is larger and decreases with increasing grit size, as shown in the **SI, Figure S7.4**.

Scratching the aluminum surface creates additional microstructures that provide more contact points for contact electrification, thereby enhancing TENG output voltage and current [35]. The maximum effective contact area between scratched Al and PDMS is achieved with the aluminum sample scratched with 220 grit size, while it may be less for aluminum samples scratched with other grit sizes (80,120,180) and (320,400) due to the presence of large and small particle sizes on the sandpapers. The experimental results are supported by optical microscopy images presented in **SI, Figure S1, S3-S4**. Therefore, it can be concluded that the highest peak-peak output voltage (727 V) and current (136 μ A) are obtained from aluminum scratched with 220 grit size, as shown in Figure 7.7(a). Further reduction in the work function of Al₂₂₀ (4.14 eV) also supports the higher output voltage and current for T5 (Al₂₂₀-PDMS) TENG device.

Table 7.3. Fabricated TENG devices code and its output voltage and current are below

S. No.	TENG device code	Output voltage (V)	Output current (μ A)
1.	T1	399.273	51.2
2.	T2	456	82.036
3.	T3	488	94.436
4.	T4	560	104.691
5.	T5	606.364	122.545
6.	T6	568.727	112.364
7.	T7	453.182	97.82
8.	T8	495.091	75.02
9.	T9	554.545	88.364
10.	T10	640.727	107.636
11.	T11	758.545	149.818
12.	T12	975.727	169.636
13.	T13	720.182	105.455
14.	T14	526.364	82.873
15.	T15	958.4	110.1
16.	T16	982.4	144.76
17.	T17	1043	153.8
18.	T18	1057.5	155.6

In the second set of the devices, ZnO nanosheet films were synthesized on different aluminum substrates (plane and scratched), and a fixed PDMS layer was used as the triboelectric layer to construct TENG devices. The output response of these devices (T1, T8-T14) was measured, and it was observed that the output voltage increased from T8 to T12 and then decreased (Figure 7.7(b)). The waveform representation of responses is shown in **SI, S7.3&Table S7.3**.

The maximum peak-peak output voltage and current were observed for device T12, with values of 1442 V and 155 μ A, respectively. Further, T12 device output voltage and current are 1.97 and 2.26 times higher than the T8 device (**SI, Table S7.3**).

The trend of the electrical output can be explained based on the effective contact area and work function difference between the triboelectric layers. The effective contact area between PDMS and scratched aluminum (grit size 220) was found to be optimum and produced the highest voltage, as discussed in the previous section. The growth of ZnO nanosheets on scratched aluminum (grit size 220) further increased the effective contact area with PDMS, resulting in the highest output for device T12. In addition to the above, the work function of the ZnO films for devices T8, T12, and T14 were determined to be 4.29, 4.08, and 4.26 eV, respectively, while the PDMS work function was 4.58 eV. The work function difference between the ZnO films and PDMS for devices T8, T12, and T14 were 0.28, 0.5, and 0.32 eV, respectively. It is evident that the work function difference is higher for device T12, which is why it exhibited the highest voltage and current. It can be concluded that ZnO nanosheets film synthesized on scratched aluminum substrate (grit size 220) is optimum for producing a high output voltage.

Further, the impact of the scratching time of aluminum with fixed sandpaper (grit size 220) on the performance of TENG devices (T12, T15-T18) was studied. The scratching time varied from 1,3,5,7, and 9 min. As shown in Figure 7.7(c) output of the TENG devices exhibited an increased trend for T15, T16, and T12 and after saturated for T17 and T18 devices. The waveform representation of responses is shown in **SI, S7.3 &Table S7.3**. The increase in the output may be due to the increased density of microstructures (surface area) on the aluminum with scratching time.[33] Increasing the scratching time (> 5 min) may not improve the effective density of microstructures on the aluminum surface, and it led to the saturation of output for T17 and T18 [73–75]. The output voltage is saturated earlier than the current in Figure 7.5(c) [73,74]. The reason might be that open-circuit voltage does not involve any dynamic charge transfer, whereas a short-circuit current involves the dynamic charge transfer

between the electrodes. From the above results, it can be concluded that T12 is the best device and is considered for further studies.

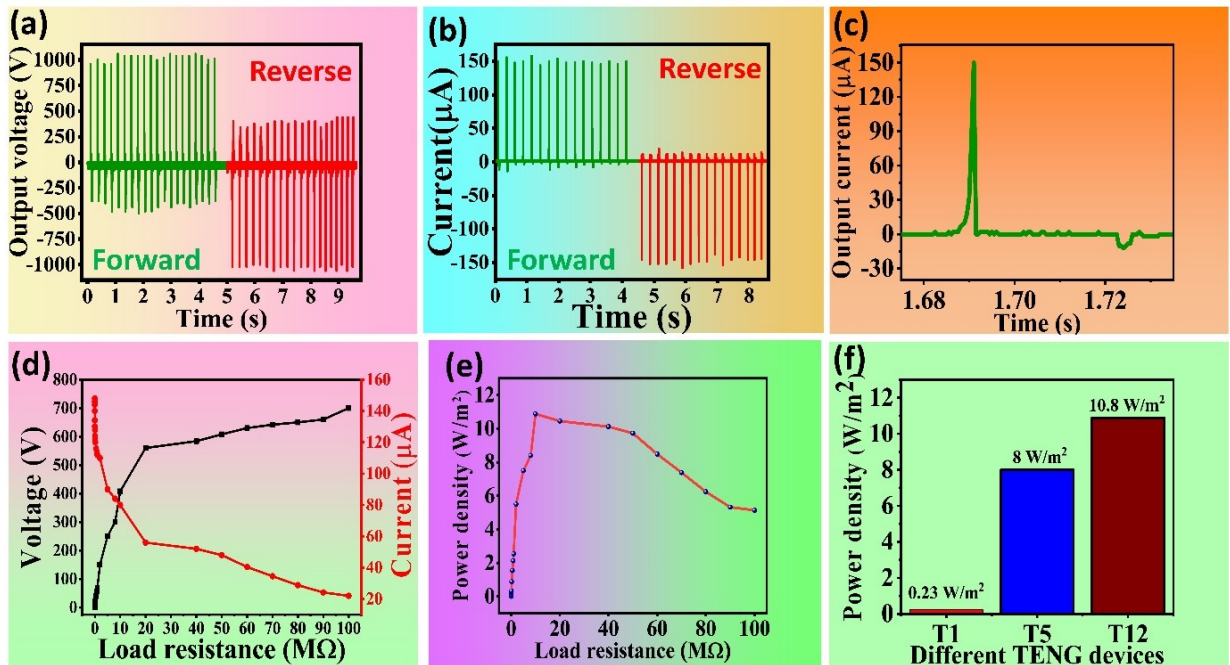


Figure 7.8. (a-b) open circuit voltage and short circuit current of the TENG(T12) , respectively; (c) Single output current response of the TENG; (d-e) output voltage, current response, and maximum power density of the TENG under the Load resistance ; (f) Plane Al, ZnO coated Plane Al, ZnO coated scratched Al(grit size 220) Power density of bar diagram, respectively.

Figures 7.8(a)-(b) shown the open circuit voltage and short circuit current of the T12 device in the switching polarity test, confirming that the output is solely from the TENG and not due to any noise in the measuring instrument. Further, the output voltage and current of the TENG were found to be the same for both connection configurations. A magnified view of the current signal in a cycle of press and release is shown in Figure 7.8 (c). Furthermore, the TENG's output voltage, current, and power density were measured under different load resistances and presented in Figure 7.8(d-e). The voltage increased with load resistance and saturated after $10 M\Omega$, while the current decreased with load resistance and saturated after $10 M\Omega$. This response is consistent with previous literature [76,77]. The power density was calculated using the formula $\text{Power} = VI/A$, where V is voltage, I is current, and A is the area of the device. The TENG's power density reached a maximum of $10.8 W/m^2$ at a load resistance of $10 M\Omega$, which can be considered as the impedance matching condition. The achieved power density in the present chapter is the highest value among ZnO-nanosheets based TENGs (SI Table S7.1). The

power density with ZnO nanosheet-based TENGs is much higher than the ZnS nanosheet-based TENGs, prepared using similar surface modification [33]. The difference in the power density can be due to many factors, such as the work function difference of triboelectric pairs, the surface roughness of the nanostructured films, and load-matching conditions of the devices.

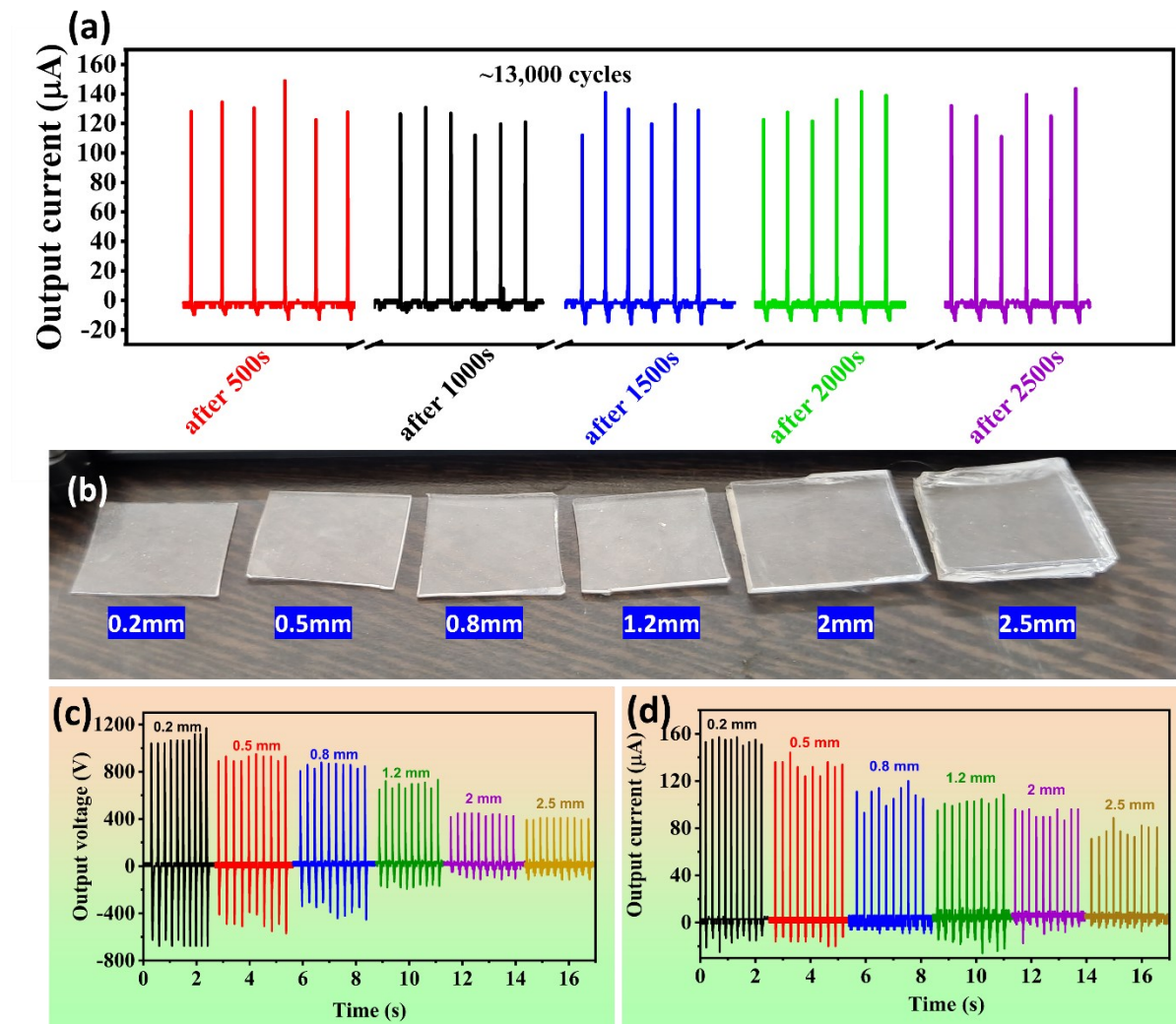


Figure 7.9. (a) Long-term stability of the T12 TENG device, (b) photographs of prepared PDMS films with different thicknesses, (c) the output voltage, and (d) current of the TENG with different thicknesses of PDMS film.

As shown in Figure 7.8 (e-f), it is essential to state that the output power density of TENG(T12) is 46.9 times and 1.35 times higher than TENG (T1) and TENG (T5), respectively. The efficiency of a TENG is an important factor to consider, along with its power density. It represents the ratio of the electrical energy produced by the TENG to the mechanical energy applied to it. The TENG's efficiency was calculated using the electrical output signal measured at the optimal load resistance of $10\text{ M}\Omega$, and was found to be 68%. The detailed calculations

for the TENG's efficiency can be found in the Chapter-2, Section-2.4.6. To assess the stability of the TENG, a stability test was performed, wherein the TENG was subjected to repeated application of force at a frequency of 4-5 Hz for over \sim 13,000 cycles. The test results indicated that the TENG exhibited consistently stable current output performance over the entire test duration, as shown in Figure 7.9(a). Further, TENG response was tested over a period of six months (100 cycles/month) and found stable.

To investigate the effect of PDMS film thickness on the performance of the TENG, we prepared PMDS films of varying thicknesses, including 0.2, 0.5, 0.8, 1.2, 2, and 2.5 mm, as depicted in Figure 7.9(b). The PDMS layer of the TENG device (T12) is replaced with different thicknesses of PDMS films while keeping the opposite triboelectric layer constant. The output voltage and current of the new TENG devices were measured and presented in Figure 7.9(c-d), and it was observed that both the current and voltage decreased significantly as the thickness of the PDMS film increased. This observation is consistent with previous studies on the relationship between dielectric thickness and TENG behavior [78,79].

Specifically, the TENG device with a 0.2 mm PDMS film performed the best. It is worth noting that TENG output typically increases as the thickness of the dielectric layer increases up to a certain point, after which it starts to decrease. This is because there is an optimum thickness value for the triboelectric layer of every TENG device, beyond which the output values begin to decrease.[80–83] This decrease in output voltage may be due to a reduction in the electrostatic induction between the electrode and triboelectric layer as the thickness of the dielectric layer increases beyond the optimal value. The optimum value of thickness changes from device to device.

Further, a finite element simulation of the TENG device was performed using COMSOL 6.0 software to verify the TENG's electrical-potential distribution and charge-transfer process and the results are presented in **SI, Figure S7.5**, the device parameters used in COMSOL simulation is listed are listed in **Table 7.4**. A finite element simulation of the TENG device was performed using COMSOL 6.0 software to verify the TENG's electrical-potential distribution and charge-transfer process.[84,85] Charge distribution and the results information are given in the supplementary **SI, Figure S7.5(a)** shows that the model comprises PDMS and ZnO as two dielectric layers and aluminum as electrodes; the detailed simulation parameters are presented in **Table 7.4**.[86] The surface charge density of PDMS and ZnO is set to $-30 \mu\text{C}/\text{m}^2$ and $+30 \mu\text{C}/\text{m}^2$, respectively, to calculate the amount of transferred charge in one cycle. The potential

distribution of the TENG in the open-circuit condition is exhibited by COMSOL simulation in **Figure S7.5(b)**. In addition, the modelled TENG, the results of V_{OC} , Q_{SC} and C calculations using the finite element method (FEM) are plotted as shown in **Figure S7.5(c-e)** as a function of distance (x). It can be clearly seen that the potential difference between the PDMS and ZnO increases dramatically with increasing distance and reaches a maximum value of 1.37×10^4 V at a distance of 0.8 cm. The considerable difference between the simulation and experiment values is mainly due to experimental conditions such as air breakdown effect, ambient humidity, and charge diffusion.

Table 7.4: Device parameters used in the COMSOL simulation

Parameter	Value
Dielectric length and width	5 cm
Max spacing distance (x)	0.8 cm
Thickness of dielectric-1(ZnO) (d_1)	0.001 mm
Thickness of dielectric-2(PDMS) (d_2)	0.8 mm
Thickness of metal electrodes (Al)	0.01 mm
Relative dielectric constant of ZnO (ϵ_{r1})	8.54 (from material list)
Relative dielectric constant of PDMS (ϵ_{r2})	2.75 (from material list)
Surface charge density of ZnO ($\sigma(x)$)	$30 \mu\text{C}/\text{m}^2$
Surface charge density of PDMS ($\sigma(x)$)	$-30 \mu\text{C}/\text{m}^2$

The effect of various experimental parameters on the TENG device (T12) was examined, including the active area of the device, frequency of the hand-tapping force, spacing between the triboelectric layers, and application of different hand-tapping forces. The response graphs under different experimental conditions are provided in Figure 7.10(a-h), which followed a similar trend with earlier chapters. The results showed that increasing the active area of the device and the applied force led to a higher TENG output. Further, increasing in spacing results in increased output upto 1 cm, after it decreased. The TENG output also increased with the applied frequency up to 4 Hz, after which it became saturated.

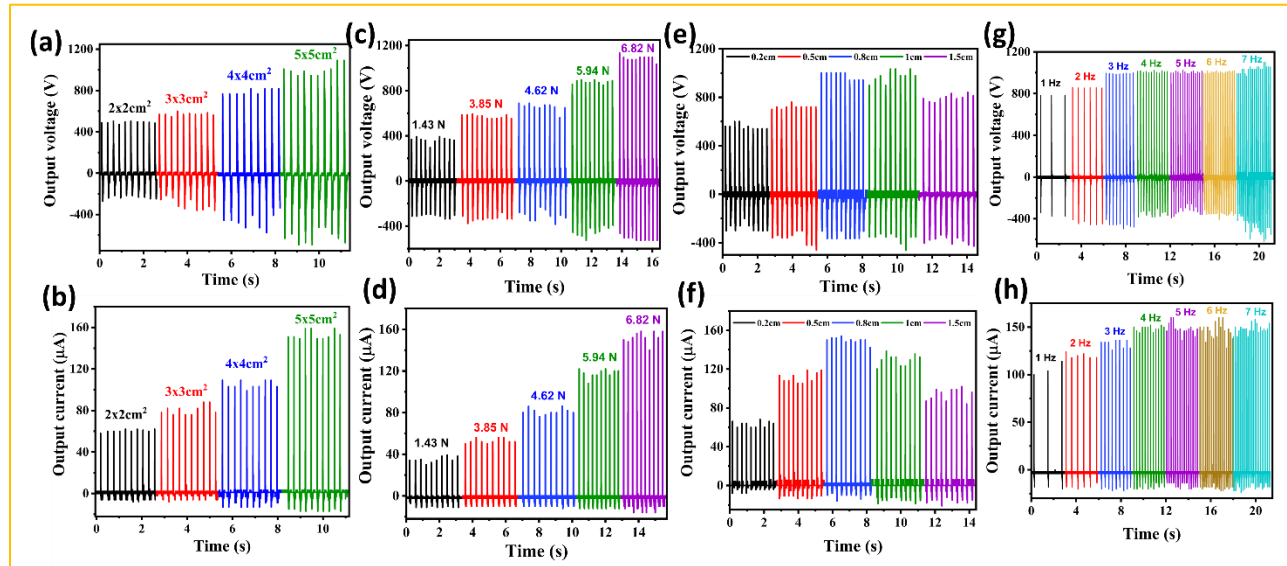


Figure 7.10. TENG device (T12) device output response as a function of (a)-(b) different active areas of the devices, (c)-(d) different applied force, (e)-(f) different spacing between the triboelectric layers, (g)-(h) different frequencies of applied force.

Further, charging curves of different capacitors (1, 4.7, 10, 22, 47, 100, 220, and 470 μF) charged by a TENG show that smaller capacitors charge faster while larger capacitors charge slower, as seen in Figure 7.11(a-b). Notably, smaller capacitance values are associated with faster charging speeds and shorter times to reach saturation voltage. The charge stored on these capacitors is determined by the product of the charged voltage (V) and capacitance C_L , as depicted in Figure 7.11(b). The graphical representation in Figure 7.11(b) illustrates that an increase in load capacitor value results in higher charge storage. Additionally, the behavior of charged voltage and stored charge is depicted in Figure 7.11(c), revealing an opposite relationship with respect to load capacitor values. The variation of maximum stored energy as a function of C_L is presented in Figure 7.11(d), indicating that the highest stored energy, amounting to 1.2 mJ, is achieved at the optimal load capacitance of 220 μF .

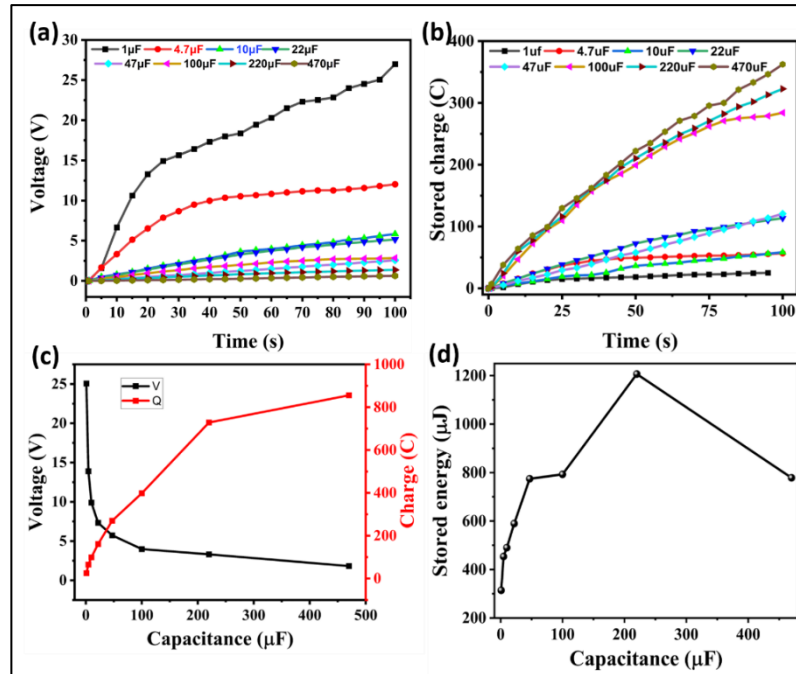


Figure 7.11. Capacitor charging curves with various capacitances charged by a TENG, (a) voltage (b) stored charge (c) the relationship between voltage and stored charge as a function of load capacitance (d) stored energy.

7.4 Applications

7.4.1 Self-powered and portable electronic devices application

Figure 7.12 (a) shows the powering of a series connected 842 light-emitting diodes (LEDs) with a single TENG (T12) device due to its high-power density. Initially, the TENG AC output was connected to a bridge rectifier circuit, and its DC output was directly connected to the series-connected LEDs ([See SI video V7.1](#)). Figures 7.12 (b-d) demonstrate the use of a TENG to power electronic devices without the use of any storage element. An electronic stopwatch, calculator, and digital watch are directly driven by a TENG ([See SI video V7.2](#)), respectively.

Furthermore, the TENG was integrated with an energy storage unit to create a self-powered system. Initially, the capacitor was charged to 3 V in 150 sec, and after, a stopwatch was connected to the capacitor while maintaining the tapping of the TENG. The energy stored in the capacitor powers the stopwatch while getting charged by TENG, which results in the continuous operation of the stopwatch ([See SI, video V7.3](#)).

The circuit diagram in Figure 7.12(e) shows a TENG connected with a rectifier, capacitor, and load. The bi-directional switch is connected to the s1 position for charging and the s2 position for powering the loads, including a thermometer, hygrometer, and vernier calipers. The voltage

across the capacitor is measured using a multimeter. Capacitors with values of $4.7 \mu\text{F}$, $47 \mu\text{F}$, and $100 \mu\text{F}$ are used to power the thermometer (See SI video V7.4), hygrometer (See SI video V7.5), and digital vernier calipers (See SI video V7.6), respectively, as shown in Figure 7.12(g-i). The curves corresponding to $4.7 \mu\text{F}$, $47 \mu\text{F}$, and $100 \mu\text{F}$ can be found in Figure 7.12(f) and SI, S7.6.

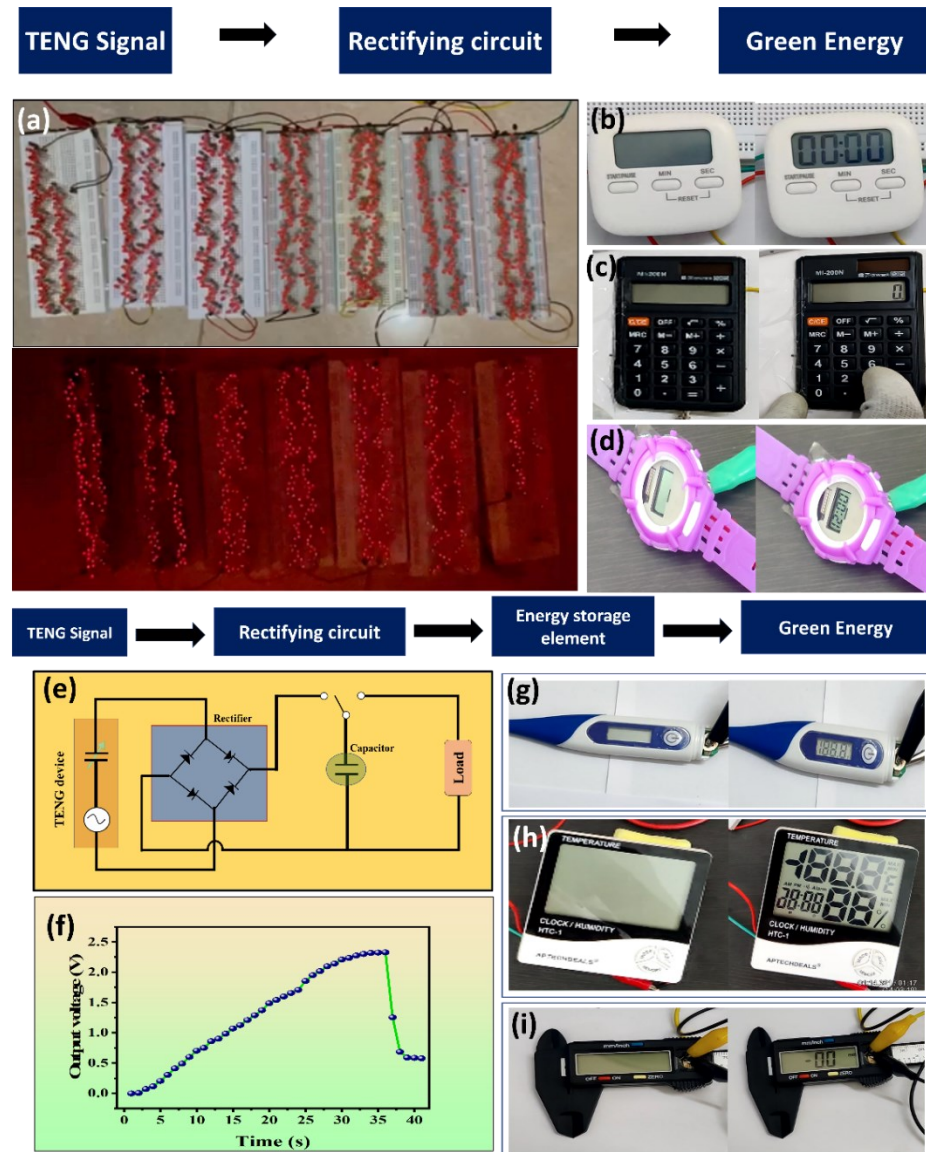


Figure 7.12. Photographs of (a) 824LEDs, (b) stopwatch, (c) calculator, (d) digital watch, directly driven by a Contact separation mode of the TENG; (e) circuit diagram of the self-powered system to power electronics with energy storage units; (f) Charging capacitor curves correspond to thermometer; Photographs of (g) thermometer, (h) hygrometer, and (i) digital vernier callipers, driven by charging capacitors of $4.7 \mu\text{F}$, $47 \mu\text{F}$ and $100 \mu\text{F}$, respectively.

7.4.2 Applications of TENG in bio-mechanical energy harvesting

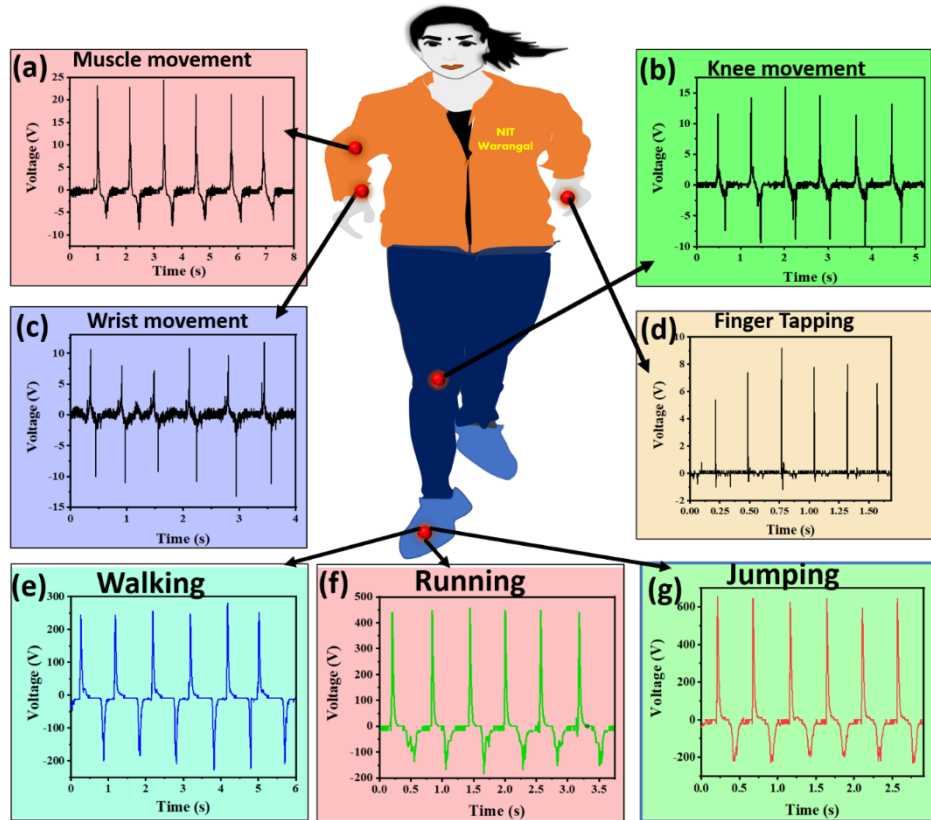


Figure 7.13. Output voltage generated by different body parts and motion states (a–b) Output voltage was driven by muscle movement and knee joint movement, (c–d) The output voltage was measured by wrist bending and finger tapping, respectively, (e–g) Output voltage was driven by walking, running, and jumping, respectively.

Further, the bio-mechanical energy harvesting capability of TENG for different bio-mechanical motions are presented in **SI, Figure 7.13(a-g)**. TENGs exhibit remarkable stability, flexibility, and sensitivity, making them an ideal candidate for wearable electronic devices. By attaching TENGs to various body parts such as muscles, knees, feet, fingers, and wrists, contact separation mode operation occurs as these body parts move, producing an output voltage dependent on the contact amplitude, as shown in Figure 7.13. TENGs was attached to the muscles of the hand and knee of the leg during their movements, and the output voltage was recorded and presented in Figure 7.13(a-b). Further, the TENG response was tested under bending of the wrist and finger tapping (Figure 7.13(c-d)). Furthermore, TENGs was placed on the soles of the feet and tested their output voltage during activities such as walking, running, and jumping, as shown in Figure 7.13(e-g) and ([See SI video V7.7](#)). By analyzing the output voltage of TENG, it is possible to determine the frequency and amplitude of human movement. Such studies on TENG offer excellent application prospects in self-powered sensing devices.

7.4.3 Applications of TENG in health monitoring

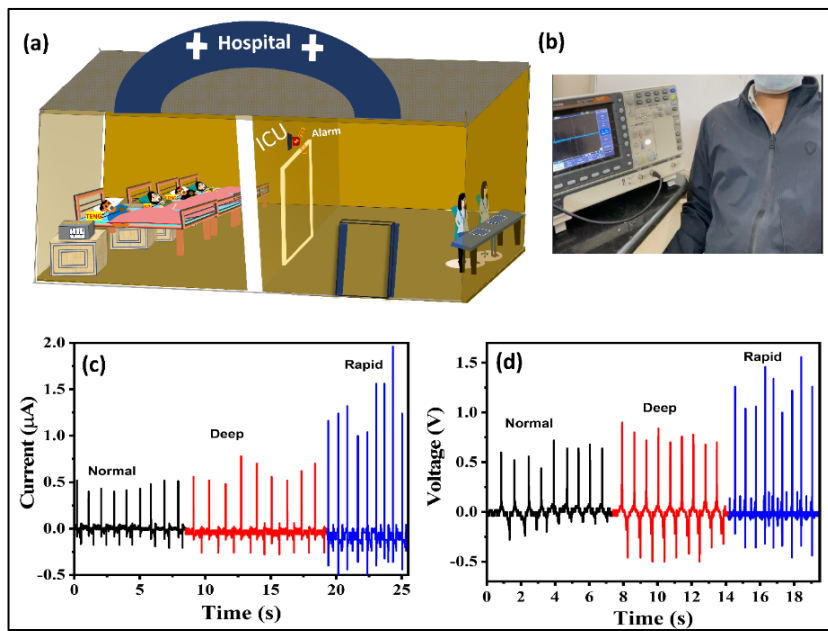


Figure 7.14. (a) Schematic of the proposed health (breath) monitoring patients in ICU using TENG, (b) real-time photograph of the person during the respiration rate testing, TENG output response for different breathing rates (c) current (d) voltage.

A wearable TENG is a useful device for health monitoring applications, particularly for respiratory monitoring, which provides critical information about a person's respiratory system and overall health. By measuring the breathing rate, depth, and pattern, respiratory and cardiac conditions, such as asthma, COPD, sleep apnea, and heart failure, can be diagnosed and managed effectively. In this study, TENG was attached to the chest of a human body to monitor the output voltage and current signals generated from different breathing patterns. Figure 7.14(a)-(b) shows the schematic representation and original photograph during the testing. The TENG device demonstrated high sensitivity, which allowed for detecting various breathing rates, including normal, deep, and rapid, as shown in Figure 7.14(c)-(d) and ([See SI video V7.8](#)). Further, TENG can be embedded in the facemask (N95) if the TENG device is made up of all flexible triboelectric layers and electrodes.

An alarm will be triggered if the TENG output voltage or current goes beyond the threshold values set in the comparator circuit and its associated algorithm to make the TENG device practical for health monitoring. If the threshold values of signal exceed. Immediate the alarm will be triggered and if there is no response of the signal, the patient condition is critical and immediate rescue of the patient. Not only this, TENG can utilised in sports training to convert the analog signal to digital conversion circuits and buffer to monitor the breathing rate of an

athletes over a period of time. Therefore, The TENG can offers a potential technology for convenient and accurate breath monitoring, which can impact heath management system and athletic performance significantly.

7.5 Conclusions

In the current study, a multifunctional, high-performance TENG was constructed by modifying the surface of one of the triboelectric layers. ZnO nanosheets on a modified aluminum surface and PDMS nanosheets were used as triboelectric layers with an area of 5x5cm² in the TENG design. The peak-to-peak voltage, current, and power density of the TENG were 1442V, 155 μ A, and 10.8 W/m², respectively. The fabricated TENG has excellent stability over \sim 13,000 cycles. The TENG can power up 824 LEDs, a stopwatch, a calculator, and a digital watch without any storage element. Its ability to power thermometer, hygrometer, and digital vernier calipers was demonstrated with the use of storage elements. Further, TENG was used to harvest different biomechanical energy. Finally, TENG is utilized as a self-powered health monitoring sensor in monitoring breathing patterns. Overall, the proposed TENG has multi-functional applications in various fields.

7.6 References

- [1] F. Arab Hassani, Q. Shi, F. Wen, T. He, A. Haroun, Y. Yang, Y. Feng, C. Lee, Smart materials for smart healthcare— moving from sensors and actuators to self-sustained nanoenergy nanosystems, *Smart Mater. Med.* 1 (2020) 92–124.
<https://doi.org/10.1016/j.smaim.2020.07.005>.
- [2] Q. Zhang, T. Jin, J. Cai, L. Xu, T. He, T. Wang, Y. Tian, L. Li, Y. Peng, C. Lee, Wearable Triboelectric Sensors Enabled Gait Analysis and Waist Motion Capture for IoT-Based Smart Healthcare Applications, *Adv. Sci.* 9 (2022) 1–13.
<https://doi.org/10.1002/advs.202103694>.
- [3] Y. Yang, S. Wang, Y. Zhang, Z.L. Wang, Pyroelectric nanogenerators for driving wireless sensors, *Nano Lett.* 12 (2012) 6408–6413. <https://doi.org/10.1021/nl303755m>.
- [4] S. Korkmaz, İ.A. Kariper, Pyroelectric nanogenerators (PyNGs) in converting thermal energy into electrical energy: Fundamentals and current status, *Nano Energy*. 84 (2021) 105888. <https://doi.org/https://doi.org/10.1016/j.nanoen.2021.105888>.
- [5] M.S. Al-ruqeishi, T. Mohiuddin, B. Al-habsi, F. Al-ruqeishi, A. Al-fahdi, A. Al-khusaibi, Piezoelectric nanogenerator based on ZnO nanorods, *Arab. J. Chem.* 12 (2019) 5173–5179. <https://doi.org/10.1016/j.arabjc.2016.12.010>.

- [6] R. Yang, Y. Qin, L. Dai, Z.L. Wang, Power generation with laterally packaged piezoelectric fine wires, *Nat. Nanotechnol.* 4 (2009) 34–39.
<https://doi.org/10.1038/nnano.2008.314>.
- [7] P. Supraja, R.K. R, S. Mishra, D. Haranath, P.R. Sankar, K. Prakash, A simple and low-cost approach for the synthesis and fabrication of ZnO nanosheet-based nanogenerator for energy harvesting and sensing, *Eng. Res. Express.* 3 (2021) 035022.
<https://doi.org/10.1088/2631-8695/ac184b>.
- [8] Z.L. Wang, Triboelectric nanogenerators as new energy technology and self-powered sensors - Principles, problems and perspectives, *Faraday Discuss.* 176 (2014) 447–458.
<https://doi.org/10.1039/c4fd00159a>.
- [9] G. Zhu, B. Peng, J. Chen, Q. Jing, Z. Lin Wang, Triboelectric nanogenerators as a new energy technology: From fundamentals, devices, to applications, *Nano Energy*. 14 (2014) 126–138. <https://doi.org/10.1016/j.nanoen.2014.11.050>.
- [10] R.K. Rajaboina, U.K. Khanapuram, V. Vivekananthan, G. Khandelwal, S. Potu, A. Babu, N. Madathil, M. Velpula, P. Kodali, Crystalline Porous Material-Based Nanogenerators: Recent Progress, Applications, Challenges, and Opportunities, *Small.* n/a (2023) 2306209. <https://doi.org/10.1002/smll.202306209>.
- [11] R. Cao, J. Wang, S. Zhao, W. Yang, Z. Yuan, Y. Yin, X. Du, N.W. Li, X. Zhang, X. Li, Z.L. Wang, C. Li, Self-powered nanofiber-based screen-print triboelectric sensors for respiratory monitoring, *Nano Res.* 11 (2018) 3771–3779.
<https://doi.org/10.1007/s12274-017-1951-2>.
- [12] Q. Zheng, H. Zhang, B. Shi, X. Xue, Z. Liu, Y. Jin, Y. Ma, Y. Zou, X. Wang, Z. An, W. Tang, W. Zhang, F. Yang, Y. Liu, X. Lang, Z. Xu, Z. Li, Z.L. Wang, In Vivo Self-Powered Wireless Cardiac Monitoring via Implantable Triboelectric Nanogenerator, *ACS Nano.* 10 (2016) 6510–6518. <https://doi.org/10.1021/acsnano.6b02693>.
- [13] J.G. Sun, T.N. Yang, C.Y. Wang, L.J. Chen, A flexible transparent one-structure tribo-piezo-pyroelectric hybrid energy generator based on bio-inspired silver nanowires network for biomechanical energy harvesting and physiological monitoring, *Nano Energy*. 48 (2018) 383–390. <https://doi.org/10.1016/j.nanoen.2018.03.071>.
- [14] F. Yi, L. Lin, S. Niu, P.K. Yang, Z. Wang, J. Chen, Y. Zhou, Y. Zi, J. Wang, Q. Liao, Y. Zhang, Z.L. Wang, Stretchable-rubber-based triboelectric nanogenerator and its application as self-powered body motion sensors, *Adv. Funct. Mater.* 25 (2015) 3688–3696. <https://doi.org/10.1002/adfm.201500428>.

- [15] X. Chen, F. Wang, Y. Zhao, P. Wu, L. Gao, C. Ouyang, Y. Yang, X. Mu, Surface Plasmon Effect Dominated High-Performance Triboelectric Nanogenerator for Traditional Chinese Medicine Acupuncture, *Research*. 2022 (2022). <https://doi.org/10.34133/2022/9765634>.
- [16] J. Yang, J. Chen, Y. Su, Q. Jing, Z. Li, F. Yi, X. Wen, Z. Wang, Z.L. Wang, Eardrum-inspired active sensors for self-powered cardiovascular system characterization and throat-attached anti-interference voice recognition, *Adv. Mater.* 27 (2015) 1316–1326. <https://doi.org/10.1002/adma.201404794>.
- [17] G. Ding, S.-T. Han, V.A.L. Roy, C.-C. Kuo, Y. Zhou, Triboelectric nanogenerator for neuromorphic electronics, *Energy Rev.* 2 (2023) 100014. <https://doi.org/10.1016/j.enrev.2023.100014>.
- [18] H. Wang, H. Wu, D. Hasan, T. He, Q. Shi, C. Lee, Self-Powered Dual-Mode Amenity Sensor Based on the Water-Air Triboelectric Nanogenerator, *ACS Nano*. 11 (2017) 10337–10346. <https://doi.org/10.1021/acsnano.7b05213>.
- [19] T. Zhao, Y. Fu, C. Sun, X. Zhao, C. Jiao, A. Du, Q. Wang, Y. Mao, B. Liu, Wearable biosensors for real-time sweat analysis and body motion capture based on stretchable fiber-based triboelectric nanogenerators, *Biosens. Bioelectron.* 205 (2022) 114115. <https://doi.org/10.1016/j.bios.2022.114115>.
- [20] Y. Han, F. Yi, C. Jiang, K. Dai, Y. Xu, X. Wang, Z. You, Self-powered gait pattern-based identity recognition by a soft and stretchable triboelectric band, *Nano Energy*. 56 (2019) 516–523. <https://doi.org/10.1016/j.nanoen.2018.11.078>.
- [21] F. Wang, L. Hou, L. Gao, P. Wu, M. Zhou, X. Chen, X. Mu, High-performance triboelectric nanogenerator via photon-generated carriers for green low-carbon system, *Nano Energy*. 108 (2023) 108206. <https://doi.org/10.1016/j.nanoen.2023.108206>.
- [22] D.W. Kim, J.H. Lee, J.K. Kim, U. Jeong, Material aspects of triboelectric energy generation and sensors, *NPG Asia Mater.* 12 (2020) 6. <https://doi.org/10.1038/s41427-019-0176-0>.
- [23] C.K. Jeong, K.M. Baek, S. Niu, T.W. Nam, Y.H. Hur, D.Y. Park, G.T. Hwang, M. Byun, Z.L. Wang, Y.S. Jung, K.J. Lee, Topographically-designed triboelectric nanogenerator via block copolymer self-assembly, *Nano Lett.* 14 (2014) 7031–7038. <https://doi.org/10.1021/nl503402c>.
- [24] W. Tang, C. Zhang, C.B. Han, Z.L. Wang, Enhancing Output Power of Cylindrical Triboelectric Nanogenerators by Segmentation Design and Multilayer Integration,

- Adv. Funct. Mater. 24 (2014) 6684–6690. <https://doi.org/10.1002/adfm.201401936>.
- [25] X. Wang, H. Zhang, L. Dong, X. Han, W. Du, J. Zhai, C. Pan, Z.L. Wang, Self-powered high-resolution and pressure-sensitive triboelectric sensor matrix for real-time tactile mapping, Adv. Mater. 28 (2016) 2896–2903.
<https://doi.org/10.1002/adma.201503407>.
- [26] S. Wang, L. Lin, Z.L. Wang, Triboelectric nanogenerators as self-powered active sensors, Nano Energy. 11 (2015) 436–462.
<https://doi.org/10.1016/j.nanoen.2014.10.034>.
- [27] Z. Ren, L. Wu, Y. Pang, W. Zhang, R. Yang, Strategies for effectively harvesting wind energy based on triboelectric nanogenerators, Nano Energy. 100 (2022) 107522.
<https://doi.org/10.1016/j.nanoen.2022.107522>.
- [28] A. Matin Nazar, K.-J. Idala Egbe, A. Abdollahi, M.A. Hariri-Ardebili, Triboelectric Nanogenerators for Energy Harvesting in Ocean: A Review on Application and Hybridization, Energies. 14 (2021) 5600. <https://doi.org/10.3390/en14185600>.
- [29] S. Uzun, S. Seyedin, A.L. Stoltzfus, A.S. Levitt, M. Alhabeb, M. Anayee, C.J. Strobel, J.M. Razal, G. Dion, Y. Gogotsi, Knittable and Washable Multifunctional MXene-Coated Cellulose Yarns, Adv. Funct. Mater. 29 (2019) 1–13.
<https://doi.org/10.1002/adfm.201905015>.
- [30] L. Gao, X. Chen, S. Lu, H. Zhou, W. Xie, J. Chen, M. Qi, H. Yu, X. Mu, Z.L. Wang, Y. Yang, Enhancing the Output Performance of Triboelectric Nanogenerator via Grating-Electrode-Enabled Surface Plasmon Excitation, Adv. Energy Mater. 9 (2019) 1902725. <https://doi.org/https://doi.org/10.1002/aenm.201902725>.
- [31] M.Y. Chougale, Q.M. Saqib, M.U. Khan, R.A. Shaukat, J. Kim, J. Bae, Novel Recycled Triboelectric Nanogenerator Based on Polymer-Coated Trash Soda Can for Clean Energy Harvesting, Adv. Sustain. Syst. 5 (2021) 1–7.
<https://doi.org/10.1002/adsu.202100161>.
- [32] G.G. Cheng, S.Y. Jiang, K. Li, Z.Q. Zhang, Y. Wang, N.Y. Yuan, J.N. Ding, W. Zhang, Effect of argon plasma treatment on the output performance of triboelectric nanogenerator, Appl. Surf. Sci. 412 (2017) 350–356.
<https://doi.org/10.1016/j.apsusc.2017.03.255>.
- [33] S. Mishra, P. Supraja, D. Haranath, R.R. Kumar, S. Pola, Effect of surface and contact points modification on the output performance of triboelectric nanogenerator, Nano Energy. 104 (2022) 107964. <https://doi.org/10.1016/j.nanoen.2022.107964>.

- [34] S. Wang, Y. Xie, S. Niu, L. Lin, C. Liu, Y.S. Zhou, Z.L. Wang, Maximum Surface Charge Density for Triboelectric Nanogenerators Achieved by Ionized-Air Injection: Methodology and Theoretical Understanding, *Adv. Mater.* 26 (2014) 6720–6728. <https://doi.org/https://doi.org/10.1002/adma.201402491>.
- [35] L. Zhao, Q. Zheng, H. Ouyang, H. Li, L. Yan, B. Shi, Z. Li, A size-unlimited surface microstructure modification method for achieving high performance triboelectric nanogenerator, *Nano Energy*. 28 (2016) 172–178. <https://doi.org/10.1016/j.nanoen.2016.08.024>.
- [36] X.W. Zhang, G.Z. Li, G.G. Wang, J.L. Tian, Y.L. Liu, D.M. Ye, Z. Liu, H.Y. Zhang, J.C. Han, High-Performance Triboelectric Nanogenerator with Double-Surface Shape-Complementary Microstructures Prepared by Using Simple Sandpaper Templates, *ACS Sustain. Chem. Eng.* 6 (2018) 2283–2291. <https://doi.org/10.1021/acssuschemeng.7b03745>.
- [37] H.Y. Li, L. Su, S.Y. Kuang, C.F. Pan, G. Zhu, Z.L. Wang, Significant Enhancement of Triboelectric Charge Density by Fluorinated Surface Modification in Nanoscale for Converting Mechanical Energy, *Adv. Funct. Mater.* 25 (2015) 5691–5697. <https://doi.org/10.1002/adfm.201502318>.
- [38] V. Vivekananthan, A. Chandrasekhar, N.R. Alluri, Y. Purusothaman, S.J. Kim, A highly reliable, impervious and sustainable triboelectric nanogenerator as a zero-power consuming active pressure sensor, *Nanoscale Adv.* 2 (2020) 746–754. <https://doi.org/10.1039/c9na00790c>.
- [39] C.K. Chung, K.H. Ke, High contact surface area enhanced Al/PDMS triboelectric nanogenerator using novel overlapped microneedle arrays and its application to lighting and self-powered devices, *Appl. Surf. Sci.* 508 (2020) 145310. <https://doi.org/10.1016/j.apsusc.2020.145310>.
- [40] B.K. Yun, J.W. Kim, H.S. Kim, K.W. Jung, Y. Yi, M.S. Jeong, J.H. Ko, J.H. Jung, Base-treated polydimethylsiloxane surfaces as enhanced triboelectric nanogenerators, *Nano Energy*. 15 (2015) 523–529. <https://doi.org/10.1016/j.nanoen.2015.05.018>.
- [41] D. Li, C. Wu, L. Ruan, J. Wang, Z. Qiu, K. Wang, Y. Liu, Y. Zhang, T. Guo, J. Lin, T.W. Kim, Electron-transfer mechanisms for confirmation of contact-electrification in ZnO/polyimide-based triboelectric nanogenerators, *Nano Energy*. 75 (2020) 104818. <https://doi.org/10.1016/j.nanoen.2020.104818>.
- [42] B. Liu, S. Wang, Z. Yuan, Z. Duan, Q. Zhao, Y. Zhang, Y. Su, Y. Jiang, G. Xie, H.

- Tai, Novel chitosan/ZnO bilayer film with enhanced humidity-tolerant property: Endowing triboelectric nanogenerator with acetone analysis capability, *Nano Energy*. 78 (2020) 105256. <https://doi.org/10.1016/j.nanoen.2020.105256>.
- [43] R. Barras, A. dos Santos, T. Calmeiro, E. Fortunato, R. Martins, H. Águas, P. Barquinha, R. Igreja, L. Pereira, Porous PDMS conformable coating for high power output carbon fibers/ZnO nanorod-based triboelectric energy harvesters, *Nano Energy*. 90 (2021) 106582. <https://doi.org/10.1016/j.nanoen.2021.106582>.
- [44] S. Wang, H. Tai, B. Liu, Z. Duan, Z. Yuan, H. Pan, Y. Su, G. Xie, X. Du, Y. Jiang, A facile respiration-driven triboelectric nanogenerator for multifunctional respiratory monitoring, *Nano Energy*. 58 (2019) 312–321. <https://doi.org/10.1016/j.nanoen.2019.01.042>.
- [45] S.N. Chen, M.Z. Huang, Z.H. Lin, C.P. Liu, Enhancing charge transfer for ZnO nanorods based triboelectric nanogenerators through Ga doping, *Nano Energy*. 65 (2019) 104069. <https://doi.org/10.1016/j.nanoen.2019.104069>.
- [46] Q.Z. Guo, C.P. Liu, Derivation of analytical equations with experimental verification for working mechanism of triboelectric nanogenerators in contact-separation mode, *Nano Energy*. 76 (2020) 104969. <https://doi.org/10.1016/j.nanoen.2020.104969>.
- [47] P.C. Lee, Y.C. Ou, R.C. Wang, C.P. Liu, Enhanced output performance of ZnO thin film triboelectric nanogenerators by leveraging surface limited ga doping and insulting bulk, *Nano Energy*. 89 (2021) 106394. <https://doi.org/10.1016/j.nanoen.2021.106394>.
- [48] Y. Sun, Y. Zheng, R. Wang, T. Lei, J. Liu, J. Fan, W. Shou, Y. Liu, 3D micro-nanostructure based waterproof triboelectric nanogenerator as an outdoor adventure power source, *Nano Energy*. 100 (2022) 107506. <https://doi.org/10.1016/j.nanoen.2022.107506>.
- [49] W. Deng, B. Zhang, L. Jin, Y. Chen, W. Chu, H. Zhang, M. Zhu, W. Yang, Enhanced performance of ZnO microballoon arrays for a triboelectric nanogenerator, *Nanotechnology*. 28 (2017) 135401. <https://doi.org/10.1088/1361-6528/aa5f34>.
- [50] D. Choi, S. Yang, C. Lee, W. Kim, J. Kim, J. Hong, Highly Surface-Embossed Polydimethylsiloxane-Based Triboelectric Nanogenerators with Hierarchically Nanostructured Conductive Ni–Cu Fabrics, *ACS Appl. Mater. Interfaces*. 10 (2018) 33221–33229. <https://doi.org/10.1021/acsami.8b10613>.
- [51] H. Patnam, S.A. Graham, J.S. Yu, Y-ZnO Microflowers Embedded Polymeric Composite Films to Enhance the Electrical Performance of Piezo/Tribo Hybrid

- Nanogenerators for Biomechanical Energy Harvesting and Sensing Applications, ACS Sustain. Chem. Eng. 9 (2021) 4600–4610.
<https://doi.org/10.1021/acssuschemeng.1c00025>.
- [52] D.H. Kim, B. Dudem, J.S. Yu, High-Performance Flexible Piezoelectric-Assisted Triboelectric Hybrid Nanogenerator via Polydimethylsiloxane-Encapsulated Nanoflower-like ZnO Composite Films for Scavenging Energy from Daily Human Activities, ACS Sustain. Chem. Eng. 6 (2018) 8525–8535.
<https://doi.org/10.1021/acssuschemeng.8b00834>.
- [53] Y.H. Ko, G. Nagaraju, S.H. Lee, J.S. Yu, PDMS-based triboelectric and transparent nanogenerators with ZnO nanorod arrays, ACS Appl. Mater. Interfaces. 6 (2014) 6631–6637. <https://doi.org/10.1021/am5018072>.
- [54] A.N. Simões, D.J. Carvalho, E. de Souza Morita, H.V. Vendrameto, L. Fu, F. Torres, A.N. de Souza, W.A. Bizzo, T. Mazon, Application of steel spring on the ZnO nanorods self-powered triboelectric nanogenerator for efficient energy harvest in transformers, 2021 14th IEEE Int. Conf. Ind. Appl. INDUSCON 2021 - Proc. (2021) 904–909. <https://doi.org/10.1109/INDUSCON51756.2021.9529416>.
- [55] A. Dos Santos, F. Sabino, A. Rovisco, P. Barquinha, H. Águas, E. Fortunato, R. Martins, R. Igreja, Optimization of zno nanorods concentration in a micro-structured polymeric composite for nanogenerators, Chemosensors. 9 (2021) 1–13.
<https://doi.org/10.3390/chemosensors9020027>.
- [56] S. Lee, W. Ko, J. Hong, Enhanced performance of triboelectric nanogenerators integrated with ZnO nanowires, J. Nanosci. Nanotechnol. 14 (2014) 9319–9322.
<https://doi.org/10.1166/jnn.2014.10114>.
- [57] W. Seung, M.K. Gupta, K.Y. Lee, K. Shin, J. Lee, T.Y. Kim, S. Kim, J. Lin, J.H. Kim, S. Kim, Nanopatterned Textile-Based Wearable Triboelectric Nanogenerator, ACS Nano. 9 (2015) 3501–3509. <https://doi.org/10.1021/nn507221f>.
- [58] P. Paydari, N. Manavizadeh, A. Hadi, J. Karamdel, The morphology effect of embedded ZnO particles-based composite on flexible hybrid piezoelectric triboelectric nanogenerators for harvesting biomechanical energy, J. Sol-Gel Sci. Technol. 105 (2023) 337–347. <https://doi.org/10.1007/s10971-022-06019-0>.
- [59] X. He, X. Mu, Q. Wen, Z. Wen, J. Yang, C. Hu, H. Shi, Flexible and transparent triboelectric nanogenerator based on high performance well-ordered porous PDMS dielectric film, Nano Res. 9 (2016) 3714–3724. <https://doi.org/10.1007/s12274-016-1198-1>.

1242-3.

- [60] W. Liao, X. Liu, Y. Li, X. Xu, J. Jiang, S. Lu, D. Bao, Z. Wen, X. Sun, Transparent, stretchable, temperature-stable and self-healing ionogel-based triboelectric nanogenerator for biomechanical energy collection, *Nano Res.* 15 (2022) 2060–2068. <https://doi.org/10.1007/s12274-021-3797-x>.
- [61] A. Srivastava, S. Badatya, A.K. Chaturvedi, D.K. Kashyap, A.K. Srivastava, M.K. Gupta, Paddy-Straw-Derived Graphene Quantum Dots Reinforced Vertical Aligned Zinc Oxide Nanosheet-Based Flexible Triboelectric Nanogenerator for Self-Powered UV Sensors and Tribotronics Application, *ACS Appl. Mater. Interfaces.* 15 (2023) 24724–24735. <https://doi.org/10.1021/acsami.3c02036>.
- [62] A. Santhoshkumar, H.P. Kavitha, R. Suresh, Spectroscopic characterisation and antibacterial activity of ZnO nanosheets, *Karbala Int. J. Mod. Sci.* 2 (2016) 196–202. <https://doi.org/10.1016/j.kijoms.2016.06.001>.
- [63] V. Gaddam, R.R. Kumar, M. Parmar, G.R.K. Yaddanapudi, M.M. Nayak, K. Rajanna, Morphology controlled synthesis of Al doped ZnO nanosheets on Al alloy substrate by low-temperature solution growth method, *RSC Adv.* 5 (2015) 13519–13524. <https://doi.org/10.1039/c4ra14049d>.
- [64] W. Muhammad, N. Ullah, M. Haroon, B.H. Abbasi, Optical, morphological and biological analysis of zinc oxide nanoparticles (ZnO NPs) using: *Papaver somniferum* L., *RSC Adv.* 9 (2019) 29541–29548. <https://doi.org/10.1039/c9ra04424h>.
- [65] M.L. da Silva-Neto, M.C.A. de Oliveira, C.T. Dominguez, R.E.M. Lins, N. Rakov, C.B. de Araújo, L. de S. Menezes, H.P. de Oliveira, A.S.L. Gomes, UV random laser emission from flexible ZnO-Ag-enriched electrospun cellulose acetate fiber matrix, *Sci. Rep.* 9 (2019) 1–10. <https://doi.org/10.1038/s41598-019-48056-w>.
- [66] X. Cui, G. Zhu, Y. Pan, Q. Shao, M. Dong, Y. Zhang, Z. Guo, Polydimethylsiloxane-titania nanocomposite coating : Fabrication and corrosion resistance, *Polymer (Guildf).* 138 (2018) 203–210. <https://doi.org/10.1016/j.polymer.2018.01.063>.
- [67] S. Chen, Y. Liu, C. Shao, R. Mu, Y. Lu, J. Zhang, D. Shen, X. Fan, Structural and optical properties of uniform ZnO nanosheets, *Adv. Mater.* 17 (2005) 586–590. <https://doi.org/10.1002/adma.200401263>.
- [68] N.E. Stankova, P.A. Atanasov, N.N. Nedyalkov, T.R. Stoyanchov, K.N. Kolev, E.I. Valova, J.S. Georgieva, S.A. Armyanov, S. Amoruso, X. Wang, R. Bruzzese, fs- and ns-laser processing of polydimethylsiloxane (PDMS) elastomer : Comparative study,

- 336 (2015) 321–328. <https://doi.org/10.1016/j.apsusc.2014.12.121>.
- [69] A.S. Cruz-Félix, A. Santiago-Alvarado, J. Márquez-García, J. González-García, PDMS samples characterization with variations of synthesis parameters for tunable optics applications, *Heliyon*. 5 (2019) e03064. <https://doi.org/10.1016/j.heliyon.2019.e03064>.
- [70] Q.Z. Guo, L.C. Yang, R.C. Wang, C.P. Liu, Tunable Work Function of Mg x Zn 1-x O as a Viable Friction Material for a Triboelectric Nanogenerator, *ACS Appl. Mater. Interfaces*. 11 (2019) 1420–1425. <https://doi.org/10.1021/acsami.8b17416>.
- [71] F. Paquin, J. Rivnay, A. Salleo, N. Stigelin, C. Silva, Multi-phase semicrystalline microstructures drive exciton dissociation in neat plastic semiconductors, *J. Mater. Chem. C*. 3 (2015) 10715–10722. <https://doi.org/10.1039/b000000x>.
- [72] J. Peng, H. Zhang, Q. Zheng, C.M. Clemons, R.C. Sabo, S. Gong, Z. Ma, L.S. Turng, A composite generator film impregnated with cellulose nanocrystals for enhanced triboelectric performance, *Nanoscale*. 9 (2017) 1428–1433. <https://doi.org/10.1039/c6nr07602e>.
- [73] H. Liu, H. Wang, Y. Fan, Y. Lyu, Z. Liu, A triboelectric nanogenerator based on white sugar for self-powered humidity sensor, *Solid. State. Electron.* 174 (2020) 107920. <https://doi.org/10.1016/j.sse.2020.107920>.
- [74] B.U. Ye, B.J. Kim, J. Ryu, J.Y. Lee, J.M. Baik, K. Hong, Electrospun ion gel nanofibers for flexible triboelectric nanogenerator: electrochemical effect on output power, *Nanoscale*. 7 (2015) 16189–16194. <https://doi.org/10.1039/c5nr02602d>.
- [75] N. Jayababu, D. Kim, Co/Zn bimetal organic framework elliptical nanosheets on flexible conductive fabric for energy harvesting and environmental monitoring via triboelectricity, *Nano Energy*. 89 (2021) 106355. <https://doi.org/10.1016/j.nanoen.2021.106355>.
- [76] P. Supraja, R.R. Kumar, S. Mishra, D. Haranath, P.R. Sankar, K. Prakash, N. Jayarambabu, T.V. Rao, K.U. Kumar, A simple and low-cost triboelectric nanogenerator based on two dimensional ZnO nanosheets and its application in portable electronics, *Sensors Actuators A Phys.* 335 (2022) 113368. <https://doi.org/10.1016/j.sna.2022.113368>.
- [77] S. Mishra, S. Potu, R. Sankar, R. Kumar, P. Kodali, H. Divi, A novel ZnS nanosheets-based triboelectric nanogenerator and its applications in sensing , self-powered electronics , and digital systems, *Mater. Today Commun.* 31 (2022) 103292.

<https://doi.org/10.1016/j.mtcomm.2022.103292>.

- [78] X. Kang, C. Pan, Y. Chen, X. Pu, Boosting performances of triboelectric nanogenerators by optimizing dielectric properties and thickness of electrification layer, *RSC Adv.* 10 (2020) 17752–17759. <https://doi.org/10.1039/D0RA02181D>.
- [79] J. He, Y. Liu, D. Li, K. Yao, Z. Gao, X. Yu, Stretchable Triboelectric Nanogenerators for Energy Harvesting and Motion Monitoring, *IEEE Open J. Nanotechnol.* 1 (2020) 109–116. <https://doi.org/10.1109/OJNANO.2020.3019425>.
- [80] Z. Zhang, X. Sun, Y. Chen, D.K. Debeli, J. Guo, Comprehensive dependence of triboelectric nanogenerator on dielectric thickness and external impact for high electric outputs, *J. Appl. Phys.* 124 (2018) 045106. <https://doi.org/10.1063/1.5031809>.
- [81] J. Wang, C. Wu, Y. Dai, Z. Zhao, A. Wang, T. Zhang, Z.L. Wang, Achieving ultrahigh triboelectric charge density for efficient energy harvesting, *Nat. Commun.* 8 (2017) 1–7. <https://doi.org/10.1038/s41467-017-00131-4>.
- [82] H.Y. Mi, X. Jing, M.A.B. Meador, H. Guo, L.S. Turng, S. Gong, Triboelectric Nanogenerators Made of Porous Polyamide Nanofiber Mats and Polyimide Aerogel Film: Output Optimization and Performance in Circuits, *ACS Appl. Mater. Interfaces.* 10 (2018) 30596–30606. <https://doi.org/10.1021/acsami.8b08098>.
- [83] X. Kang, C. Pan, Y. Chen, X. Pu, X. Kang, Y. Chen, X. Pu, C. Pan, X. Pu, Boosting performances of triboelectric nanogenerators by optimizing dielectric properties and thickness of electrification layer, *RSC Adv.* 10 (2020) 17752–17759. <https://doi.org/10.1039/d0ra02181d>.
- [84] A.A. Mathew, S. Vivekanandan, Design and Simulation of Single-Electrode Mode Triboelectric Nanogenerator-Based Pulse Sensor for Healthcare Applications Using COMSOL Multiphysics, *Energy Technol.* 10 (2022) 1–12. <https://doi.org/10.1002/ente.202101130>.
- [85] Y. Su, Y. Yang, X. Zhong, H. Zhang, Z. Wu, Y. Jiang, Z.L. Wang, Fully enclosed cylindrical single-electrode-based triboelectric nanogenerator, *ACS Appl. Mater. Interfaces.* 6 (2014) 553–559. <https://doi.org/10.1021/am404611h>.
- [86] H.W. Park, N.D. Huynh, W. Kim, C. Lee, Y. Nam, S. Lee, K.B. Chung, D. Choi, Electron blocking layer-based interfacial design for highly-enhanced triboelectric nanogenerators, *Nano Energy.* 50 (2018) 9–15. <https://doi.org/10.1016/j.nanoen.2018.05.024>.

7.7 Supporting information

Table S7.1: Comparison table of various surface modification methods and their TENG output performance.

S.No.	Surface Modification Process	Process details	Materials surface modified	TENG Output-Before surface modification		TENG Output-After surface modification		Increment in the TENG output	References
				V_{oc}	I_{sc}	V_{oc}	I_{sc}		
1.	Manual polishing using sand paper	Simple, and cost effective	Al, Kapton	~20 V	Not mentioned	~65 V	Not mentioned	3 times	[35]
2.	Sandpaper Templates	Simple and cost Effective	PDMS	~35V	Not mentioned	~200 V	~ 0.389 $\mu\text{A}/\text{cm}^2$	~5.5 times	[36]
3.	Inductive-coupled plasma etching	Time consuming as well as not cost effective	Polyethylene terephthalate (PET)	~80 V	~ 2.88 $\mu\text{A}/\text{cm}^2$	~220 V	~ 7.2 $\mu\text{A}/\text{cm}^2$	3 times	[37]
4.	Sand paper assisted soft lithography	Simple and fast	silicone elastomer film	~100 V	~ 0.17 $\mu\text{A}/\text{cm}^2$	~370 V	~ 0.68 $\mu\text{A}/\text{cm}^2$	~3.7 times	[38]
5.	CO2 laser ablation and PDMS casting	Not cost effective	Al and PDMS	~33 V	~ 0.98 $\mu\text{A}/\text{cm}^2$	~123 V	~ 3.6 $\mu\text{A}/\text{cm}^2$	~3.66 times	[39]
6.	Base treated PDMS Surface	Simple and fast	PDMS surface	~3.8 V	~ 10.4 nA/cm^2	~49.3 V	~ 185.6 nA/cm^2	~15 times	[40]
7.	Manual polishing using sand paper	Simple, fast and cost Effective	Aluminum	57.25 V	~ 0.454 $\mu\text{A}/\text{cm}^2$	~262 V	~ 2.33 $\mu\text{A}/\text{cm}^2$	~5 times	[33]
8.	Manual polishing using sand paper	Simple, fast and cost Effective	Aluminum	399.3V	~2.05$\mu\text{A}/\text{cm}^2$	975.73V	~ 6.78 $\mu\text{A}/\text{cm}^2$	~3 times	Current Work

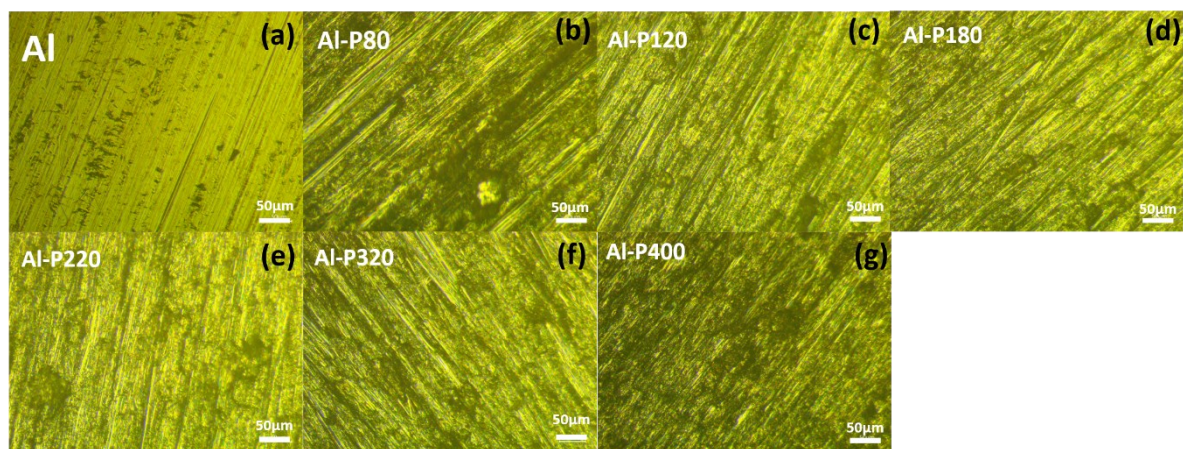


Figure S7.1: Optical images of the surface of plane aluminum and scratched aluminum with different grit sizes (a) Plane (b) P80, (c) P120, (d) P150, (e) P180, (f) P320, and (g) P400 respectively.

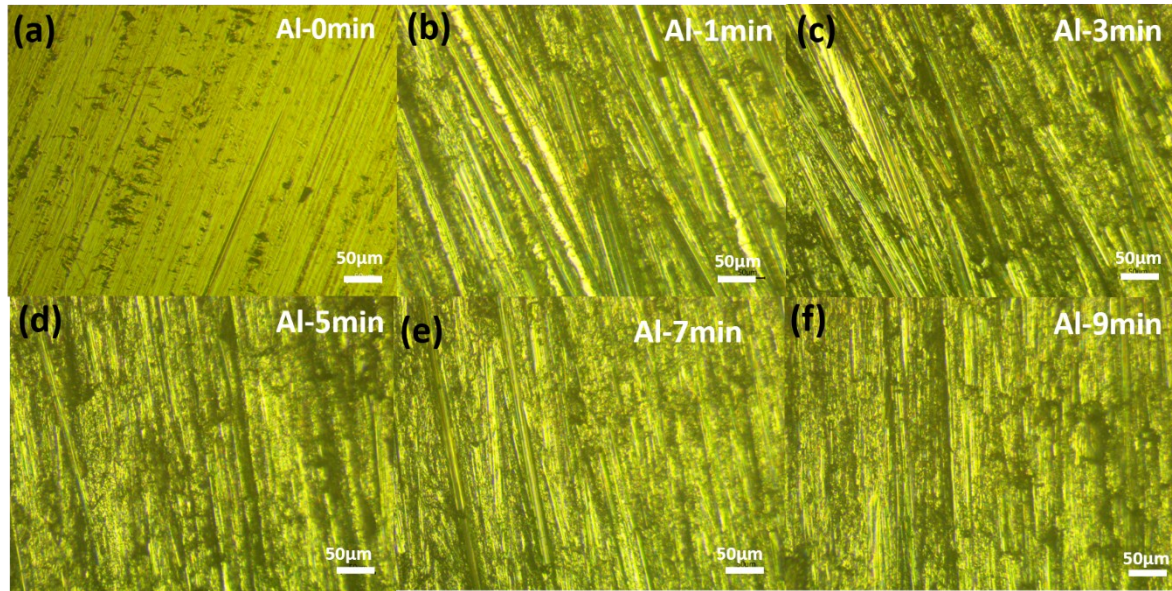


Figure S7.2: Optical images of aluminum scratched for various time durations of (a) 0 min, (b) 1 min, (c) 3 min, (d) 5 min, (e) 7 min, (f) 9 min with fixed grit size sandpaper of P220.

Table S7.2: Different TENGs with fixed PDMS as another tribo-layer: device codes, device structure and output responses listed below.

S.No.	TENG code	Tribolayer-1	Device structure	S.No.	TENG code	Tribolayer-1	Device structure
1.	T1	Plan aluminum	Aluminum PDMS Aluminum	10.	T10	ZnO nanosheets on scratched aluminum with sandpaper (grit size- P120, scratching time-5min)	Al120 ZnO PDMS Aluminum
2.	T2	Aluminum scratched with sandpaper grit of P80	Aluminum PDMS Al80	11.	T11	ZnO nanosheets on scratched aluminum with sandpaper (grit size- P180, scratching time-5min)	Al180 ZnO PDMS Aluminum
3.	T3	Aluminum scratched with sandpaper grit of P120	Aluminum PDMS Al120	12.	T12	ZnO nanosheets on scratched aluminum with sandpaper (grit size- P220, scratching time-5min)	Al220 ZnO PDMS Aluminum
4.	T4	Aluminum scratched with sandpaper grit of P180	Aluminum PDMS Al180	13.	T13	ZnO nanosheets on scratched aluminum with sandpaper (grit size- P320, scratching time-5min)	Al320 ZnO PDMS Aluminum
5.	T5	Aluminum scratched with sandpaper grit of P220	Aluminum PDMS Al220	14.	T14	ZnO nanosheets on scratched aluminum with sandpaper (grit size- P400, scratching time-5min)	Al400 ZnO PDMS Aluminum

Surface-Engineered High-Performance TENG.... Health Monitoring and Electronics

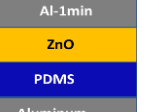
6.	T6	Aluminum scratched with sandpaper grit of P320		15.	T15	ZnO nanosheets on scratched aluminum with sandpaper (grit size- P220, scratching time-1min)	
7.	T7	Aluminum scratched with sandpaper grit of P400		16.	T16	ZnO nanosheets on scratched aluminum with sandpaper (grit size- P220, scratching time-3min)	
8.	T8	ZnO nanosheets on Plan aluminum		17.	T17	ZnO nanosheets on scratched aluminum with sandpaper (grit size- P220, scratching time-7min)	
9.	T9	ZnO nanosheets on scratched aluminum with sand paper(grit size- P80, scratching time-5min)		18.	T18	ZnO nanosheets on scratched aluminum with sandpaper (grit size- P220, scratching time-9min)	

Table S7.3: Amount of enhancement in the output voltage and current of ZnO on Scratched Al with respect to the ZnO on plane Al TENG devices.

Sample code	V _{oc}	I _{sc}	enhancement with respect to T8	
			V _{oc}	I _{sc}
T8	495.091	75.02		
T9	554.545	88.364	1.12	1.18
T10	640.727	107.636	1.29	1.43
T11	758.545	149.818	1.53	2.00
T12	975.727	169.636	1.97	2.26
T13	720.182	105.455	1.45	1.41
T14	526.364	82.873	1.06	1.10

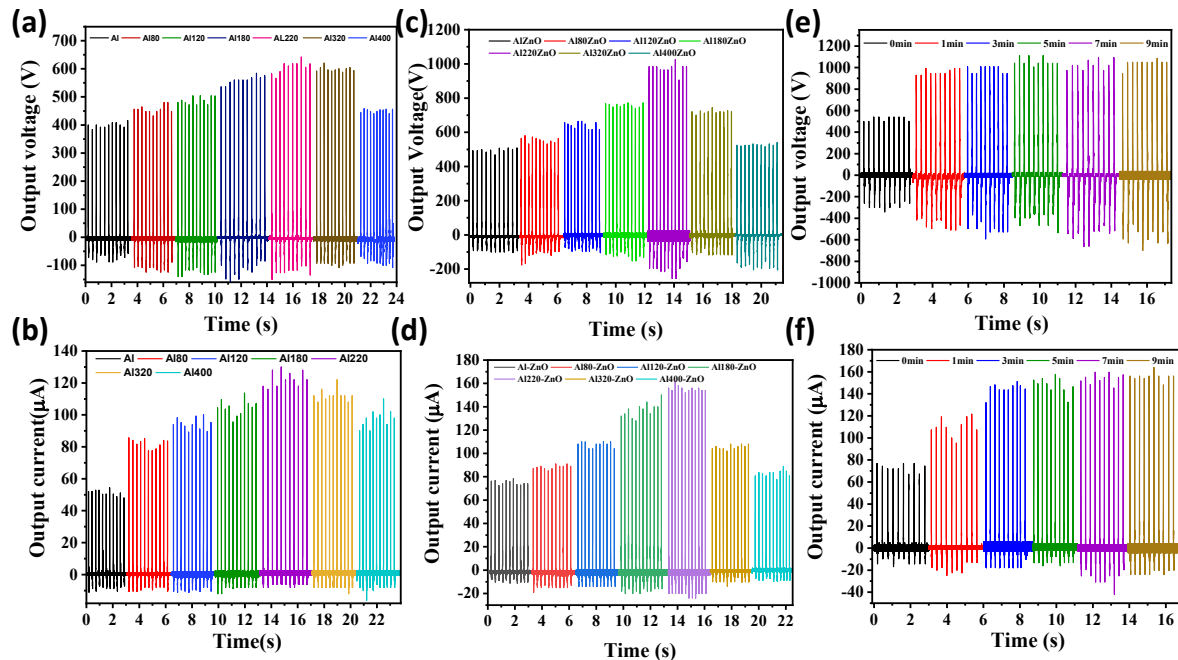


Figure S7.3: Output voltage and current response of the TENG, (a-b) plane and scratched aluminum with different grits (80, 120, 180, 220, 320, 400), (c-d) ZnO nanosheets deposited on scratched aluminum with different grits, and (e-f) ZnO sheets deposited on aluminum with 220 grits size at different scratching timings (0 min, 1 min, 3 min, 5 min, 7 min, 9 min), respectively.

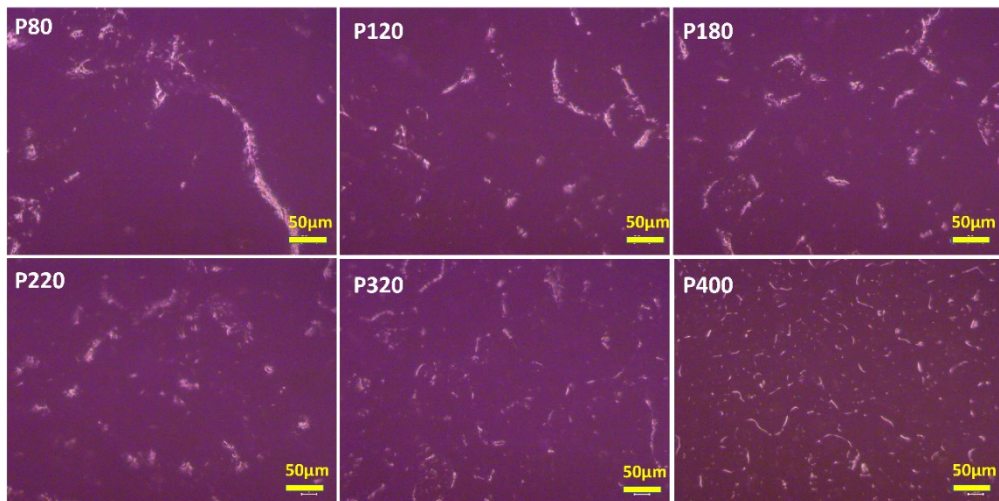


Figure S7.4: Optical microscope images of sand papers with different grit sizes (80,150,180,220,320,400).

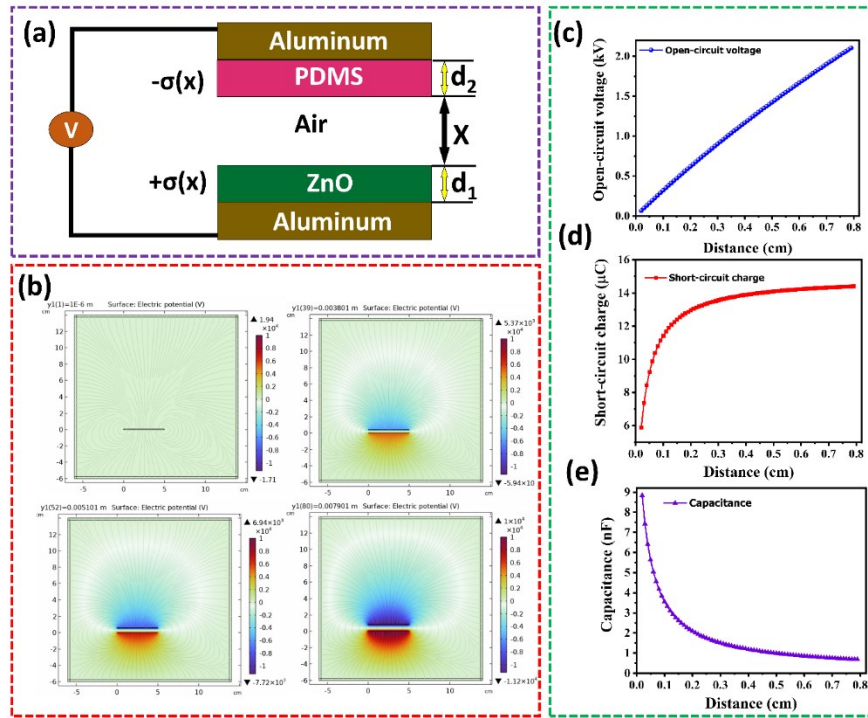


Figure S7.5: Finite element simulation of TENG: (a) schematic configuration TENG device model, (b) Time lapse images of the electric potential distribution from contact to separate state of triboelectric layers, (c) open-circuit voltage as a function of spacing distance (x), (d) transferred short-circuit charge as a function of spacing distance(x), and, (e) capacitance between the electrodes as a function of spacing distance (x).

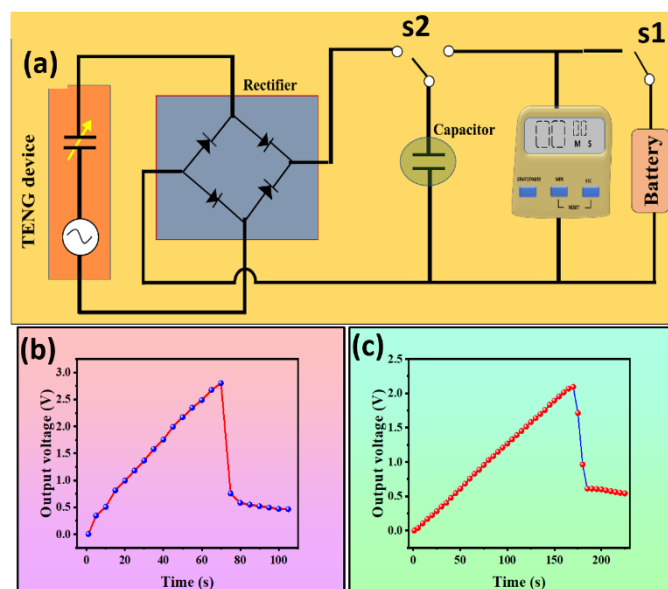


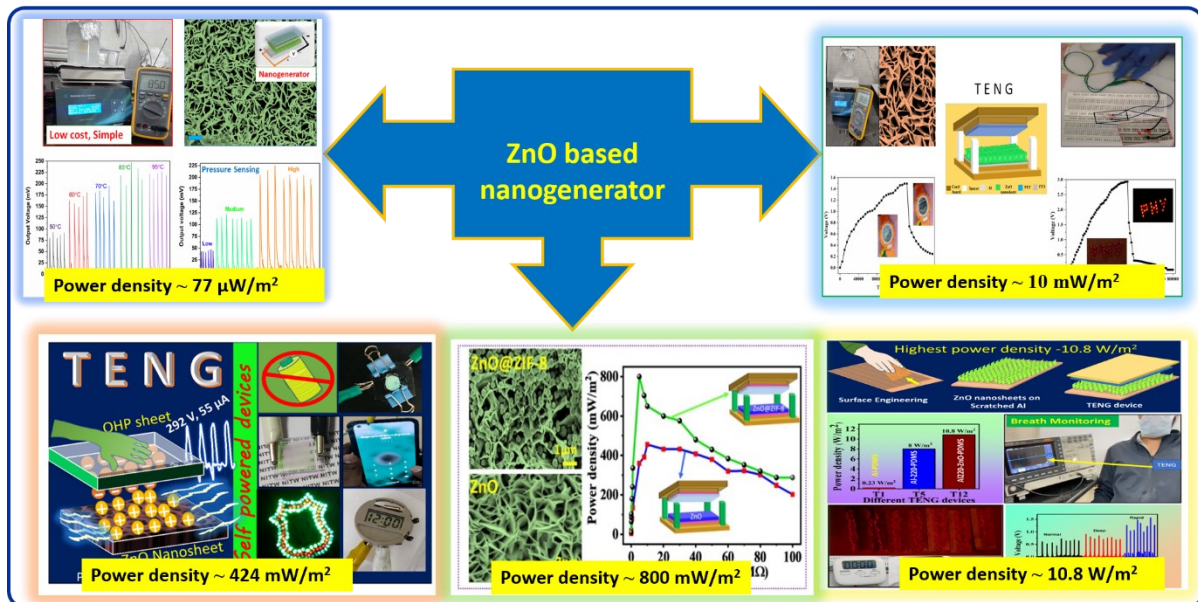
Figure S7.6: (a) Schematic representation of TENG with rectifier circuit and rectified out directly connected to LEDs, (b-c) Charging capacitor curves corresponds to hygrometer and digital vernier callipers.

Chapter-8

Summary, Conclusions and Scope for Future work

The summary and outcomes from the research done on ZnO-based nanogenerators (PENG/TENG) are presented in the last chapter. Recommendations and directions for future research are outlined.

8.1 Summary and conclusions



- Successful synthesis of ZnO nanosheets was achieved through a cost-effective hot-plate-assisted hydrothermal method.
- Extensive optical, structural, morphological, and microstructural analyses were conducted for all samples. Fabrication and in-depth characterization of Piezoelectric and Triboelectric Nanogenerator (PENG and TENG) devices were conducted.
- The PENG device, which featured ZnO nanosheet film between ITO and aluminum electrodes, produced an output voltage of 220 mV and a power density of 77 μ W/m² at a load resistance of 0.2 M Ω . The TENG device, employing ZnO nanosheet film, ITO, and aluminum electrodes, generated an output voltage, current, and power density of 2.5 V, 8 μ A, and 1.6 mW/m², respectively, operating under vertical contact separation mode through hand tapping. The TENG demonstrated the ability to charge a 1 μ F capacitor up to 1.8 V, stored a maximum energy of 2.8 μ J, and directly powered one LED for each hand tapping.
- The TENG performance was further enhanced with a novel tribo pair, utilizing ZnO nanosheets and PET surfaces as triboelectric layers. This development resulted in an output voltage, current, and power density of 4.9 V, 10 μ A, and 10 mW/m², respectively. The TENG could directly drive three LEDs, a digital watch, and 24 LEDs with a storage element. The device exhibited robust stability under both hand and machine tapping, maintaining consistent output over three months.
- This study introduced a new tribo-layer of OHP sheets (PET surface having a pre-charged). This innovative setup yielded an impressive output voltage, current, and power density of 292 V, 55 μ A, and 424 mW/m², respectively. The TENG was successfully integrated with a self-powered Cholesteric Liquid Crystal (CLC) device, opening up applications in security, display technology, and smart windows. Moreover, it directly powered an electroluminescence device, illuminating 130 LEDs with each hand-tapping force, making it suitable for e-paper and digital billboard applications.
- Using a surface modification approach, zeolitic imidazolate framework-8 (ZIF-8) crystals are directly grown on the ZnO nanosheets by adopting a simple and low-cost hydrothermal method. The surface modification using ZnO@ZIF-8 substantially increased the number of contact points between the triboelectric materials, leading to remarkable improvements in the output performance of the TENG. Specifically, the Z8-TENG demonstrated a remarkable increase in output voltage, current, and power density by 1.39, 1.44, and 1.76 times, respectively, compared to the Z-TENG. Additionally, ZnO@ZIF-8 TENG was

Summary, Conclusions and Scope for Future work

demonstrated the capability to power multiple electronic gadgets (digital watch, thermometer, and calculator) by charging capacitors and powering 180 LEDs directly. This TENG has potential in various energy harvesting and self-powered applications.

- The development of a high-performance TENG was achieved by surface engineering one of the triboelectric layers, utilizing emery papers with different grit sizes. The TENG, featuring ZnO nanosheets on aluminum and flexible PDMS as triboelectric layers, delivered maximum output voltage, current, and power density of 1442 V, 155 μ A, and 10.8 W/m² at a load resistance of 10 M Ω , respectively. It could power 824 LEDs and multiple electronic devices without the need for a storage element. Due to its high-power density and sensitivity, it was explored as a wearable device, attached to various body parts to act as a self-powered breath monitoring sensor.

Table 8.1: Efficiency of the TENG devices

S. No.	TENG Design	Power density	Efficiency
1	ZnO-ITO	1.6 mW/m ²	0.032%
2	ZnO-PET	10 mW/m ²	0.44%
3	ZnO-OHP	424 mW/m ²	6.3%
4	ZnO-PMMA	800 mW/m ²	41.36%
5	ZnO-PDMS	10.8 W/m ²	68%

8.2 Scope for future work

- ❖ To enhance the power density of TENG, promising strategies include the exploration of novel materials, improvement of contact intimacy, optimization of operational conditions, and the incorporation of thin films as dielectric layers.
- ❖ Ensuring the long-term durability of TENG for sustained high-power generation is a critical consideration, particularly for its large-scale applications.
- ❖ The advancement of TENG technology for blue energy harvesting is an area that demands attention. While significant efforts have been made to boost energy harvesting efficiency, the adaptability of TENG in real marine environments should be a focus in future research.
- ❖ The commercialization of optimized TENG designs and the expansion of their utility into various other potential applications is an important next step in realizing the full potential of this technology.
- ❖ Develop new TENG designs that produce the DC output voltage and develop new power management circuits for TENG.

List of Publications

(A) Publications related to Ph.D. Thesis

(a) SCI Journal Publications

1. “*A Simple and Low-Cost Approach for the Synthesis and Fabrication of ZnO Nanosheet-Based Nanogenerator for Energy Harvesting and Sensing*”, **Supraja Potu**, Rakesh Kumar, Siju Mishra, D Haranath, P Ravi Sankar and K Prakash, **Engineering Research Express**, Vol 3, No 3, 2021, 035022. <https://doi.org/10.1088/2631-8695/ac184b>.
2. “*A Simple and Low-Cost Triboelectric Nanogenerator Based on Two Dimensional ZnO Nanosheets and Its Application in Portable Electronics*”, **Supraja Potu**, R. Rakesh Kumar, Siju Mishra, D. Haranath, P. Ravi Sankar, K. Prakash, N. Jayaram babu, T. Venkatappa Rao, K. Uday Kumar, **Sensors Actuators A Phys.** 2022, 335, 113368. <https://doi.org/10.1016/J.SNA.2022.113368>.
3. “*High-Performance and Low-Cost Overhead Projector Sheet-Based Triboelectric Nanogenerator for Self-Powered Cholesteric Liquid Crystal, Electroluminescence, and Portable Electronic Devices*”. **Supraja Potu**, Navaneeth M, Rakesh Kumar R, Buchaiah G, Jayalakshmi V, Siju Mishra, Haranath D, Anjaly Babu, Uday Kumar K, and Prakash K, **ACS Applied Energy Materials**. 2022. <https://doi.org/10.1021/acsadem.2c02359>.
4. “*Enhancing Triboelectric Nanogenerator Performance with Metal-Organic Framework Modified ZnO Nanosheets for Self-Powered Electronic Devices and Energy Harvesting*”. **Supraja Potu**, M. Navaneeth, Anshika Bhadoriya, Arbacheena Bora, Yuvaraj Sivalingam, Anjaly Babu, Mahesh Velpula, Buchaiah Gollapelli, Rakesh Kumar Rajaboina*, Uday Kumar Khanapuram, Haranath Divi, Prakash Kodali, and Lakshakoti Bochu, **ACS Applied Nano Materials**, 2023, <https://doi.org/10.1021/acsanm.3c03430>.
5. “*Surface-Engineered High-Performance Triboelectric Nanogenerator for Self-Powered Health Monitoring and Electronics*”, **Supraja Potu**, Navaneeth Madathil, Siju Mishra, Arbacheena Bora, Yuvaraj Sivalingam, Anjaly Babu, Mahesh Velpula, Lakshakoti Bochu, Balaji Ketharachapalli, Anu Kulandaivel, Rakesh Kumar Rajaboina*, Uday Kumar Khanapuram, Haranath Divi, Prakash Kodali, Banavoth Murali, and Ravi Ketavath, **CS Appl. Eng. Mater.** 2023, 1, 10, 2663–2675, <https://doi.org/10.1021/acsadem.3c00416>.

(b) Chapter in Book

1. "Advances in Zinc Oxide (ZnO) Nanostructure-Based Nanogenerators: Challenges and Opportunities", **Supraja Potu**, Siju Mishra, R. Rakesh Kumar, D. Haranath, K. Uday Kumar, and Hitesh Borkar, Nova Science Publishers, Inc., 43-71, 36, 2022.

(c) International/National Conferences

1. **Poster presentation** at the National Conference on Luminescence and its Application (NCLA-2021) with the title "*Piezoelectric nanogenerators for energy harvesting*" organized at Department of Physics, NIT Warangal during Feb. 10-12, 2020, Warangal, Telangana, India.
2. Presented a Paper on the topic entitled "*Triboelectric Nanogenerator Based on ZnO Nanosheet Networks for Mechanical Energy Harvesting*" at 2nd International Conference on Power Electronics & IoT Applications in Renewable Energy and its Control (PARC) organized by GLA Institute of Technology and Management, India, during Jan. 21-22, 2022 published in **IEEE XPLOR**,2022, <https://doi.org/10.1109/PARC52418.2022.9726684>
3. Presented a Paper on the topic entitled "*Study of ZnO nanosheets growth parameters effect on the performance of the triboelectric nanogenerator*" at 2nd International Conference on Advancements in Materials Science and Technology (iCAM) organized by the Sathyabama Institute of Science and Technology, India, during Nov 2022, published in **Materials today proceedings**, <https://doi.org/10.1016/j.matpr.2023.02.087>.

(B) Journal Publications other than Thesis

(a) Publications

1. "*Piezoelectric flexible nanogenerator based on ZnO nanosheet networks for mechanical energy harvesting*", Y. Manjula, R. Rakesh Kumar, P. Missak Swarup Raju, G. Anil Kumar, T.Venkatappa Rao, A. Akshaykranth, **Supraja Potu**, **Chemical Physics**, 533, 1 May 2020,110699, <https://doi.org/10.1016/j.chemphys.2020.110699>
2. "*Characteristics of 2D ZnO-based piezoelectric nanogenerator and its application in non-destructive material discrimination*", **Supraja Potu**, P Ravi Sankar, R Rakesh Kumar, K Prakash, N Jayarambabu and T Venkatappa Rao, **Adv. Nat. Sci: Nanosci. Nanotechnol.** 12 025011,2021, [DOI 10.1088/2043-6262/ac079a](https://doi.org/10.1088/2043-6262/ac079a).
3. "*Enhanced output of ZnO nanosheet-based piezoelectric nanogenerator with a novel device structure*", Siju Mishra, **Supraja Potu**, Vishnu V Jaiswal, P Ravi Sankar, R Rakesh Kumar,K Prakash, K Uday Kumar and D Haranath, **Eng. Res. Express** 3 045022, 2021, DOI 10.1088/2631-8695/ac34c3.

4. "A novel triboelectric nanogenerator based on only food packaging aluminium foils", P. Ravi Sankar, **Supraja Potu**, Siju Mishra, K. Prakash, R. Rakesh Kumar, D. Haranath, **Materials letters**, 310, 1 March 2022, 131474, <https://doi.org/10.1016/j.matlet.2021.131474>
5. "A triboelectric nanogenerator based on food packaging Aluminum foil and Parafilm for self-powered electronics", P Ravi Sankar, K Prakash, **Supraja Potu**, R Rakesh Kumar, Siju Mishra and D Haranath, 2021 **Phys. Scr.** 96 125005, DOI 10.1088/1402-4896/ac2086.
6. "A Novel ZnS Nanosheets-Based Triboelectric Nanogenerator and Its Applications in Sensing, Self-Powered Electronics, and Digital Systems", Siju Mishra, **Supraja Potu**, P. Ravi Sankar, R.Rakesh Kumar, K. Prakash and, Haranath Divi, **Materials Today Communication** 2022, 31 103292. <https://doi.org/10.1016/j.mtcomm.2022.103292>.
7. "Controlled Synthesis of Luminесcent ZnS Nanosheets with High Piezoelectric Performance for Designing Mechanical Energy Harvesting Device", Siju Mishra, **Supraja Potu**, P. Ravi Sankar, R. Rakesh Kumar, K. Prakash and, Haranath Divi, **Material Chemistry and Physics** 2022, 277, 125264. <https://doi.org/10.1016/j.matchemphys.2021.125264>.
8. "Plant-Based Triboelectric Nanogenerator for Biomechanical Energy Harvesting". Anjaly Babu, D. Rakesh, **Supraja Potu**, Siju Mishra, K. Uday Kumar, R. Rakesh Kumar, D. Haranath, Estari Mamidala, Raju Nagpuri, **Results in Surfaces and Interfaces**, Volume 8, 1 August 2022, 100075. <https://doi.org/10.1016/j.rsurfi.2022.100075>
9. "Mechanically stable ultrathin flexible metallic Au/Pt/Au tri-layer as an alternative transparent conducting electrode for optoelectronic device applications", Reddivari Muniramaiah, Jean Maria Fernandes, M. Manivel Raja , Dilli Babu Padmanaban, **Supraja Potu**, M. Rakshita , Nandarapu Purushotham Reddy , Gouranga Maharana , M Kovendhan , Ganapathy Veerappan , Gangalakurti Laxminarayana , R. Rakesh Kumar, D. Haranath, D. Paul Joseph, **Vacuum**, 206, December 2022, 111487, <https://doi.org/10.1016/j.vacuum.2022.111487>.
10. "ZIF-67 metal-organic frameworks based triboelectric nanogenerator for self powered devices", Sachin Barsiwal, Anjaly Babu, Uday Kumar Khanapuram, **Supraja Potu**, Navneeth Madathil, Rakesh Kumar Rajaboina, Siju Mishra, Haranath Divi, Prakash Kodali, Raju Nagapuri and Thirmal Chinthakuntla, **Nano energy Adv.** 2022, 2(4), 291-302; <https://doi.org/10.3390/nanoenergyadv2040015>.
11. "Effect of Surface and Contact Points Modification on the Output Performance of Triboelectric Nanogenerator", Siju Mishra, **Supraja Potu**, D. Haranath, R. Rakesh Kumar, Someshwar Pola, **Nano Energy**, 104, Part A, 15 December 2022, 107964, <https://doi.org/10.1016/j.nanoen.2022.107964>.
12. "Energy harvesting properties of the Nafion thin films", Babu Anjaly, **Supraja Potu**, Mishra Siju, Kumar, K Uday, Rakesh Kumar R, Haranath D, Thirmal C, Raju N, T VenkatappaRao, Balaji, K Rajinikanth, **Engineering Research Express**, 2022, DOI:10.1088/2631-8695/ac9e8c.
13. "A Triboelectric nanogenerator based on commercial ITO-PET sheets for mechanical energy harvesting and self-powered indicator display applications", M. Navaneeth, **Supraja Potu**, Anjaly Babu, K. Uday Kumar, K. Prakash, R. Rakesh Kumar, **Materials Letters**, 336, 2023, 133866, <https://doi.org/10.1016/j.matlet.2023.133866>.
14. "Medical Waste X-ray Film Based Triboelectric Nanogenerator for Self-Powered Devices, Sensors, and Smart Buildings", M. Navaneeth, **Supraja Potu**, Anjaly Babu,

- Rakesh Kumar Rajaboina, Uday Kumar K, Haranath Divi, Prakash Kodali and Balaji K, **Environ. Sci.: Adv.**, 2023, 2, 848-860, <https://doi.org/10.1039/D3VA00018D>.
15. "Electronically Robust Self-Assembled Supramolecular Gel as a Potential Material in Triboelectric Nanogenerators", Arun Kumar Rachamalla, **Supraja Potu**, Vara Prasad Rebaka, Tohira Banoo, Yogendra Kumar, Dr. C. Uma Maheswari, Dr. Vellaisamy Sridharan, Dr. Rakesh Kumar Rajaboina, **Chemistry – A European Journal**, 29, 34, 2023, e202301076, <https://doi.org/10.1002/chem.202301076>.
 16. "Sputter-deposited highly flexible noble metal multi-layer electrode viable for energy and luminescent devices", Reddivari Muniramaiah, Gouranga Maharana, Jean Maria Fernandes, M. Manivel Raja, Dilli Babu Padmanaban, **Supraja Potu**, M. Rakshita, Nandarapu Purushotham Reddy, M. Kovendhan, Gangalakurti Laxminarayana, R. Rakesh Kumar, D. Haranath, D. Paul Joseph, **Surfaces and Interfaces**, 39, 2023, 102949, <https://doi.org/10.1016/j.surfin.2023.102949>.
 17. "A Unique Contact Points Modification Technique for Boosting the Performance of a Triboelectric Nanogenerator and its Application in Road Safety Sensing and Detection", Siju Mishra, M. Rakshita, Haranath Divi, **Supraja Potu** and R. Rakesh Kumar, **ACS Applied Materials and Interfaces**, 2023. <https://doi.org/10.1021/acsami.3c04848>.
 18. "High-performance triboelectric nanogenerator based on 2D graphitic carbon nitride for self-powered electronic devices", K. Ruthvik, Anjaly Babu, **Supraja Potu**, M. Navaneeth, V. Mahesh, K. Uday Kumar, R. Rakesh Kumar, B. Manmada Rao, D. Haranath, K. Prakash, 350, 2023, 134947, <https://doi.org/10.1016/j.matlet.2023.134947>.
 19. "Wood plastic composites (WPC) waste based triboelectric nanogenerator for mechanical energy harvesting and self-powered applications", V. Lakshmi Sunitha, **Supraja Potu**, K.A.K. Durga Prasad, M. Navaneeth, Anjaly Babu, V. Mahesh, K. Uday Kumar, D. Haranath, R. Rakesh Kumar, **Materials Letters**, 351, 2023, 134995, <https://doi.org/10.1016/j.matlet.2023.134995>.
 20. "Transforming Medical Plastic Waste into High-Performance Triboelectric Nanogenerators for Sustainable Energy, Health Monitoring, and Sensing Applications", M. Navaneeth, **Supraja Potu**, Anjaly Babu, B. Lakshakoti, Rakesh Kumar Rajaboina, Uday Kumar K, Haranath Divi, Prakash Kodali, and K. Balaji, **ACS Sustainable Chem. Eng.** 2023, 11, 32, 12145–12154, <https://doi.org/10.1021/acssuschemeng.3c03136>.
 21. "Facile Direct Growth of ZIF-67 Metal–Organic Framework for Triboelectric Nanogenerators and Their Application in the Internet of Vehicles", Anjaly Babu, Lakshakoti Bochu, **Supraja Potu**, Ruthvik Kaja, Navaneeth Madathil, Mahesh Velpula, Anu Kulandaivel, Uday Kumar Khanapuram*, Rakesh Kumar Rajaboina*, Haranath Divi, Prakash Kodali, Balaji Ketharachapalli, and Rajanikanth Ammanabrolu, **ACS Sustainable Chem. Eng.** 2023, 11, 47, 16806–16817, <https://doi.org/10.1021/acssuschemeng.3c05198>.
 22. "High-performance triboelectric nanogenerator using ZIF-67/PVDF hybrid film for energy harvesting", Anjaly Babu, K. Ruthvik, **Supraja Potu**, M. Navaneeth, K. Uday Kumar, R. Rakesh Kumar, K. Prakash & N. Raju, **Journal of Materials Science: Materials in Electronics**, 34, 2195, (2023), <https://doi.org/10.1007/s10854-023-11644-8>.

(b) Conference Proceedings

1. "Effect of Growth-Temperature on Morphology and Piezoelectric Characteristics of ZnS Nanostructure", Siju Mishra; **Supraja Potu**; R. Rakesh Kumar; D. Haranath, IEEE XPLOR, 2022, <https://doi.org/10.1109/PARC52418.2022.9726549>.
2. "A Triboelectric Nanogenerator Based on PDMS and Parafilm For Biomechanical Energy Harvesting", P. Ravi Sankar; **Supraja Potu**; K. Prakash; R. Rakesh Kumar, IEEE XPLOR, 2022 <https://doi.org/10.1109/PARC52418.2022.9726560>.
3. "Enhancing the Output of ZnO Nanosheet based Piezoelectric Nanogenerator by Molar Ratio Modifications", Siju Mishra; **Supraja Potu**; R. Rakesh Kumar; D. Haranath, **Materials Today Proceedings**, 2023. <https://doi.org/10.1016/j.matpr.2023.04.224>.

(c) Review papers

1. "Crystalline Porous Material-Based Nanogenerators: Recent Progress, Applications, Challenges, and Opportunities", Rakesh Kumar Rajaboina, Uday Kumar Khanapuram, Venkateswaran Vivekananthan, Gaurav Khandelwal, **Supraja Potu**, Anjaly Babu, Navaneeth Madathil, Mahesh Velpula, Prakash Kodali, 2023, <https://doi.org/10.1002/smll.202306209>.
2. "Advances in Ferrofluid-Based Triboelectric Nanogenerators: Design, Performance, and Prospects for Energy Harvesting Applications", Anu Kulandaivel, **Supraja Potu**, Anjaly Babu, Navaneeth Madathil, Mahesh Velpula, Rakesh Kumar Rajaboina, Uday Kumar Khanapuram, Nano Energy 120, 2024, 109110, <https://doi.org/10.1016/j.nanoen.2023.109110>.

Curriculum vitae

Potu Supraja (Ph.D.)

Full Correspondence Address: Bhupalpally, Jayashankar
bhupalpally-506169, Telangana, INDIA.Telangana, India.

Mobile: +91 7330993889, 8328183122

Email: suprajapotu@gmail.com, supraja1210@student.nitw.ac.in

❖ Personal Details:

1. Father Name:	Mr. Potu Balreddy
2. Mother Name:	Mrs. Vinodha
3. Date of Birth:	20th August 1994
4. Sex:	Female
5. Marital Status:	Unmarried
6. Language Skills:	Telugu, Hindi, English (Read & Write)
7. Whether differently abled (Yes/No):	No

❖ Academic Profile:

- M.Sc. Physics with specialization in Material Science (May 2018) from Dept. of Physics, **Kakatiya Degree College, Kakatiya University, Warangal** with a Percentage of **65.8%**.
- B.Sc. (MPCs) (May 2015) from **Sangamitra degree College, Kakatiya University, Warangal** with Percentage of **77.8%**.
- Intermediate (10+2) (MPC) (May 2012) from **SS Junior College (Board of Intermediate Education A.P)** with a Percentage of **85%**.
- SSC (10th) (May 2010) from **Cambridge High School (Board of Secondary Education A.P)** with a Percentage of **81.6%**.

❖ Research interest:

- Energy harvesting
- Nanogenerators, Nanomaterials
- Sensor devices

❖ Research Experience:

Research Designation: Senior Research Fellow (Four Years: 2019 – 2024)

Institute/University: National Institute of Technology Warangal - 506 004, Telangana.

Title of the Research Work: *“Design and Development of ZnO Nanosheet based Nanogenerators to Drive Self-Powered Systems”* Department of Physics, National Institute of Technology Warangal (NITW), Telangana, INDIA.

❖ Technical Experience:

➤ Computer/software experience:

- Design and Simulation Softwares: Origin lab, ImageJ, X-pert High score, Chem-Draw, COMSOL.

➤ Instruments handled:

- Electrospinning,
- Keithley source meter.

➤ Data Analysis Instruments:

- XRD, TEM, SEM, AFM, SKP, Raman Spectroscopy, UV-Vis Spectroscopy, Photoluminescence, FTIR, etc.

➤ Synthesis/Fabrication Techniques:

- Hydrothermal, Solvothermal, Doctor Blade Method, Spin, and Dip Coating.

❖ Academic Achievements:

1. Achieved an All-India Rank (AIR) of 1452 in **GATE-2019**.
2. qualified in the Joint Entrance Screening Test (**JEST**) in 2019.
3. qualified in the State Eligibility Test (**SET**) in 2019.

❖ Research web links:

SCI Papers: <https://www.researchgate.net/profile/Supraja-Potu>,
<https://orcid.org/0000-0001-5612-4035>.

Citations: <https://scholar.google.com/citations?user=1x62tpIAAAAJ&hl=en>

REFERENCES:**1. Dr. Rakesh Kumar**

Assistant Professor

Energy Materials & Devices Group

Department of Physics

National Institute of Technology Warangal

Warangal 506 004, Telangana State, INDIA

E-mail: rakeshr@nitw.ac.in

Declaration

I hereby declare that the above-written particulars are true and correct to the best of my knowledge and belief.

Date: 5th January 2024

Place: Warangal.

Yours sincerely



(P Supraja)